



TECHNISCHE
UNIVERSITÄT
WIEN
Vienna University of Technology

DISSERTATION

Ionic Nanoparticle Networks: Hybrid Materials with Versatile Properties

ausgeführt zum Zweck der Erlangung des akademischen Grades eines

Doktors der Naturwissenschaften

unter der Leitung von

Prof. Dr. Marie-Alexandra Néouze

E165

Institut für Materialchemie

Eingereicht an der Technischen Universität Wien

Fakultät für Technische Chemie

von

Dipl.-Chem. Martin Kronstein

Matr.Nr. 1128465

Max-Winter-Platz 21/22, 1020 Wien

Wien, am 05.08.2014

Früher starben die Menschen mit 35 Jahren,
heute schimpfen sie bis 95 auf die Chemie.

Carl H. Krauch

Danksagung

Besonderer Dank gilt meiner Betreuerin Prof. Marie-Alexandra Néouze für die Möglichkeit an diesem interessanten Thema zu arbeiten und für die Freiheit meine eigenen Ideen einzubringen und umzusetzen. Prof. Ulrich Schubert danke ich für die Möglichkeit diese Arbeit in seiner Arbeitsgruppe durchzuführen. Des Weiteren danke ich Prof. Herwig Peterlik für die Übernahme der Zweitgutachtertätigkeit.

Vielen Dank an alle Leute ohne deren Hilfe diese Arbeit nicht möglich gewesen wäre: Johanna Akbarzadeh und Prof. Herwig Peterlik für die zahlreichen SAXS Messungen, Elisabeth Eitenberger für die REM-Messungen, Prof. Johannes Bernardi für die TEM-Messungen, Christian Gierl-Mayer für die TGA/MS Messungen. Des Weiteren bedanke ich mich bei Prof. Nathaniel D. Robinson und seiner Arbeitsgruppe an der Universität Linköping (Schweden), für die Hilfe bei den QCM Messungen und bei den elektrischen Charakterisierungen der Materialien, sowie für die angenehme Arbeitsatmosphäre während meiner zwei Aufenthalte in Schweden. Frederik Tielens und Christel Gervais von der Sorbonne Université Paris danke ich für die DFT und *ab-initio* Berechnungen, sowie für die Aufnahme der Festkörper-NMR Spektren, Prof. Arne Thomas und Jérôme Roeser für die katalytischen Messungen an der TU Berlin, Thibault Cantat and Enguerrand Blondiaux für die katalytischen Messungen am CEA Saclay (Frankreich), Michael Puchberger für die Aufnahme von Festkörper als auch Lösungs-NMR-Spektren, Florian Bitto für die Aufnahme von Lösungs-NMR-Spektren an der TU Bergakademie Freiberg, Prof. Hinrich Grothe für die Raman-Messungen als auch für den gewährten freien Zugang zum Fluoreszenzmessgerät. Des Weiteren danke ich Annegret, Matthias, Christine, Sven und Felix für das Korrekturlesen dieser Arbeit.

Großer Dank gilt meinen Kollegen, Mitarbeitern und Freunden am Institut für Materialchemie der TU Wien für die gute Zeit, die wir in den letzten 3 Jahren zusammen hatten. Im Besonderen natürlich dem „Gute Laune Office“: meinem best IKEA shopping buddy Christian für die ständige Bereitschaft mit mir Konzerte aller Art zu besuchen, Felix für den Unterricht in sprachlichen Besonderheiten von hinterm Arlberg, Marco, dafür dass er mir hier am Institut alles gezeigt hat und besonders dafür, dass er mir die österreichische Wurschtigkeit näher gebracht hat, Matthias für die zahlreichen Fachgespräche im Bereich des Fußballs, Politik und Grammatik und Sarah dafür, dass wir den gleichen Sinn für Humor teilen, denn so ziemlich alles ist wie ein Cordon Bleu... Des Weiteren danke ich Anita für die Hilfe bei vielen organisatorischen Dingen, Aparna, Bernhard für den ganzen Spaß in meinen ersten vier Wochen in Wien, Catarina, Christine für die gute Zeit im Synthesepraktikum und für die immer wohlüberlegten Geburtstagsgeschenke, Elisabeth für die gemeinsamen Ausflüge zum SAXS, Harald, Jasmin, Jingxia, Johannes, Melitta, Michael, Miriam für

ihre Hilfe beim Bewerbungen schreiben, Patrik, Rupali, Rupert, Stefan, Stephan, Sven für die ständige Diskussionsbereitschaft, Valeria, unserer neuen Würstchenprinzessin Van An, Wenjing und meinen beiden Wahlpraktikanten Christina und Konstantin.

Dank gilt auch meinen Freunden aus Annaberg für die notwendige Nicht-Chemie in meinem Leben.

Großer Dank gilt meiner Familie die mir Leben, Schule und Studium ermöglichte und mich bei allen meinen Entscheidungen unterstützte.

Vielen Dank an meine liebste Annegret, dass du diese Zeit mit mir zusammen durchlebt hast, auch wenn wir dafür zu Anfang viel Zug fahren mussten.

Danke!!!

Kurzfassung

Im Zuge dieser Arbeit wurden sowohl die Synthesemöglichkeiten als auch die vielfältigen Eigenschaften von ionischen Nanopartikelnetzwerken (INN) untersucht. Die mit Hilfe des Sol-Gel-Prozesses hergestellten Metalloxidnanopartikel wurden mittels unterschiedlich substituierten Trimethoxysilanen modifiziert. Die endgültige Bildungsreaktion der Hybridmaterialien wurde durch eine nukleophile Substitution zwischen mit zyklischen Stickstoffbasen modifizierten Nanopartikeln und mit choralkylmodifizierten Nanopartikeln oder mit zweifach chlormethylensubstituierten (-CH₂Cl) Linkermolekülen realisiert. Die so erhaltenen Materialien boten vielfältige Verarbeitungsmöglichkeiten und wurden mittels zahlreicher Analysemethoden charakterisiert. Die Kinetik der Bildungsreaktion wurde außerdem mittels einer Quartzkristallmikrowaage untersucht. Des Weiteren wurden Röntgenkleinwinkelstreuungsmessungen durchgeführt, welche eine Nahordnung im Material zeigten, die mit hoher Wahrscheinlichkeit auf π - π -Wechselwirkungen zwischen den aromatischen Ringen des Materials zurückzuführen ist. Für einen besseren Einblick in die Zusammensetzung des Materials und die Wechselwirkungen der Komponenten untereinander wurden Festkörper-NMR-Messungen, sowie *ab-initio*-Berechnungen als auch DFT-Berechnungen durchgeführt. Diese Untersuchungen bestätigten die Präsenz von π - π -Wechselwirkungen zwischen den aromatischen Ringen der INN Materialien.

Den Kern der Arbeit bildeten Untersuchungen der Photolumineszenzeigenschaften der INN-Materialien. Dabei wurde speziell die Regulierbarkeit der Anregungs- und Emissionswellenlängen durch Variation der Substituenten an der C2-Position des Imidazoliumringes oder durch die Variation des Linkermoleküls zwischen den Imidazoliumringen, für über zwanzig verschiedene INN-Materialien untersucht. Zudem wurde der Einfluss der verschiedenen Linkermoleküle auf die Nahordnung im Material und die daraus resultierenden Veränderungen der Photolumineszenzeigenschaften bestimmt.

Darüber hinaus wurden Metallchloride, die für die Bildung von Chlorokomplexen bekannt sind, mit den Chloridionen der INN-Materialien komplexiert und die daraus resultierenden Eigenschaften der Materialien, wie Thermochromie oder Photolumineszenz, untersucht.

Des Weiteren konnte gezeigt werden, dass die Reaktion von CO₂ und unterschiedlichen Epoxiden zu organischen zyklischen Carbonaten durch die INN-Materialien effektiv katalysiert wird. Für Reaktionen mit Epichlorhydrin wurden für alle getesteten Materialien quantitative Umsetzungen beobachtet. Die INN-Materialien konnten dabei bis zu vier Mal ohne erkennbare Minderung des Umsatzes, allerdings mit einem signifikanten Rückgang der Selektivität, wiederverwendet werden.

Abschließend wurden Versuche unternommen SiO₂-nanopartikelbasierte selbstheilende Materialien herzustellen, indem Prinzipien von selbstheilenden Polymeren auf SiO₂-Nanopartikelnetzwerke übertragen wurden.

Abstract

In the course of this work the synthesis and versatile properties of novel inorganic-organic hybrid materials, so-called Ionic Nanoparticle Networks (INN), were investigated. The metal oxide nanoparticles, prepared by sol-gel processing, were modified with various differently substituted trimethoxysilanes. The final synthesis of the hybrid materials was the crosslinking of cyclic nitrogen base modified nanoparticles and chloroalkyl modified nanoparticles or chloromethylene (-CH₂Cl) disubstituted aromatic linker molecules by a nucleophilic substitution. The obtained hybrid materials showed a very versatile processing and were characterized by various analysis techniques. The kinetics of the INN materials formation was also investigated by Quartz Crystal Microbalance (QCM). Short Angle X-ray Scattering (SAXS) measurements were executed on the INN materials revealing a short range order in the material, which most likely is caused by π - π stacking interactions between the aromatic rings in the material. For a deeper understanding of the interactions in the material as well as of the composition of the INN materials solid state NMR measurements, *ab-initio* calculations and DFT calculations were conducted. These measurements confirmed the presence of π - π stacking interactions between the aromatic rings in the INN materials.

The core of the work was the investigation of the photoluminescence properties of the materials. Especially the tailoring of the excitation and emission wavelengths, by varying the substituents on the C2 position of the imidazolium moiety as well as by variation of the aromatic linker, was investigated for more than twenty different INN materials. The influence of the different linker molecules on the short range order and the resulting changes in photoluminescence activity was also evaluated.

Furthermore, metal chlorides, which are known to form chloro metalate complexes, were used for the complexation with the chloride ion of the INN materials and the resulting properties, such as thermochromism and photoluminescence features, of the INN materials were explored.

In addition, it could be shown that the INN materials are efficient heterogeneous catalysts for the conversion of CO₂ and different epoxides into organic cyclic carbonates. Reactions with epichlorohydrin showed that a quantitative conversion could be reached for all the tested materials under relatively mild conditions. The INN materials could be easily recycled for at least four runs without a loss in conversion, but a decrease in selectivity was observed.

Finally, first attempts on silica nanoparticle based self-healing materials were made by the transfer of principles from self-healing polymers to silica nanoparticle networks.

Parts of this work have been published:

M.-A. Neouze, M. Kronstein, M. Litschauer, M. Puchberger, C. Coelho, C. Bonhomme, C. Gervais, F. Tielens, "Exploring the Molecular Structure of Imidazolium-Silica Based Nanoparticle Networks by Combining Solid State NMR and First Principles Calculations"; *Chem. Eur. J.* **2014**, accepted.

M.-A. Neouze, M. Kronstein, F. Tielens, "Ionic Nanoparticle Networks: Development and Perspectives in the Landscape of Ionic Liquid Based Materials"; *Chem. Commun.* **2014**, accepted. DOI: 10.1039/C4CC02419B

M. Kronstein, J. Akbarzadeh, C. Drechsel, H. Peterlik, M.-A. Neouze, "Tailoring fluorescence properties in Ionic Nanoparticle Networks"; *Chem. Eur. J.* **2014**, *20*, 10763 - 10774. DOI: 10.1002/chem.201400392

M. Kronstein, K. Kriechbaum, J. Akbarzadeh, H. Peterlik, M.-A. Néouze: "Irreversible thermochromism in copper chloride Imidazolium Nanoparticle Networks"; *Phys. Chem. Chem. Phys.* **2013**, *15*, 12717 - 12723. DOI: 10.1039/C3CP50430A

M.-A. Néouze, M. Litschauer, M. Puchberger, M. Kronstein, H. Peterlik, "Tuning the Pore Size in Ionic Nanoparticle Networks"; *Journal of Nanoparticles* **2013**. DOI: 10.1155/2013/682945

J. Roeser, M. Kronstein, M. Litschauer, A. Thomas, M.-A. Néouze: "Ionic Nanoparticle Networks as solid state catalysts"; *Eur. J. Inorg. Chem.* **2012**, *32*, 5305 - 5311. DOI: 10.1002/ejic.201200581

Contents

1	Introduction	1
1.1	Hybrid Materials.....	1
1.2	Nanoparticles and Sol-Gel Processing.....	4
1.3	Surface Modification of Nanoparticles	9
1.4	Ionic Liquids in Materials Science	12
2	Research Goals.....	17
3	Results and Discussion	18
3.1	Syntheses.....	18
3.1.1	Nanoparticle Syntheses	18
3.1.2	Precursor Synthesis and Nanoparticle Surface modification	19
3.1.3	Synthesis of the INN hybrid materials	22
3.1.4	Processing of the INN hybrid materials	25
3.2	Characterization	26
3.2.1	Chemical Analysis of the INN hybrid materials	26
3.2.2	Thermal Analysis on the INN hybrid materials	32
3.2.3	Structural Analysis of the INN Materials by Short Angle X-ray Scattering (SAXS).....	37
3.2.4	Kinetic determination of the INN material building reaction by quartz crystal microbalance (QCM)	41
3.2.5	NMR spectroscopy on INN materials	47
3.2.6	DFT calculations on the INN materials	51
3.2.7	Investigation of the electrical properties of the INN materials.....	55
3.3	Fluorescence properties of INN materials	58
3.3.1	Photoluminescence properties of the mono-imidazolium INN materials	59
3.3.2	Photoluminescence properties of the bis-imidazolium INN materials	60

3.3.3	Photoluminescence properties of the pyrazolium INN materials.....	65
3.3.4	Photoluminescence properties of the mono-pyridinium INN materials.....	66
3.3.5	Photoluminescence properties of bis-pyridinium INN materials.....	67
3.3.6	Photoluminescence properties of the so-called mixed INN materials.....	68
3.3.7	The influence of the short range order on the photoluminescence properties of the INN materials.....	69
3.4	Complexation of metal salts in INN materials and resulting properties.....	74
3.4.1	Complexation of $\text{CuCl}_2 \cdot 2\text{H}_2\text{O}$ in INN materials and resulting thermochromic properties of the hybrid material.....	74
3.4.2	Complexation of PdCl_2 and $\text{EuCl}_3 \cdot 6\text{H}_2\text{O}$ in INN materials and the resulting photoluminescence properties of the hybrid materials.....	82
3.5	INN materials as solid state catalysts.....	87
3.6	Attempts on silica nanoparticle based self-healing materials.....	95
3.6.1	Dicyclopentadiene based silica nanoparticle networks.....	95
3.6.2	Vitrimer-type cross-linked silica nanoparticle networks.....	98
4	Summary and Outlook	101
5	Experimental.....	105
5.1	Materials.....	105
5.2	Analysis Techniques	106
5.3	Syntheses.....	113
5.3.1	Nanoparticle Syntheses	113
5.3.2	Syntheses of different functionalized trimethoxysilanes.....	113
5.3.3	Syntheses of precursor molecules for silica nanoparticle based self-healing materials	120
5.3.4	Linker syntheses	123
5.3.5	Nanoparticle modification reactions.....	123
5.3.6	INN Materials syntheses.....	125
5.3.7	Anion Metathesis and Metal Complexation reactions.....	129

5.3.8	Silica nanoparticle based self-healing materials	130
5.3.9	Materials overview	131
6	Appendix.....	135
6.1	Abbreviations	135
6.2	Bibliography.....	136

1 Introduction

1.1 Hybrid Materials

Hybrid materials are materials that include two moieties blended on the molecular scale. Usually one of the molecular compounds is inorganic and the other one organic.^[1] The materials combine the advantages of the individual compounds to form high performance materials. Nowadays, hybrid materials are often used for protective and smart coatings, *e.g.* as corrosion protecting coatings for aircrafts, “easy-to-clean” coatings for glass or scratch resistant clear coatings for the automotive industry.^[2] Another striking example is their application in so-called dye-sensitized solar cells, which are based on the use of interpenetrating network of nanocrystalline oxide and conducting electrolyte.^[3,4]

The first hybrid materials can be found in nature, where optimal balance between durability, mechanical properties and other important properties such as density, permeability, color, hydrophobicity *etc.* could be observed.^[2] In the most cases the inorganic part provides mechanical strength and the overall structure, while the organic part connects the inorganic building blocks and/or the soft matter of the material.^[1] These natural made inorganic-organic nanocomposites are formed under soft and sustainable conditions. Examples for this are the human bones and teeth and mollusc shells.^[5] In some cases inorganic-organic interfaces play an important role in the construction of living systems, *e.g.* as catalysts for natural processes like the polypeptide synthesis by the catalytic activation of organic compounds by clays or zeolites.^[6,7]

Some selected examples for early man-made hybrid materials are china ceramics, blue Maya pigments and some prehistoric frescos.^[2] Especially the Maya blue is an illustrative example of man-made hybrid materials. It combines the resistance of the inorganic clay palygorskite with the color of the organic pigment indigo.^[8,9]

The industrial manufacturing of inorganic organic hybrid materials started in the middle of the 20th century. One of the first hybrid material products were paints, which are inorganic nano-pigments suspended in organic solvents by closer examination. Another product is paper, where the cellulosic polymers were cross linked by metal oxides, such as titania, alumina and zinc oxide.^[2]

The interest on the concept of inorganic-organic nanocomposites exploded in 1980s by the development of soft inorganic chemistry processes, like the sol-gel chemistry.^[3] This type of chemistry opened the door to numerous new synthesis pathways and application possibilities of today’s tailor-made functional hybrid materials.

Hybrid materials can be divided in two classes^[1]:

- **Class I Hybrid Materials:** The inorganic and the organic components are only connected by weak interactions, like van der Waals, hydrogen bonding or electrostatic interactions.
- **Class II Hybrid Materials:** The inorganic and the organic components in the material show strong interactions, like ionic or covalent bonding, between the components.

The most important system of this work, the Ionic Nanoparticle Networks (INN), belongs to Class II hybrid materials.

For different classes of hybrid materials various synthetic pathways are possible^[2,8]:

Route A:

This route corresponds to molecular growing processes including sol-gel chemistry, the application of bridged polyfunctional precursors and hydrothermal synthesis of *e.g.* coordination polymers such as Metal Organic Frameworks.^[2] In conventional sol-gel chemistry metal alkoxides or metal halides react in a polycondensation reaction, which usually results in a three-dimensional cross-linked network. (The sol-gel process will be discussed more in detail in chapter 1.2.) The advantage of this synthesis method is that the starting compounds are simple and low cost. Moreover, the products are very versatile and exhibit interesting properties. However, the main disadvantage is that the products are typically polydisperse in size and locally heterogeneous in their chemical composition. Therefore it is very important to get control about the local structure of the hybrid materials. There are two methods to improve the organization within the materials. The first is the use of bridging precursors, such as silsesquioxanes $X_3Si-R'-SiX_3$ (R' = organic spacer, X = Cl, Br, OR), which allow the formation of homogenous molecular hybrid inorganic-organic materials with a higher degree of local ordering.^[3,10] The second method is the hydrothermal synthesis in polar solvents in the presence of organic templates. This synthesis resulted in numerous zeolites with applications as adsorbents or catalysts. Another type of hybrid materials, which can be obtained by this method, are the Metal Organic Frameworks (MOFs). These materials are coordination polymers synthesized by the linkage or coordination of polymerizable or polyfunctional spacers to metal-containing small oligomers,^[2] *e.g.* metal oxo-clusters.^[11] In the last 15 years the synthesis and applications of these MOFs were investigated by a large number of research groups all over the world building an own research community. These hybrid materials exhibit very high surface areas (from 1000 to 4500 m^2/g)^[3,12-14] and thus they are extremely high promising for catalytic and gas adsorption based applications, *e.g.* hydrogen storage.^[15]

Route B:

This route corresponds to the assembly or dispersion of well-defined nanobuilding blocks (NBB), which can be clusters, pre- or post- functionalized nanoparticles (metal or metal oxide), nano-core-shell structures^[16,17] or layered compounds (clays or lamellar phosphates or oxides) that can host organic compounds.^[2,18–20] For this reaction pathway the NBB are synthesized prior to the real material synthesis and thus they retain their shape and physicochemical properties in the final hybrid material.^[21] The hybrid material synthesis itself is the assembly or dispersion of the NBBs. One big advantage of this synthesis strategy is that once synthesized the NBB are quite resistant against hydrolysis and nucleophilic attacks compared to the metal alkoxides. One further advantage is that the pre-synthesized NBB can be monodisperse and show well defined forms and surface, which facilitates the characterization of the final hybrid materials.^[2,3]

The hybrid materials developed in this work, the Ionic Nanoparticle Networks, were synthesized via this route.^[22]

Route C:

The synthesis strategy of this route is based on the self-assembly of amphiphilic molecules or polymers coupled with sol-gel polymerization.^[2] It could alternatively be described as a template growth of the nanomaterials by organic surfactants.^[3,23] One example for this strategy is the synthesis of mesoporous solids from the calcination of aluminosilicate gels in the presence of surfactants.^[24] Furthermore silsesquioxanes can be used as precursors for this reaction. The resulting hybrid materials are nanoporous and present a high degree of order. Due to their mesoporosity it is possible to modify the surface afterwards with organic functionalities by grafting reactions with for example different substituted alkoxysilanes.^[25]

These different synthesis routes give access to hybrid materials with a controlled design and a tailorable assembly of the components in the nanoscopic to mesoscopic range. Furthermore, chemistry, physics and processing are strongly coupled for these synthesis pathways.^[2]

For all these routes sol-gel processing can be used as it is in general a “chimie douce” procedure.

1.2 Nanoparticles and Sol-Gel Processing

Usually particles can be defined as nanoparticles, if the dimension of every three spatial directions is located between 1 nm and 100 nm. At this size it is not possible to apply quantum chemistry and the rules of solid state physics are not valid anymore. These phenomena can be assigned to two effects^[26]:

1. Finite-size effect: The electronic structure of a nanoparticle is located between the electronic structure of a molecular material and the electronic structure of a bulk material. By scaling down the size of the particle to the lower nanometer regime, the electronic bands split to molecular orbitals. However, the discrete energy levels of molecular compounds have not been reached yet.^[26]
2. Surface and interface effects: A high percentage of atoms in nanomaterials are surface atoms. Thus they can be considered as surface matter in macroscopic quantities.^[26]

Due to their very special properties, nanoparticles are extremely high promising for numerous applications, *e.g.* for electronic and sensor applications^[27], for surface active paints^[28,29] and superhydrophobic coatings.^[30,31] Another branch of applications is their wide use in medicine and biology for drug delivery^[32,33] and for cell markers.^[34,35]

For the synthesis of nanoparticles two main synthesis pathways exist: the top-down and the bottom-up strategy.^[36]

In the top-down processes the synthesis of the nanoparticles started from macroscopic initial structures. The synthesis itself can be realized, on the one hand, by ball milling or grinding techniques applying mechanical forces on the starting material^[37,38] and, on the other hand, template techniques.^[39,40] The “crude” top down methods like ball milling and grinding typically offer less control on parameters like particle size and size distribution and the shape of the particles deviates significantly from spherical.^[41] Chemical bonds are broken during the ball milling and new surfaces are created. The dangling bonds on these newly created surfaces usually show a high chemical reactivity.^[42] The template based techniques lead to a better control of the particle size and shape, and are mainly applied in microelectronics. However these techniques are also characterized by a low sample throughput and expensive procedures.^[43]

The bottoms-up techniques start with molecular building blocks for the synthesis of the nanoparticles. The driving force of the assembly of the molecular building blocks is the achievement of low energetic states.^[8] As only the bottom-up strategy was used for the synthesis of the nanoparticles in this work this method will be discussed in detail in the following pages.

A very important bottom-up synthesis strategy in materials chemistry and also for the nanoparticle synthesis in this work is the sol-gel process. At this point the terms *sol* and *gel* have to be defined:

A *sol* is a stable suspension of colloidal solid particles or polymers in a liquid. Thereby the particles can be amorphous or crystalline.^[26] Thereby, colloidal particles are defined by a diameter between 1 nm and 1000 nm.

A *gel* consists of a porous, three-dimensionally continuous solid network surrounding and supporting a continuous liquid phase. In colloidal gels, the network forms by agglomeration of dense colloidal particles, whereas in “polymeric” gels the particles have a polymeric sub-structure made by aggregation of sub-colloidal chemical units. In general, the sol particles can be connected by covalent bonds, van der Waals forces, or hydrogen bonds.^[26]

The sol-gel process can be defined as the synthesis of inorganic or hybrid materials from molecular precursors.^[44] It can be described as a green chemistry process, because toxic reactants are not required and it is executed at relatively low temperatures, typically between room temperature and 100 °C.^[45] The precursors are predominantly silicon or metal alkoxides or metal salts. One advantage of the sol-gel chemistry is that the processing is quite simple. Thin films of the material can be obtained by dip-, spray- or spin coating, fibers can be directly spun from the sol, monoliths can be obtained by a slowly drying procedure and powders by simply drying of the sol (Figure 1).^[26]

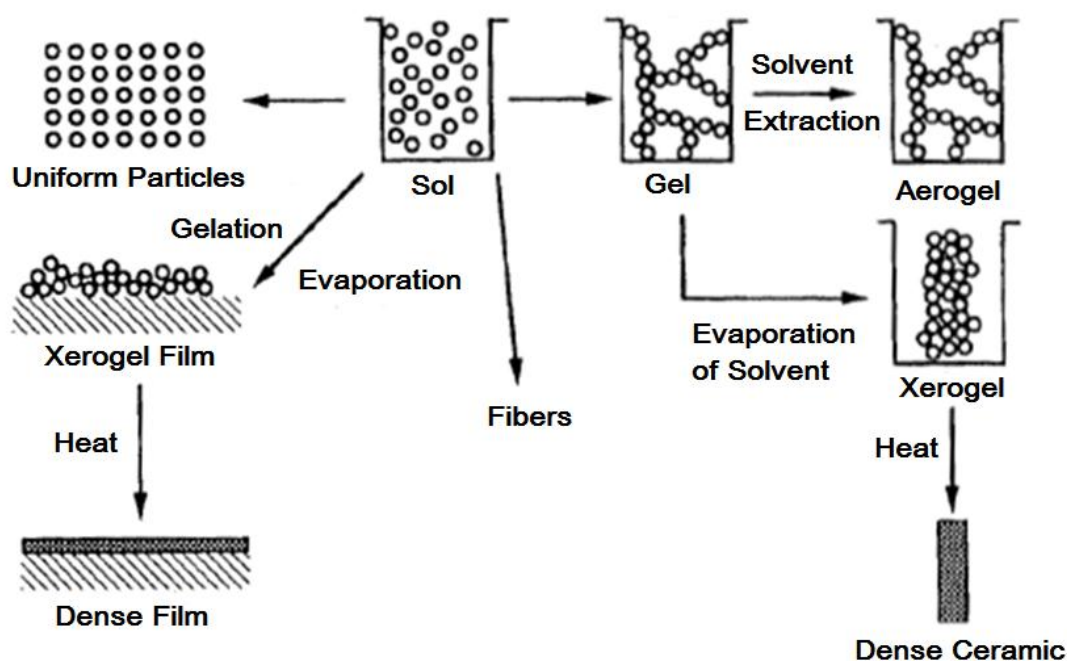
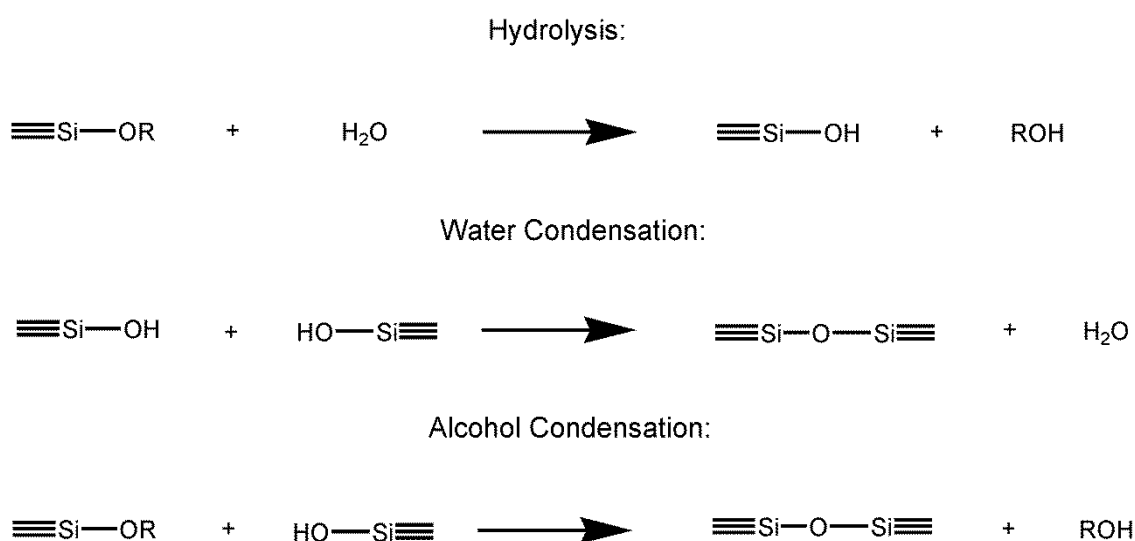


Figure 1 Possibilities of processing in sol-gel chemistry.^[44]

As in this work predominantly silica based materials were synthesized, the sol-gel process of silicon alkoxides will be discussed in detail in the following pages. The sol-gel process of silicon alkoxides mainly consists of two steps. The first step is the reaction of a silicon alkoxide group Si-OR with water forming a silanol group Si-OH and a simultaneous elimination of the respective alcohol ROH (Scheme 1). There are two possibilities for the second reaction step: The fresh formed silanol group can react with another silanol group (water condensation) or with a silicon alkoxide group of an unreacted precursor molecule (alcohol). At this point it has to be highlighted that the condensation usually starts before the hydrolysis of the silicon alkoxide is completed.^[26] The sol-gel transition (gel point) is reached when a continuous network has been formed, which can be seen macroscopically by a sharp increase of viscosity until no flowing of the liquids is possible.



Scheme 1 Basic reactions of sol-gel processing of silicon alkoxides.

The sol-gel processing of silicon alkoxides and metal alkoxides take place in a similar way. The main difference of silicon alkoxides and metal alkoxides lies in the reactivity regarding the hydrolysis and condensation reactions. Silicon, depending on its low electrophilicity, shows a rather low reactivity regarding these reactions. Transition metals, such as Ti, Zr, Mn *etc.* show a more electropositive character and thus a higher reactivity towards hydrolysis reactions.^[46] Furthermore, most metals offer several stable coordination numbers, which also increases the reactivity in hydrolysis and condensation reactions.^[26]

In general sol-gel reactions are carried out in alcoholic solutions to get a homogeneous reaction mixture, because many alkoxy silanes are immiscible with water. The most common precursors for silicon alkoxide sol-gel processes are tetramethoxysilane (TMOS) and tetraethoxysilane (TEOS).

Typically, the sol-gel reactions of alkoxy silanes are catalyzed by adding acidic or basic catalysts to the reaction mixture. In fact there are three different regions of the pH value, which influence the

reactivity of the precursors and the morphology of the resulting material in different ways: $\text{pH} < 2$, $\text{pH} 2-7$ and $\text{pH} > 7$ (Figure 2). The point of zero charge, where the surface charge of silica is zero, and the isoelectric point, where the electrical mobility of silica particles is zero, are both located in the pH range between 1 and 3.^[44]

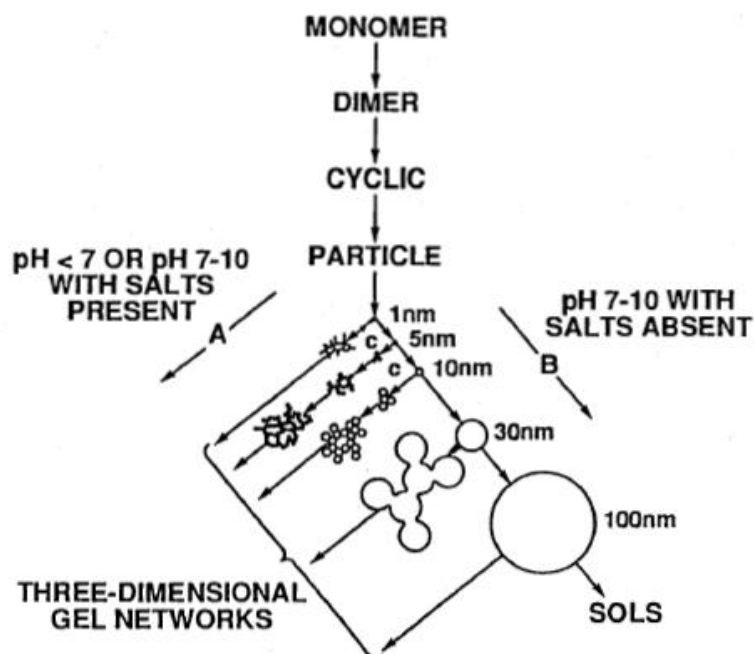
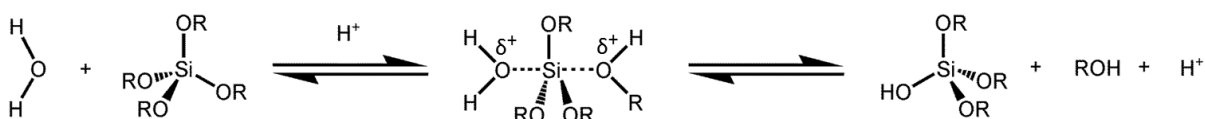


Figure 2 Dependence on the pH value of the morphology of the silica material.^[44]

At pH values lower than 2, the oxygen atom of a Si-OH or Si-OR group is protonated in a rapid first step (Scheme 2). Thereby a good leaving group, like water or alcohol, is formed. The reaction rate of the condensation reaction depends on the H^+ concentration. The gel time, which can be defined as time at which the gel point is reached after starting hydrolysis and condensation reactions, is quite long. This acid catalyzed condensation involves protonated silanol species which increase the electrophilicity. Thereby monomers and weakly branched silanols are easy to protonate. In consequence, this condensation type usually occurs at monomers and end groups of chains. Under acidic conditions the resulting material consists of particles of maximum 2 nm in diameter.^[26,44]

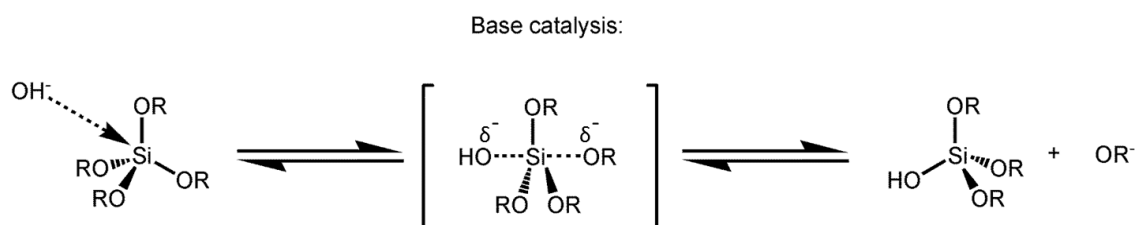
Acid catalysis:



Scheme 2 Acid catalyzed silicon alkoxide sol-gel reaction.^[1]

At $\text{pH} 2-7$ the hydroxide anion attacks the silicon atom by an $\text{S}_{\text{N}}2$ -type mechanism (Scheme 3). The reaction rate of the condensation is proportional to the concentration of OH^- ions. In consequence,

a higher condensation rate can be monitored by increasing the pH value. Here the condensation reaction takes place by the nucleophilic attack of a deprotonated silanol species on a neutral silanol species. Therefore the condensation reaction preferentially occurs between highly branched silanols, because they are easy to deprotonate, and weakly branched neutral silanols. The obtained materials consist of particles, which are 2 -4 nm in diameter.^[1,44]



Scheme 3 Base catalyzed silicon alkoxide sol-gel reaction.^[1]

By the application of basic catalysis ($\text{pH} > 7$) the condensation reaction occurs by the same nucleophilic mechanism as shown in Scheme 3. All the condensed species are ionized and preferentially react with monomeric species. The particle growth occurs primarily by the addition of monomers on already existing particles, instead of the formation of new particles. In consequence the obtained nanoparticle suspensions or materials consist of relatively large particles (Figure 2).^[26,44]

The nanoparticles used in this work were synthesized at $\text{pH} > 7$. More in detail, the silica particles were synthesized by the Stöber process.^[47] This process is well known as ammonium-catalyzed hydrolysis of tetraethoxysilane (TEOS) in methanol or ethanol to form spherical silica particles.^[48]

Further steps of the sol-gel process are ageing and the drying of the obtained gel. During the ageing the gel may contain some fluid sol. This contains particles or monomers which are able to condense to the existing network. Additionally the structure of the network can be modified by the condensation of neighboring Si-OH or Si-OR groups. Also a ripening process can occur. That means some mass of the particle is dissolved from thermodynamically unfavorable regions and the solutes condense to thermodynamically more suitable regions. In consequence this process results in the reduction of the network curvature, the disappearance of small particles and the filling of small pores.^[26]

The drying process is a critical step in the material synthesis, because it determines the form of the final product. By conventional drying methods, like the evaporation of solvent or increasing the temperature, xerogels are obtained, because of the collapse of the network. Aerogels can be obtained by replacing the pore filling liquid by air or another gas, *e.g.* by the supercritical drying with CO_2 .^[49]

1.3 Surface Modification of Nanoparticles

As discussed in chapter 1.2 nanoparticles show very special properties, *i.e.* finite size effects and surface effects, when compared to their bulk counterparts. In consequence there are some reasons for the surface modification of nanoparticles.^[26,50] First of all, the modification of the surface can prevent agglomeration of the nanoparticles.^[51,52] Furthermore, the shape and size of the nanoparticles can be controlled by this approach.^[53] One further reason for the surface modification is to establish the compatibility with another phase, *e.g.* to enable the water solubility of nanoparticles, which is quite important for biological applications. For example this can be reached by the addition of a peptide to a citrate stabilized silver nanoparticle suspension.^[54] The surface modification also can improve mechanical properties of the particles by preventing heterogeneities and incompatibilities.^[55] Another field of interest for the modification is to facilitate the self-assembly of the nanoparticles.^[56]

The suitable group or ligand for the surface modification depends on the chemical properties of the nanoparticle itself.^[50] Inorganic oxides like SiO_2 ,^[51,57,58] ZnO ^[59] and Al_2O_3 ^[60] can be modified by different silane ligands; TiO_2 ,^[61,62] SnO_2 ,^[63] Fe_3O_4 ^[64,65] and Y_2O_3 ^[66] can be modified by phosphorous based ligands and amorphous Fe_2O_3 by sulfonic acids.^[67] For the noble metal nanoparticles, like Au ,^[68,69] Ag ^[70] or Pd ,^[71] the most important ligands for the surface modification are thiols, but also amines can be used to modify Pd nanoparticles^[72] and carboxylic acids for Ag nanoparticles.^[73]

In general there are three important synthesis pathways for the surface modification of nanoparticles:^[26]

1. The nanoparticles are synthesized in the presence of a stabilizing organic ligand, like the synthesis of gold nanoparticles in the presence of citrate.^[74]
2. Ligands, which were used for stabilization during the nanoparticle synthesis, can be later exchanged against ligand with the favored properties, *e.g.* for functionalization the surface or a better stabilization of the nanoparticles.^[75]
3. Postsynthetic modification of the ligand shell: Thereby, organic functional groups can be modified by standard organic reaction, *e.g.* the quaternization of amine groups with chloroalkyl terminated modifying reactants.^[76]

In the following only the surface modification by silane ligands will be discussed, as only they were used for the surface modification of the synthesized metal oxide nanoparticles in this work.

Very often silanes are used for the modification of the surfaces of metal oxides. The use of silanes offers many advantages, as they are commercially available with numerous functionalities, *e.g.*

amino, cyano, mercapto *etc.* and the postsynthetic modification of metal alkoxide surfaces is quite simple.^[50] For these modification reactions in general alkoxysilanes and chlorosilanes can be used (Scheme 4).



Scheme 4 Chemical structure of organotrichloro- and organotrialkoxysilanes.

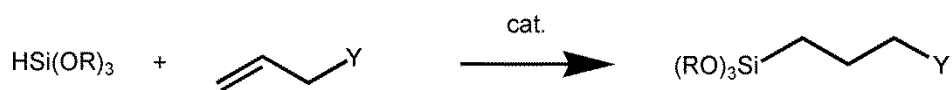
Depending on the comparable weak Si-Cl bond strength and the oxygen affinity of silicon in general,^[77] di- ($\text{R}'_2\text{SiCl}_2$) and trichlorosilanes ($\text{R}'\text{SiCl}_3$) showed a very high reactivity for the silica surface modification reaction. This high reactivity causes the building of multidentate attachments, which results in less ordered siloxane layers on the silica surface. For the formation of well-defined siloxane layers chlorosilanes ($\text{R}'_3\text{SiCl}$) can be used for the silica surface modification, but due to their low reactivity they have to be activated by amines.^[50] One disadvantage of the surface modification with chlorosilanes is the formation of HCl, which may have a negative influence on the resulting material by initiating subsequent reactions. Depending on this fact it is more elegant to use alkoxysilanes for the surface modification, as only alcohols are formed as side products. Thereby the favored alkoxy groups are methoxy and ethoxy, as they show quite low molecular weights, which is an advantage in their purification after synthesis. In fact the organotrialkoxysilanes can only be purified by distillation, because purification via column chromatography will lead to an irreversible modification of the stationary phase with the respective silane. Thereby, various synthesis pathways are possible for trialkoxysilanes, *e.g.* the functional group of the alkyl chain R' can be exchanged by nucleophilic substitution,^[78] an unsaturated alkyl chain and the silicon atom of trimethoxy- or triethoxysilane can be connected by a hydrosilylation^[79] or the chlorine atoms of organochlorosilanes can be exchanged by alkoxy groups *via* alcoholysis reactions (Scheme 5).^[80]

Organochlorosilanes can be obtained from the direct synthesis of silicon and alkylchlorides in the Müller-Rochow synthesis.^[81]

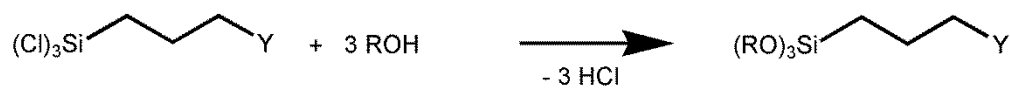
Nucleophilic Substitution:



Hydrosilylation:



Alcoholysis:



Scheme 5

Examples for possible synthesis pathways for trialkoxysilanes (R = Me, Et).

1.4 Ionic Liquids in Materials Science

Ionic liquids (IL), per definition, are salts with melting points below 100 °C. Therefore, the synthesis of ethanolanmonium nitrate (melting point = 52 – 55 °C) could be designated as the first ionic liquid, which was reported by S. Gabriel and J. Weiner in 1888.^[82] Furthermore, it is possible to prepare ionic liquids that are liquid at and below room temperature, which are known as room temperature ionic liquids (RTIL).^[83] Ethylammonium nitrate could be named as the first room temperature ionic liquid offering a melting point of 13 °C.^[84] This first RTIL was synthesized and reported in 1914 by Paul Walden,^[85] who is also famous for the confirmation of the “Walden Inversion” in S_N2 type nucleophilic substitutions in organic chemistry.^[86] After their discovery no or only some investigations were reported for room temperature ionic liquids for more than 50 years. In 1964 L. King initiated a research project aimed at finding a replacement for LiCl-KCl molten salt electrolyte used in thermal batteries, where he was working on chloroaluminates.^[87] These ionic liquids are known as excellent catalysts and solvents in many processes, but they offer a big disadvantage: their moisture sensitivity.^[88,89] In the 1970s J. Atwood discovered a compound class he named “liquid clathrates”, which were composed of a salt and an aluminum alkyl with the formula M[Al₂(CH₃)₆X] (M = inorganic or organic cation, X = halide).^[87,90] However in the last two decades the interest in the properties and applications of ionic liquids increased dramatically.

Invariably, ionic liquids are organic salts or mixtures consisting of at least one organic component. The most common cations used for ionic liquids are N,N'-dialkylimidazolium, N-alkylpyridinium, N-dialkylpyrrolidinium, alkylammonium, alkylsulfonium and alkylphosphonium (Figure 3).^[83,91]

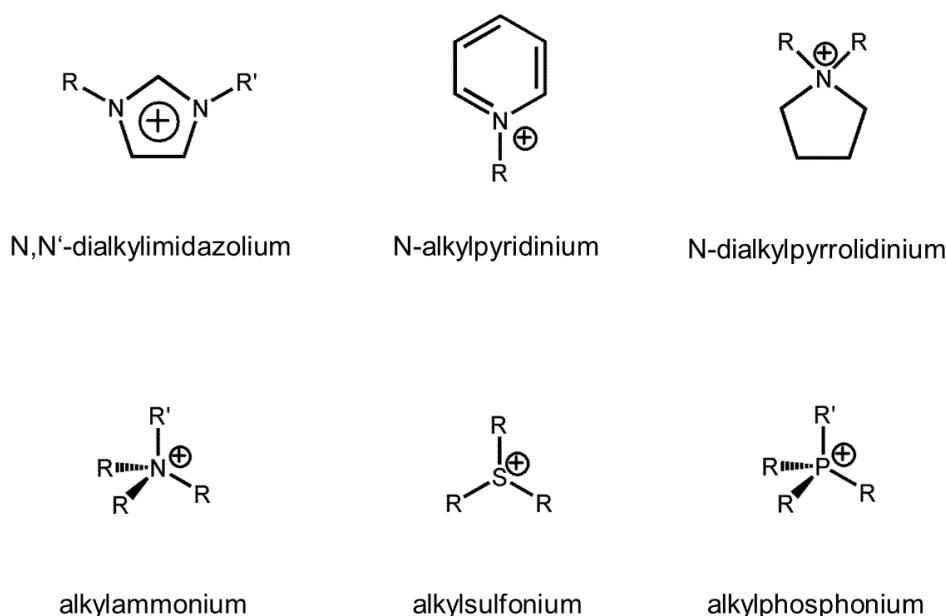


Figure 3 Chemical structure of typical cations for ionic liquids.

The most common anions for ionic liquids are: halide, nitrate, tetrafluoroborate (BF_4^-), hexafluorophosphate (PF_6^-), chloroaluminates (AlCl_4^- and Al_2Cl_7^-), alkylsulfate (RSO_4^-), tosylate (TsO_3^-) and triflate (CF_3CO_2^-).^[92]

There are some methods for the preparation of ionic liquids. A well-known method is a nucleophilic substitution between the appropriate halogenoalkane and the amine, *e.g.* alkylamines, pyridines^[93] and imidazoles.^[94] A very common RTIL is 1-butyl-3-methyl-imidazolium chloride ([bmim]Cl), which can be prepared by heating the reactants (1-methylimidazole and 1-chlorobutane) in toluene under reflux.^[95] In general, ionic liquids can be synthesized at low temperatures with high yields by using no or non-toxic solvents. Therefore ionic liquids are often named as “green” solvents.^[88] A possibility for the modification of ionic liquids is the anion metathesis, *e.g.* by AgBF_4 in methanol,^[96] NH_4BF_4 in acetone,^[97] NaBF_4 in acetone or KPF_6 in acetone.^[98] In addition, monoalkylammonium nitrate salts could be synthesized by the neutralization of aqueous solutions of the amine with nitric acid.^[99] In a similar reaction tetraalkylammonium sulfonates were prepared by mixing equimolar amounts of the sulfonic acid and the tetraalkylammonium hydroxide.^[100] An additional method for the preparation of halogenoaluminates (III) and chlorocuprates (I) is the direct combination of a halide salt with a metal halide.^[83,101,102] Except the halogenoaluminates(III) and the chlorocuprates(I), ionic liquids are generally known to be air and moisture stable.

Ionic liquids have been described as “designer solvents”, which means that their properties can be adjusted to suit the requirements of a chemical process.^[103] Properties such as melting point, viscosity, density and hydrophobicity can be varied by simple changes to the structure of the ions and the alkyl chains.^[88] For example the melting points of 1-alkyl-3-methylimidazolium tetrafluoroborates and hexafluorophosphates are a function of the length of the 1-alkyl chain.^[104,105] Moreover, ionic liquids in general show further advantageous properties, *e.g.* low vapor pressure, thermal stability and electric conductivity.^[87,91]

Depending on these adjustable properties ionic liquids are used as solvent for numerous chemical reactions, *e.g.* ionic liquids were reported to be excellent solvents for the Diels-Alder reaction.^[106,107] The results of reactions, conducted in ionic liquids, showed a significant conversion enhancement compared to water, which is known to enhance the rate and selectivity of this chemical reaction.^[108] Furthermore the selectivities for this reaction can be improved by the addition of a mild Lewis acid such as zinc(II) iodide.^[109] One further advantage of ionic liquids as solvent for this reaction type is that the ionic liquid and the catalyst can be recycled and reused after solvent extraction or the product can be purified by direct distillation from the ionic liquid.^[88] Other examples for the application of ionic liquids as solvent for chemical reactions are the regioselective alkylation of indole and 2-naphthole derivatives,^[110,111] selective oxidation reactions,^[112] hydrogenation reactions

of C=C bonds catalyzed by transition metal complexes,^[113] ruthenium and rhodium complex catalyzed hydroformylation reactions of olefins,^[114,115] palladium (II) catalyzed cross-coupling Heck reactions,^[116–119] Baeyer-Villiger reactions^[120] and Beckmann rearrangements.^[121] In addition, the chloroaluminate(III) based ionic liquids are used as solvents/reactants for Friedel-Crafts reactions^[122,123] and oligomerization of olefins in the presence of homogenous nickel(II) catalysts.^[124,125]

In the chemical industry ionic liquids found their application at the BASIL™ process (**B**iphasic **A**cid **S**cavenging utilizing **I**onic **L**iquids), developed by BASF. The BASIL™ process was originally developed to scavenge HCl in the production of diethoxyphenylphosphine (Scheme 6, R = phenyl) to prevent the formation of undesirable side reactions. In contrast to the common method with triethylamine 1-methylimidazole acts as HCl scavenger in this process. This procedure offered the advantage in contrast to the triethylamine method, that no formed salt has to be filtered off. The formed 1-methylimidazoliumchloride (melting point = 75 °C)^[126] and the pure product can be simply separated by a phase separation.^[127,128]



Scheme 6 Basic reaction equation of the BASIL™ process.

Depending on their negligible vapor pressure, non-flammability, low toxicity and tunable physicochemical properties ionic liquids in particular are used as solvents for liquid-liquid extraction processes.^[129,130]

In the recent years ionic liquids also showed versatile applications in materials science. Thereby, ionic liquids simply can act as the reaction medium, *e.g.* they can be used as solvent for sol-gel reactions for the synthesis of aerogels, which can be dried without a supercritical drying procedure.^[131,132] A further sol-gel application of ionic liquids was reported by Zhou et al. They hydrolyzed titanium tetrachloride in 1-butyl-3-methylimidazolium tetrafluoroborate [bmim][BF₄] with small amounts of water (water-poor conditions) in a low-temperature synthesis (T = 80 °C) to get TiO₂ nanocrystals, which form mesoporous spherical aggregates by self-assembly.^[133] Interesting material properties were also obtained by using mixtures of ionic liquids and organic solvents, as reported by Nakashima and Kimizuka.^[134] The authors reported the use of an ionic liquid-toluene mixture for the single step synthesis of hollow titania microspheres. Here the ionic liquid and the toluene are hydrophobic and immiscible. In this case titanium *tert*-butoxide is hydrolyzed by water traces in the reaction mixture and the ionic liquid itself act as a stabilizer for the hollow spheres.^[135]

Another application for ionic liquid as reaction medium is the ionothermal synthesis, which describes reactions that are conducted in ionic liquids at high temperature. In comparison to conventional hydrothermal or solvothermal synthesis, these reactions offer the advantage that they can be executed at ambient pressure, because of the negligible vapor pressure of the used ionic liquids, which eliminates the safety risk caused by high pressure reactions.^[134] The first ionothermal fabricated material is the zeolite SIZ-1, which contains 4- and 5-coordinated aluminum atoms.^[136] Further examples are the LaCO_3OH nanoparticle and nanowire ionothermal synthesis from La_2O_3 in a mixture of ionic liquid (1,1,3,3-tetramethylguanidinium lactate) and water^[137], the synthesis of alumino phosphate chain structures^[138] and molecular sieves^[139] and also iron and manganese oxalato-phosphonates with a three-dimensional network structure were synthesized ionothermally.^[140]

Also so-called “all-in-one” ionic liquids have been reported. In these cases the ionic liquid is not only used as a solvent, but it acts as a molecular precursor with a well-defined composition, structure and reactivity.^[134] One example for this application is the synthesis of unusual CuCl morphologies from ionic liquid crystal, which can act as the precursor, the template and the reactant at the same time. In this case the ionic liquid precursor is a mixture of bis(dodecylpyridinium)tetrachlorocuprate and a derivate of ascorbic acid forming a thermotropic liquid crystal. The copper(I) chloride (CuCl) is formed during heating by the reduction of the copper(II) species with the ascorbic acid. The CuCl adopted the layered architecture of the ionic liquid crystal precursor by the formation of an unusual plate morphology.^[134,141]

In material synthesis ionic liquids are also used as molecular building blocks, *e.g.* in the polymerized ionic liquids (PIL). Thereby some of the unique properties of ionic liquids are incorporated in polymer chains.^[142] The poly-ionic liquids can be generally synthesized by the direct radical polymerization of ionic liquid monomers, *i.e.* vinylimidazolium based ionic liquids.^[143] These PILs are used as polymer electrolytes in batteries and fuel cells, because they eliminate the known disadvantages of liquid electrolytes such as leakage, flammability, toxicity and instability.^[144] Furthermore they are used as polymeric surfactants in the synthesis of conductive organic polymer dispersions.^[145]

Ionic liquids can also be immobilized on solid surfaces, *e.g.* on porous silica^[146] or silica nanoparticles.^[147] The unique physicochemical properties of ionic liquids can be transferred to the substrates.^[148] The anchoring of ionic liquids on silica materials can be executed by the condensation reaction of trimethoxysilyl groups on the silica surface, as shown in chapter 1.3. Mainly these immobilized ionic liquids are used for catalysis applications, because in comparison to the pure ionic liquids, they are not leaching by the catalytic reaction and, because of the high

surface area of the used silica materials, only small amounts of the catalyst have to be used.^[149] Furthermore, immobilized ionic liquids are used for solid-phase extraction^[150] and for chromatographic separation techniques, *i.e.* for stationary phase in liquid chromatography columns.^[151,152]

The synthesis of ionogels is a further possibility to immobilize ionic liquids in a solid material, while keeping their specific properties. The second component beside the ionic liquid can be organic (polyethylene oxide, cellulose *etc.*), inorganic (silica, carbon nanotubes *etc.*) or organic-inorganic (silsesquioxane *etc.*). The various types of ionogels can be divided in two groups: physical and chemical gels. The physical gels are characterized by only weak interactions between the compounds, *e.g.* hydrogen bonds, hydrophobic interactions, π - π interactions *etc.* They can be obtained by adding a low molecular weight organic gelator, like carbohydrates, such as β -D-Glucose or α -cyclodextrin, which build the gel by self-assembly. In general, physical gels show a limited mechanical stability, as they are often jellies or pastes. In contrary chemical gels are cross-linked by covalent bonds. They consist of organic or inorganic oxide matrices, which can be prepared by sol-gel process from a metal alkoxide precursor. In comparison to the physical gels, the chemical gels show a significantly higher mechanical stability.^[153] Depending on their physicochemical and electrical properties ionogels are high promising for numerous applications such as electrolytic membranes for lithium batteries^[154,155] fuel cells^[156] and solar cells^[157] and for gas separation membranes^[158] *etc.*

The Ionic Nanoparticle Networks, developed in this work, are closely related to the chemical ionogels, as the silica nanoparticles are covalently bonded to ionic liquid-like moieties.

2 **Research Goals**

The main goal of this work was the synthesis of novel ionic nanoparticle networks (INN) hybrid materials and the investigation of their resulting versatile properties.

In the first part silica nanoparticle networks were synthesized by grafting organic linker molecules on the surface of metal oxide nanoparticles and connecting them by a nucleophilic substitution. Afterwards, the chemical composition of the materials was investigated by numerous analysis techniques. The thermal stability, the short range order and the kinetics of the building reaction of the INN materials were also investigated. Furthermore, solid state NMR measurements, *ab-initio* calculations and DFT studies gave a deeper insight in the structural development at the nanometer scale of these hybrid materials. Based on these investigations, experiments on the electrical properties of the materials were executed.

The core of this work was the investigation of the photoluminescence properties of the INN materials. The tailoring of the excitation and emission wavelengths of INN materials was investigated by the modification of the organic linker molecules between the nanoparticles. The influence of the different linker molecules on the short range order and the resulting changes in photoluminescence activity was also determined.

In the third part of this work metal chlorides, which are known to form chloro metalate complexes, were tested for the complexation reaction with the chloride ions of the INN materials. Afterwards, the resulting properties, such as thermochromism and photoluminescence features of the INN materials were explored.

Depending on the fact that ionic liquids show a high affinity to carbon dioxide and that nowadays the CO₂ transformation into usable chemicals is of capital importance, the INN materials were tested as heterogeneous catalysts for the synthesis of cyclic carbonates from epoxides and CO₂. Thereby, the influence of the substituents on the imidazole and of different linkers between the silica nanoparticles on the catalytic reaction was evaluated.

The last point of interest was to synthesize silica nanoparticle network based self-healing materials. Therefore, principles of self-healing polymers were transferred to nanoparticle networks. Afterwards, the self-healing abilities of the resulting materials were tested.

3 Results and Discussion

3.1 Syntheses

3.1.1 Nanoparticle Syntheses

All nanoparticles used in this work were prepared by “chimie douce” process. In the most cases, silica nanoparticles were used for the synthesis of the Ionic Nanoparticle Networks materials, which will be referred hereafter as INN materials. The silica nanoparticles were synthesized by Stöber process,^[47] in which tetraethoxysilane acts as silicon source. The reaction (Figure 4) was carried out in methanol with a small amount of water and a basic catalyst. In this case an aqueous solution of NH_3 was used. The catalyst plays a very important role and has to be handled very carefully, because if the concentration of the ammonia solution is too high on the one hand, the particles will grow very fast and get too big, while offering a quite bad particle size distribution. On the other hand, if the ammonia solution is concentrated too low, the particles will not grow at all. Empirical studies, in the course of this work, showed that ammonia solutions with a concentration of about 30 w% NH_3 are best for growing silica nanoparticles with an average hydrodynamic diameter (determined by DLS) of about 16 nm after three days of stirring.

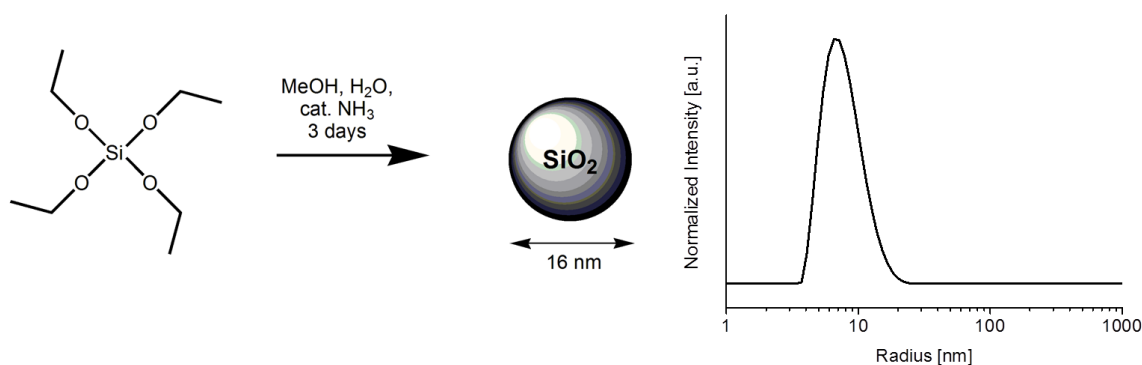


Figure 4 (left) synthesis of silica nanoparticles, (right) DLS of a methanolic silica nanoparticle solution.

Alternatively, zinc oxide nanoparticles were used for the synthesis of so-called mixed INN hybrid materials. These zinc oxide nanoparticles were synthesized by a procedure published by Dejene *et al.*^[159] Therefore, zinc(II) acetate dihydrate was dissolved in ethanol. This was followed by cooling with an ice bath and the addition of an ethanolic sodium hydroxide solution. After two days of stirring zinc oxide nanoparticles with an average diameter of 6 nm were formed (Figure 5).

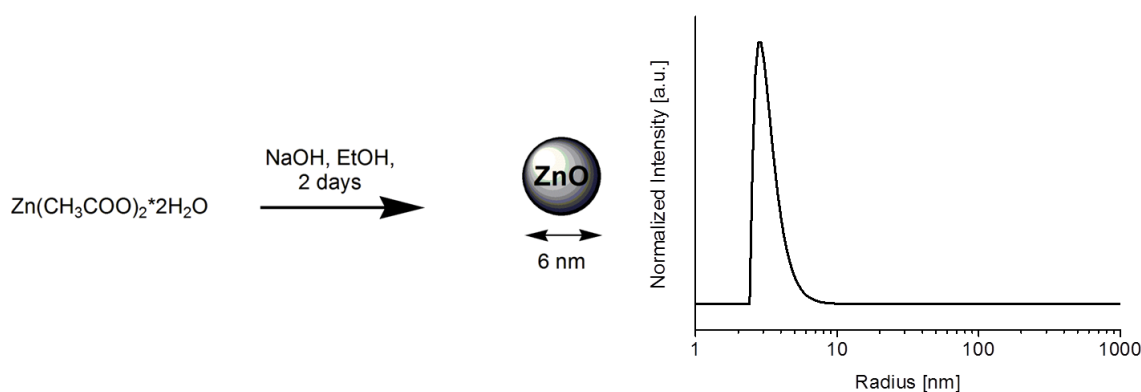
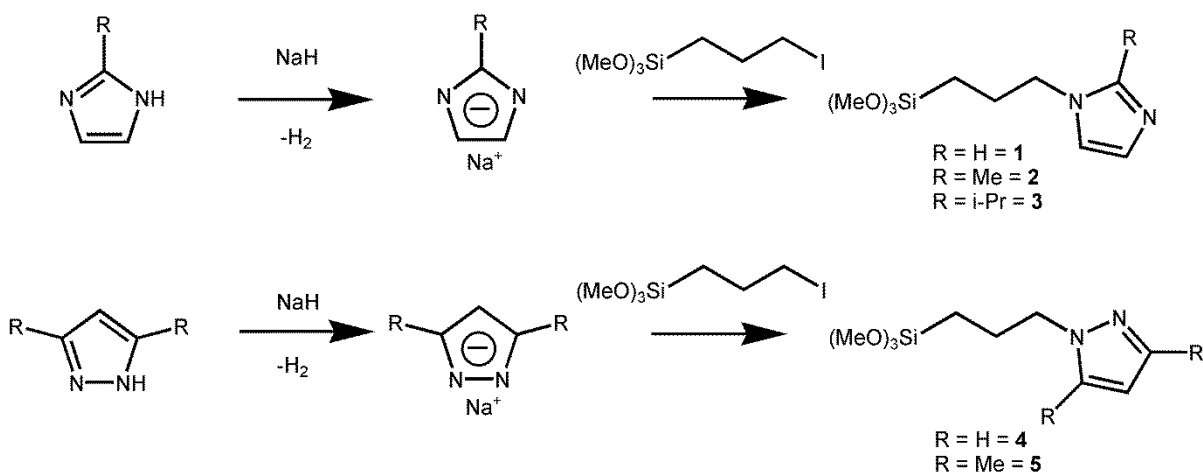


Figure 5 (left) synthesis of zinc oxide nanoparticles, (right) DLS of an ethanolic zinc oxide nanoparticle solution.

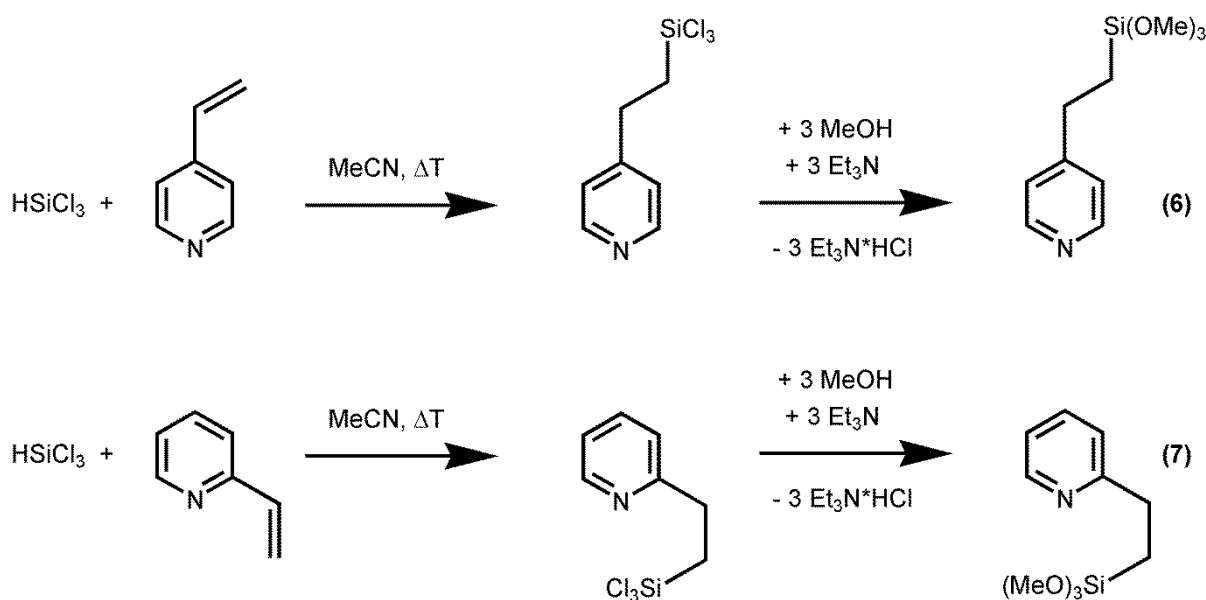
3.1.2 Precursor Synthesis and Nanoparticle Surface modification

The precursor molecules, that are required to modify the surface of the nanoparticles, were in all cases different substituted trimethoxysilanes, which were obtained by nucleophilic substitution reactions or hydrosilylation reactions. The nucleophilic substitutions, used for the synthesis of the respective trimethoxysilanes, were carried out with different substituted diazoles, such as imidazoles and pyrazoles (Scheme 7).^[160] In the first step the hydrogen atom was removed by sodium hydride in dry tetrahydrofuran to get the respective sodium imidazolide or pyrazolide. Afterwards this salt reacted in a nucleophilic substitution with 3-iodopropyltrimethoxysilane to get the respective N-(3-propyltrimethoxysilane)imidazole or N-(3-propyltrimethoxysilane)pyrazole.



Scheme 7 Synthesis of various N-(3-propyltrimethoxysilane)imidazoles and N-(3-propyltrimethoxysilane)pyrazoles.

Another possibility for the synthesis of nitrogen base linked trimethoxysilanes is a metal catalyst free hydrosilylation. This alternative method was chosen for the pyridine derivatives, because the method used for imidazole and pyrazole was not applicable in this case, depending on the fact that there is no second nitrogen atom available to bond the trimethoxysilylpropyl group in a nucleophilic substitution. In the first step of this reaction the trichlorosilane reacts with 2- or 4-vinylpyridine by refluxing in dry acetonitrile to form the respective trichlorosilylethylpyridine (Scheme 8).^[161] The second step of the reaction is the substitution of the three chlorine atoms by three methoxy groups. The complete reaction was carried out in a one pot synthesis. After purification by distillation a colorless transparent liquid was successfully obtained, with yields of 33 % and 75 % for the 2-(2-trimethoxysilylethyl)pyridine (**7**) and the 4-(2-trimethoxysilylethyl)pyridine (**6**), respectively. It turned out that the yield of the 4-(2-trimethoxysilylethyl)pyridine was significantly higher than for the 2-(2-trimethoxysilylethyl)pyridine. One possible explanation for this phenomenon could be the formation of a pentacoordinated silicon species for the first step of the building reaction, which was observed by G.W. Fester.^[162] Most likely, the pentacoordinated silicon compound hinders the second part of the reaction from a kinetic point of view. The formation reaction of 4-(2-trimethoxysilylethyl)pyridine was also executed on the common hydrosilylation reaction pathway with a Karstedt catalyst, but a yield of only about 5 % was obtained. Due to this fact, the metal catalyst free hydrosilylation followed by a methanolysis reaction was chosen for the synthesis of this kind of trimethoxysilanes.



Scheme 8 Formation of 4-(2-trimethoxysilylethyl)pyridine and 2-(2-trimethoxysilylethyl)pyridine in a one pot synthesis.

The synthesized trimethoxysilanes were analyzed by NMR spectroscopy, which is exemplarily shown in the ¹H NMR spectrum of 4-(2-trimethoxysilylethyl)pyridine in Figure 6. The signals of the ethyl

group were observed at a chemical shift of 2.20 ppm and 0.45 ppm. Due to the sterically hindered rotation of the ethyl group, the hydrogen atoms of the CH₂ groups show geminal and vicinal coupling at the same time, leading to a doublet on a triplet signal. The same phenomenon was also observed in the ¹H NMR spectrum of 2-(2-trimethoxysilylethyl)pyridine. The hydrogen atoms of the trimethoxysilyl group correspond to the signal at a chemical shift at 3.04 ppm. The signals at a chemical shift of 7.97 ppm and 6.62 ppm can be assigned to the C-H groups of the pyridine ring.

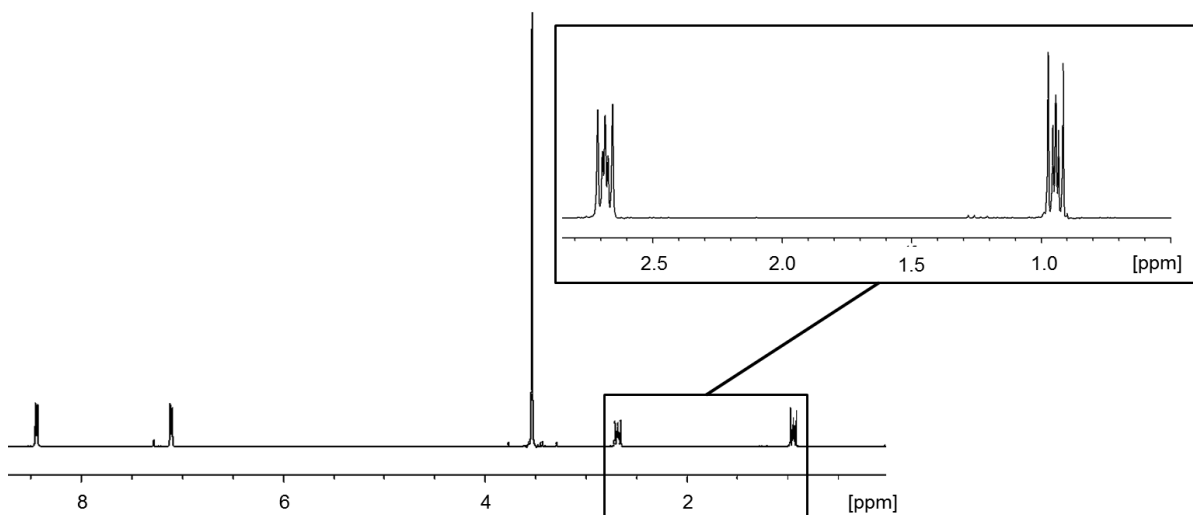


Figure 6 ¹H NMR spectrum of 4-(2-trimethoxysilylethyl)pyridine.

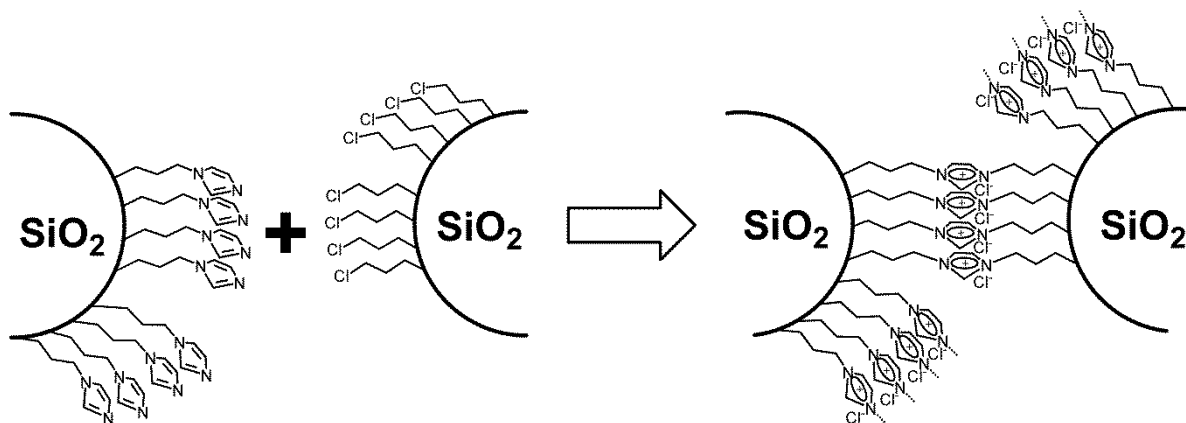
This type of a metal catalyst free hydrosilylation was also tried for the reaction of HSiCl₃ and 1-vinylimidazole, but only a hexacoordinated silicon compound was formed, which was determined by ²⁹Si NMR (one signal at a chemical shift of -195 ppm). For the synthesis of trimethoxysilanes with a longer alkyl chain in order to get a better self-assembly of the ligands in the materials many attempts were performed. Additionally, some other nitrogen bases were tried to couple with a trimethoxysilane. Unfortunately, most of these reactions did not work. The main problem of the synthesis of this type of trimethoxysilanes was the purification of the product after the respective building reaction. To be more precise, if the molar mass was too high (about > 300 g/mol), it was not possible to purify the trimethoxysilanes by vacuum distillation. Additionally, due to the trimethoxysilyl groups, the purification of the products by column chromatography was not possible, because the trimethoxysilane species would link covalently to the stationary phase of the column. Besides that, it was supposed that some of the products were destroyed by the distillation (see experimental part).

For the allocation of functional groups on the nanoparticle surface, trimethoxysilanes were chosen since they show controllable reactivity in sol-gel reactions.^[44] The following materials synthesis requires trimethoxysilanes containing a halogen or nitrogen base end group. After the synthesis of

the respective trimethoxysilane the surface of the silica nanoparticles was modified directly in the suspension obtained by the Stöber process. For a systematic investigation of the properties of the INN hybrid materials, numerous different nitrogen base substituted trimethoxysilanes were used to modify the surface of the nanoparticles.

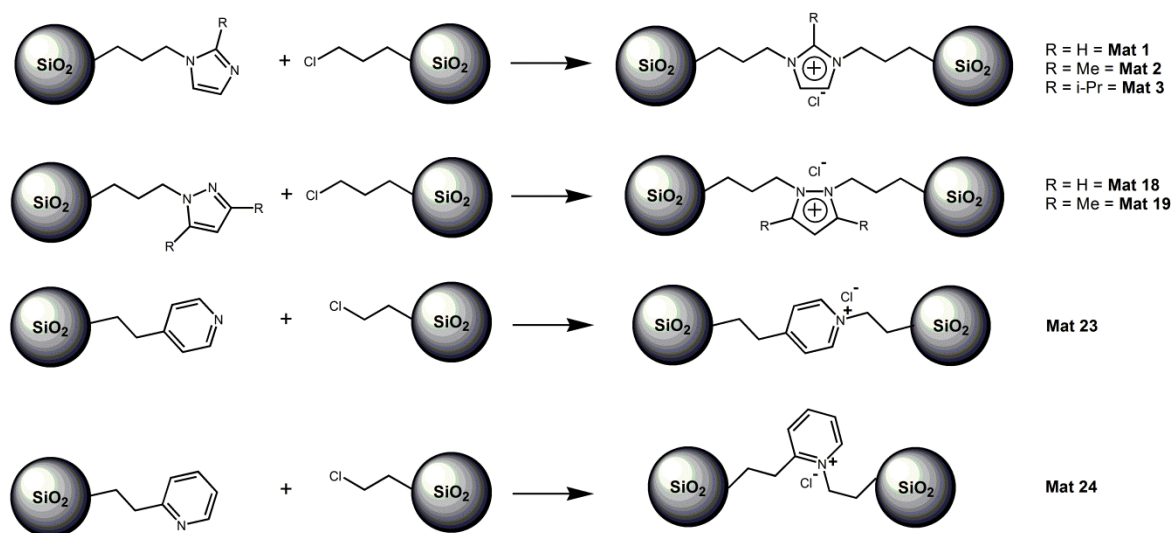
3.1.3 Synthesis of the INN hybrid materials

The final synthesis of the basic hybrid material is based on a nucleophilic substitution between the 1-propylimidazole and chloropropyl modified silica nanoparticles (Scheme 9).



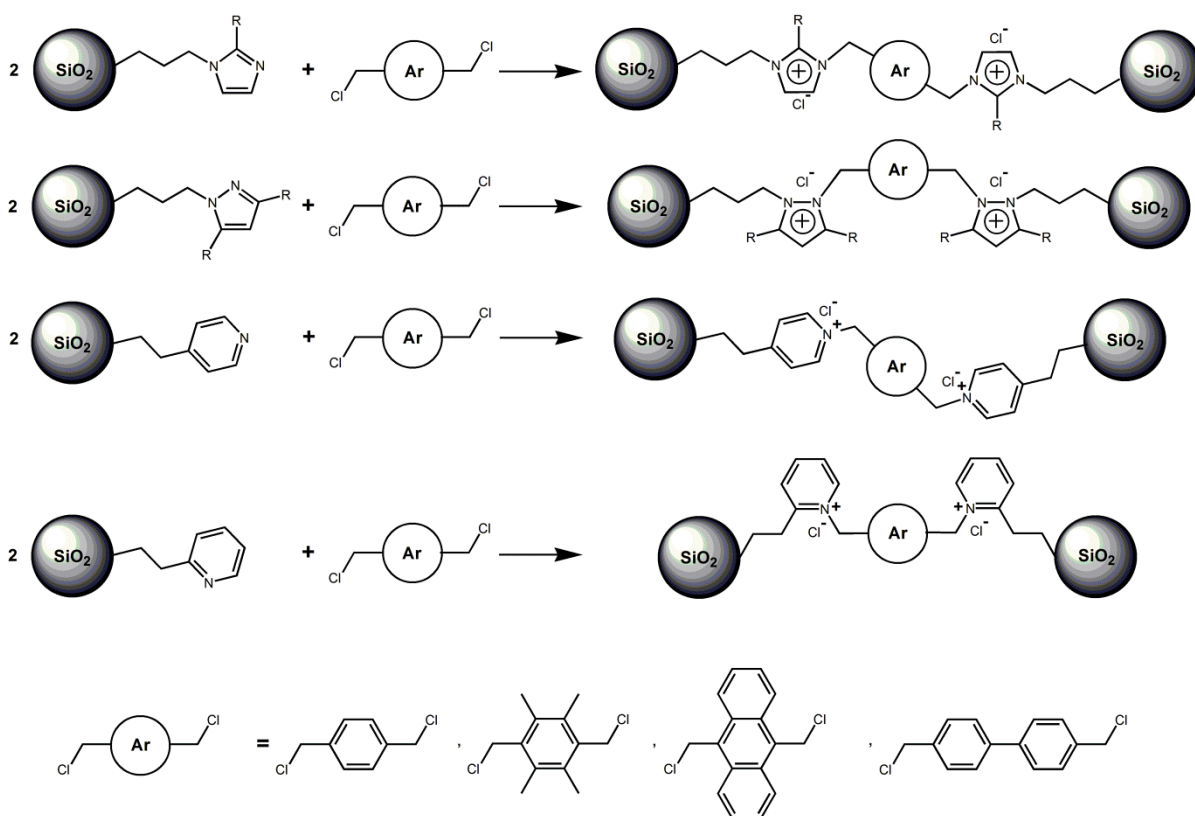
Scheme 9 Reaction of imidazole modified silica nanoparticles with chloroalkyl modified silica nanoparticles to form the INN hybrid material.

The reaction led to the formation of imidazolium moieties between the silica nanoparticles and is related to the common synthesis of ionic liquids. The biggest difference is that there is no need to heat the reaction mixture to reflux. The reaction takes place by stirring the different nanoparticle species in methanol in a volume ratio of 1 : 1 for two to three days at room temperature. After this procedure, the solvent was removed under vacuum conditions and the product was dried carefully. This reaction was applied to various different five-membered nitrogen heterocyclic ring bases, such as different substituted imidazoles and pyrazoles (Scheme 10), modified silica nanoparticles as well as for ethylpyridine derivative modified silica nanoparticles. For the coupling of the pyridine bases with a chloroalkyl chain, due to the symmetry of the particle bridging, chloroethyl instead of chloropropyl modified silica nanoparticles were used for the material synthesis (Scheme 10).



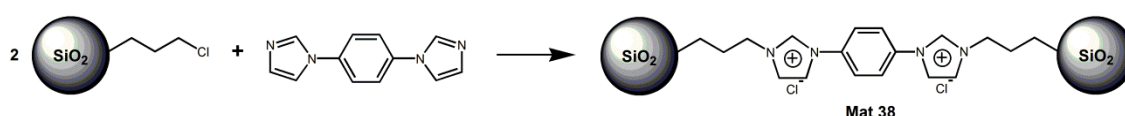
Scheme 10 Formation of the various mono nitrogen base bridged INN materials.

Another possible synthesis of the hybrid materials is the reaction of two equivalents of nitrogen base modified silica nanoparticles and one equivalent of a chloromethylene (-CH₂Cl) disubstituted aromatic linker molecule, *e.g.* α,α' -dichloro-*p*-xylene (Scheme 11).



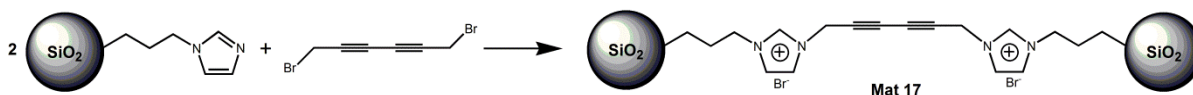
Scheme 11 Various coupling possibilities between nitrogen base modified silica nanoparticles and chloromethylene (-CH₂Cl) disubstituted aromatic linker molecules to form INN hybrid materials.

For this nucleophilic substitution it is very important to use aromatic molecules which exhibit two chloromethylene groups ($-\text{CH}_2\text{Cl}$). It is not possible to couple the nitrogen base modified silica nanoparticles directly to a dihalogeno substituted aromatic system. Because, in this case the reaction type changes from nucleophilic substitution to an aromatic nucleophilic and this would require completely different reaction conditions.^[163] One strategy to get a full conjugated three ring system is to synthesize a diimidazole, *e.g.* 1,4-bis(1H-imidazol-1-yl)benzene can be synthesized by an aromatic nucleophilic substitution of 1,4-dibromobenzene and imidazole with CuSO_4 as the catalyst. Afterwards this diimidazole can be used to react in a nucleophilic substitution with two chloropropyl modified silica nanoparticles to form the INN materials (Scheme 12).



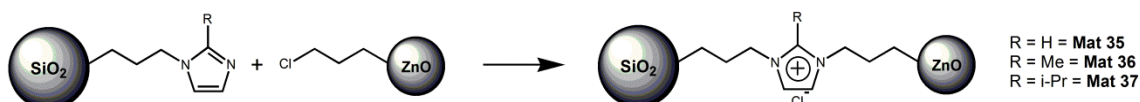
Scheme 12 Synthesis of a full conjugated three ring system based INN material.

Furthermore, a full conjugated π -system can be introduced by using 1,6-dibromo-2,4-hexadiyne as the linking unit to connect the imidazole units. Therefore two equivalents of imidazole modified silica nanoparticles were allowed to react with one equivalent of 1,6-dibromo-2,4-hexadiyne, which was provided by the University of Montpellier (Scheme 13).



Scheme 13 Synthesis of the bis-imidazolium based diacetylene linked INN material.

Additionally, so-called mixed Ionic Nanoparticle Networks were obtained by the reaction of imidazole modified silica nanoparticles and chloro modified zinc oxide nanoparticles (Scheme 14). The surface modification of the zinc oxide nanoparticles was only possible with 3-chloropropyltrimethoxysilane. While using the nitrogen base substituted trimethoxysilanes for surface modification the nanoparticles agglomerated immediately and formed a colorless precipitate. This may occur due to the more basic zeta potential of the zinc oxide nanoparticles compared to the silica nanoparticles (10.2 and 2.1 respectively).^[164,165]



Scheme 14 Formation of the so-called mixed zinc oxide containing INN materials.

A general overview of all synthesized materials and their abbreviation can be found at the end of the experimental part.

3.1.4 Processing of the INN hybrid materials

The Ionic Silica Nanoparticle Networks could be processed into various forms. Essential for the processing of the hybrid materials is the drying process. After a quick drying procedure with high temperatures and under vacuum conditions, colorless powders or transparent self-standing films with an average thickness of 35 μm could be obtained (Figure 7). At this point it has to be highlighted that the self-standing films are really flexible. Performing a slow drying procedure in the oven at 45 $^{\circ}\text{C}$ on a petri dish, transparent gels could be obtained. Moreover, the INN hybrid materials can be processed into monolithic gels by drying them slowly under air over a period of eight weeks. Per definition a gel monolith is a free-standing bulky gel. Furthermore, the INN hybrid materials can be processed into thin films. Therefore a methanolic solution of the material has to be dip coated on to glass slabs or other substrates. These manifold processing possibilities open the door for several investigations on the materials, *e.g.* electric measurements and catalytic investigations. The so-called mixed, zinc oxide containing, INN materials could only be processed into colorless powders.

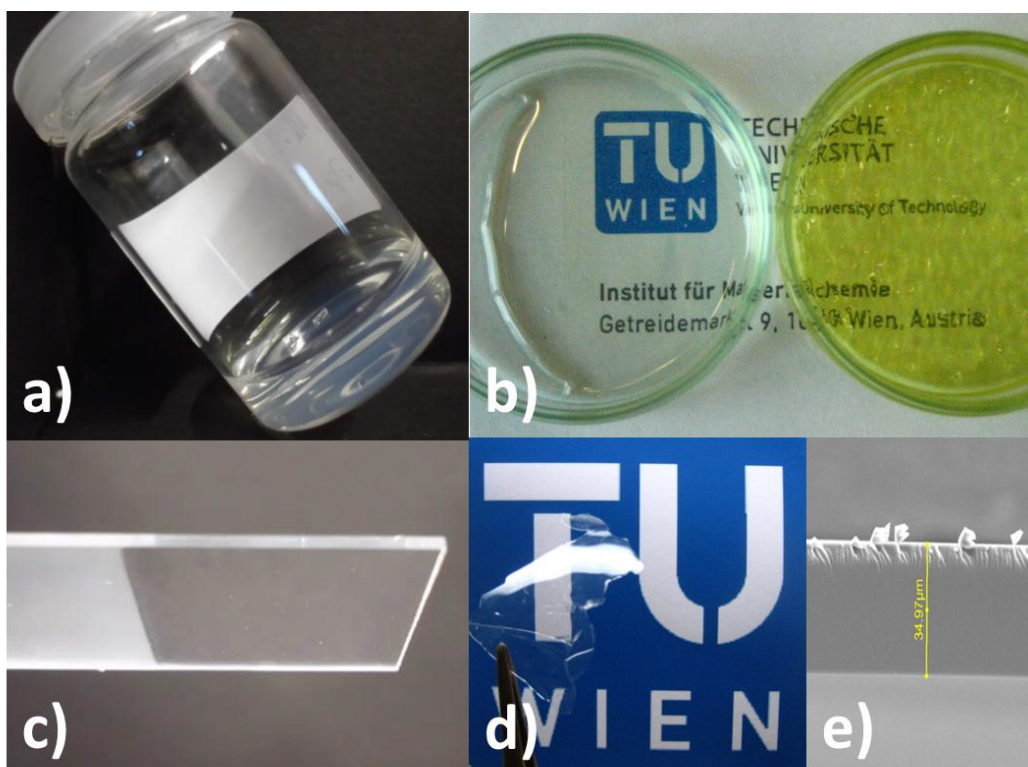


Figure 7 Versatile processing of the INN hybrid materials: a) monolithic gel of **Mat 1** b) (left) transparent colorless gel of **Mat 8**, (right) transparent yellow gel of **Mat 11** c) **Mat 1** coated on a glass slab d) self-standing film of **Mat 1** e) SEM Image of the self-standing film of **Mat 1**.

3.2 Characterization

3.2.1 Chemical Analysis of the INN hybrid materials

To prove that the respective INN materials were synthesized indeed, numerous analysis techniques were executed on the materials.

One possibility to get proof of the formation of the ionic network is to change the anion of the INN material.^[166] Therefore the solid materials were mixed with NaBF₄ or KPF₆ in a weight ratio of 1 : 1 (about 0.3 g each) and were stirred in acetone for 24 hours. The used salts were in excess compared to the amount of exchangeable anions in the material. The reason for choosing acetone as the solvent was that sodium chloride and potassium chloride are nearly insoluble in acetone. Therefore, the driving force of the metathesis reaction is the precipitation of these salts.^[167] When the reaction was complete the solvent and the product were separated by centrifugation. Afterwards the product was washed with water, ethanol and acetone. After each washing step the respective solvent was separated from the product by centrifugation. This procedure was followed by combining the washing phases and the reaction solvent. The combined phases were evaporated and the resulting corresponding salt was further investigated.

One possibility to evaluate the success of the metathesis reaction were powder XRD investigations of the solid residue after the evaporation combined washing and reaction phases. In the XRD pattern of the residue of the dried phases, the signals of NaCl and KCl, respectively, were observed (schematically shown for an anion exchange of **Mat 1** in Figure 8). However, the salts for the anion exchange, NaBF₄ and KPF₆ were added in large excess. In consequence the XRD patterns of these salts were dominant in the powder XRD investigations. The procedure of anion exchange was executed on all of the different INN materials and led to almost equal results. Alternatively, the presence of the exchanged chlorine anion in the residue could be proven by a quite simple and fast reaction: the residue was dissolved in water and the chlorine was detected as AgCl after adding some drops of a 0.1 molar solution of AgNO₃.

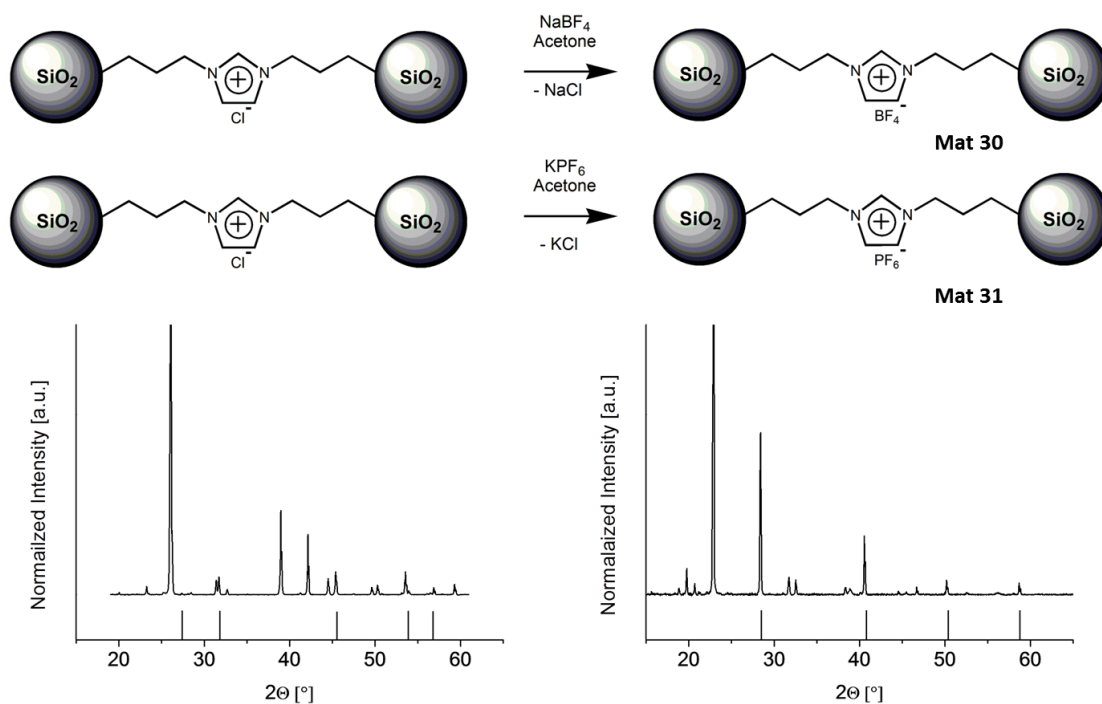


Figure 8 (top) reaction equation for the anion metathesis at **Mat 1** to form **Mat 30** and **Mat 31**, (bottom left) XRD pattern of the solid residue after the anion metathesis of **Mat 1** with NaBF_4 and the comparison spectrum for NaCl (JCPDS # 02-0818), (bottom right) XRD pattern of the solid residue after the anion metathesis of **Mat 1** with KPF_6 and the comparison spectrum for KCl (JCPDS # 01-0786).

Furthermore, the resulting material after the anion metathesis could be investigated by solid state NMR spectroscopy. This was done for **Mat 30** by ^{11}B CP/MAS NMR spectroscopy and for **Mat 31** by ^{31}P CP/MAS NMR spectroscopy. The changed properties of the material, due to the exchanged anion, were investigated and published by M. Litschauer *et al.* ^[166]

Elemental analysis, as another direct analysis method, was executed on the INN materials. In Table 1 selected results are presented. The samples showed a quite heterogeneous composition. This heterogeneity arises from the amorphous character of the hybrid materials, caused by polydisperse nanoparticles and various coverage densities of the organic groups on the surface of the nanoparticles. Due to this fact the presented weight percent for carbon, hydrogen, nitrogen and chlorine were calculated out of the average values from triple and in some case from four way determinations of the respective elements. It was not possible to verify the composition of the presented very accurately by this analytical method, but some trends have to be mentioned and discussed. The INN materials listed in Table 1 offer carbon values in a range between 20 and 38 w%. As expected, the mono-imidazolium based INN materials show lower amounts of carbon compared to the bis-imidazolium based INN materials. Furthermore, by comparing the 2-methylimidazolium based INN materials and the imidazolium based INN materials (**Mat 1** & **Mat 2**, **Mat 4** & **Mat 5** *etc.*) the expected higher carbon content for the 2-methylimidazolium based can be confirmed. This

circumstance was also monitored for the mixed ZnO nanoparticle containing INN materials (**Mat 35 & 36**). The obtained hydrogen content is located between 3.6 and 5.2 w% for the INN materials and it is dependent on the carbon content of the respective INN material. The nitrogen values should be dependent on the imidazolium/imidazole content of the investigated material. For the presented materials the nitrogen value is located between 5.7 and 11.3 w% and it is obvious that for the mono-imidazolium based INN materials a lower nitrogen content was observed compared to the bis-imidazolium based INN materials. The chlorine content shows a very interesting behavior and gives a reason for a more detailed discussion. The weight percent values for the chlorine content are located between 1.0 and 10.6 w%. The highest amount of chlorine was observed for the mono-imidazolium based (**Mat 1 & 2**) and the bis-imidazolium based xylene linked INN materials (**Mat 4 & 5**). Especially for the bis-imidazolium based INN materials the chlorine content can be a measure of the number of coupled imidazolium moieties, because after the synthesis of the materials, they were washed with water, ethanol and acetone. During this washing procedure non-reacted linker molecules were separated from the product. That means after the washing procedure only linker molecules, which are covalently bonded on the imidazolium units, remain in the material, which is in direct correlation to the chlorine content of the material. In Table 1 it can be seen that xylene (**Mat 4 & 5**) linker based INN materials are coupled very well, followed by the biphenyl linker containing materials (**Mat 7 & 8**), while the anthracene linked materials (**Mat 10 & 11**) showed the worst coupling, considering this hypothesis. This correlation will be discussed later in the thesis. In addition, a lower content of chlorine was observed for the so-called mixed INN (**Mat 35 & 36**) compared to the respective pure silica INN materials (**Mat 1 & 2**). This fact could be explained by the different sizes of ZnO and SiO₂ nanoparticles. In fact, the ZnO nanoparticles, which can only be modified with 3-chloropropyltrimethoxysilane, offer only half the hydrodynamic diameter in comparison to the silica nanoparticles. In consequence they can be modified with less chloropropyl groups compared to the silica nanoparticles and this is why lower chlorine contents were observed for the mixed INN materials (**Mat 35 & 36**) compared to the pure silica INN materials (**Mat 1 & 2**).

Table 1 Average weight% values of selected INN materials.

Sample	w% C	w% H	w% N	w% Cl
Mat 1	20.1	4.3	5.7	9.4
Mat 2	21.3	4.4	6.0	6.0
Mat 4	32.9	5.2	7.7	10.6
Mat 5	34.0	5.2	8.0	8.4
Mat 7	30.5	4.6	10.4	3.6
Mat 8	37.6	5.1	10.3	3.0
Mat 10	28.8	4.3	9.8	2.8
Mat 11	35.4	4.9	11.3	1.0
Mat 35	24.9	3.6	7.1	4.9
Mat 36	26.8	4.2	6.5	3.4

Additionally, scanning electron microscopy (SEM) coupled with energy dispersive X-ray spectroscopy (EDX) was carried out on a piece of self-standing film of **Mat 1**. In Figure 9 a picture of the breaking edge of the 35 μm thick film is presented. The EDX spectrum showed the expected reflexes for the silica nanoparticles (silicon and oxygen), for the 1,3-dipropylimidazolium bridging unit (carbon and nitrogen) and chlorine at an energy of about 2.6 keV. The gold signal at 2.2 keV belongs to the SEM sample preparation, where the gold is vapor deposited on the surface of the INN material to generate electric conductivity on the material surface and to prevent a positive charging of the INN material. Furthermore, it should be kept in mind that EDX analysis is not as accurate (especially for light elements) compared to other characterization methods (*e.g.* elemental analysis), but it is accurate enough to demonstrate some trends in the elements ratio and to answer the question of the existence of an element into a sample.

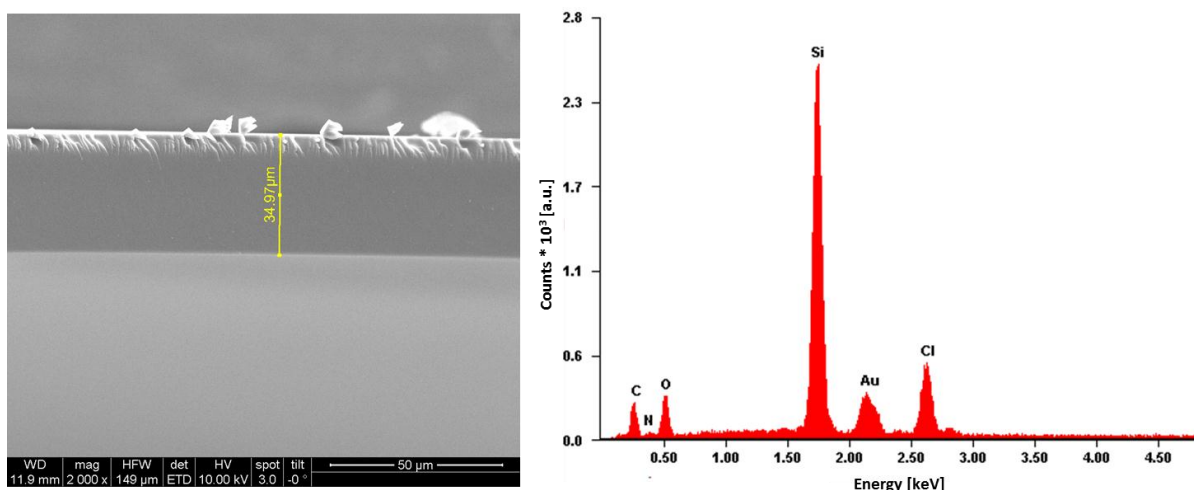


Figure 9 (left) SEM image of a piece of self-standing film of **Mat 1**, (right) EDX measurement of a piece of self-standing film of **Mat 1**.

On the same piece of self-standing thin film of **Mat 1** Raman investigations were executed. From this spectrum no conclusions about the structure of the materials can be made, but due to the high absorption of the INN material, interference features could be monitored.

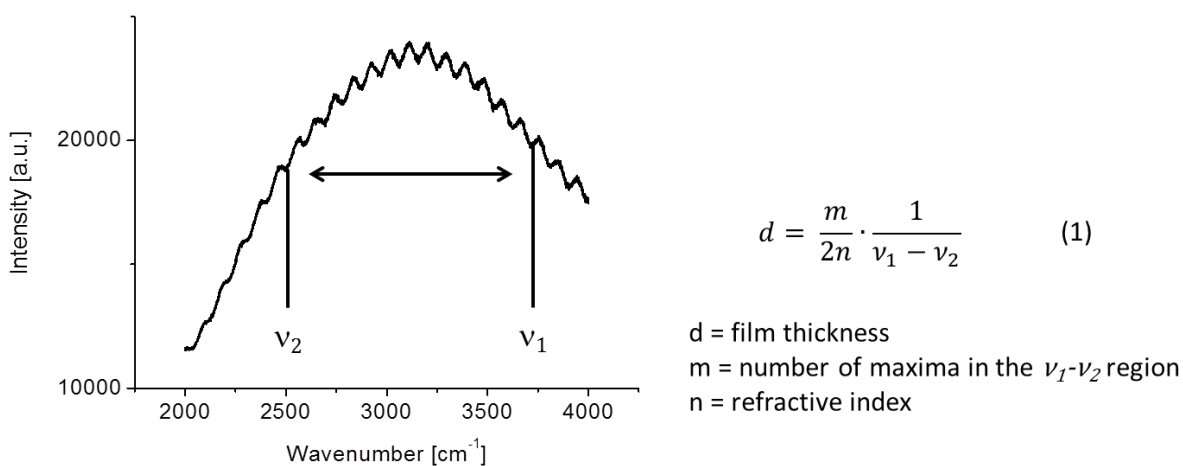


Figure 10 Raman spectrum of the self-standing film of **Mat 1** and equation (1) for the calculation of the refractive index of the material.

Depending on this interference, the refractive index of the material was calculated to 1.63 by using equation (1). Due to the simplicity of the determination method the accuracy of the value of this refractive index should be regarded with suspicion.

For the so-called mixed ZnO nanoparticle containing INN material **Mat 36** TEM measurements coupled with energy dispersive X-ray spectroscopy (EDX) were carried out. In Figure 11 three TEM

images of the material **Mat 36** are shown and it attracts attention that the ZnO nanoparticles (the bright points in the TEM images) looks like well-arranged while offering exactly defined distances between each other. This clearly suggests the formation of a well-defined three dimensional network of SiO₂ and ZnO nanoparticles connected by 1,3-dipropyl-2-methylimidazolium chloride units. The EDX analysis of this material reinforced the hypothesis of a well-defined three dimensional network (Table 2). The atomic % of Si and Zn offer a ratio of about 1 : 2, which correlates to the fact that the diameter ratio of these two different nanoparticle species exhibit the same ratio. Additionally, chlorine was found in the samples. Carbon and nitrogen were also found in the material, but the peaks overlapped one another, and, for this reason, it was not possible to integrate them.

For all of the pure silica based INN materials TEM imaging was not applicable, because of the bad z-contrast of silica nanoparticles placed in an organic matrix.

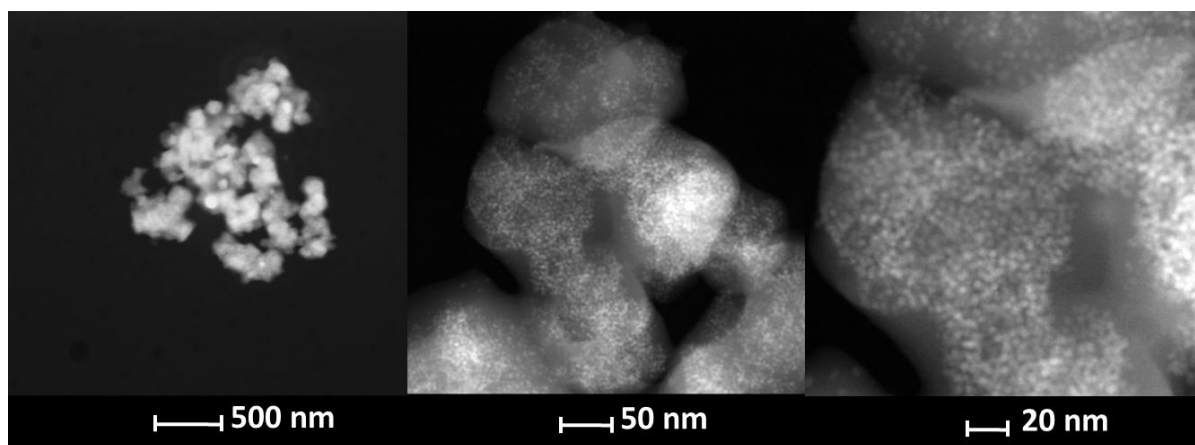


Figure 11 TEM images of **Mat 36** at increasing magnifications (from left to right).

Table 2 EDX analysis for **Mat 36** for the elements O, Si, Cl and Zn.

Element	Weight %	Atomic %
O	27	49
Si	29	30
Cl	8	7
Zn	35	15

The application of numerous analysis techniques showed that all the different INN materials were synthesized at the expected reaction pathway.

3.2.2 Thermal Analysis on the INN hybrid materials

Thermogravimetric analyses under air were carried out for the reference material (**Mat 1**) and for the chloropropyl modified silica nanoparticles as well as for the 1-propylimidazole modified silica nanoparticles. For the chloropropyl and 1-propylimidazole modified silica nanoparticles onset temperatures were observed at 170 °C and 250 °C respectively. It was determined that the mass loss below 170 °C corresponds to the degradation of absorbed solvent molecules (water and methanol) and above, until 250 °C, the degradation of unbound ligands was observed. However, for the final hybrid material (**Mat 1**) an elevated degradation onset temperature, starting at 300 °C, was monitored.^[168] Recent measurements (Figure 12 and Figure 13) of the reference material (**Mat 1**) reinforced these observations. Further TGA measurements on **Mat 1** and on the bis-imidazolium based INN materials with different aromatic linkers (**Mat 4**, **Mat 7** and **Mat 10**) were carried out to explore the influence of the linker molecules on the thermal behavior of the INN materials. For the reference material (**Mat 1**) a mass loss of 4.2 w% was monitored below 300 °C. At temperatures above 300 °C the material was decomposed in two steps. The first decomposition step took place at a temperature of 300 °C and the second step at about 580 °C. At a temperature higher than 650 °C the decomposition of the organic part of the hybrid material has been finished and a colorless residue, SiO₂, was left over. The positions of the decomposing steps were quite similar for all investigated materials. However, the materials showed different values for the mass loss at each step (see Figure 12). The bis-imidazolium based material, consisting of the xylene linker (**Mat 4**), showed the biggest mass loss (72 w%) compared to the reference material (**Mat 1**) (54 %), which corresponds to the higher organic content in the material. Furthermore the two-step decomposition is very distinct for this material. The bis-imidazolium based material, containing the biphenyl linker (**Mat 7**), showed a slightly higher mass loss (58 %) compared to the reference material (54 %) and the bis-imidazolium based material, containing the anthracene linker (**Mat 10**), showed a slightly lower mass loss (50 %) compared to the reference material. The comparison of the three bis-imidazolium based materials reinforces the trend that by increasing the organic content in the material the mass loss is decreased. This phenomenon, which looks paradox in the first moment, can be explained by the goodness of the network inside the materials. After the synthesis of the materials, they were washed with water, ethanol and acetone to remove excessive non-reacted linker. In consequence a bigger amount of non-reacted linker was removed by this step for the biphenyl and especially for the anthracene linker. This leads to the conclusion that the coupling reaction worked better for α,α' -Dichloro-*p*-xylene than for 4,4'-bis(chloromethyl)-1,1'-biphenyl and 9,10-bis(chloromethyl)anthracene.

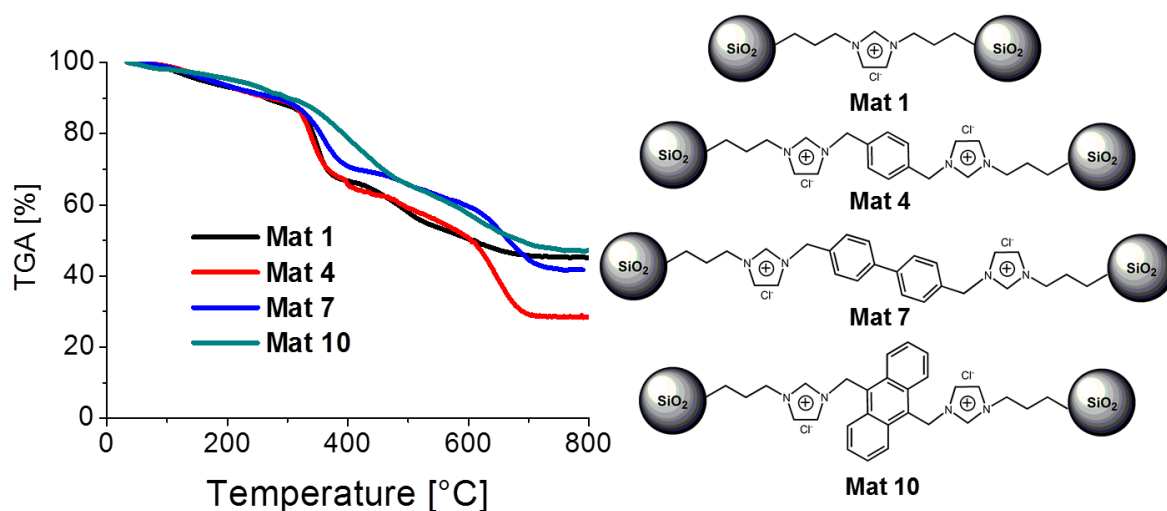


Figure 12 TGA measurement of **Mat 1**, **Mat 4**, **Mat 7** and **Mat 10** at a heating rate of 10 K min^{-1} .

On top of that, TGA/MS measurements were executed under argon on the reference material (**Mat 1**) and the anion exchange products (**Mat 30** and **Mat 31**) to explore the degradation process more in detail. The materials seem to decompose at slightly higher temperatures compared to the TG analyses. One explanation for this phenomenon could be the fact that the TG was measured in air and TGA/MS under argon atmosphere. That means in the TG measurements some oxidation processes could be responsible for the slightly lower onset temperature. At this point it has to be mentioned that both, TG and TGA/MS investigations, were executed at a heating rate of 10 K min^{-1} . For **Mat 1** (Figure 13) at temperatures lower than 300 °C and a mass loss of 4.2 w\% the evaporation of water and methanol could be proven by mass spectrometry (mass numbers 18, 28 and 32).

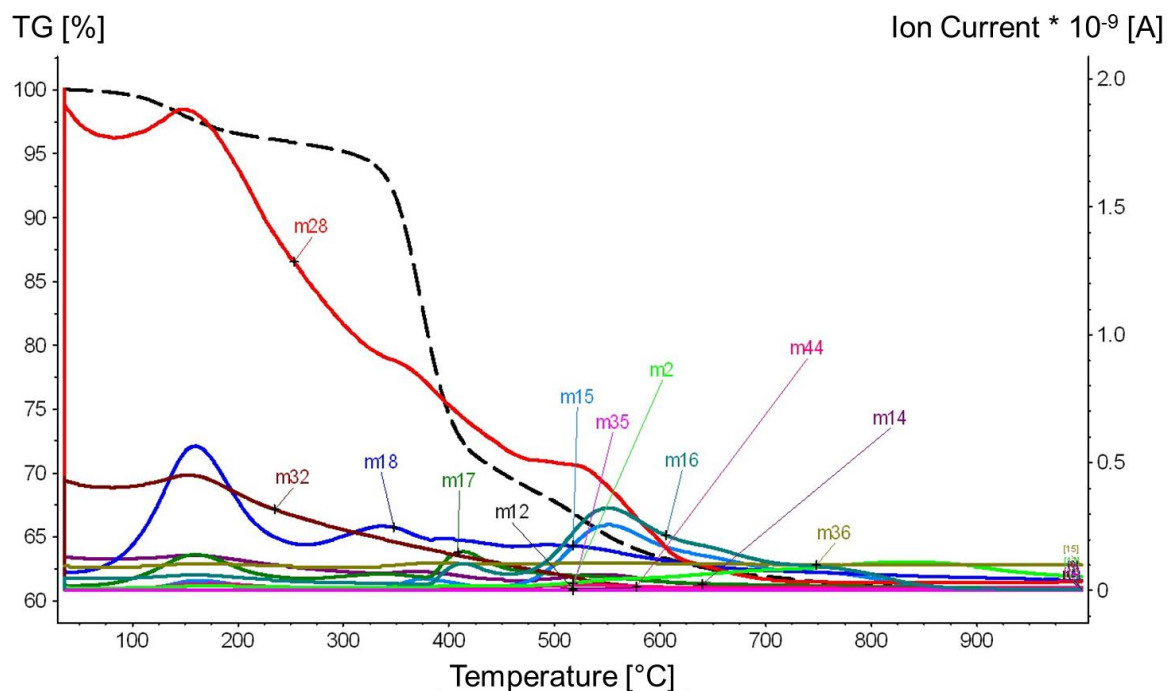


Figure 13 TG/MS measurement of **Mat 1**, dotted black line: TGA, solid lines: MS measurements for several mass numbers.

For a better visibility of the change of the remaining mass numbers in the MS measurement at the temperature area above 300 °C, the ion current of the MS measurement (y-axis) was plotted logarithmically in Figure 14. At a temperature above 300 °C the main decomposition of the material started, as observed in previous TGA measurements. For this first decomposition step the mass spectrum showed two different events. At mass number 17 there are OH groups visible, but due to the high temperature, they have their origin not in adsorbed water. Most likely they are corresponding to silanol groups (Si-OH) grafted on the surface of the silica nanoparticles. Furthermore, organic fragments (28), nitrogen (14) and chlorine (35) could be observed in the mass spectrum. This proves the decomposition of the organic part of the hybrid material at this temperature. Most likely, the decomposition step at this temperature corresponds to the decomposition of the ionic part of the material, as the decomposition of chlorine based ionic liquids takes place in this temperature area as well.^[87,169,170] For the second decomposition step organic nitrogen fragments were found as well. In addition, HCl (36) could be monitored. This suggests that at the first decomposition step some of the imidazolium chloride may be converted into imidazole hydrochlorides, which were decomposing in a second step at higher temperatures.

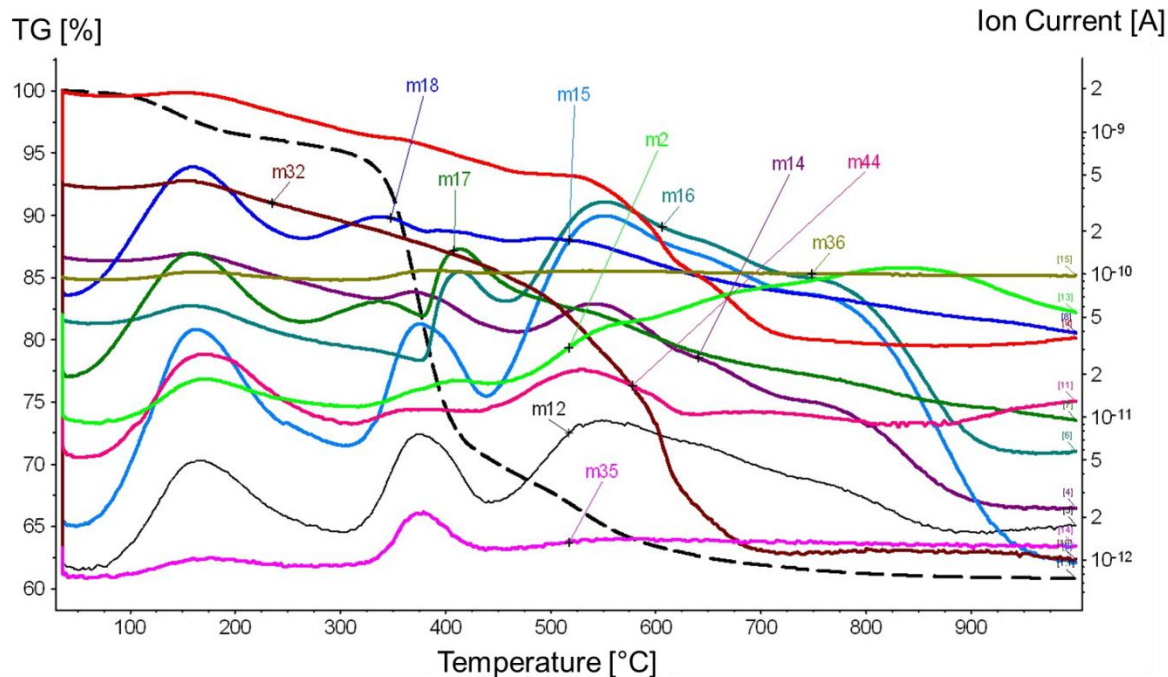


Figure 14 TG/MS measurement of **Mat 1**, dotted black line: TGA, solid lines: logarithmic plot of the MS measurements for several mass numbers.

For the anion exchanged BF_4^- containing material (**Mat 30**) the TGA curve looks quite similar compared to the curve of **Mat 1** (Figure 15). At temperatures below 300 °C and a mass loss of 3.7 % water and methanol were detected again. At temperatures above 300 °C two less well developed decomposition steps were observed. In the first step quite the same fragments were detected as for **Mat 1**. The difference here lies only in the anion. In consequence, F (19) and B (11) were detected for the first decomposing step. For the second step of **Mat 30** an escape of organic and BF_4^- (86) fragments was observed. In consequence, the TGA/MS delivered an additional proof that the anion has been exchanged. For the anion exchanged PF_6^- containing material (**Mat 31**) the TG/MS analysis looks quite similar compared to **Mat 30**, except that the presence of the PF_6^- was verified at the first decomposing step at temperatures higher than 300 °C.

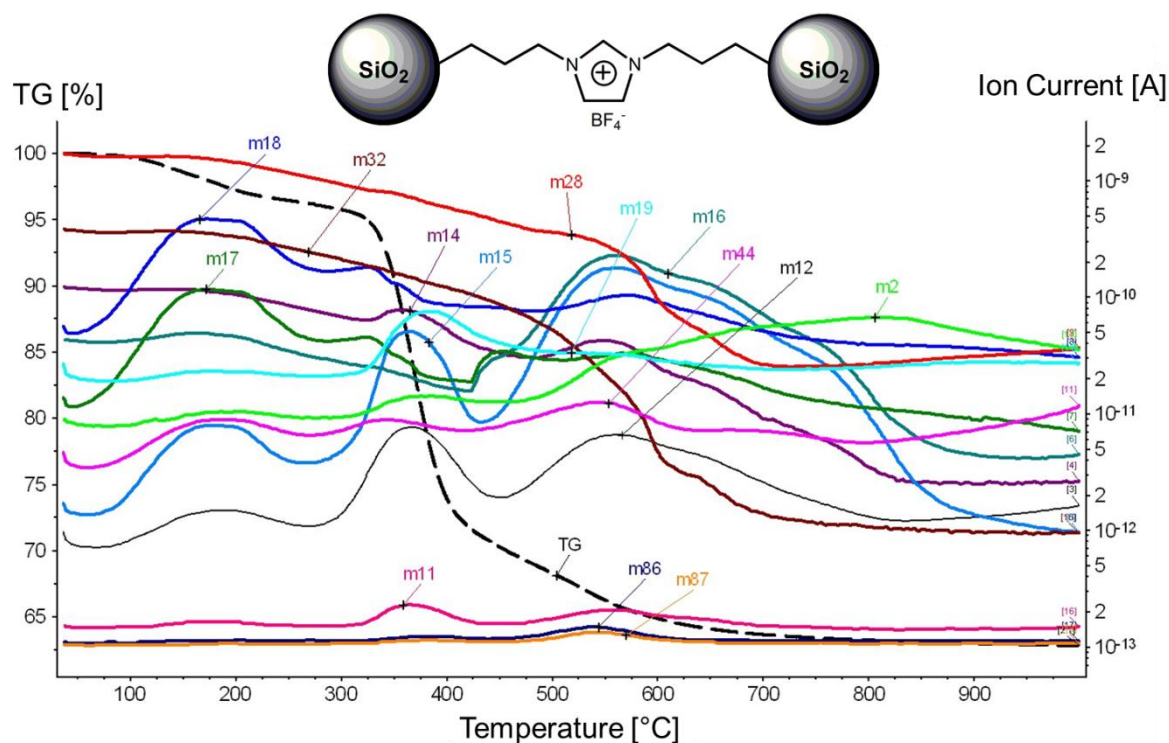


Figure 15 TG/MS measurement of **Mat 30**, dotted black line: TGA, solid lines: logarithmic application of the MS measurements for several mass numbers.

In conclusion the thermal characterization methods were very suitable method to verify the formation of INN hybrid materials. The organic content of the INN materials was in the range between 50 % and 70 %. In addition, it could be proven that the mass loss below 300 °C corresponds to water and methanol. For the INN materials this solvent content was determined between 3 % and 5 %. Furthermore, the assumptions of Marco Litschauer on the thermal decomposition of the INN material above 300 °C were reinforced by the TG/MS measurements. Additionally, the decomposing mechanism was quite similar for the three investigated INN materials, and the influence of the anion was not significant for the thermal stability of the materials.

3.2.3 Structural Analysis of the INN Materials by Short Angle X-ray Scattering (SAXS)

The INN inorganic-organic hybrid materials exhibit a short-range order. Depending on this fact, small angle X-ray scattering (SAXS) was the method of choice to investigate the organization of the INN materials at the nanometer scale. These measurements granted an insight view into size, distance and arrangement at the nanosized objects discussed in this work.^[171]

Figure 16 shows exemplarily scattering curves (black symbols) for **Mat 1 – Mat 3** and the respective fits (red lines). The first shoulder or peak at about $q = 0.4 \text{ nm}^{-1}$, which corresponds to distance in real space of about 16 nm, was assigned to the size and distance of the silica nanoparticles. The broad peaks in the area from $q = 3$ to 6 nm^{-1} , corresponding to distances in real space of approximately 1 – 2 nm, were attributed to the interparticle distance resulting from the bridging of the linker molecules. The intensity slope towards small q -values is exactly -4, caused by the electron density contrast, suggesting a sharp interface between the inorganic and organic part of the material.

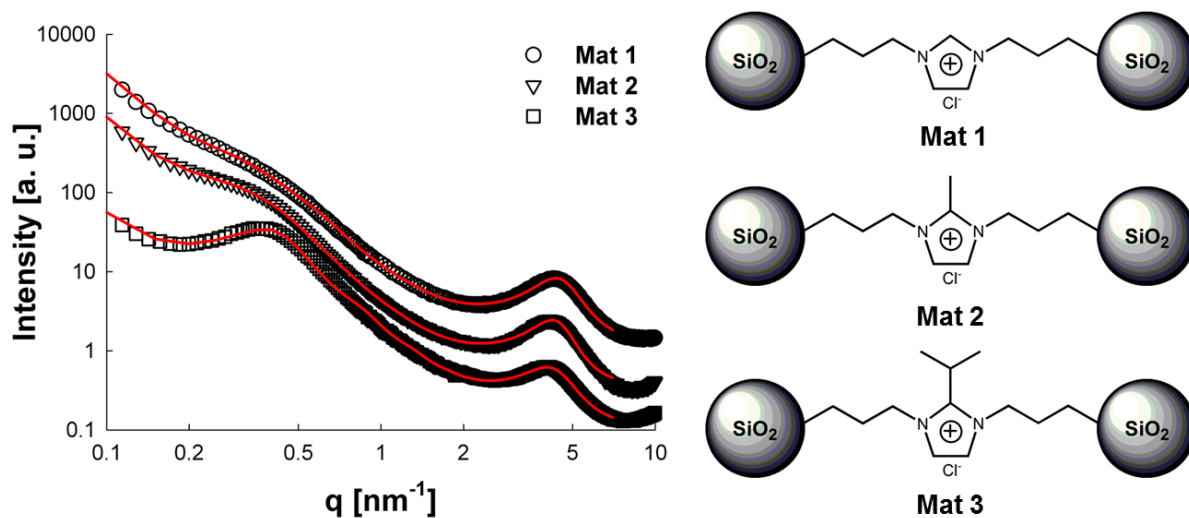


Figure 16 Scattering curves (black symbols) of **Mat 1, 2** and **3** and the respective fits (red lines).

Due to the fact that the scattering curve presents a two-level system (the larger silica nanoparticles and the smaller bridging ligands) a unified model, proposed by Beaucage for hierarchical structures, was applied for the data evaluation.^[172,173] The visible scattering intensity $I(q)$ is described by:

$$I(q) = a \cdot q^{-4} + P(q) \cdot S(q) + bgr \quad (2)$$

In this equation a is a constant containing experimental parameters such as beam intensity, phase contrast between the two phases and additional variables due to the setup of the experiments,^[171] q is the scattering vector $P(q)$ is the form factor, $S(q)$ is the structure factor, and bgr is a constant value, which corrects remaining background scattering. For the data evaluation the unified form factor $P(q)$, suggested by Beaucage, was used:^[172]

$$P(q) = G \cdot e^{\left(-\frac{q^2 r_g^2}{3}\right)} + B \left(\frac{q}{\left[\operatorname{erf} \left(\frac{q r_g}{\sqrt{6}} \right) \right]} \right)^{-p} \quad (3)$$

In this equation erf is the error function, G and B are numerical prefactors and r_g is the gyration radius. Furthermore, an effective structure factor^[173] $S(q)$ from a hard sphere model^[174,175] was used:^[176]

$$S(q) = \frac{1}{1 + 24\eta \frac{G(A)}{A}} \quad (4)$$

$G(A)$ is defined as:

$$\begin{aligned} G(A) = & \alpha \frac{(\sin A - A \cos A)}{A^2} \\ & + \beta \frac{(2A \sin A + (2 - A^2) \cos A - 2)}{A^3} \\ & + \gamma \frac{[-A^4 \cos A + 4\{(3A^2 - 6) \cos A + (A^3 - 6A) \sin A + 6\}]}{A^5} \end{aligned}$$

and:

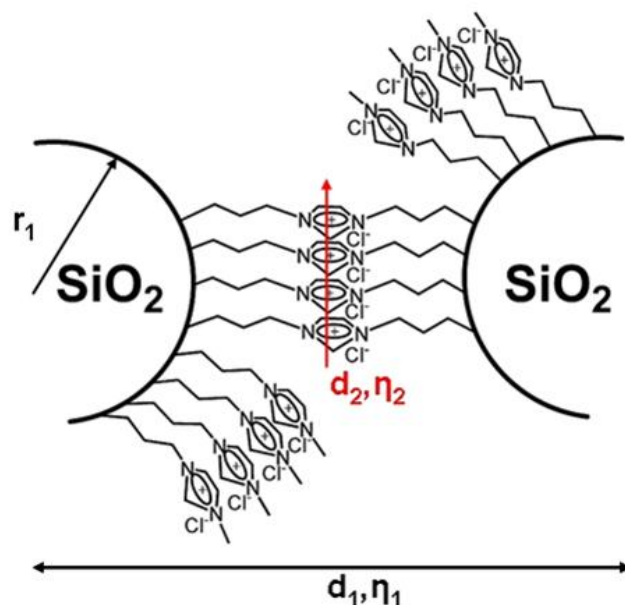
$$\begin{aligned} A &= qd_s \\ \alpha &= \frac{(1 + 2\eta)^2}{(1 - \eta)^4} \\ \beta &= -6\eta \frac{(1 + \eta^2)^2}{(1 - \eta^2)} \\ \gamma &= \frac{\eta\alpha}{2} \end{aligned}$$

The values for the mean distance d_s of the particles and for the hard sphere volume fraction η were deduced from this hard sphere model.^[174] Only two parameters are needed to describe the particle-particle interaction. That is the reason for using η_i and d_i . One of the fitted parameters is the radius

of gyration r_g of the silica nanoparticles, which can be converted into the equivalent particle diameter \varnothing_p by the following equation (5).

$$\varnothing_p = 2r = 2 \sqrt{\frac{5}{3}} r_g \quad (5)$$

Additional fitting parameters are the distance d_1 of the silica nanoparticles and the hard sphere volume fraction η_1 . This value gives the probability of finding a neighboring silica particle in the vicinity of another one. Furthermore, the degree of order of the imidazolium rings was described by two values: their distance to each other d_2 and the hard sphere volume fraction η_2 . The hard sphere volume fraction η_2 is a measure of the degree of order of the imidazolium rings in the material. That means the higher the η_2 value, the higher the agglomeration, the stronger the short range order and the more pronounced the peak in the scattering intensities. ^[176,177] The set of parameters for the silica nanoparticles is given the subscript 1 (d_1 and η_1), and the subscript 2 is given to the linker regarding parameters (d_2 and η_2). Scheme 15 shows a sketch of the INN material and the parameter describing the nano-structural arrangement.



Scheme 15 Definition of the SAXS parameters on the example of a non-substituted mono-imidazolium based INN material (**Mat 1**).

The resulting numerical data of the described parameters of **Mat 1** are presented in Table 3. The diameter \varnothing_p of the silica nanoparticles is about 12.4 nm. This is in agreement with the values obtained from the DLS measurements for the particle diameter without a solvent shell. Additionally, the distance of correlation, d_1 , of 13.5 nm was determined by fitting the SAXS curve. This distance corresponds to two nanoparticle radii plus, in this case, the length of the linking 1,3-

dipropylimidazolium chloride moiety. Thereby the length of the linking unit was about 1 nm, which fits the assumed size of the 1,3-dipropylimidazolium chloride unit quite good. At this point, it has to be highlighted that numerical values of the particle size, determined by different methods, should be carefully interpreted, because not only the type of the material, but also its shape and porosity might have a significant influence.^[178] The interparticle distance d_2 is assigned to the distance of the imidazolium units and correlates with the measure of the degree of the short range order in the INN material, the hard sphere volume fraction η_2 .

Table 3 Parameters obtained from the mathematical fitting of the SAXS measurements of **Mat 1**.

r [nm]	\varnothing_p [nm]	η_1	d_1 [nm]	η_2	d_2 [nm]
6.2	12.4	0.08	13.5	0.31	1.37

SAXS measurements on the INN materials revealed a short range order of the silica nanoparticles in the material. The phenomenon of short range order in hybrid materials was also discussed in literature, *e.g.* the self-assembly of room temperature ionic liquids in silica wormlike pores reported by Antonietti *et al.*^[179] Most likely, this short range order is caused by π - π -stacking interactions between the aromatic rings between the silica nanoparticles.^[180,181] The numerous SAXS measurements of all the different INN materials and the influence of the short range order on the respective properties of the materials will be discussed later in this work.

3.2.4 Kinetic determination of the INN material building reaction by quartz crystal microbalance (QCM)

In all preliminary works on INN materials, that were performed in our group, the chosen reaction time for the final synthesis step of the hybrid materials was 48 hours, in order to make sure that the nucleophilic substitution is completed. Thus, it remained very interesting to investigate the kinetics of the building reaction of the INN materials. Quartz crystal microbalance (QCM) measurements were carried out, to realize these kinetic investigations, at Linköping University (Sweden) in cooperation with Prof Nathaniel D. Robinson and his research group. At first, the QCM crystals (sensors) were cleaned in a multi-stage cleaning process (for more details see experimental part). Afterwards, the clean and dry crystals were measured several times and were removed after each single measurement to get the error variation. Then, the sensors were silanized *ex situ*. That means the sensors were treated with two to three drops of the respective N-(3-propyltrimethoxysilane)imidazole (compound **1** or **2**) and let them react for 15 minutes. This was followed by washing the crystals with methanol. Then the crystals were dried for several hours and were measured again dry to figure out the mass of the deposited trimethoxysilane. Afterwards, the equipment, containing a peristaltic pump to run the reactants in circle for the building reaction of the INN material, was setup. For the formation of the INN material like film on the SiO₂ QCM crystal, two different reaction pathways were tried. On the one hand, 1-propylimidazole modified QCM crystals were allowed to react with a methanolic solution of chloropropyl modified SiO₂ nanoparticles for modelling the reaction between 1-propylimidazole and chloropropyl modified silica nanoparticles. On the other hand, 1-propylimidazole modified QCM crystals were treated with a 0.1 molar methanolic solution of α,α' -dichloro-*p*-xylene for the simulation of the reaction of two equivalents of 1-propylimidazole modified silica nanoparticles and α,α' -dichloro-*p*-xylene.

At first, the reaction between a 1-propyl-2-methylimidazole modified crystal and chloropropyl modified silica nanoparticles (Figure 17) will be discussed.

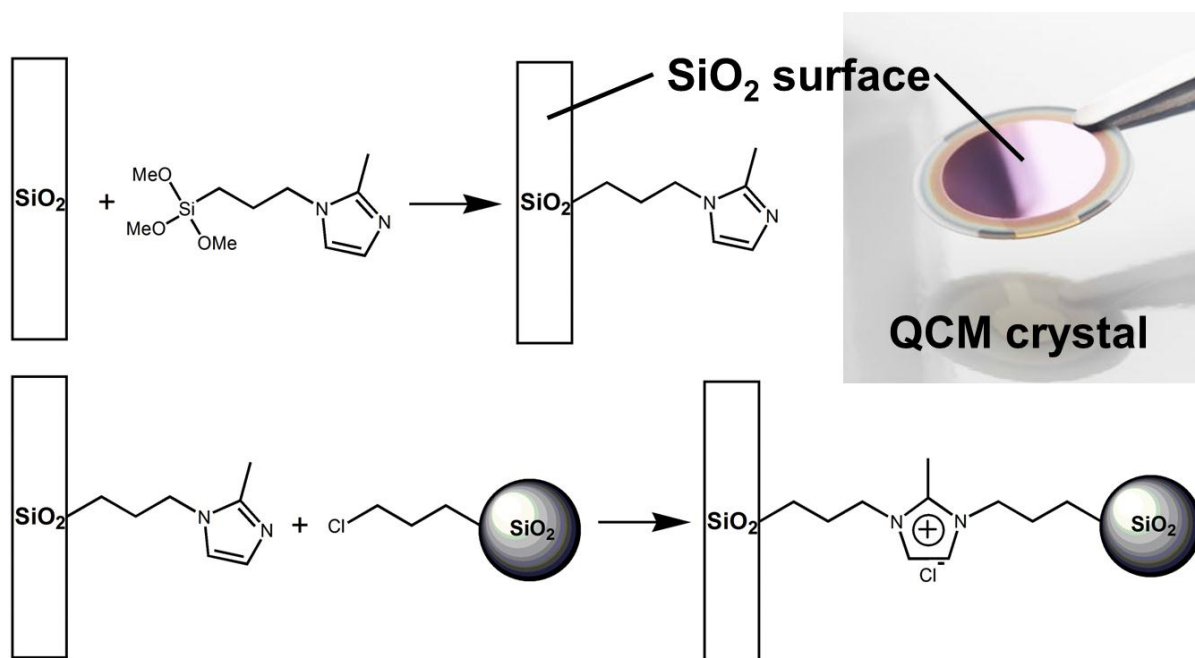


Figure 17 Schematic reaction pathway of the reaction of the 1-propyl-2-methylimidazole modified SiO₂ crystal surface and the chloropropyl modified SiO₂ nanoparticles for the formation of an INN material like film.

The amount of condensed trimethoxysilane on the SiO₂ surface of the crystal was determined by measuring the resonant frequencies for the odd overtones between the 1st and 11th harmonic of the crystal, which can be calculated using the mass change Δm by the Sauerbrey relationship.^[182,183]

$$\Delta m = - \frac{C \cdot \Delta f}{n} \quad (6)$$

$$C = 17.7 \text{ ng Hz}^{-1} \text{ cm}^{-2} \text{ for 5 MHz quartz crystal}$$

$$n = 1,3,5,7,9,11 \text{ (overtone number)}$$

Due to the big error for the 1st and 11th overtone in the measurements, the respective calculated Δm was excluded for further discussions. In Table 4 the mass changes, after the silanization and after completing the coupling reaction between the 1-propyl-2-methylimidazole modified SiO₂ crystal surface and the chloropropyl modified SiO₂ nanoparticles, are presented. For the silanization the average mass change was about 770 ng/cm². The mass of received material after completing the reaction was about 1390 ng/cm².

Table 4 Mass of deposited silane and material for the reaction between 1-propyl-2-methylimidazole modified SiO₂ crystal surface and the chloropropyl modified SiO₂ nanoparticles.

Overtone number	f3	f5	f7	f9	average
Mass silane [ng/cm ²]	780.0	740.1	753.6	806.2	770
Mass material [ng/cm ²]	1318.0	1505.2	1372.9	1366.1	1390

The kinetics of the building reaction of the INN material like film were followed by the change of the frequency Δf , which can be calculated to mass change Δm , and the change of the dissipation ΔD by the time. The dissipation D is defined as the ratio of the energy dissipated in one period of crystal oscillation to the energy stored in the oscillator.^[184] In the q-Sense instrument, this value is calculated from the time constant τ , associated with the decay in the oscillation after the driving potential was removed.^[183,185]

$$D = - \frac{1}{\pi f_s \tau} \quad (7)$$

In the equation above f_s is the resonance frequency of the crystal for the overtone being sampled. The plotting of the frequency overtones f_3 , f_5 , f_7 , f_9 and f_{11} against the time of the QCM measurement of the reaction between the 1-propyl-2-methylimidazole modified SiO₂ crystal surface and the chloropropyl modified SiO₂ nanoparticles as well as an enlarged picture of the time range of the coupling reaction of this QCM measurement are shown in Figure 18. In general, a drop in frequency is equal to an increase of mass on the crystal surface. At the beginning of the measurement MeOH was introduced to the crystal. This was observed in the measurement by a decrease of the frequency overtones. In this case no mass was added on the crystal, but the viscosity changed dramatically between the gaseous and the liquid phase. The methanol was circulated until the frequency values were stabilized to get a stable baseline before adding the reactant. The switch from methanol to the methanolic chloropropyl modified silica nanoparticle suspension was executed after 80 minutes. This can be seen in Figure 18 by a drop of all frequency overtones. There are two possible explanations for this observation. On the one hand, the change from the solvent to the reactant could cause a change of the viscosity of the fluid phase again. On the other hand, it looks like a significant amount of mass was deposited on the crystal surface in a short time. Most likely, a mixture of these two scenarios took place here. After the drop of the frequency overtones a slightly increasing for about 90 minutes was observed. This means some deposited mass was removed from the crystal. Probably, during this period of time, the freshly formed INN material layer was arranged and, in the course of the self-assembly of the material, some of the chloropropyl modified silica nanoparticles were removed from the surface. After this,

the frequency overtones seemed to be very stable, but to get sure that the reaction was completed, the methanolic chloropropyl modified silica nanoparticle suspension was applied on the crystal overnight. After about 17 hours reaction time methanol was applied on the crystal again and a strong increase for the frequency overtones was monitored. The explanation for this phenomenon can be, either, a change in the viscosity of the fluid phase by switching from the nanoparticle solution to methanol or, on the other hand, a removal of non-reacted chloropropyl modified silica nanoparticles from the crystal surface. In general, the application of the D-values against the time Figure 18 shows a reciprocal behavior compared to the application of the frequency overtones. At this point, it has to be highlighted that in this case the coupling reaction between the 1-propyl-2-methylimidazole modified crystal surface and the chloropropyl modified silica nanoparticles only took 90 minutes.

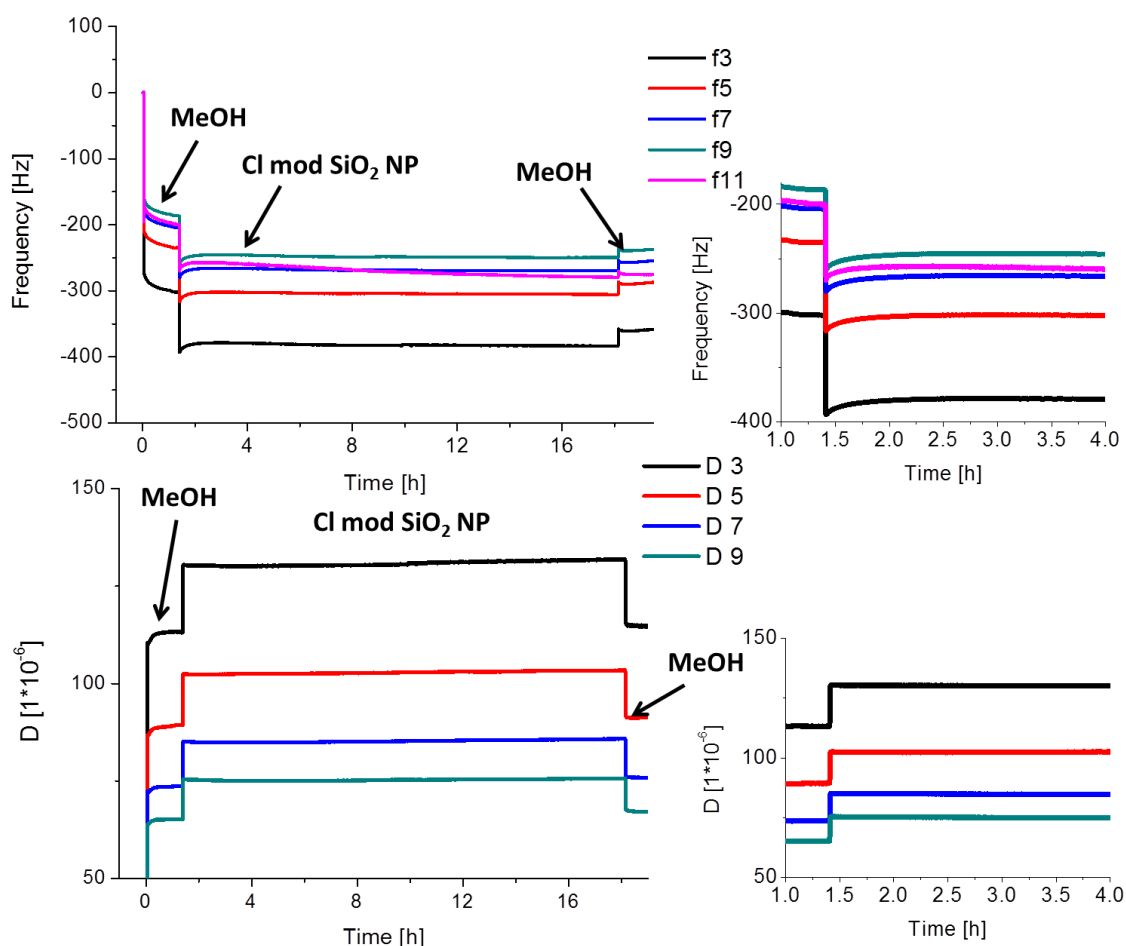
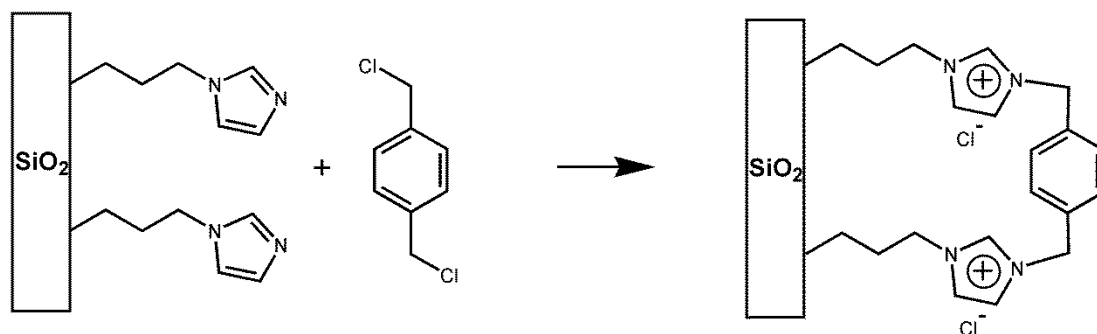


Figure 18 (top left) plot of the f -values against the time for the QCM measurement of the reaction between the 1-propyl-2-methylimidazole modified SiO_2 crystal surface and the chloropropyl modified SiO_2 nanoparticles, (top right) enlarged image of this plot for the reaction time, (bottom left) plot of the D -values against the time for the QCM measurement of the reaction between the 1-propyl-2-methylimidazole modified SiO_2 crystal surface and the chloropropyl modified SiO_2 nanoparticles, (bottom right) enlarged image for this plot for the reaction time.

The second reaction, which was investigated by QCM, is the formation of an INN material from 1-propylimidazole modified QCM crystal and α,α' -dichloro-*p*-xylene (Scheme 16).



Scheme 16 Schematic reaction pathway of the reaction of 1-propylimidazole modified SiO₂ crystal surface and α,α' -dichloro-*p*-xylene for the formation of an INN material like film.

The plot of the frequency overtones f₃, f₅, f₇, f₉ and f₁₁ against the time for the QCM measurement of the reaction between the 1-propylimidazole modified SiO₂ crystal surface and the α,α' -dichloro-*p*-xylene as well as a zoom of this QCM measurement are shown in Figure 19. At the beginning of the measurement, MeOH was introduced to the crystal and an identical decrease, as explained previously, of the frequency overtones was observed. The methanol was moved in cycle until the frequency values were stabilized again and then, after 45 minutes, the fluid phase was switched from methanol to a 0.1 molar methanolic solution of α,α' -dichloro-*p*-xylene. This can be seen in Figure 19 by a little drop of all frequency overtones. This suggests only a small change in the viscosity of the liquid phase and that only a small amount of α,α' -dichloro-*p*-xylene was coupled between the imidazole groups. After the drop of the frequency overtones a slightly increasing of the frequency overtones was observed for about 30 minutes. One explanation for this behavior can be that, at the point of time when the linker solution is introduced to the crystal only one of the chloromethylene (-CH₂Cl) groups of the linker coupled rapidly in a nucleophilic substitution with one imidazole group on the crystal and then it took 30 minutes to couple the second chloromethylene group with an imidazole group. After this period of time the frequency overtones looked very stable. However, it was impossible to determine the ratio of once and twice coupled α,α' -dichloro-*p*-xylene molecules by this method. The fact that the linker molecule is coupled twice on the imidazole moieties also explains the comparably small amount of added mass, mentioned above. After about 2 hours reaction time methanol was applied on the crystal again and a slightly decrease was monitored for the frequency overtones. The explanation for this phenomenon could be the same as for the first reaction, namely, a change in the viscosity of the fluid phase by switching from the α,α' -dichloro-*p*-xylene solution to methanol or a removal of non-reacted α,α' -dichloro-*p*-xylene molecules from the crystal surface. Furthermore, after switching to methanol, the frequency overtone values were drifting to lower values and it was not possible to get a solid baseline within

48 hours. This phenomenon can be explained by the fact that the combination of methanol and the heat, caused by the movement of the peristaltic pump, destroyed the pump tubing. Most likely parts of the pump tubing were dissolved in methanol and, therefore, the drifting of the frequencies corresponded to a deposition of the tubing material on the crystal surface. Due to this fact, it is not possible to make any statement about the mass of INN material like film on the crystal. However, it has to be remarked that, in this case, the coupling reaction between the 1-propylimidazole modified crystal surface and α,α' -dichloro-*p*-xylene was completed in 30 minutes.

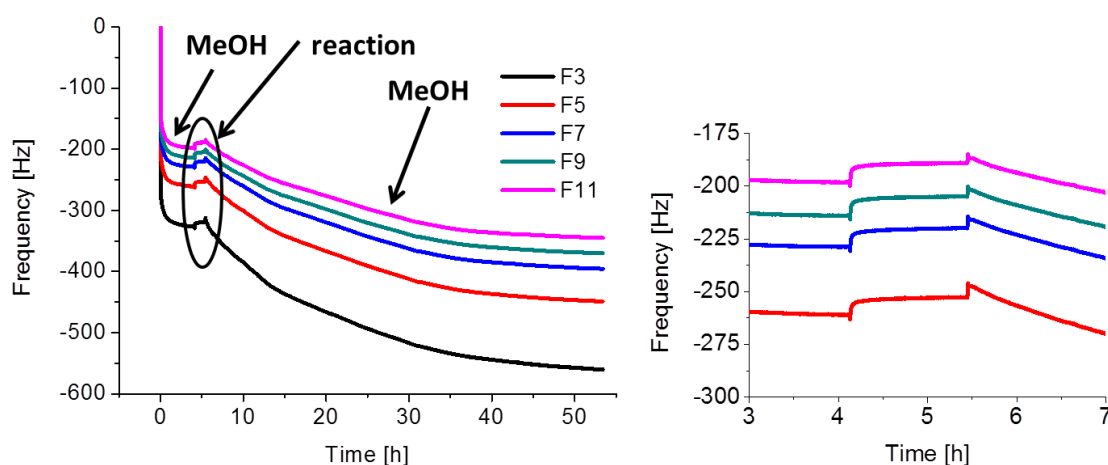


Figure 19 (left) QCM measurement of the reaction between the 1-propyl-2-methylimidazole modified SiO_2 crystal surface and a 0.1 molar methanolic solution of α,α' -dichloro-*p*-xylene, (right) zoom of the marked area with “reaction” on the left.

In this chapter, it could be illustrated that the formation of an INN material like film on a QCM crystal only takes between 30 and 90 minutes. However, it has to be distinguished that the reaction on a plane surface is not equal to a reaction between two nanoparticle species in solution or 1-propylimidazole modified nanoparticles with a chloromethylene disubstituted linker. In solution it should take a longer time for the molecules to find and interact with each other. Nevertheless, these QCM studies suggested a faster reaction process than assumed. Depending on the facts that one complete QCM measurement takes about one week, and that some setup problems occurred during these measurements, only two investigations of the kinetics of the building reaction of INN materials could be carried out. In the future, it will be interesting to execute more of these measurements to analyze the kinetics of the INN building reaction more in detail.

3.2.5 NMR spectroscopy on INN materials

A very common method for the characterization of non-crystalline chemical compounds is the NMR spectroscopy. Due to the bad solubility of the INN materials solid state NMR spectroscopy was chosen for the analysis of the materials. The practical realization of these experiments sometimes generated some problems, *e.g.* some samples could not be rotated at a constant frequency, because of the gel state of the materials, which caused a really diffuse NMR spectrum. Because of this fact only some interpretable spectra could be measured, *e.g.* the ^{15}N CP/MAS NMR spectrum of the reference material **Mat 1** in Figure 20. In this spectrum a strong signal at a chemical shift of 142 ppm could be observed, which can be assigned to imidazolium groups in the material (blue rings in Figure 20). On this signal a shoulder is visible as well. This shoulder can be assigned to non-reacted imidazole groups in the material. This one and numerous more solid state NMR investigations were executed and published by Marco Litschauer et al. [78,168]

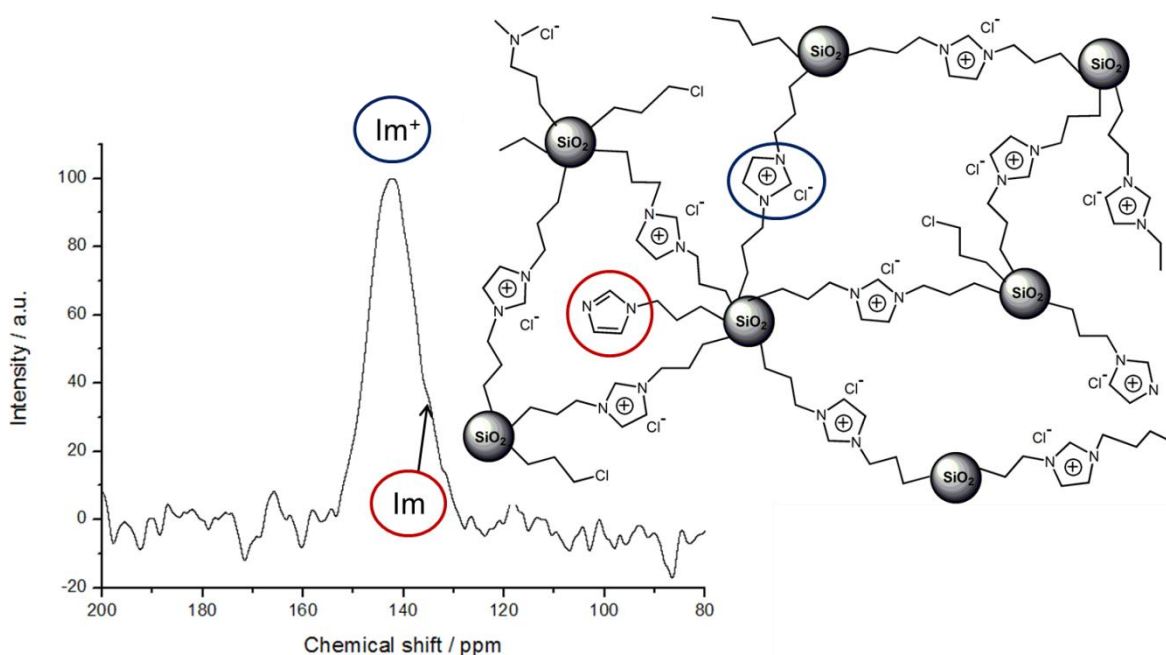


Figure 20 (left) ^{15}N CP/MAS NMR spectrum of the reference INN material (**Mat 1**), (right) schematic constitution of the INN material consisting of imidazolium chloride moieties (blue ring) and unreacted imidazole groups (red ring).

Additionally, $\{^1\text{H}\}\text{-X}$ ($\text{X} = ^{11}\text{B}, ^{31}\text{P}$) HETCOR CP MAS experiments were performed on BF_4^- and PF_6^- containing INN materials (**Mat 30** and **Mat 31**) with the aim to try to locate the counter anions by Christel Gervais at the Sorbonne Université Paris. Indeed, these HETCOR experiments are based on the $^1\text{H}\text{-X}$ dipolar couplings which are related to the distance between the X and H groups. For this reason, it is possible to identify the nature of the protons that are located close to the counter anions. In the case of BF_4^- , the boron signal, observed at -1.2 ppm, shows cross peaks with signals at 1.7, 4.4 and 7.7 ppm corresponding to Si-CH_2 -, $-\text{CH}_2\text{-N}$ and imidazolium protons respectively. The

relative intensities of the cross peaks at 1.7 and 7.7 ppm are comparable, suggesting that BF_4^- is located in both ways, close to the surface and close to the imidazolium rings. For PF_6^- the phosphorus signal, located at -144.6 ppm, shows also three cross peaks, but the one at 7.7 ppm is much more intense, suggesting a closer proximity to the imidazolium rings.

Also, ^{19}F MAS NMR spectra were recorded for both systems to investigate whether the fluorine chemical shift values were sensitive to the position of the counter anions. Then the idea was to compare these values with the calculated ones for the various models proposed. A preliminary study was done on crystalline compounds to evaluate the precision of the NMR calculations. For this purpose, fluorinated imidazolium salts $[\text{C}_6\text{H}_4(\text{CH}_2(\text{C}_4\text{H}_6\text{N}_2)_2)^{2+}] 2[\text{A}]^-$ (with $\text{A} = \text{BF}_4, \text{PF}_6$) were chosen, whose structures were reported recently.^[186] The compound with $\text{A} = \text{BF}_4^-$ was synthesized and the corresponding solid-state NMR spectra were recorded while NMR parameters were calculated for both relaxed structures. A satisfying agreement could be found for the experimental and computed ^1H , ^{11}B , ^{13}C and ^{15}N NMR data in $[\text{C}_6\text{H}_4(\text{CH}_2(\text{C}_4\text{H}_6\text{N}_2)_2)[\text{BF}_4]_2$ (Figure 21).

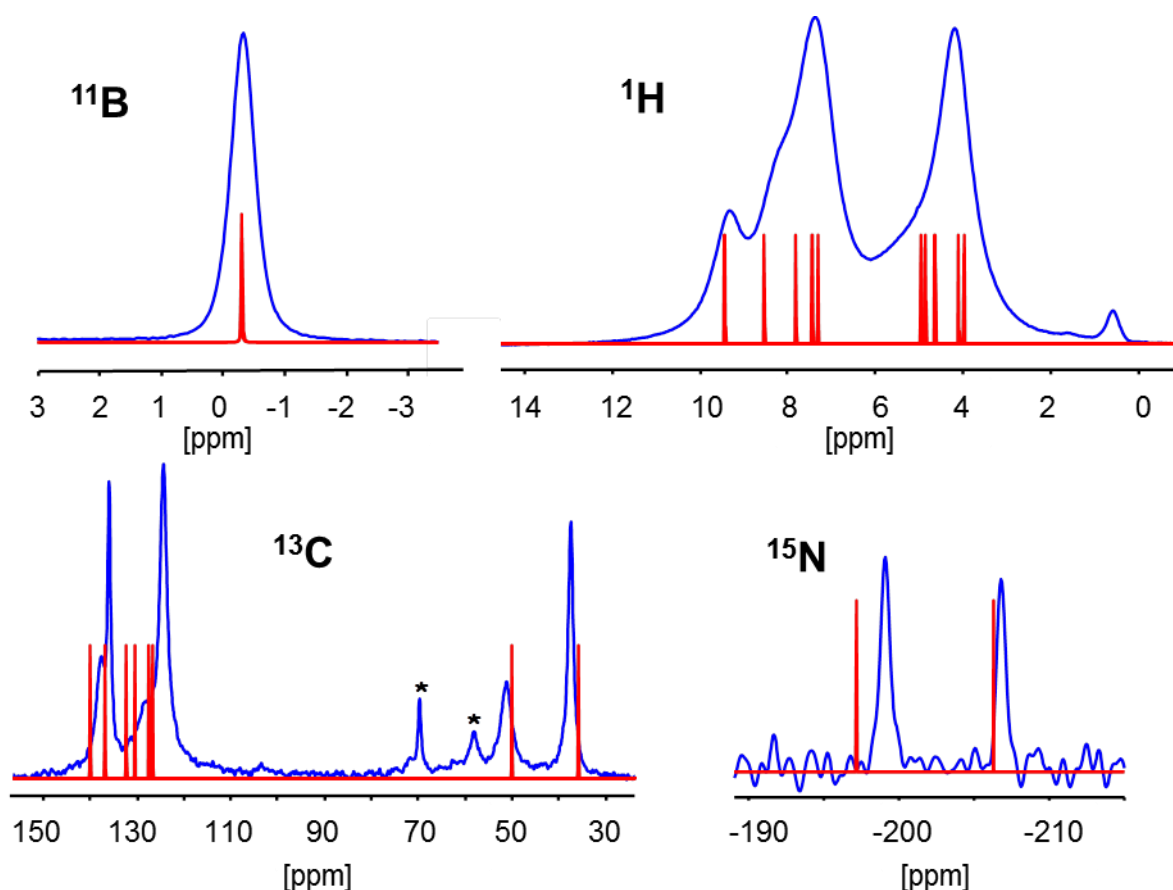


Figure 21 Experimental (blue line) and calculated (red line) ^1H , ^{11}B , ^{13}C and ^{15}N NMR spectra of fluorinated imidazolium salts $[\text{C}_6\text{H}_4(\text{CH}_2(\text{C}_4\text{H}_6\text{N}_2)_2)[\text{BF}_4]_2$.

In the case of ^{19}F , a single signal was observed experimentally, while the calculated values of the four sites in BF_4 are clearly distinct within a range of 16 ppm. This suggests that the correlation time

for fluorine, hopping between the four B-F sites, is small on the NMR time scale. Therefore, it appears reasonable to compare the experimental fluorine shift with the average of the four/six calculated values for $\text{BF}_4^-/\text{PF}_6^-$ sites. It should be noticed that the comparison between the experimental data with the calculated ones show a correlation between δ_{iso} and calculated isotropic shielding with a slope, that deviates significantly from -1. This suggests that better agreement between calculated and experimental chemical results will be obtained by the introduction of a scaling factor, k , such that $\delta_{\text{iso}} = -k[\sigma - \sigma^{\text{ref}}]$. Linear regression yields k of 0.74, which is consistent with other scaling factors, reported recently for ^{19}F in the literature.^[187,188]

Afterwards, ^{19}F NMR parameters were calculated for six models, characterized by three or five 1,3-dipropylimidazolium chains (Im) per super cell, BF_4^- and PF_6^- as counter anions, hydrated (in the case of five 1,3-dipropylimidazolium chains) or not.

For the BF_4^- sample, calculated ^{11}B parameters were consistent with the experiments (signal centered at -1.2 ppm) for all models, but a better agreement of the ^{19}F parameters was observed for the five 1,3-dipropylimidazolium chain systems (Figure 22).

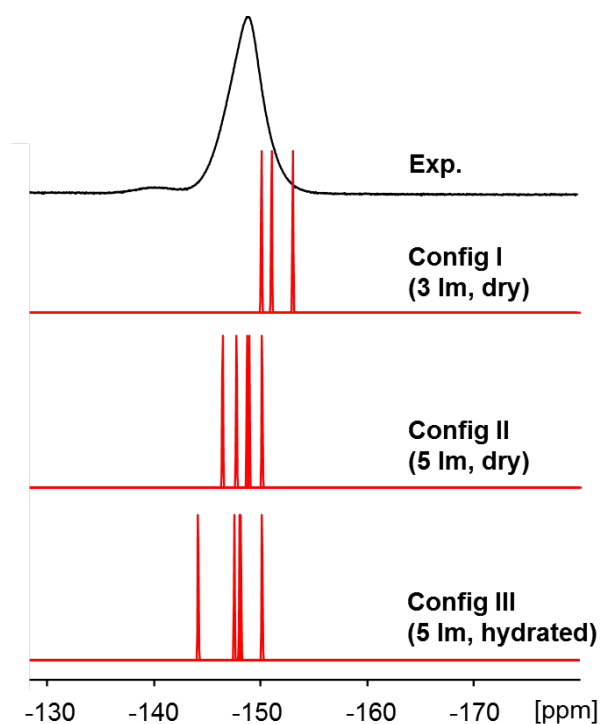


Figure 22 Experimental and calculated ^{19}F spectra of **Mat 30** containing BF_4^- counter anions.

Similarly, in the case of PF_6^- sample, five 1,3-dipropylimidazolium chain models showed a better agreement between the calculated and experimental values (Figure 23). It should be noticed that the Si-O-P linkage, formed in model IV (three 1,3-dipropylimidazolium chains), shows a calculated ^{31}P chemical shift at -150.8 ppm, which is very far from the observed value (-144.6 ppm).

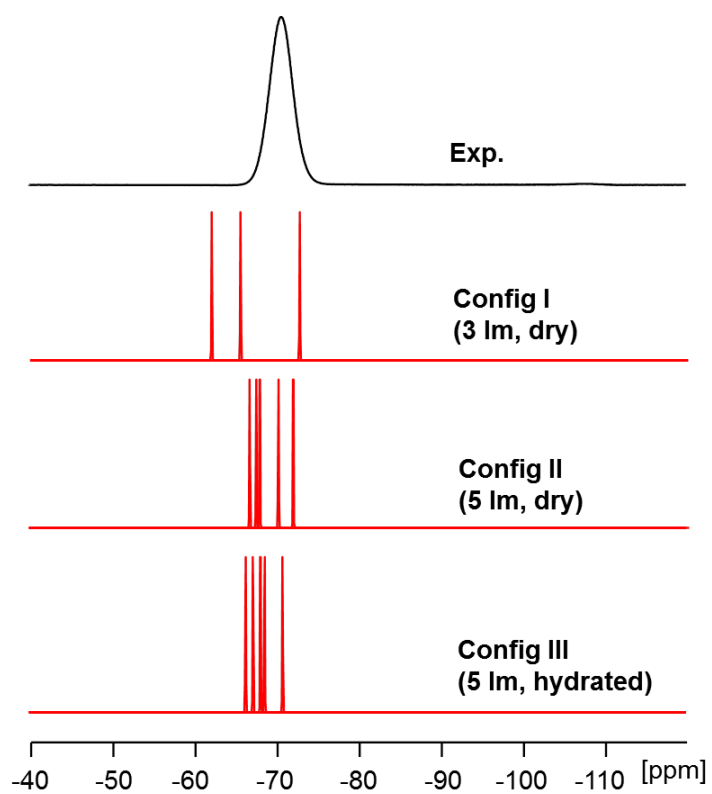


Figure 23 Experimental and calculated ^{19}F spectra of **Mat 31** containing PF_6^- counter anions.

3.2.6 DFT calculations on the INN materials

To get a deeper understanding about the structural development of the INN materials at the nanometer scale, DFT calculations were carried out by Frederick Tielens at the Sorbonne Université Paris. Therefore, the construction of the INN material unit cell (Figure 24) is based on the results of the thermogravimetric analysis and TGA/MS studies, as shown in part 3.2.2. For the detailed model description see the experimental part. As observed from the TGA results, an inorganic part (SiO_2) of 57.5 % and an organic part of 38.5 % was assumed for the calculation. Furthermore, the density of the silica nanoparticles was taken at 2.2 g/cm^3 and the size of the silica nanoparticles was estimated to $15 \pm 3 \text{ nm}$. The accuracy, depending on the number of ligands per surface unit, resulted from the accuracy of the results of thermogravimetric analysis. But the most important influence had the accuracy of the size and density of the silica nanoparticles. In the used SiO_2 model this result corresponds to a number of three to five 1,3-dipropylimidazolium chains per unit cell. It has to be mentioned that for this model it had been assumed that two silica slabs are connected by three to five 1,3-dipropylimidazolium chains, under consideration of the hypothesis that the curvature of the silica nanoparticles in INN material is large enough to be negligible for the number of 1,3-dipropylimidazolium chains.

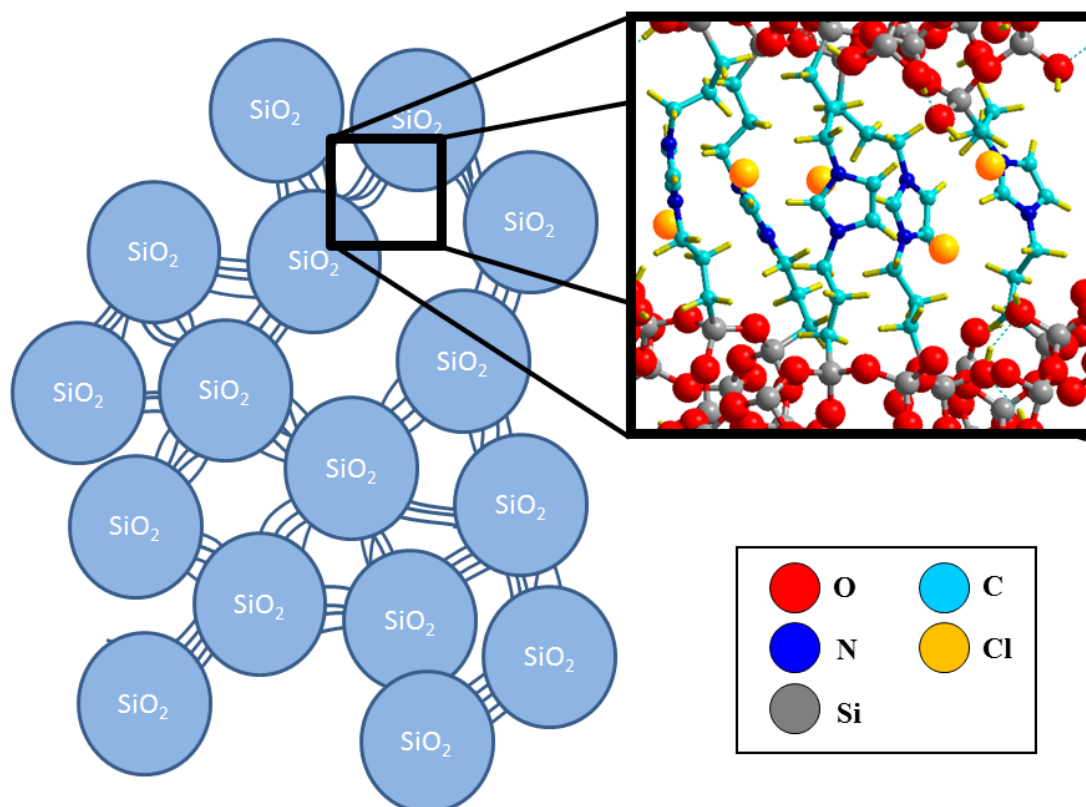


Figure 24 Model of the unit cell used for DFT calculations.

For each counter anion investigated (Cl^- , BF_4^- , and PF_6^-), a possible molecular structure is proposed from geometry optimization, for three and five 1,3-dipropylimidazolium chains per super cell, hydrated or not. The separation distance between the silica surfaces is calculated to be 11 Å (total z dimension of the unit cell used, $c \pm 15.5$), which can be related to the distance between the silica nanoparticles. This distance of 11 Å, obtained from the relaxation of the unit cell, is in good agreement with the distance observed in SAXS experiments (see 3.2.3.), where this distance was assigned to the peak at about 5 nm^{-1} .

Surprisingly, the chloride ions (Cl^-) are predominantly found to interact with surface silanol groups of the silica particles, while the other anion species (BF_4^- and PF_6^-) were found between the imidazolium rings, not perpendicular to the rings, but aside the C-H bonds of the rings. Indeed, after the anion exchange no change in the characteristic structural distance was observed in SAXS experiments, even though, the fluorinated anions are larger compared to the chloride anions. If the anion would have been situated between the imidazolium rings, the aromatic rings would have been further away from one another after the anion exchange and changes in the SAXS as well as in the photoluminescence data would be expected. Increasing the 1,3-dipropylimidazolium chain density in the model unit cell from three to five, the chloride anions were still predominantly found next to the imidazolium rings, which is in line with the fact, that the number of surface silanol groups decreases with increasing the number of IM chains. Indeed every 1,3-dipropylimidazolium chain consumes two silanol groups of the silica surface.

After the introduction of water molecules in the super cell, they interacted with the available surface silanol groups, but no significant expansion of the unit cell was observed. In fact the water molecules did not interact with the imidazolium rings, but with the silanol groups of the silica surface.

The larger tetrafluoroborate anions (BF_4^-), in comparison to the chloride (Cl^-), are also located closer to the imidazolium rings than to the silica surface. Increasing the 1,3-dipropylimidazolium chain density leads to more BF_4^- ions in closer interaction with them.

The largest of the investigated anions, hexafluorophosphate (PF_6^-), showed a similar behavior than the BF_4^- and Cl^- anions. Nevertheless, it has to be highlighted that a reaction between the anion and the silica surface was observed in the dry low chain density model. In these cases a Si-O-P linkage and HCl were formed. Indeed, it is well known that in the “real” ionic liquids, water is always present, owing to the hygroscopic behavior of imidazolium units.^[87] For the INN materials this circumstance was confirmed by the TGA/MS results. At higher chain density the bigger cations, caused by the steric hindrance of the chains and the presence of water, were forced between the 1,3-dipropylimidazolium chains. The different anions were usually located between the imidazolium rings and not close to the surface of the silica nanoparticles. These observations are in agreement

with the literature, where a limited stability of imidazolium tetrafluoroborate (BF_4^-) and imidazolium hexafluorophosphate (PF_6^-) is described, because of the microwave or high temperature induced leaving of one fluoride anion.^[189–192]

The various characterization techniques, performed on the INN materials, have led to assume the existence π - π stacking interactions between the aromatic imidazolium rings, which could be the origin of the modification of the electronic properties of the complete silica nanoparticle system. This assumption is also strengthened by literature.^[193] The phenomenon of π - π stacking interactions between imidazolium units was also reported for other materials.^[181,194] Furthermore, the distance between the linking units is in the range in which an extra stabilization can be obtained by π - π stacking of the imidazolium rings.^[180] However, the magnitude of the π - π stacking interaction is dependent on the relative orientation of the imidazolium rings. Thereby, it is difficult to organize the imidazolium linkers symmetrically on the amorphous surface of the silica particle. In consequence, this particular van der Waals interaction was expected to be weak.

The electronic structure was also evaluated. In Figure 25 the density of state of the proposed model is plotted. Therefore, the model, containing five 1,3-dipropylimidazolium chains in hydrated conditions, was chosen. In the case of the model containing PF_6^- as counter ion, the band gap was calculated to about 3.17 eV. The difficulties to evaluate the band gap with DFT techniques were considered. The total density of state curve is drawn in green (Figure 25). The partial density of state of the imidazolium unit plus the anions is drawn in red. The partial density of state depending on the C and N atoms (the imidazolium atoms) is applied in blue. The density of state correlating to the molecular part of the system (C, N, P, and F atoms) determines the band gap (Figure 25).

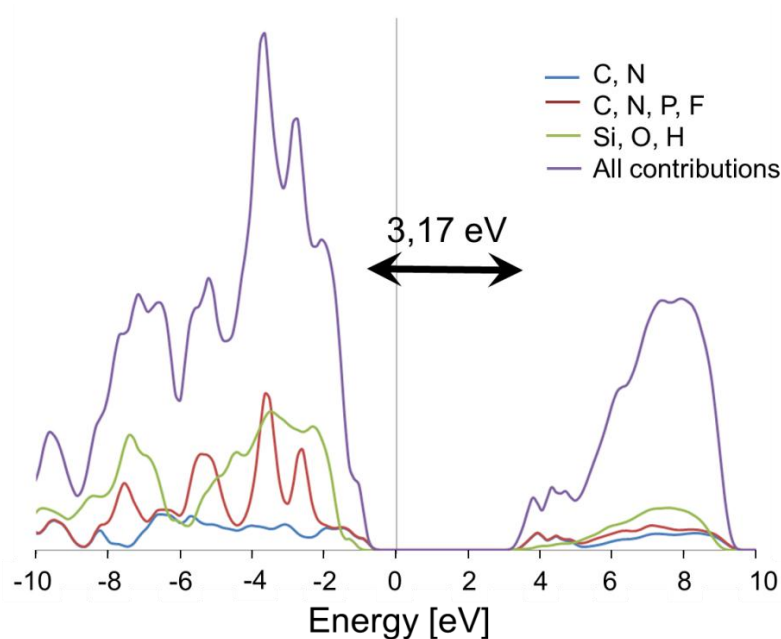


Figure 25 Density of State of the model INN materials (**Mat1**, **Mat 30** and **Mat 31**).

In conclusion, for the silica INN materials, the distances of the silica nanoparticles to each other were found of about 11 Å. The chain density was well reproduced and allowed to understand the effect of hydration in the structure. Furthermore, the calculations on the structural organization of the INN materials seem to confirm the hypothesis of π - π stacking interactions between the imidazolium rings.

3.2.7 Investigation of the electrical properties of the INN materials

The INN materials, investigated in this work, consist of ionic moieties. Furthermore a band gap of about 3.17 eV was determined by DFT calculations. These facts and observations and the assumed π - π stacking interactions of the aromatic rings led to investigations of the electrical properties of the INN materials. Preliminary conductivity measurements showed conductivity values in a range which are typical for semiconductors. Depending on these facts, transistor measurements were executed on the hybrid materials. The basic assembly of a field effect transistor (FET) is shown in Figure 26. For the preparation of the FETs patterned ITO substrates, which are commercially available from Ossilia, were dip coated with a methanolic solution of the respective INN material. The dielectric layer, which has to be an insulator, was placed on the previously prepared ITO substrates by spray coating. Therefore, polyvinylphenol (PVPPh) was dissolved in ethyl acetate (10 w%) and was sprayed by an airbrush gun on the materials surface by using a T-shaped mask. After drying the dielectric layer, the gate electrode material (PEDOT = Poly-3,4-ethylenedioxythiophene) was painted on the dielectric layer by using the T-shaped mask again. The polymer (PEDOT), used for the gate electrode, has to be a very good electric conductor.^[195]

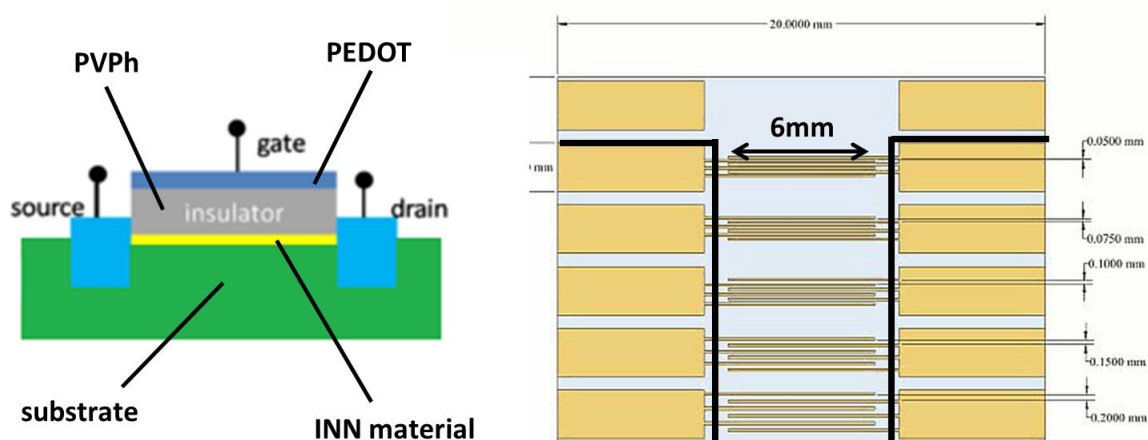


Figure 26 (left) principal setup of the INN material based field effect transistor, (right) principal assembly of the commercial available ITO patterned substrates from Ossilia (the solid black lines show the position of the T-shaped mask on the substrate, the dielectricum and the gate material were deposited on this position).

For the transistor measurements, gate voltages between -20 and 20 V and drain voltages in the range of -30 to 30 V were applied. For the current-voltage characteristic of the transistor, the drain current was plotted against the drain voltage. The measurements were carried out under ambient light, UV-light and under dark conditions. In Figure 27 the current-voltage characteristic of a transistor based on the bis-imidazolium biphenyl linker containing INN material (**Mat 7**) is presented under dark conditions.

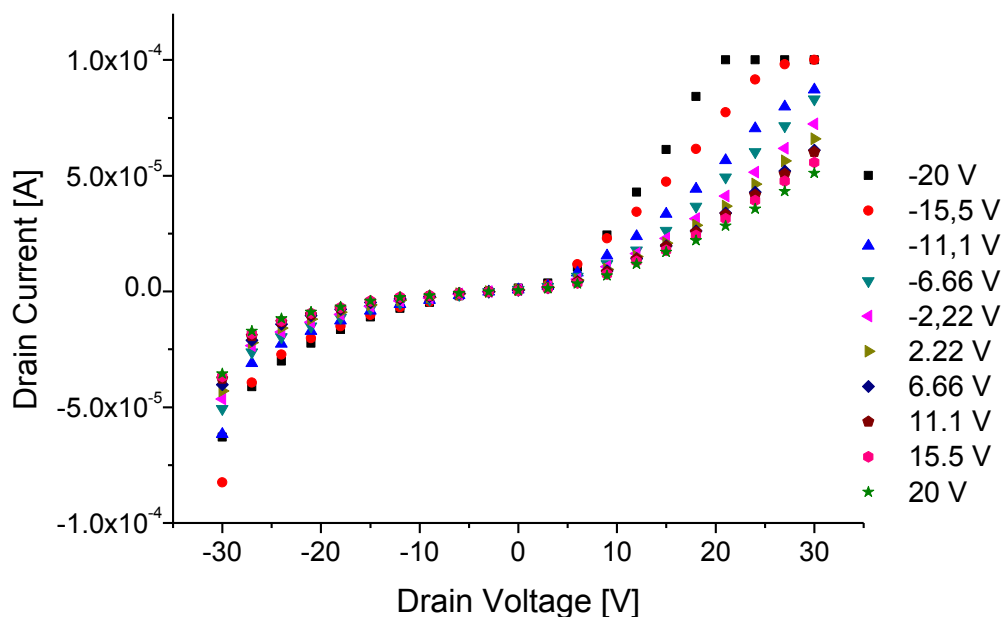


Figure 27 Current-voltage characteristic of a working transistor (under dark conditions) based on **Mat 7**.

The sample seems to work like a field effect transistor, but only under dark conditions. This phenomenon could be explained by a photoinduced electron transfer of the ionic liquids under light and UV-light conditions, as published by Paul *et al.* ^[196] This process may have disturbed the electrical conduction processes in the material for the measurements under ambient and UV light.

Unfortunately, the “working” transistor only worked once and during four weeks of daily transistor measurements this result was not reproducible. The major problem at these transistor measurements was that a gate current in μA range was measured for numerous transistor samples, which suggested a leakage in the dielectric layer. On the microscope images in Figure 28 it can be seen that dissolving the PVPh in ethyl acetate leads to a dewetting of the surface of the substrates. This problem was fixed after several days by using methanol as solvent for the insulating material. However, gate currents in μA range were still measured and could not be fixed during the measurements in Sweden.

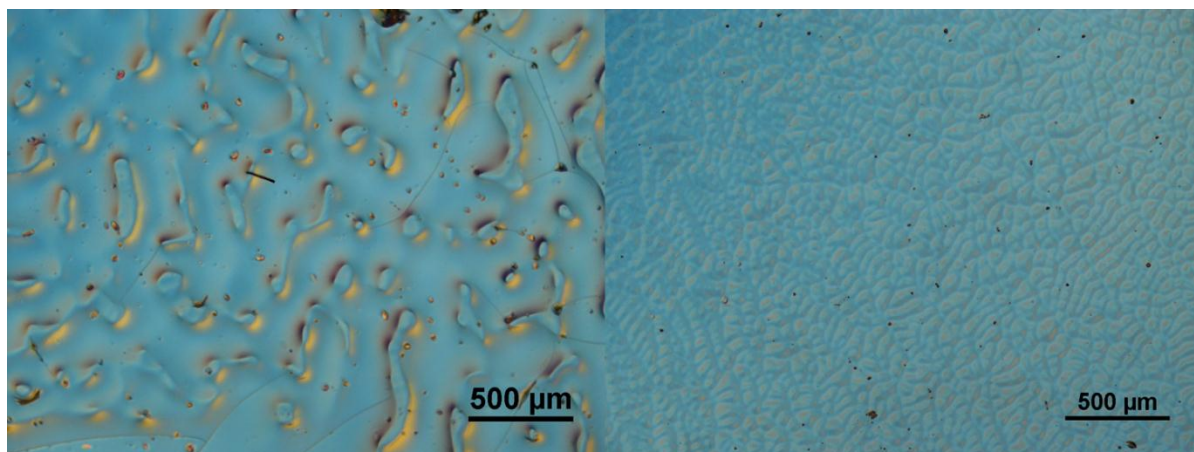


Figure 28 Microscope images of (left) dielectric layer made of PVPPh dissolved in EtOAc, (right) dielectric layer made of PVPPh dissolved in MeOH.

The facts, that the transistor only worked once and the continuing problems with the setup, suggested that the silica INN materials are minor applicable for the preparation of field effect transistors. One reason for the malfunction of the INN material based field effect transistor could be the insulating properties of the silica nanoparticles. Due to the semiconducting properties of zinc oxide,^[197] the so-called mixed INN materials will be highly attractive for the application as a transistor material, but until now it was not possible to produce thin films on a substrate of these materials.

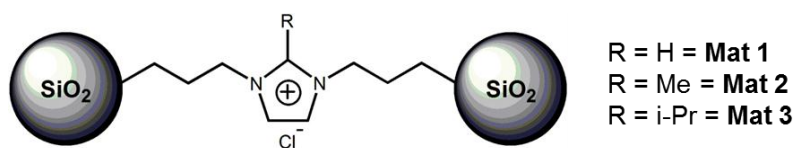
3.3 Fluorescence properties of INN materials

Numerous light emitting materials were published in the last years. Some of these materials consist of lanthanide ions^[198–201] or platinum-group metal ions^[202–204] owing to their photophysical properties. Due to the fact that lanthanides as well as platinum-group metals are rare and expensive, metal-free photoluminescence active materials have been developed.^[205,206] In the course of the development of luminescent materials, the hybrid materials community started to focus on ionic liquids, which were proven to be luminescent.^[207,208] Especially 1-butyl-3-methylimidazolium tetrafluoroborate [bmim][BF₄] and 1-ethyl-3-methylimidazolium tetrafluoroborate [emim][BF₄] showed emission at wavelengths in the range at about 450 nm.^[209] Furthermore, imidazolium salts in general showed interesting fluorescence properties, *e.g.* C.W. Bielawski *et al.* published the synthesis and application of benzobis(imidazolium) salts and also their use in fluorescent block ionomers and liquid crystals.^[210–213] Thus room temperature ionic liquids (RTIL), *e.g.* 1-butyl-3-methylimidazolium based ionic liquids, were used to improve the electroluminescence properties of light emitting compounds. R. Martín *et al.* reported the beneficial influence of ionic liquids on the efficiency of electroluminescent cells. Therefore, they modified a diphenylanthracene moiety with two imidazolium units and investigated their use in OLEDs. They measured a significant efficiency enhancement compared to the parent molecule. The authors suppose that this effect arises from the blocking of spurious current flow and a more efficient charge injection into the active layer of the OLED.^[214] R.C. Evans and P.C. Marr reported the use of ionic liquids in a hybrid material made of poly(9,9-dioctylfluorene), tetraethoxysilane (TEOS) and 1-butyl-3-methylimidazolium bis(trifluoromethanesulfoimide) [bmim][Tf₂N]. In this case the ionic liquid caused that the polymer built a β -phase and nice photoluminescence features were observed.^[215] Depending on these interesting photoluminescence features of ionic liquids or photoluminescence features of hybrid materials, which were improved by ionic liquids, the INN materials were also investigated relating to their photoluminescence properties in the past and they also showed promising photoluminescence properties.^[216] In this photoluminescence experiment an emission for **Mat 1** of 400 nm was observed. This can be assigned to a band gap of about 3.11 eV, which is in quite good agreement with the calculated band gap of 3.17 eV presented in chapter 3.2.6.

In this work the tailoring of the excitation and emission wavelengths of INN materials was investigated more in detail. Therefore the substituents on the C2 position of the imidazolium moiety as well as, in the case of the bis-imidazolium based INN materials, the aromatic linker was varied. The photoluminescence properties as well as the SAXS profiles of mono- and bis-

imidazolium based INN materials, with or without substituents on the C2 position, as well as of pyrazolium and pyridinium based INN materials were investigated and compared. Furthermore, the optical properties and SAXS curves of the mixed INN materials were investigated. The photoluminescence properties of the various INN materials were determined in the solid state.

3.3.1 Photoluminescence properties of the mono-imidazolium INN materials



Scheme 17 Mono-imidazolium INN materials **Mat 1** – **Mat 3**.

The excitation spectra of the substituted and non-substituted mono-imidazolium INN materials, **Mat 1** to **Mat 3** (Scheme 17), are characterized by a broad band in the region between 300 – 400 nm (dotted lines in Figure 29). Additionally, a shift for the absorption maxima was detected. **Mat 1** shows a maximum in absorption at 320 nm, **Mat 2** at 365 nm and **Mat 3** at 345 nm. By exciting the samples at the wavelength of these maxima, emission in the range between 350 nm and 550 nm was detected (solid lines in Figure 29), with emission maxima for **Mat 1** to **3** situated at 380, 440 and 400 nm respectively. These maxima are corresponding to an emission maximum in the violet area for **Mat 1** and **Mat 3** and in the blue area of the light spectrum for **Mat 2**. Due to the broadness of these emission bands the materials seem all to emit in the blue region to the naked eye. When modifying the C2 position of the imidazolium ring, either with a methyl or an isopropyl group, a clear shift for the emission maxima was monitored, **Mat 2** and **3** as compared to **Mat 1**. The largest shift of the excitation as well as for the emission maxima was observed for the material substituted with a methyl group on the C2 position of the imidazolium ring (**Mat 2**). For the isopropyl substituted mono-imidazolium INN material (**Mat 3**) a slightly smaller value of the shift of excitation and emission maximum, compared to **Mat 2**, was detected. For **Mat 1** - **Mat 3** a small peak in the emission spectrum was observed at about 540 nm. Therefore, the samples were measured twice to exclude a possible contamination of the samples, but the peak did not disappear. This suggests that this peak is an artefact maybe caused by the measurement instrument.

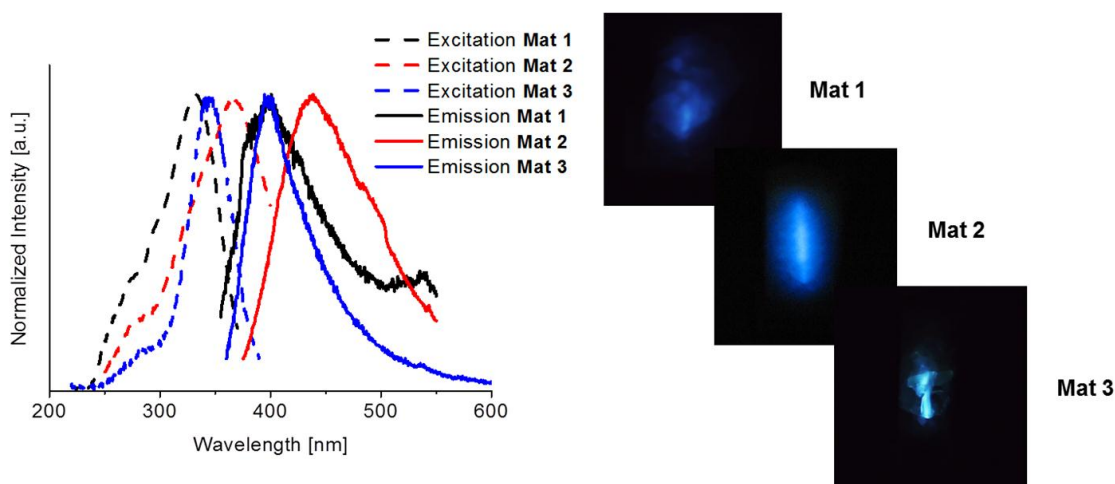
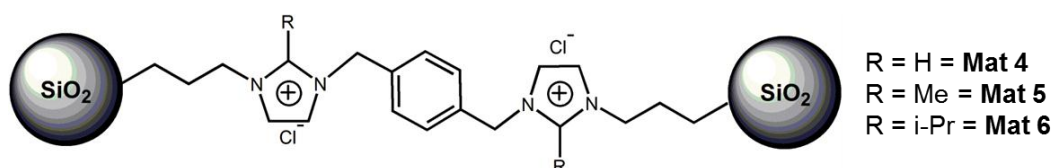


Figure 29 (left) Excitation (dotted lines) and emission spectra (solid lines) of the substituted and non-substituted mono-imidazolium materials (**Mat 1 – Mat 3**), (right) digital photos of the emission of the materials **Mat 1**, **Mat 2** and **Mat 3** under excitation at 320 nm, 365 nm and 345 nm respectively.

It has to be highlighted at this point that the silica nanoparticles had no influence on the luminescence mechanism. They were measured separately and no quantum yield could be estimated from these emission curves as the intensity was far too low.

3.3.2 Photoluminescence properties of the bis-imidazolium INN materials

The study of the photoluminescence properties of bis-imidazolium INN materials containing the α,α' -dichloro-*p*-xylene linker (**Mat 4**, **5** and **6**, Scheme 18) reinforced the previous observations. At this point it has to be highlighted that the here used linker molecule, α,α' -dichloro-*p*-xylene, was proven to be not active in photoluminescence.



Scheme 18 Bis-imidazolium *p*-xylene linked INN materials **Mat 4 – Mat 6**.

The excitation spectra of these materials show broad bands in the region between 320 and 380 nm and a second local maximum can be distinguished between 200 and 280 nm. The origin of these two distinct maxima in the spectra could not be assigned yet, however a similar observation was reported by Paul *et al.* in a work dedicated to the optical properties of imidazolium ionic liquids.^[217,218] By exciting the materials with the wavelength corresponding to the excitation maxima, emission maxima were observed in a range between 410 and 450 nm (solid lines in Figure

30), with emission maxima for **Mat 4** to **6** at 410, 450 and 440 nm respectively. By comparing **Mat 4**, **5** and **6**, a shift of the excitation as well as of the emission maxima could be observed. Here, the same effect of the substituents as for **Mat 1** to **3** was monitored. Namely, the largest shift, for the excitation as well as for the emission maxima, was observed for the material substituted with a methyl group on the C2 position of the imidazolium ring (**Mat 5**). For the isopropyl modified bis-imidazolium INN material (**Mat 6**) a slightly smaller shift of excitation and emission maximum, compared to **Mat 5**, was detected. The explanation for this phenomenon is the same as for **Mat 1** to **Mat 3**: the methyl groups on the C2 position of the imidazolium moieties of **Mat 5** cause a positive inductive effect on the imidazolium rings while offering only a weak steric hindering. For **Mat 6** the steric effect dominates the positive inductive effect. In consequence a larger shift in the excitation and emission maxima could be detected for **Mat 5** than for **Mat 6** compared to **Mat 4**.

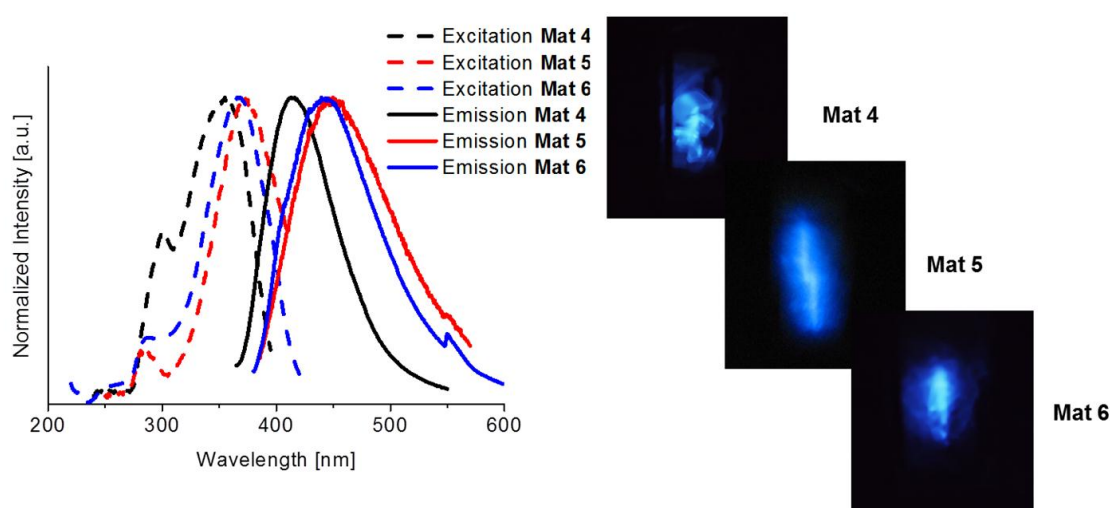
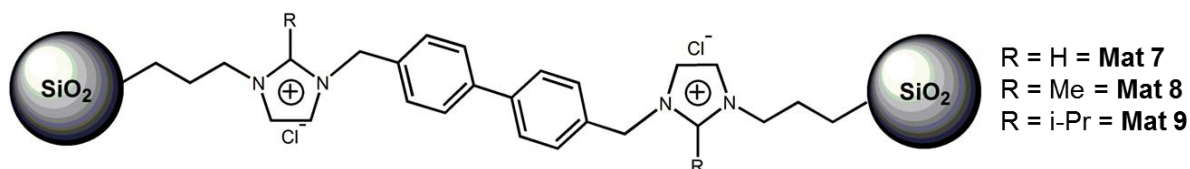


Figure 30 (left) Excitation (dotted lines) and emission spectra (solid lines) of the substituted and non-substituted bis-imidazolium materials containing the xylene linker (**Mat 4**, **5** and **6**), (right) digital photos of the emission of the materials **Mat 4**, **Mat 5** and **Mat 6** under excitation at 350 nm, 370 nm and 370 nm respectively.

In summary, it turns out that the general trend of the shift between the different substituted imidazolium moieties in these materials is very similar to the mono-imidazolium INN materials. The comparison between the mono-imidazolium and bis-imidazolium INN hybrid materials illustrates that the α,α' -dichloro-*p*-xylene linker containing INN materials (**Mat 4** to **Mat 6**) in general show higher wavelengths for the excitation maxima as well as for the emission maxima. This can be explained by the red shift of aromatic rings.^[219,220]

For a higher content of delocalized electrons in the material in combination with free rotatability of the aromatic rings, 4,4'-bis(chloromethyl)-1,1'-biphenyl was used as the linking unit. The corresponding INN materials are thus derivatives of a bis-imidazolium biphenyl (**Mat 7**, **8** and **9**, Scheme 19).



Scheme 19 Bis-imidazolium biphenyl linked INN materials **Mat 7 – Mat 9**.

The excitation spectra and emission spectra of these materials (**Mat 7** to **Mat 9** in Figure 31) are more complex than of the materials **Mat 1** to **Mat 6**. Regarding the excitation spectra it can be noticed that the excitation bands for **Mat 7** and **Mat 8** look quite similar to each other and show excitation maxima at nearly the same wavelength, namely at 300 nm. **Mat 7** showed one global absorption maximum at 305 nm (black dotted line in the left spectrum in Figure 31). By exciting the material with this wavelength, an emission maximum was observed at 350 nm (see supporting information). Additionally, in a range between 310 nm and 380 nm three local maxima in absorption could be detected. The most intensive one (375 nm) was chosen for exciting the material which resulted in an emission band with a global maximum at 425 nm (blue area of the light spectrum) and two other local maxima. This suggests that the material could be used for an emission at two different wavelengths depending on the excitation wavelength. For **Mat 8**, with a similar excitation spectrum as **Mat 7**, an emission band was observed for an excitation at 300 nm. This emission band shows a broad maximum plateau between 320 nm and 390 nm. At this stage the origin of this behavior cannot be explained. **Mat 9** shows a different behavior: The very broad absorption band shows two maxima at 370 nm and 420 nm (blue dotted line). By exciting the material at these wavelengths the resulting emission spectra are similar to each other. In both cases a maximum in emission was detected at 475 nm. It can be noticed that by replacing the hydrogen atom on the C2 position of the imidazolium ring by a methyl group, **Mat 8**, the color of the emitted light could be changed from blue to purple and by replacing the methyl group with an isopropyl group, **Mat 9**, the color of the emitted light changes to green (Figure 31, right).

By comparing the luminescence spectra of **Mat 7** to **Mat 9** to these of **Mat 1** to **Mat 6**, large differences can be found. This difference lies in the presence of the biphenyl linker, which already emits by itself (Figure 31, bottom right). For comparison with these INN materials the photoluminescence properties of the pure linker molecule, 4,4'-bis(chloromethyl)-1,1'-biphenyl, were investigated. It turned out that the linker molecule shows an emission for an excitation at 375 nm, too (red solid line on the right in Figure 31), but quite weak in comparison to **Mat 7** (black solid line). The luminescence spectra were recorded by measuring the emission of a cuvette fully filled with the compound to investigate. In consequence in the bottom right spectra in Figure 31 a compound containing only around 20 w% of biphenyl, the INN **Mat 7** is compared with 100 w% of

pure biphenyl. It can be claimed that the luminescence observed for **Mat 7** to **Mat 9**, is due to the organization forced during the formation of the INN. However, it seems that in this case the luminescent behavior of the materials containing bis-(imidazolium)biphenyl linkers is governed by the biphenyl. In conclusion the materials combining imidazolium and linker luminescence (**Mat 7** to **Mat 9**) present adjustable photoluminescence properties.

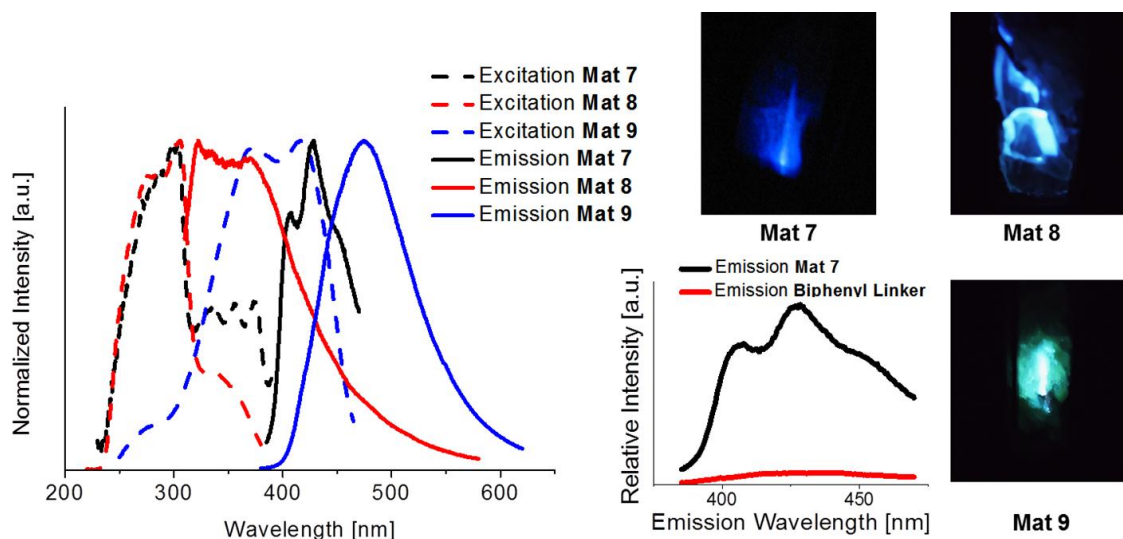
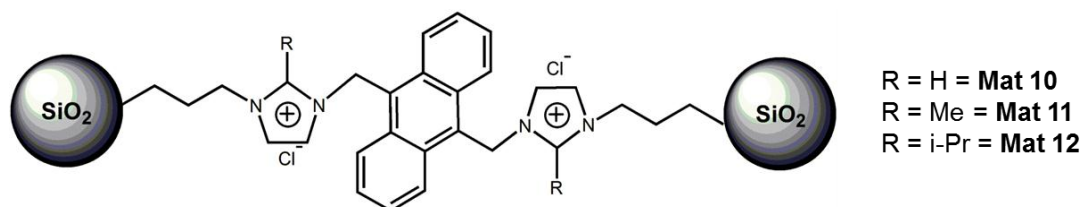


Figure 31 (left) Excitation (dotted lines) and emission spectra (solid lines) of the substituted and non-substituted bis-imidazolium materials connected by the biphenyl linker (**Mat 7**, **8** and **9**), (right) Digital photos of the emission of the materials **Mat 7**, **Mat 8** and **Mat 9** under excitation at 375 nm, 300 nm and 370 nm respectively and, (bottom) for comparison, emission spectra of **Mat 7** and the pure biphenyl linker under an excitation at 375 nm.

For a further increasing of the content of delocalized electrons, but in this case combined with a rigid adjustment of the aromatic rings in the material, 9,10-bis(chloromethyl)anthracene was used as the linking reactant for the nucleophilic substitution. The corresponding INN materials are thus derivatives of a bis-imidazolium anthracene (**Mat 10** to **Mat 12**, Scheme 20).



Scheme 20 Bis-imidazolium anthracene linked INN materials **Mat 10** – **Mat 12**.

Similarly, as for **Mat 7** to **Mat 9**, **Mat 10** to **Mat 12** showed a complex behavior in the excitation as well as in the emission spectra (Figure 32). **Mat 10** shows an excitation maximum at 380 nm. **Mat 11** and **Mat 12** exhibit an emission maximum in the same area. Additionally, two local maxima were detected in the excitation spectra. These relative maxima are typical for anthracene

chromophores.^[214] By exciting **Mat 10** at 380 nm an emission maximum was observed at 490 nm in the green area of the light spectrum. The emission spectra for **Mat 11** and **Mat 12** show similar behavior. The emission maxima are centered at 430 nm for an excitation at 375 nm and 380 nm respectively. One origin for this behavior could be the self-absorption of the material combined with a partial quenching of the fluorescence in the wavelength area around 500 nm. This suggests that the linker molecule adsorbs the emitted light caused by π - π stacking interactions in the material and is able to emit visible light by its own (Figure 32). This conversion could be responsible for the numerous different maxima in the excitation as well as in the emission spectra for the INN materials **Mat 10**, **Mat 11** and **Mat 12**. Compared to the reference material (**Mat 1**) the anthracene linked bis-imidazolium INN materials show red shifted excitation as well as emission maxima, but they have in common that these bands are very broad. In consequence, it seems to the naked eye that they are emitting green light (Figure 32, right). Furthermore, the linker molecule itself, the 9,10-bis(chloromethyl)anthracene, shows photoluminescence properties as well (solid red line on the left in Figure 32). This molecule was used for the synthesis of some other compounds and materials bearing interesting photoluminescence properties.^[221,222] Compared to **Mat 10** the emission for an excitation at 375 nm of the pure linker is quite weak as well as observed for the biphenyl containing materials and the pure biphenyl linker. Here, as described for the biphenyl in the precedent paragraph, the difference in the relative intensity is significant.

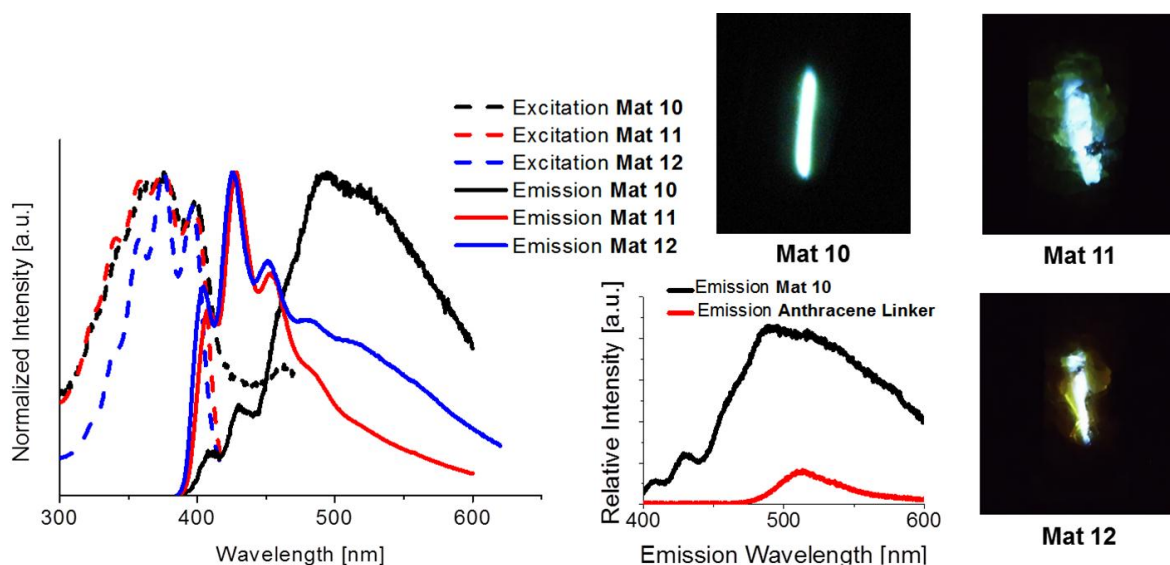


Figure 32 (left) Excitation (dotted lines) and emission spectra (solid lines) of the substituted and non-substituted bis-imidazolium materials connected by the anthracene linker (**Mat 10**, **Mat 11** and **Mat 12**), (right) Digital photos of the emission of the materials **Mat 10**, **Mat 11** and **Mat 12** under excitation at 380 nm, 375 nm and 380 nm respectively and (bottom) for comparison, emission spectra of **Mat 10** and the pure anthracene linker under an excitation at 380 nm.

3.3.3 Photoluminescence properties of the pyrazolium INN materials

To get a better understanding of the photoluminescence properties of the INN hybrid materials in general, the imidazolium moieties were replaced by a pyrazolium unit (**Mat 18**) or by 3,5-dimethylpyrazolium moiety (**Mat 19**). The excitation spectrum of **Mat 18** shows a maximum at 310 nm (Figure 33). By exciting the material at this wavelength a broad emission band with a maximum at 375 nm could be observed. In comparison to **Mat 1** the bands of the pyrazolium based materials (**Mat 18** and **Mat 19**) show a shift towards lower wavelengths from 380 nm to 375 nm. This fact could be explained by the different geometry of the bridging organic part of the INN material. The two nitrogen atoms of the pyrazolium are localized right next to each other. In consequence, a linear connection of the nanoparticles is impossible, as opposed to the linking in imidazolium based INN materials, such as **Mat 1**. The excitation spectrum of **Mat 19** shows two maxima: at 275 nm and at 320 nm. By exciting the material at these wavelengths one emission maxima could be detected at 380 nm. By comparing the emission maxima of **Mat 18** and **Mat 19** only a small difference was observed. This may be caused by the methyl groups in C3 and C5 position of the pyrazolium moiety by generating slightly repulsive steric interactions to the propyl groups located on the nitrogen atoms of the pyrazolium unit in combination with the positive inductive effect. Both, **Mat 18** and **Mat 19**, absorb and emit light at lower wavelengths compared to the imidazolium based INN reference material (**Mat 1**).

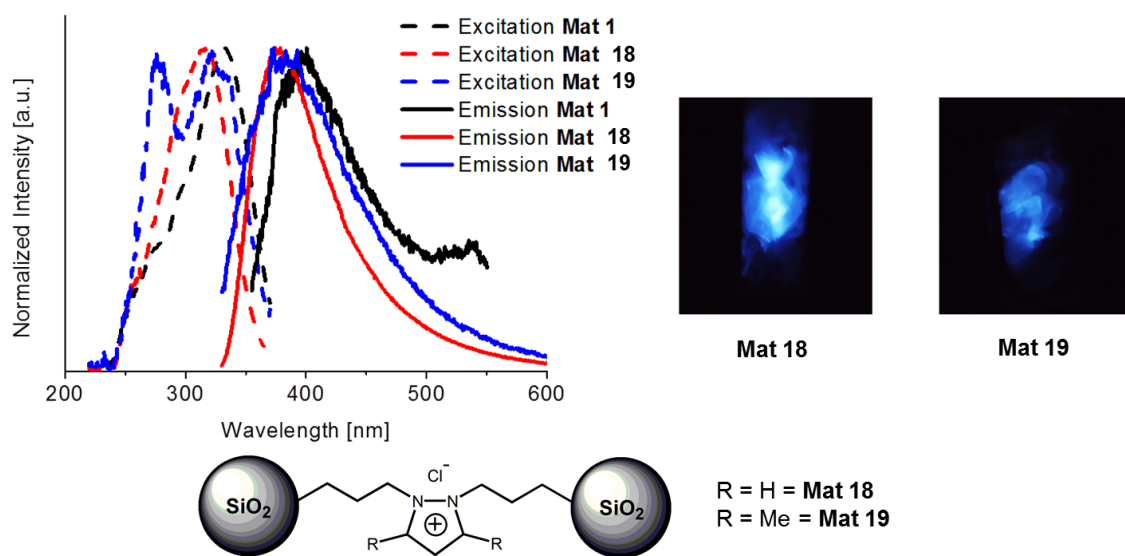


Figure 33 (left) Excitation (dotted lines) and emission (solid lines) spectra of the substituted and non-substituted pyrazolium based materials (**Mat 18** and **Mat 19**) and, for comparison, of the reference material **Mat 1**, (right) digital photos of the emission of the respective materials under excitation at 320 nm.

3.3.4 Photoluminescence properties of the mono-pyridinium INN materials

To extend the photoluminescence investigations to six atom rings, *ortho*- or *para*- linked pyridinium based INN materials (**Mat 23** and **Mat 24**) were investigated. The excitation spectrum of the *para*-linked pyridinium based INN material (**Mat 23**) shows a maximum at 365 nm (Figure 34). The excitation of the material at this wavelength leads to a broad emission band with a maximum at 420 nm, which is localized in the blue area of the light spectrum. By comparing **Mat 23** to **Mat 1** it was observed, that the pyridinium containing material shows a red shifted excitation as well as emission spectra. This could be explained by the different electronic properties of the pyridinium unit compared to the imidazolium unit in the INN material. Similarly, the excitation spectrum of the *ortho*-linked pyridinium based INN material (**Mat 24**) shows a maximum at 320 nm. By exciting the material at this wavelength two emission maxima could be detected: one global maximum at 430 nm and one local maximum at 490 nm. This may be caused by the different geometry: In **Mat 23** the silica nanoparticles are linearly linked, whereas in **Mat 24** the linking angle is more acute (Figure 34). Compared to the reference imidazolium based INN material (**Mat 1**), the materials **Mat 23** and **Mat 24** absorb and emit at higher wavelengths. For **Mat 23** and **Mat 24** a local maximum in the emission spectrum was observed at about 500 nm. Therefore, the samples were measured twice to exclude a possible contamination of the samples or something like that, but the maximum did not disappear. This suggests that this maximum is an artefact maybe caused by the measurement instrument.

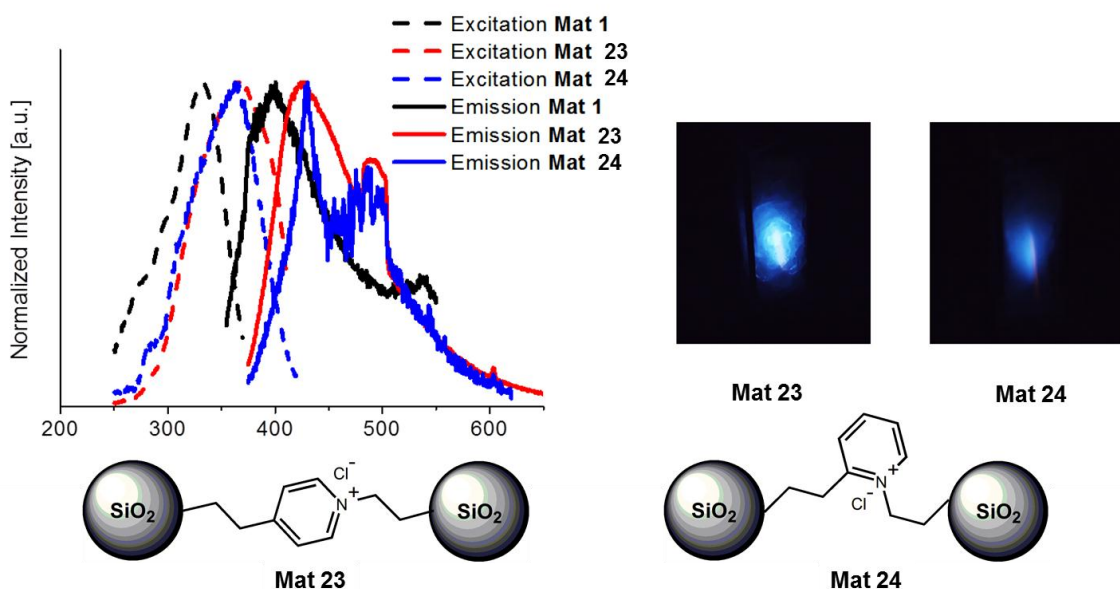


Figure 34 (left) Excitation (dotted lines) and emission (solid lines) spectra of the *para*- and *ortho* linked pyridinium based materials (**Mat 23** and **Mat 24**) and, for comparison, of the reference material **Mat 1**, (right) digital photos of the emission of the respective materials under excitation at 365 nm.

3.3.5 Photoluminescence properties of bis-pyridinium INN materials

For a higher content of delocalized electrons in the material in combination with free rotatability of the aromatic rings, α,α' -dichloro-*p*-xylene and 4,4'-bis(chloromethyl)-1,1'-biphenyl were used as linking unit for *para* linked bis-pyridinium materials (see Figure 35). The obtained materials (**Mat 25** and **Mat 27**) offer excitation maxima around 350 nm. By exciting the materials at these wavelengths the resulting emission maxima were quite different compared to each other. The maximum for the α,α' -dichloro-*p*-xylene containing bis-pyridinium material (**Mat 25**) is located at 400 nm on the border between blue and violet area of the light spectrum. Compared to the mono-pyridinium material (**Mat 23**) a blue shift of 20 nm was observed. By exciting the 4,4'-bis(chloromethyl)-1,1'-biphenyl containing bis-pyridinium material (**Mat 27**) at 350 nm a maximum in emission at a wavelength of 450 nm, in the blue region of the light spectrum, was observed. In consequence, compared to **Mat 23**, a red shift of 30 nm occurred for this emission maximum. By comparing the α,α' -dichloro-*p*-xylene containing bis-pyridinium material (**Mat 25**) and its bis-imidazolium analogue (**Mat 4**) (see Table 5) it was observed that form and position of the bands are similar to each other. However, comparing the 4,4'-bis(chloromethyl)-1,1'-biphenyl containing bis-pyridinium material (**Mat 27**) with the corresponding bis-imidazolium material (**Mat 7**) differences in form of the bands and position of the emission maxima were observed. The excitation as well as the emission behavior of **Mat 7** is quite complex and offer local maxima in addition to the global maximum (see Figure 31). **Mat 27** showed a broad excitation band with a global maximum at 350 nm and a shoulder at 280 nm. By exciting the material at 350 nm a broad emission band with a maximum at 450 nm was observed (Figure 35).

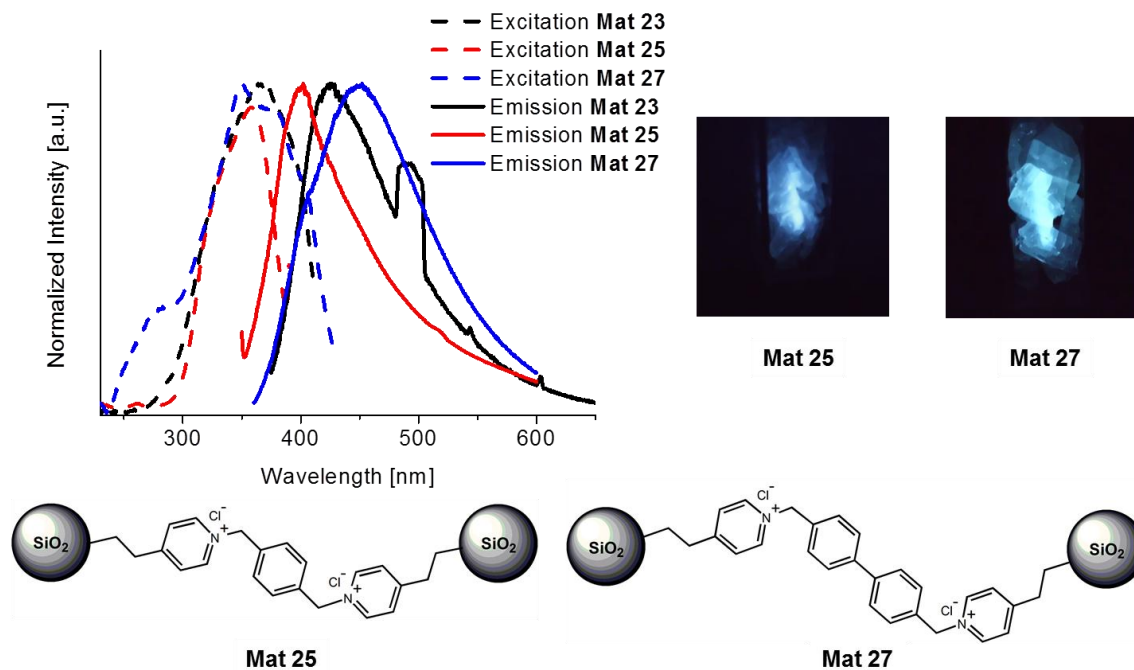


Figure 35 (left) Excitation (dotted lines) and emission (solid lines) spectra of the *para* linked bis-pyridinium based materials (**Mat 25** and **Mat 27**) and, for comparison, of the mono-pyridinium based material **Mat 23**, (right) digital photos of the emission of the materials under excitation at 340 nm and 350 nm, respectively.

3.3.6 Photoluminescence properties of the so-called mixed INN materials

In addition to the silica nanoparticle based INN materials the photoluminescence properties of the so-called mixed ZnO nanoparticle containing INN materials (**Mat 35** and **Mat 36**) were investigated. The excitation maxima for these two materials are located at 320 nm and 330 nm respectively (see Figure 36). Furthermore, at higher wavelengths a sharp decrease of the absorption was monitored. By exciting these two materials with the wavelength of the respective excitation maximum a really broad band was observed. Additionally, it turned out that **Mat 35** and **Mat 36** have exactly the same emission spectra. Due to this only one band is visible in the emission spectrum for **Mat 35** and **Mat 36** in Figure 36. This indicates that for these materials the substitution on the C2 position of the imidazolium unit had no influence on the photoluminescence properties. The emission maximum was located at 555 nm for both materials. Furthermore, by comparing with the reference material (**Mat 1**) it can be noticed that the mixed INN materials (**Mat 35** and **Mat 36**) emit at drastically lower energies. The photoluminescence properties of ZnO nanoparticles were often discussed in literature and the emission maximum is described to be located at 555 nm.^[159,197,223,224] This suggests that not the aromatic moieties between nanoparticles, but the ZnO nanoparticles itself, are responsible for the green emission of the so-called mixed INN materials.

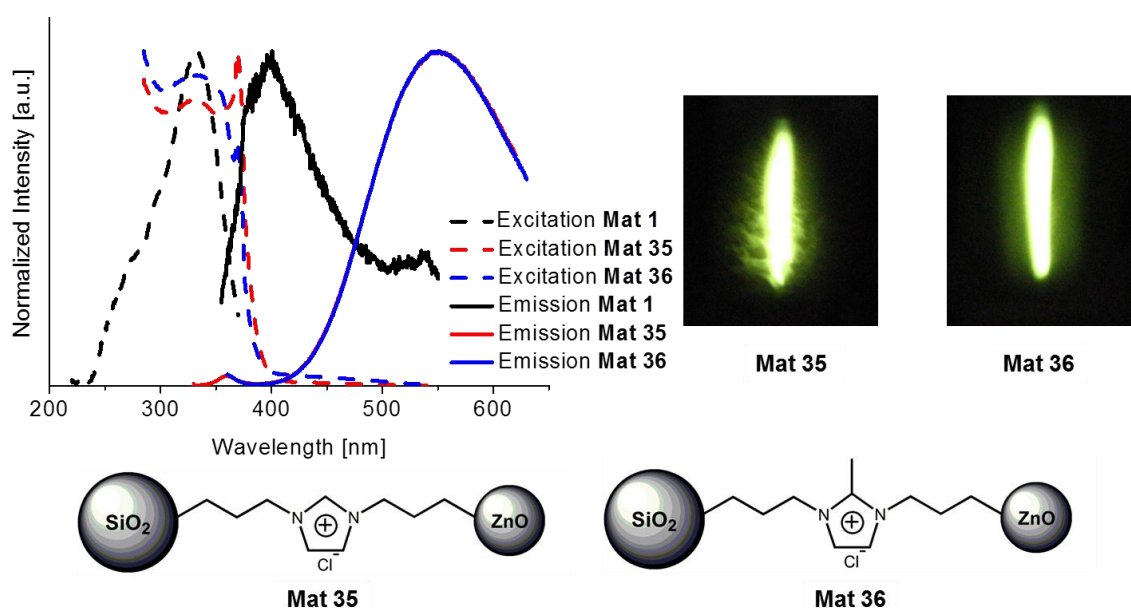


Figure 36 (left) Excitation (dotted lines) and emission (solid lines) spectra of the mixed INN materials (**Mat 35** and **Mat 36**) and, for comparison, of the reference material **Mat 1**, (right) digital photos of the emission of the materials under excitation at 320 nm and 330 nm respectively.

3.3.7 The influence of the short range order on the photoluminescence properties of the INN materials

It is supposed that the luminescence properties of the INN materials are dependent on the degree of the short range order of the linking units, only the structural parameters, η_2 and d_2 , are discussed in this part. The numerical values η_2 and d_2 as well as the measured emission/excitation maxima are listed in Table 5.

Table 5 Photoluminescence excitation/emission maxima and quantum yields compared with the hard sphere volume fraction η_2 and distance d_2 of linkers obtained from the fitting of SAXS-WAXS curves for the various INN materials.

Material	Excitation Max. [nm]	Emission Max.[nm]	Quantum Yield [%]	$\eta_2 \pm 0.02$	$d_2 \pm 0.05$ nm
Mat 1	320	380	10	0.31	1.37
Mat 2	365	440	15	0.33	1.40
Mat 3	345	400	4	0.29	1.40
Mat 4	350	410	11	0.25	1.70
Mat 5	370	450	18	0.25	1.50
Mat 6	370	440	9	0.11	1.50
Mat 7	305	350	6	--	--
	375	425	14	--	--
Mat 8	275	320	12	0.27	1.20
	300	390	16	--	--
Mat 9	370	475	12	0.26	1.60
	420	475	15	--	--
Mat 10	380	490	4	--	--
	470	550	7	--	--
Mat 11	375	430	5	0.3	1.40
	470	540	8	--	--
Mat 12	375	430	2	0.29	1.54
	490	550	4	--	--
Mat 18	320	375	4	0.13	0.88
Mat 19	320	380	6	0.29	1.34
Mat 23	365	420	4	0.33	1.11
Mat 24	365	430	5	0.30	1.40
Mat 25	340	400	1	0.27	1.52
Mat 27	350	450	4	0.2	1.52
Mat 35	320	555	5	0.27	1.04
Mat 36	330	555	6	0.27	1.06

The scattering curves of the INN materials exhibit a short range order peak, caused by the self-organization of the aromatic linkers in the material. The photoluminescence features were interpreted as a consequence of π - π stacking interactions between these aromatic rings. Therefore, differently substituted imidazolium based INN materials in combination with various aromatic linker molecules as well as pyrazolium and pyridinium based INN materials were used for a systematic investigation and their dependence on the structural organization at the nanometer scale. The photoluminescence phenomena in these aromatic-unit-containing INN materials are caused by the transition of the π^* excited state to the π energy level.^[225,226] The origin of the broad excitation as well as emission bands could be attributed to slight differences in the distances d_2 between the aromatic rings. Thus various “conjugation lengths” are generated, causing numerous HOMO-LUMO energy band gaps in the INN material.^[214,227] The associated quantum yields were also determined by photoluminescence measurements. These values are reported in Table 5. In order to compare the structural parameters obtained from the fits of the SAXS curves with the photoluminescence quantum yields, the mean values of η_2 , d_2 and QY were calculated for the different substituents on the C2 position of the imidazolium moiety (H-, Me-, i-Pr-). Although not all of the numerical values for η_2 and d_2 differ at a level of statistical significance (Figure 37, right). However, it is possible to identify a general trend between the substituents on the C2 position of the imidazolium unit, the obtained structural parameters and the photoluminescence quantum yields (Figure 37, left).

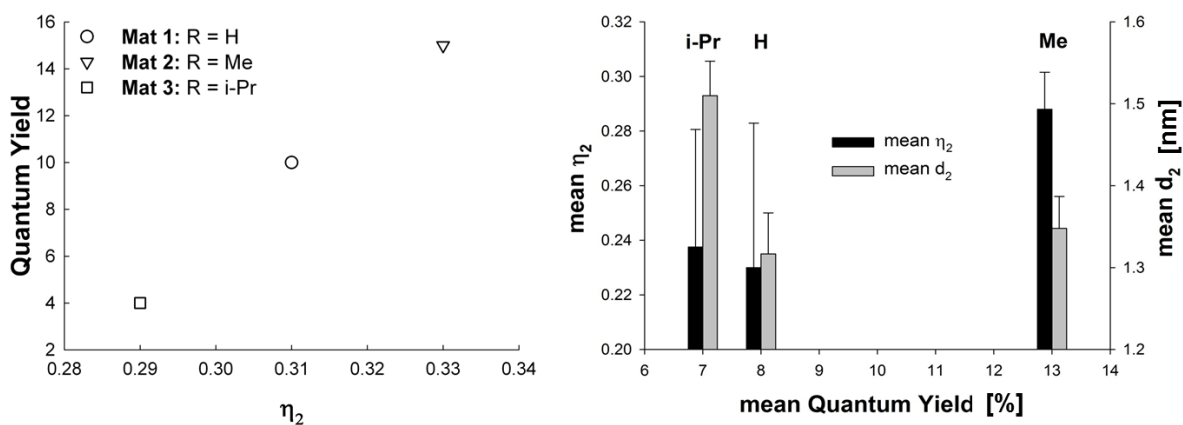


Figure 37 (right) Correlation between η_2 and quantum yield, (left) correlation between η_2 , d_2 and quantum yield.

The highest quantum yields correspond to the highest short range order and small mean distance, observed for the methyl substituted materials (Figure 37). A reasonable explanation for this phenomenon is that the methyl groups, on the C2 position of the imidazolium ring, induce only a weak steric hindrance. The positive inductive effect of this group is responsible for a slightly higher electron density in the imidazolium ring. The combination of these two effects lowers the

electrostatic repulsion between the positive charged imidazolium units in the material and thus leads to a better ordering of the imidazolium rings in the material and high quantum yields. The materials, which are substituted with an isopropyl group on the C2 position on the imidazolium unit, show the lowest η_2 and the smallest quantum yields. This observation can be explained in a way that the steric hindering of the isopropyl moieties dominates the positive inductive effect. Due to their small size, the hydrogen substituted materials show intermediate short range order as well as the smallest mean distances. In consequence, they show intermediate quantum yields. As mentioned above, the shifts of the excitation maxima as well as the emission maxima of the materials **Mat 1** to **Mat 6** have the same origin. The biphenyl linked bis-imidazolium INN materials **Mat 7 – Mat 9** showed quantum yields comparable to **Mat 1 – Mat 6** and also similar η_2 values. The anthracene linked bis-imidazolium materials **Mat 10 - Mat 12** showed lower quantum yields compared to **Mat 7 – Mat 9**. This observation leads to the conclusion that the free rotatability and flexibility of the linking molecules between the imidazolium moieties plays an important role for photoluminescence properties of the bis-imidazolium INN materials. Additionally, the pyrazolium as well as the pyridinium based INN materials (**Mat 18, 19, 23 – 25** and **Mat 27**) showed quite low quantum yields compared to the mono-imidazolium based INN materials (**Mat 1 – Mat 3**). This phenomenon may have its origin, for the pyrazolium based INN materials (**Mat 18** and **Mat 19**), in the different electronic structure of the pyrazolium ring, where the two nitrogen atoms are placed right next to each other. For the pyridinium based INN materials (**Mat 23 – 25** and **Mat 27**) the origin of the comparably low quantum yields could be attributed to the different electronic structure, compared to the imidazolium based INN materials (**Mat 1 – Mat 3**) as well. The mixed INN materials (**Mat 35** and **Mat 36**) are also well ordered and offer quantum yields of 5 and 6 %, respectively, but it is supposed that the luminescence activity is caused by the ZnO nanoparticles.

In conclusion, the photoluminescence investigations of the INN materials showed exciting photoluminescence features. For the imidazolium based INN materials the change of the substituent on the C2 position of the imidazolium ring from hydrogen to methyl or isopropyl group caused a red shifted maximum in the excitation as well as in the emission spectrum. Furthermore, the spectral area of the emission as well as for the excitation was changed by varying the linker molecule between the imidazolium moieties for the bis-imidazolium INN materials. It was shown that the photoluminescence activity results from the self-organization of the aromatic rings in the material by π - π stacking interactions. All the materials, which were investigated here, have in common that the photoluminescence activity is strongly enhanced by the self-organization of the aromatic rings in the material, compared to the educts of the nucleophilic substitution, to the bare silica nanoparticles and to the neat imidazolium salts.

Small and wide angle X-ray scattering experiments were executed, revealing the impact of different substituted imidazoles in combination with various aromatic chloromethylene (-CH₂Cl) disubstituted linker molecules on the structure and thus on the optical properties of the INN materials. It was shown that the quantum yield of the presented materials is affected by structural parameters. The combination of small distance and high degree of short range order improves the quantum yields, which is visible for the materials offering methyl substituted imidazolium moieties. In contrast, materials with isopropyl modified imidazolium units exhibited the lowest quantum yields due to the large distance of the aromatic units as a consequence of the steric hindering of this substituents. Furthermore, the results of the photoluminescence investigations of biphenyl and anthracene linked bis-imidazolium INN materials suggest that free rotatability and flexibility of the aromatic linker molecule increase the photoluminescence activity of the material.

3.4 Complexation of metal salts in INN materials and resulting properties

Some metal chlorides are able to build chloro metalate complexes. These metal complexes show remarkable features, *e.g.* $[\text{NH}_2(\text{Et})_2]_2[\text{CuCl}_4]$ ^[228] is proven to be thermochromic. Thus it is promising for the application as sensors.^[229–231] Due to the quaternization reaction during the materials synthesis, the INN materials consist of halogenide ions, which are chloride ions in the most cases. Depending on this fact and on the promising properties of tetrachlorometalate complexes, complexation reactions of metal chlorides, which are known to build chloro complexes, like $\text{CuCl}_2 \cdot 2\text{H}_2\text{O}$, PdCl_2 ^[232] and $\text{EuCl}_3 \cdot 6\text{H}_2\text{O}$,^[77,233] with the chloride ions of the INN materials were investigated.

3.4.1 Complexation of $\text{CuCl}_2 \cdot 2\text{H}_2\text{O}$ in INN materials and resulting thermochromic properties of the hybrid material

Diethylammoniumchloride is able to complex copper dichloride salts to form the thermochromic diethylammonium tetrachlorocuprate(II) complex. The coordination of solvent molecules on the copper(II) ion causes a square planar configuration of the copper(II) ion at room temperature (Figure 38). The square planar bis-diethylammonium tetrachlorocuprate(II) complex forms green crystals. When the temperature is increased, the configuration of the bis-diethylammonium tetrachlorocuprate(II) complex switches to a tetrahedral configuration (Figure 38) with a lower band gap as the interaction with the solvent molecules is degraded. As a consequence a color change from green to yellow is observed at 52 °C. These thermochromic properties were reported for ammonium tetrachlorocuprate(II) complexes^[229,231] as well as for imidazolium metal complexes.^[234,235] The investigation of the influence of the water on benzimidazolium tetrachlorocuprate(II) was reported by Bhattacharya *et al.*^[236] This compound showed a thermochromic behavior as well, however its thermal stability is limited to 140 °C.



Figure 38 Schematically drawing of the square-planar (left) and tetrahedral configuration (right) of $[\text{CuCl}_4]^{2-}$.

In this chapter the complexation of copper dichloride salt in INN materials to form thermochromic hybrid materials was investigated. Also the structural and thermochromic properties were determined and compared to two reference compounds. These were 1,3-butylmethylimidazolium tetrachlorocuprate(II) and the reference INN material (**Mat 1**).^[237]

The complexation reaction was executed by adding copper(II) chloride dihydrate to a methanolic suspension of the reference material (**Mat 1**) (see Figure 39).

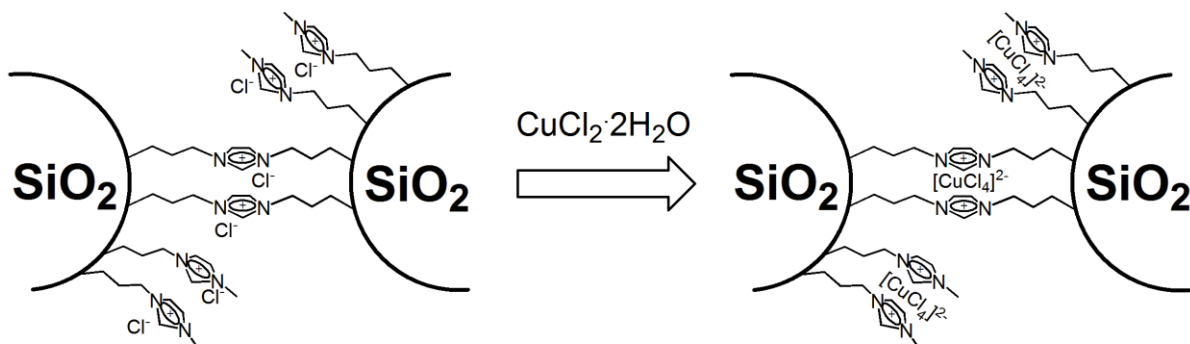


Figure 39 Formation of the tetrachlorocuprate(II) based INN material (**Mat 32**).

The amount of copper(II) chloride added to the methanolic suspension of **Mat 1**, was chosen to get a molar ratio of copper : imidazolium of 1 : 2. Therefore half of the molar amount of copper(II) chloride compared to the molar amount of N-(3-trimethoxysilanepropyl)imidazole, which was introduced for the preparation of **Mat 1**, was used. After adding the copper(II) chloride the suspension was stirred overnight at room temperature, it was washed and dried, resulting in a green transparent gel (**Mat 32**) (see Figure 40).

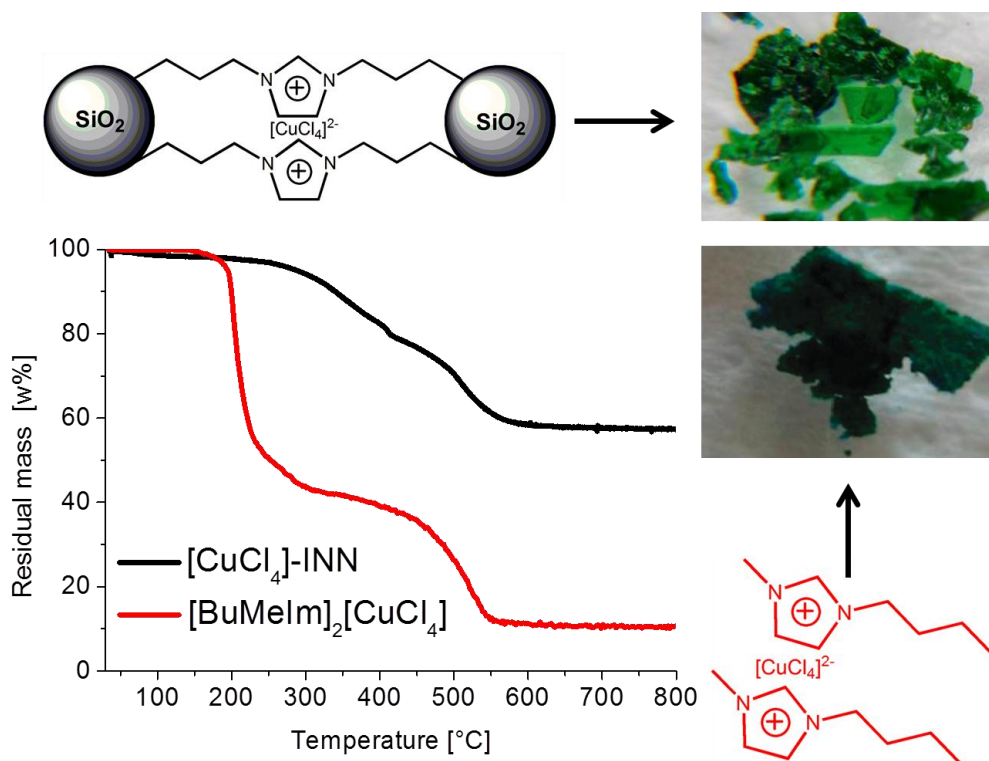


Figure 40 (top) the green transparent **Mat 32**, (bottom, left) TG analysis of **Mat 32** ([CuCl₄]-INN) and the reference compound [BuMelm]₂[CuCl₄], (bottom, right) reference compound [BuMelm]₂[CuCl₄].

The thermal stability of **Mat 32** was determined by a thermogravimetric analysis (black line in Figure 40). Here no decomposition was observed until 250 °C in air. For the reference compound, [BuMelm]₂[CuCl₄], the TG analysis showed distinct decomposition steps. A first step was observed in the temperature range between 165 °C and 320 °C and a second step from 350 °C to 550 °C. Only 11 w% remained after the decomposition, which corresponds to the copper(II) oxide residues. By comparing the thermal stability of [BuMelm]₂[CuCl₄] and **Mat 32**, a clear gain in stability was observed, arising from the formation of the INN network. This phenomenon was observed for the INN materials in general (see 3.2.2).

Powder XRD analysis was executed on the green material (**Mat 32**) (left, Figure 41). Only the very broad reflection characteristic of amorphous silica at 20° and no crystalline copper salt was observed. In addition the approximate atomic composition, indicating a molar ratio of 1 : 4 : 35 of Cu : Cl : C, of the material was determined by EDX (right, Figure 41). These values should be handled with care, as the error in defining molar ratios by EDX from heavy atoms (Cu) to very light atoms (C, Cl) is significant. Nevertheless, the ratio of Cu to Cl is about 1 : 4, which was expected for the tetrachlorocuprate(II) anion. The high content of carbon atoms is attributed to three reasons: first, the error on the determination of the amount of light elements is quite high in EDX; second, carbon

atoms, which belong to non-reacted ligand; third, some additional carbon atoms may belong to side groups due to the incomplete condensation of the trimethoxysilanes.

Similar to the reference material (**Mat 1**) the green material (**Mat 32**) can be processed into thin films by dip coating a concentrated methanolic suspension onto glass slabs (Figure 42).

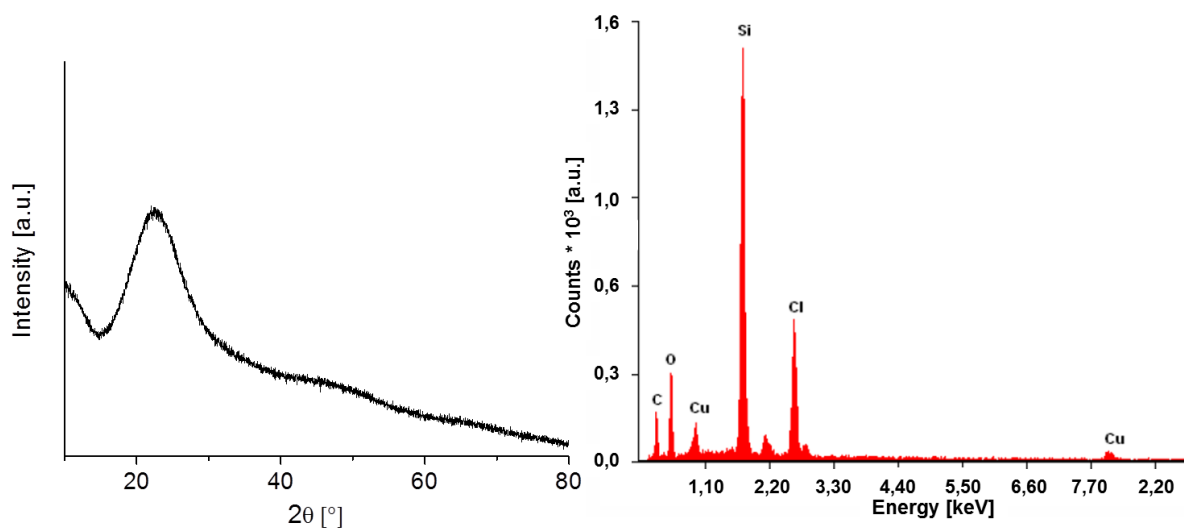


Figure 41 (left) powder XRD pattern of **Mat 32**, (right) EDX measurement of **Mat 32**.



Figure 42 Digital photos of INN materials thin films, (left) **Mat 1**; (middle) **Mat 32** before heating; (right) **Mat 32** after heating at 180 °C.

Preliminary investigations on the thermochromic behavior of **Mat 32** were carried out by depositing the dip coated glass slab on a heating plate and increasing the temperature. A clear color change was observed when the temperature reached 190 °C. The film remained transparent, but the color turned from slightly green to yellow (Figure 42). Optical microscopy on a Kofler bench reinforced the clear color change for **Mat 32** starting at around 180 °C (Figure 43). However, when the material was cooled to room temperature, it maintained its yellow color. This indicates that the

thermochromic behavior of **Mat 32** is not reversible. To identify the structural origin of this color change, *e.g.* a possible phase transition, differential scanning calorimetry (DSC) was executed on the green material. The DSC curve at a heating rate of 5 K per minute from 40 °C to 250 °C showed a strong endothermic peak centered at 180 °C (Figure 43). It is very probable that this peak corresponds to a change in configuration of the tetrachlorocuprate(II) complex from a square planar configuration to a compressed tetrahedral configuration, as known for thermochromic tetrachlorocuprate(II) compounds.^[238] During cooling at an identical ramp as in the heating process, the curve remains flat and no further change in configuration was observed. Further heating-cooling cycles showed no color change, hence no configuration change of the copper(II) complex in the material.

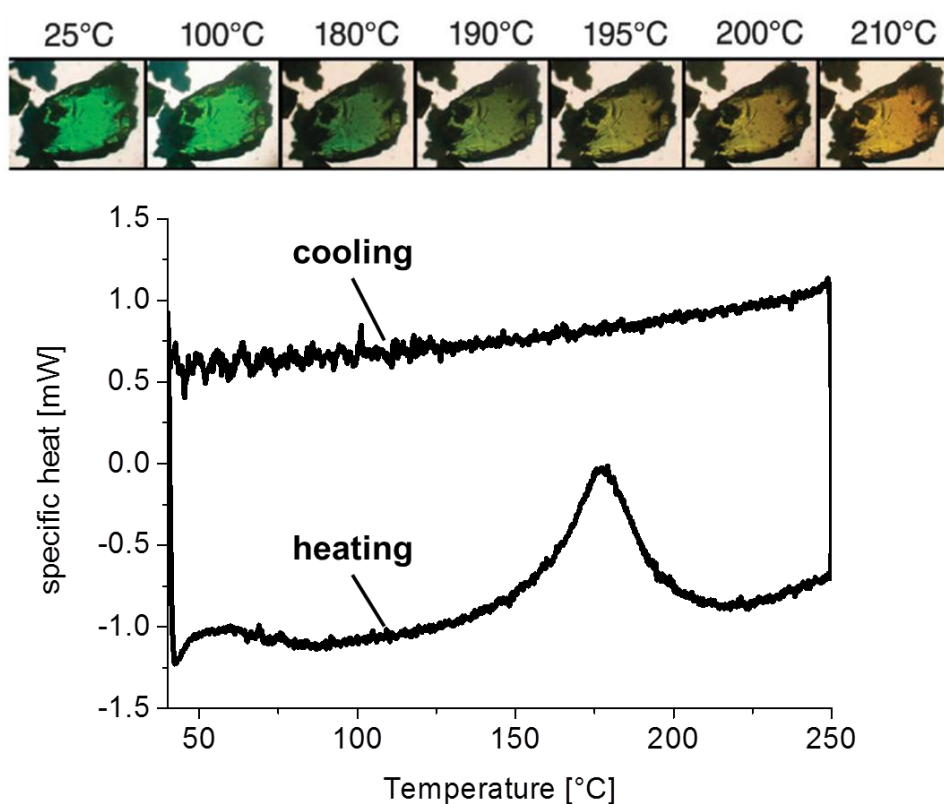


Figure 43 (top) microscope observation of the color change of **Mat 32** on a Kofler bench; (bottom) DSC curve of **Mat 32**.

For comparison the equivalent compound without nanoparticles, bis(1-butyl-3-methylimidazolium) tetrachlorocuprate $[\text{BuMeIm}]_2[\text{CuCl}_4]$ was prepared. The synthesis was quite similar to the synthesis of **Mat 32**. Equimolar amounts of 1-methylimidazole and 1-chlorobutane were allowed to react in ethylacetate at room temperature overnight. After evaporating the solvent, copper(II) chloride dihydrate was added in a 1 : 2 molar ratio of the copper salt to the 1-butyl-3-methylimidazolium chloride. Immediately after mixing, the temperature increased significantly, indicating an exothermic chemical reaction. At the same time, the color changed from blue, due to the unreacted

copper(II) salt, to deep green. The mixture was stirred overnight at room temperature. As the reaction was carried out solvent-free, the elimination of water, from the copper(II) chloride dihydrate, was easily observed. The thermal behavior of the reference compound $[\text{BuMeIm}]_2[\text{CuCl}_4]$ was also investigated on a Kofler bench under an optical microscope (Figure 44). Melting was observed at 140 °C, corresponding to the first endothermic peak in the DSC curve. At higher temperatures the melted $[\text{BuMeIm}]_2[\text{CuCl}_4]$ changed its color from green to brown. This is in good agreement with the decomposition temperature of 165 °C observed TG analysis (Figure 40). By cooling the sample it was observed that this process is irreversible.

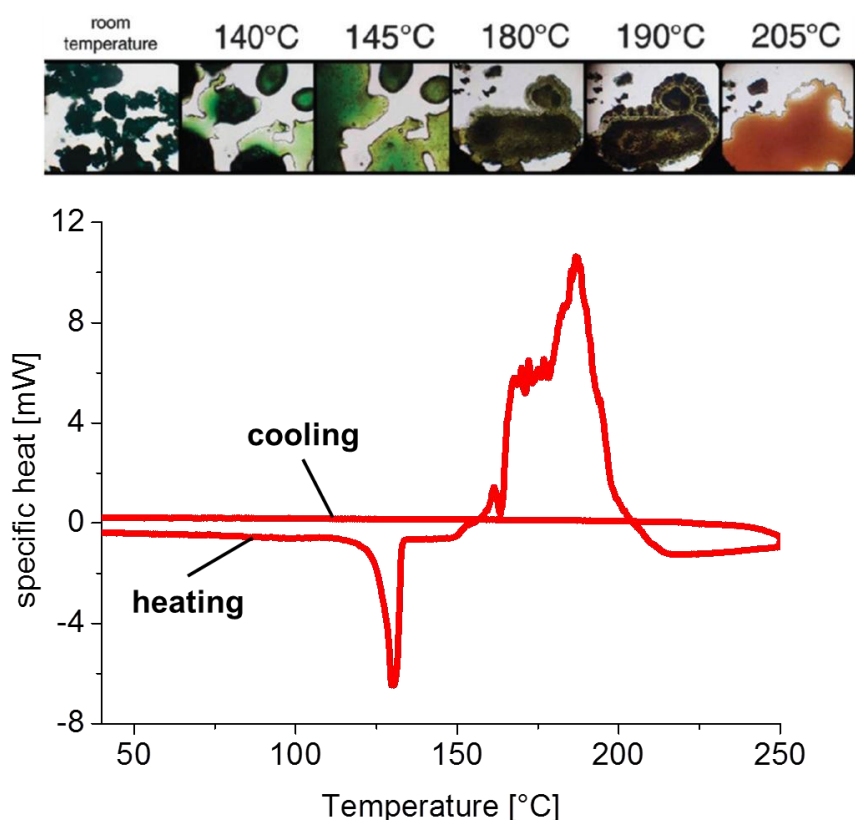


Figure 44 (top) microscope observation of the color change of $[\text{BuMeIm}]_2[\text{CuCl}_4]$ on a Kofler bench; (bottom) DSC curve of $[\text{BuMeIm}]_2[\text{CuCl}_4]$.

The structural development at the nanometer scale of the reference material (**Mat 1**), the reference compound ($[\text{BuMeIm}]_2[\text{CuCl}_4]$) and the thermochromic material (**Mat 32**) was investigated by using *in situ* SAXS during heating. Therefore, the samples were placed into capillaries and placed into an X-ray transparent furnace. The samples were then heated at a heating rate of less than 2 K per minute and at each step (5 °C intervals) a pattern was taken for 15 minutes.

The SAXS results for **Mat 1** were already reported in part 3.2.3. Since the arrangement of the imidazolium ligands is of primary interest in this investigation Figure 45 only shows the scattering intensities in the q -range between 2 and 15 nm^{-1} . In good agreement with previous observations

(3.2.2) **Mat 1** is stable in air up to 290 °C. No change of the structure during heating up to 200 °C was observed (Figure 45). Neither the intensity nor the position of the short range order peak at about $q = 5.8 \text{ nm}^{-1}$ exhibits any change and the structure at the nanometer scale is maintained. Furthermore, no degradation of the hybrid material was observed at the macroscopic scale.

In contrast, the SAXS data of the second reference compound, $[\text{BuMelm}]_2[\text{CuCl}_4]$, is strongly temperature dependent (Figure 45). All crystalline peaks disappeared at temperatures higher than 150 °C, which is good agreement with the DSC results. In addition, it should be noted that at temperatures above 100 °C, an additional ordered phase seems to develop, visible by an additional peak at about $q = 8.3 \text{ nm}^{-1}$ (arrow in Figure 45). Whereas the peaks of the original crystalline phase disappeared, this additional phase seems to be more stable. In fact this additional peak disappeared between 150 °C and 160 °C.

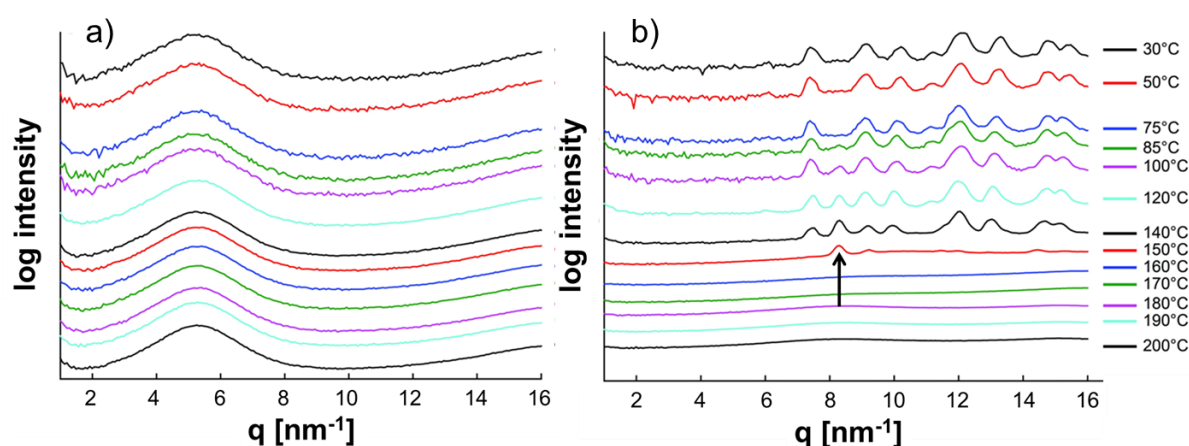


Figure 45 SAXS intensities depending on temperature (measured in situ) of the reference compounds; a) **Mat 1**; b) $[\text{BuMelm}]_2[\text{CuCl}_4]$.

The temperature dependence of the SAXS intensities of **Mat 32** is shown in Figure 46. Here, a linear scale was chosen for a better presentation of the peaks. For the material at room temperature, one small short range order peak is visible at about $q = 10 \text{ nm}^{-1}$, corresponding to a distance in real space of the units of about $d_2 = 0.6 \text{ nm}$. By heating the material above 150 °C, this peak disappears and a different peak arises at about $q = 5.6 \text{ nm}^{-1}$, corresponding to a distance of $d_2 = 1.1 \text{ nm}$ in real space. Furthermore, there is no gradual shift of the peak position, which indicates a phase transition from one configuration to another. This clearly suggests a configurational change of the tetrachlorocuprate(II) complexes from a square planar configuration to a compressed tetrahedral configuration, as known for thermochromic tetrachlorocuprate(II) compounds.^[234,238] This structural transformation was completed above 175 °C, which is in perfect agreement with the appearance of the thermochromic behavior, *i.e.* the color change from green to yellow.

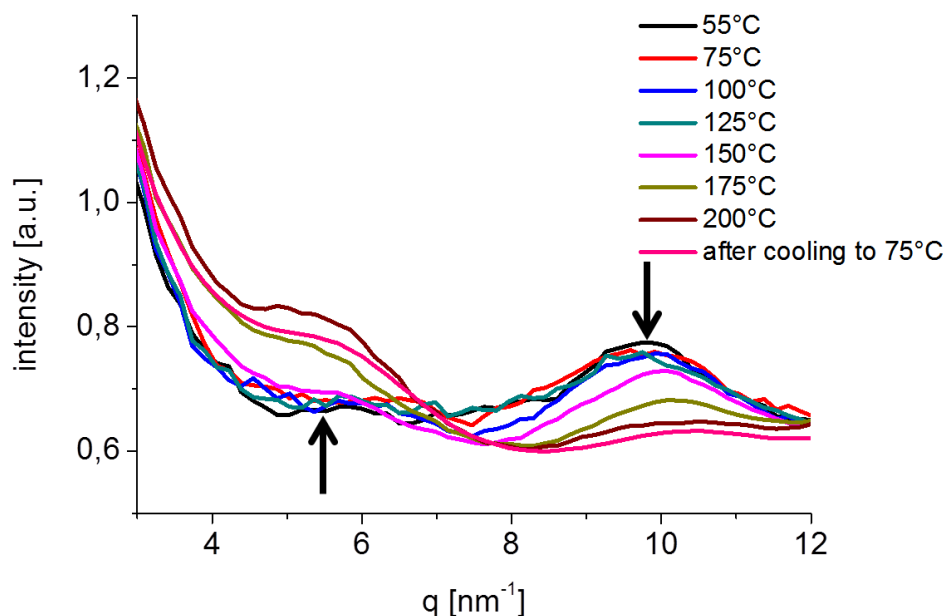


Figure 46 Temperature depending SAXS intensities of **Mat 32**, the arrows indicate a phase transition from a planar (small distance, peak at $q = 10 \text{ nm}^{-1}$) to a tetrahedral configuration (large distance, peak at $q = 5.6 \text{ nm}^{-1}$)

In contrast to the reference compound $[\text{BuMeIm}]_2[\text{CuCl}_4]$ the thermochromic material (**Mat 32**) is stable up to a temperature of 200 °C. This suggests that the confined space between the silica nanoparticles allows not only thermochromic behavior at significantly higher temperatures than in pure bis-diethylammonium tetrachlorocuprate(II), but also stabilizes the material itself. The introduction of $\text{CuCl}_2 \cdot 2\text{H}_2\text{O}$ into **Mat 1** induces two effects on the short range order of the material. On the one hand, the intensity of the short range order peak is lower in the thermochromic material (**Mat 32**) compared to the reference material (**Mat 1**). On the other hand, at low temperatures, the position of the short range order peak is located at higher q -values in the thermochromic material (**Mat 32**) than in the reference material, located at 10 nm^{-1} and 5.8 nm^{-1} , respectively. At temperatures above 150 °C the short range order peak for both materials is located at around 6 nm^{-1} .

The complexation of the chloride anions in **Mat 32** most likely causes a re-organization, which results in a de-organization of the imidazolium units compared to **Mat 1**. The change and decrease of the short range order also resulted in a strong change in the photoluminescence properties of the material. Indeed before the complexation of the copper(II) salt **Mat 1** showed a strong emission band with an emission maximum at 380 nm for an excitation of 320 nm (see 3.3.1). In contrast **Mat 32** showed almost no photoluminescence activity. It can be assumed that the imidazolium rings are involved in the coordination sphere of the square planar tetrachlorocuprate(II) complex at room

temperature in a similar way as reported for the solvent molecules in the thermochromic ammonium tetrachlorocuprate(II).^[238] This interaction could explain why the electrons of the aromatic rings are not able to interact with each other. As a consequence no photoluminescence activity was observed for **Mat 32**.^[237]

In conclusion copper(II) chloride was successfully complexed in the mono-imidazolium INN material. The resulting material showed an irreversible thermochromic behavior, which was observed by a color change from green to yellow at 180 °C. Additionally, this phenomenon was investigated by TGA and DSC measurements. The configurational change of the tetrachlorocuprate(II) complex from a square planar to a tetrahedral configuration at 180 °C was proven by *in situ* SAXS measurements. For the future it would be interesting to test other alkyl chain lengths, to change the substituents on the imidazole or change the nitrogen base itself, *e.g.* pyridine to obtain configuration changes at different temperature ranges.

3.4.2 Complexation of PdCl₂ and EuCl₃·6H₂O in INN materials and the resulting photoluminescence properties of the hybrid materials

Synthesis of the tetrachloropalladate(II) and tetrachloroeuropate(III) containing INN materials

Due to the ability to form tetrachloropalladate(II) complexes,^[239] PdCl₂ was also used for complexation within the INN materials. Therefore, palladium(II) chloride was added to a methanolic suspension of the reference material (**Mat 1**). The amount of palladium (II) chloride added to the methanolic suspension of **Mat 1**, was chosen to get a molar ratio of palladium : imidazolium of 1 : 2. Therefore, the half molar amount of palladium(II) chloride compared to the molar amount of N-(3-trimethoxysilanepropyl)imidazole, which was introduced for the preparation of **Mat 1**, was used. After adding the brown palladium(II) chloride the suspension was stirred overnight at room temperature. After washing and drying an olive green gel was obtained (**Mat 33**). The color change of the palladium(II) species from brown to olive green during the reaction indicates that the complexation reaction proceeded.

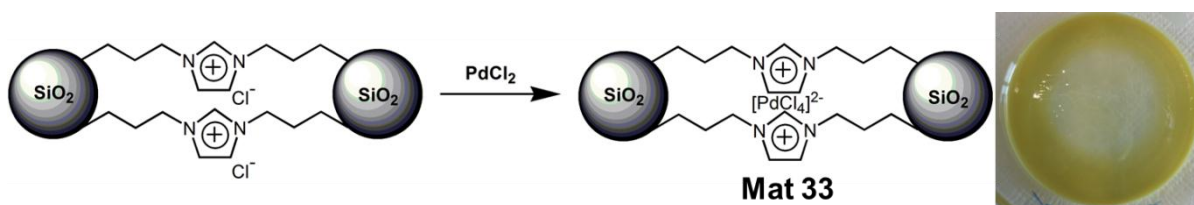


Figure 47 Synthesis of the tetrachloropalladate(II) material (**Mat 33**).

Europium(III) ions are well known for their intensive fluorescence, even when they are imbedded in metal oxides^[240] or other materials.^[241] Due to this fact $\text{EuCl}_3 \cdot 6\text{H}_2\text{O}$ was also used for the complexation in INN materials. According to literature only small amounts of the quite expensive europium(III) salts are necessary to dope the materials with europium(III) for photoluminescence studies on materials.^[242] Therefore, the amount of europium(III) chloride added to the methanolic suspension of **Mat 1** was about 10 w% compared to the molar amount of N-(3-trimethoxysilanepropyl)imidazole, which was introduced for the preparation of **Mat 1**. The suspension was stirred overnight at room temperature. After washing and drying a colorless transparent gel was obtained (**Mat 34**).



Figure 48 Synthesis of the tetrachloroeuropate(III) material (**Mat 34**).

Structural and thermal analysis of the palladium(II) and the europium(III) containing INN material

Preliminary investigations on a heating plate of possible thermochromic properties of **Mat 33** and **Mat 34** showed no color change in both cases. Especially for **Mat 33** this behavior was expected because of the high stability of the square-planar complex coordination for Pd(II) d^8 electron configuration. The thermogravimetric analysis of the two materials showed degradation in two steps (Figure 49), which is typical for these INN materials. For these two materials a second step occurs at temperatures higher than 600 °C. This suggests a conversion of the chloro metalate complex into the respective metal oxide, which may causes the loss of some chlorine in any form of chemical compound. Unfortunately, no TGA/MS measurements were executed on these materials at this stage. Hence there is no information of the chemical process causing the mass loss at 600 °C or the nature of the inorganic residues of **Mat 33**.

Additionally, SAXS measurements were carried out on the materials. For **Mat 34** a clear short range order peak was observed at $q = 5 \text{ nm}^{-1}$. For **Mat 33** a very broad peak in a q -range between 5 and 10 nm^{-1} could be observed. Due to the broadness of this peak it overlaps with the area, which is typical for amorphous silica in the SAXS spectrum. Hence no conclusions can be drawn about the short range order of this INN material.

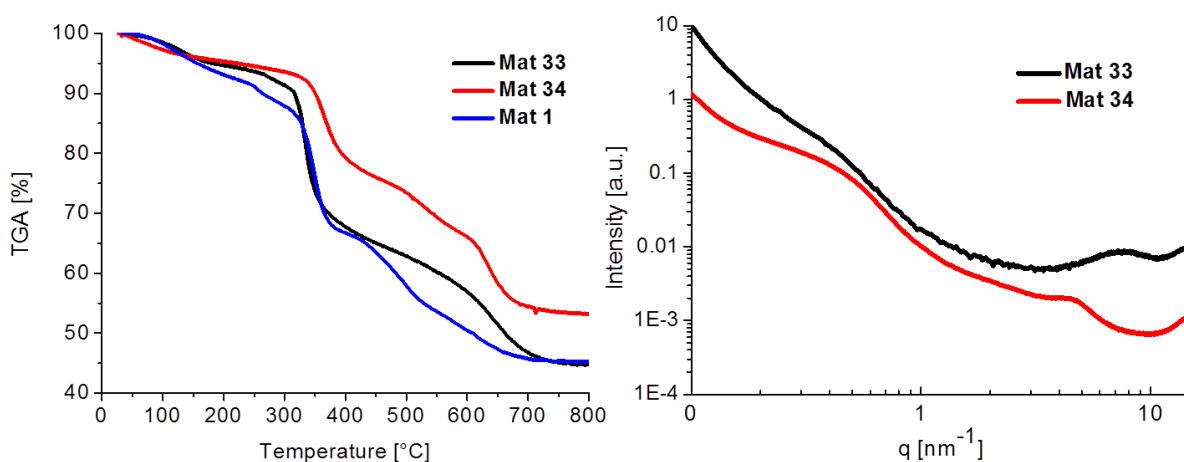


Figure 49 (left) TGA of **Mat 33**, **Mat 34** and for comparison **Mat 1**, (right) SAXS measurement of **Mat 33** and **Mat 34**.

Photoluminescence properties of the palladium(II) and the europium(III) containing INN material

As observed for the tetrachlorocuprate(II) containing INN material (**Mat 32**) before, the tetrachloropalladate(II) containing INN material (**Mat 33**) showed no photoluminescence activity at all. The explanation of this phenomenon could be the same as for **Mat 32**. The imidazolium rings participate in the coordination of the palladium(II) ion. This interaction could explain why the electrons of the aromatic rings could not interact with each other anymore. As a consequence no photoluminescence activity was observed for **Mat 33**.

A completely different behavior was observed for the europium(III) ion doped INN material (**Mat 34**). The excitation spectrum (Figure 50, on the left) shows a broad band with an excitation maximum at around 320 nm. By exciting the material at this wavelength a broad emission band with a maximum at 390 nm as well as two sharp emission bands in the region between 590 nm and 620 nm were observed. The broad band at 390 nm is typical for the INN materials (see 3.3.1). The sharp bands in the red area of the light spectrum are typical for Eu^{3+} ions.^[243] The mixture of these two emission maxima leads to an intensive purple emission, which could be seen in the picture in Figure 50. The excitation spectrum for an emission at 620 nm showed sharp bands with maxima in the range between 350 and 410 nm and a global maximum at 390 nm (Figure 50, on the right). By exciting the material with this wavelength only the characteristic bands for Eu^{3+} related to the $^5\text{D}_0 \rightarrow ^7\text{F}_j$ transitions were observed,^[244] while the characteristic bands for the INN material disappeared. This leads to an intensive red emission of the material. For comparison André Vioux *et al.* reported the same europium(III) induced photoluminescence feature in the range of 590 nm to 620 nm for europium(III) doped ionogels.^[245]

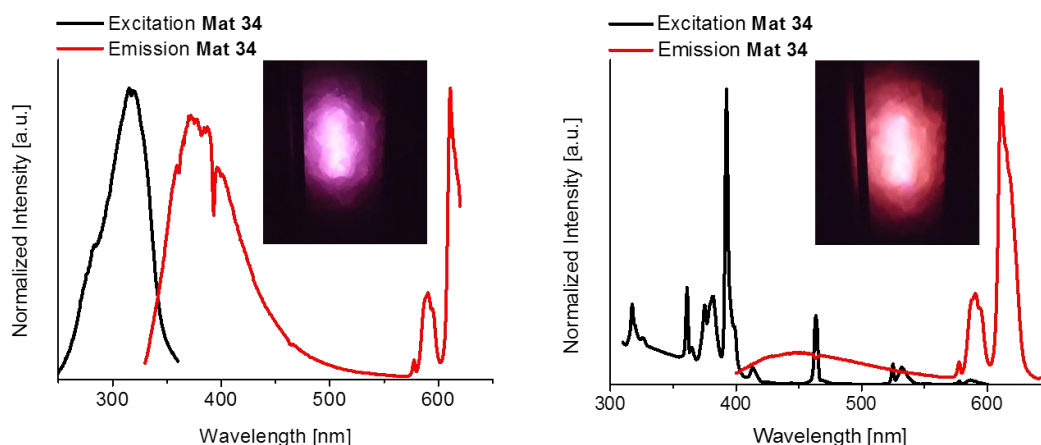


Figure 50 (left) Excitation spectrum for **Mat 34** (black solid line), the emission spectrum for an excitation of 320 nm (red solid line) and a digital photo of the emission at an excitation of 320 nm, (right) excitation spectrum of **Mat 34** (black solid line), the emission spectrum for an excitation of 390 nm (red solid line) and a digital photo of the emission at an excitation of 390 nm.

There are two possibilities for the coordination of the europium(III) ion: First, it is surrounded by four chlorine atoms in a tetrahedral coordination and second, by six chlorine atoms in an octahedral coordination.^[77] The presence of the typical bands of the INN material in the excitation as well as in the emission spectrum suggests that the tetrahedral $[\text{EuCl}_4]^-$ and not the octahedral $[\text{EuCl}_6]^{3-}$ exist in the material. If the trivalent $[\text{EuCl}_6]^{3-}$ exists in the INN material, no photoluminescence phenomena, caused by the INN material, can be observed, because the trivalent anion $[\text{EuCl}_6]^{3-}$ needs three imidazolium cations to saturate its own charge in that way that no interaction between the aromatic rings is possible.

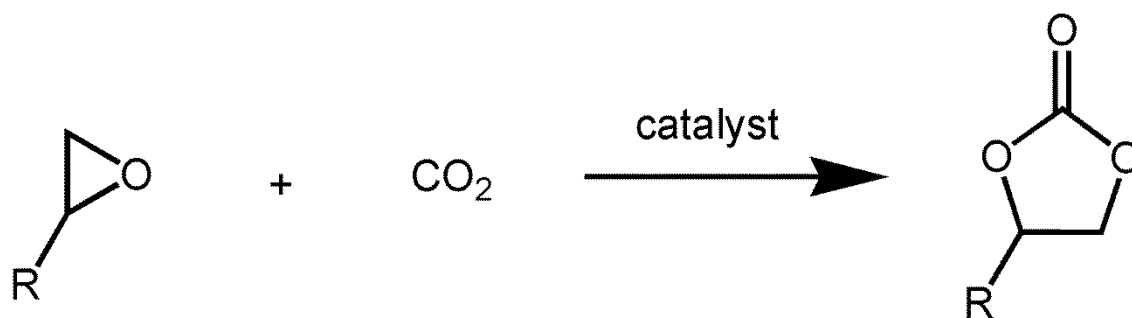
In conclusion, it was shown that the presence of bivalent metal complex anions inhibits the photoluminescence activity of the INN materials. Additionally, it was shown that the complexation of $\text{EuCl}_3 \cdot 6\text{H}_2\text{O}$ leads to photoluminescent active INN material. The color of the emission can be set by the excitation wavelength. For an excitation at 320 nm two emission maxima exist and cause an intensive purple emission. Otherwise for an excitation at 390 nm the typical bands for the INN materials disappear and only the photoluminescence feature of Eu^{3+} was observed. In that way, an INN material with controllable photoluminescence properties was synthesized. Furthermore, a palladium(II) complex containing material was synthesized. Due to the fact that it showed no photoluminescence activity at all, it helped to understand the influence of bivalent metal complexes in the photoluminescence activity of INN materials in general. In fact at this stage all investigated bivalent metal complexes interfered with the photoluminescence activity of the INN hybrid material. However, the palladium(II) complex containing INN material will be highly attractive for some catalytic investigations, *e.g.* in Heck reactions.^[246,247]

For the future, it will be interesting to complex especially cobalt (II) chloride and nickel (II) chloride within the INN hybrid materials, because $[\text{N}(\text{Me})_4]_2[\text{CoCl}_4]$ shows seven phase transitions^[248] and $[\text{NH}_2(\text{Et})_2]_2[\text{NiCl}_4]$ was proven to be thermochromic.^[249] Furthermore, tetrachloronickelate(II) complexes were used as catalysts, *e.g.* for the selective oligomerization of ethylene^[250] and the selective dehydration of fructose.^[251]

3.5 INN materials as solid state catalysts

In recent years it was reported that ionic liquids offer a high affinity to carbon dioxide.^[252–254] Therefore, ionic liquid containing hybrid materials can be used for CO₂ capture and storage^[255–258] and gas separation.^[259] Another approach is the direct conversion of CO₂, which can also be seen as a sustainable carbon source in terms of renewability, abundance and non-toxicity.^[260] In this context cyclic carbonates, due to their high oxidation state, appear to be an interesting synthetic target from CO₂ from a thermodynamic point of view. These compounds are industrially important chemicals and form the basis for polycarbonate or polyurethane production (*i.e.* as a phosgene substitute),^[261] or can be used as fuel additives,^[262] as co-solvents or solubilizer in cosmetics^[263] and electrolytes in lithium batteries.^[264]

Ionic liquids are known to catalyze the cycloaddition of CO₂ and epoxides to form cyclic carbonates efficiently (Scheme 21). Since the first study of the catalytic activity of ionic liquids in these reactions,^[265] numerous organic cations^[266] and anions^[267] have been investigated. Different heterogeneous ionic liquid based systems were also reported to efficiently catalyze the formation of organic cyclic carbonates from CO₂,^[268] including supports such as silica,^[269,270] various other metal oxides,^[271] polymers^[272] and metal organic frameworks.^[273,274] Thereby, various mechanisms were suggested to explain the catalytic activity of imidazolium based ionic liquids,^[275,276] *e.g.* a mechanism where the anion is the catalytic active part.^[277]



Scheme 21 Cyclic carbonate formation by cycloaddition of CO₂ to epoxides.

One main benefit of the immobilization of the catalytic species is that a heterogeneous system is obtained, which could be easily removed from the reaction mixture and also improves the recycling process of the catalyst. Additionally, in some cases it has been shown that the immobilization enhanced the catalytic activity compared to a free-standing catalytic active species. Imidazolium based ionic liquids cross-linked within a polymer matrix, for instance, showed notably higher catalytic activity than the free standing monomer analogues.^[278] The immobilization of the catalytic active species is believed to be the main reason for this gain in activity brought on by circumventing the poor solubility of the epoxide and the free-standing catalyst in the solvent-free synthesis. Beside

the active catalytic site itself, it has been demonstrated that the choice of an appropriate support is of capital importance. For this reason silica based supports were often chosen, not only due to their relatively easy preparation, but also due to their high chemical and thermal stability, their structural versatility (different types of porosity) and the potential synergetic effects caused by uncondensed hydroxy groups on the silica surface. Another key parameter is the loading and the accessibility of the catalytically active moieties. A high loading of active moieties was reported to be convenient in the case of polymer matrices and copolymers.^[278,279]

Recently, the grafting of bis-vinylimidazolium salts within porous silica supports was reported by Aprile *et al.* and the resulting materials showed significant activity in the synthesis of cyclic carbonates from epoxides and CO₂.^[280]

For these reasons the INN materials were tested as heterogeneous catalysts for the synthesis of cyclic carbonates from epoxides and CO₂ (Scheme 21). Furthermore, the influence of the C2 position of the imidazolium unit on the catalytic activity of the material was investigated by modifying this position with a methyl group. In addition, the so-called mixed INN materials were investigated to study the influence of the support on the course of the catalytic reaction.^[281]

The catalytic tests were executed by Jérôme Roeser and Prof. Arne Thomas at the Technische Universität Berlin. Therefore, 100 mg of the catalyst and 18 mmol of the starting epoxide were put in a stainless steel autoclave in solvent free conditions. The CO₂ pressure was adjusted to 6.9 bar after several degassing cycles and the mixture was typically heated at 130 °C for four hours. The crude reaction mixture was centrifuged, filtered and analyzed by GC-MS with toluene as internal standard, as well as ¹H NMR spectroscopy.

In a first step, reference reactions were performed with epichlorohydrin (Scheme 21, R = CH₂Cl) without catalyst as well as with bare silica nanoparticles, chloropropyl and 1-propylimidazole modified silica nanoparticles.

Table 6 Reference catalytic runs with epichlorohydrin (R = CH₂Cl in Scheme 21).

Catalyst	Time [h]	Conversion [%]	Selectivity [%]
blank	4	2.3	100
SiO₂	4	7.7	21.8
SiO₂ Cl	4	7.7	0
SiO₂ Im	4	83.4	86.7

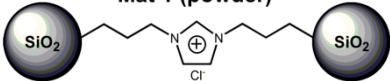
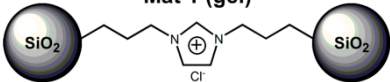
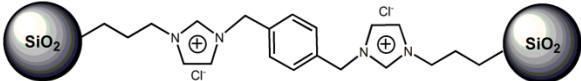
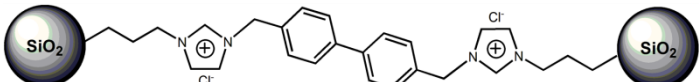
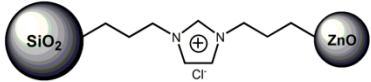
While the bare silica and the chloropropyl modified silica nanoparticles presented almost no catalytic activity on the conversion of the epoxides, the 1-propylimidazole modified silica nanoparticles allowed a conversion of slightly more than 80 % (Table 6). This observation is in good agreement with the literature, where basic amine groups are described to be catalytically active in this reaction.^[276]

The quaternization of the imidazolium moiety during the formation of the INN material significantly increases the activity of the catalyst. Indeed the reference material **Mat 1** (powder) (Table 7) was able to fully convert the starting epoxide under similar conditions as **SiO₂ Im** after four hours. For this reaction a selectivity of 88.7 % towards the cyclic carbonate formation was observed. The side products were diols and dimers of epichlorohydrin. These were also observed for other immobilized imidazolium species under similar reaction conditions.^[282] For comparison the reaction was also executed with a free-standing gel monolith of the reference material (**Mat 1** gel, Table 1). The conversion proved to be quantitative in four hours. This fact confirms the accessibility of the functional units in the three-dimensional network owing to the interparticle porous structure of the material.^[283,284] The selectivities towards the formation of the cyclic carbonate were 88.7 % and 93.0 % for the powder and the gel monolith, respectively. In both cases the catalyst was easily removed after the reaction by filtration of the reaction mixture.

The second category of INN materials, on which catalytic tests were performed, were the bis-imidazolium INN materials (**Mat 4** and **Mat 7**, Table 7). The catalytic activities of **Mat 4** and **Mat 7** are comparable with the results of **Mat 1**, reaching 100 % of conversion and selectivities between 84 % and 89 %.

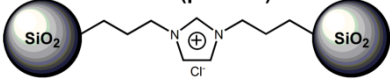
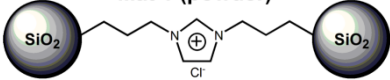
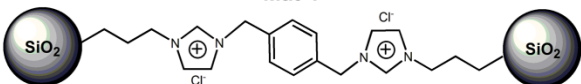
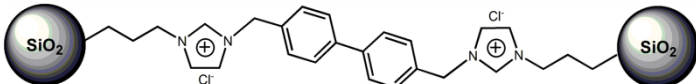
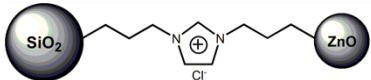
Furthermore, the catalytic activity of the so-called mixed INN material (**Mat 35**) was investigated to explore the influence of the nanoparticles species on the catalytic reaction. The zeta potential on ZnO surfaces is more basic compared to silica surfaces (10.2 and 2.1, respectively).^[164,165] Nevertheless, the catalytic activity of **Mat 35** is comparable to the activity of **Mat 1**. This suggests that in this case the nanoparticle species has no significant influence on the catalytic activity of the INN material.

Table 7 Conversion and selectivity of the cycloaddition reactions of CO₂ to epichlorohydrin (R = CH₂Cl in Scheme 21) in presence of mono- and bis-imidazolium based INN materials (**Mat 1**, **Mat 4** and **Mat 7**) as well as so-called mixed INN material (**Mat 35**) as the catalyst.

Catalyst	Time [h]	Conversion [%]	Selectivity [%]
 <p>Mat 1 (powder)</p>	4	100	88.7
 <p>Mat 1 (gel)</p>	4	100	93.0
 <p>Mat 4</p>	4	100	89.1
 <p>Mat 7</p>	4	100	84.1
 <p>Mat 35</p>	4	98.3	86.2

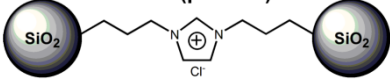
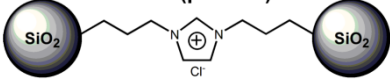
The catalytic activity of the INN materials in the conversion of propylene oxide and styrene oxide was also investigated. These two epoxides are known to be comparably less reactive than epichlorohydrin.^[285,286] As expected, a lower catalytic activity was observed when propylene oxide was used as the starting epoxide. In fact none of the materials used as catalyst gave full conversion after four hours reaction time. A drop in conversion and selectivity was observed when propylene oxide was converted in the presence of **Mat 1** as the catalyst (Table 8) compared with the quantitative conversion obtained by using epichlorohydrin (Table 7). A conversion of 95 % can be reached after eight hours reaction time, while maintaining a selectivity of around 90 %. Furthermore, **Mat 4** is significantly more active than **Mat 1** in converting propylene oxide in the cycloaddition reaction, as 93 % conversion can be reached under similar reaction conditions after only four hours (Table 8). These values are comparable with those from a work of Pescarmona *et al.* who reported the activity of bis-imidazolium xylene grafted on porous SBA-15 for the same reaction, presenting relatively low conversion of propylene oxide (up to 55 %) under even harsher conditions (150 °C, 100 bar).^[280] Additionally, the introduction of the biphenyl linker (**Mat 7**) slightly lowers the catalytic activity in comparison to **Mat 4**.

Table 8 Conversion and selectivity of the cycloaddition reactions of CO₂ to propylene oxide (R = CH₃ in Scheme 21) in presence of mono- and bis-imidazolium based INN materials (**Mat 1**, **Mat 4** and **Mat 7**) as well as so-called mixed INN material (**Mat 35**) as the catalyst.

Catalyst	Time [h]	Conversion [%]	Selectivity [%]
 <p>Mat 1 (powder)</p>	4	81.0	95.4
 <p>Mat 1 (powder)</p>	8	95.0	89.1
 <p>Mat 4</p>	4	93.0	95.6
 <p>Mat 7</p>	4	88.4	89.4
 <p>Mat 35</p>	4	82.3	95.4

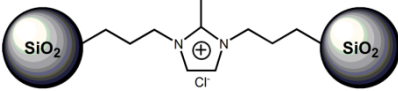
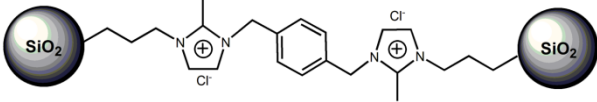
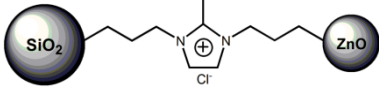
Considering the cycloaddition of CO₂ of styrene in oxide in the presence of **Mat 1**, a quantitative conversion of the styrene oxide was obtained after twelve hours. For this reaction a selectivity of 88.8 % was determined. The catalytic activity of **Mat 1** for this reaction is in the same range as those for supported imidazolium based ionic liquids reported by Zheng and coworkers.^[287]

Table 9 Conversion and selectivity of the cycloaddition reaction of CO₂ to styrene oxide (R = C₆H₅ in Scheme 21) in presence of the reference INN material (**Mat 1**) as the catalyst.

Catalyst	Time [h]	Conversion [%]	Selectivity [%]
 <p>Mat 1 (powder)</p>	8	63.7	93.4
 <p>Mat 1 (powder)</p>	12	100	88.8

On dealing with the catalytic activity of imidazolium species in general, the influence of the C2 position of the imidazolium ring, was often pointed out. Moreover, the mechanisms proposed to explain the CO₂ cycloaddition, describe the predominant role of a carbene on this C2 position which directly interacts with the CO₂ molecules.^[288–290] To evaluate this influence in the present catalytic reactions, INN materials modified with a methyl group on the C2 position of the imidazolium moiety (**Mat 2**, **Mat 5** and **Mat 36**), were used for the catalytic investigations (Table 10). For **Mat 2** and **Mat 5** the methylation of the C2 position lowers the catalytic activity, as seen by a significant drop in conversion under identical conditions compared to **Mat 1** and **Mat 4**. This is most notable for **Mat 2**, where a drop of up to 24 % in conversion was observed. From this observation it can be concluded that the C2 position of the imidazolium plays a role in the catalytic cycloaddition reaction. It cannot be excluded that carbene species played an important role in the catalytic mechanism,^[288–291] which will be discussed later on. However, the high conversions observed (between 76 % and 89 %), even when the C2 position is not accessible, suggest that further activation mechanisms are possible for imidazolium based catalysts. Interestingly, **Mat 2** showed 100 % selectivity towards the building of the carbonate.

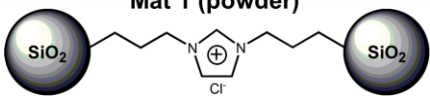
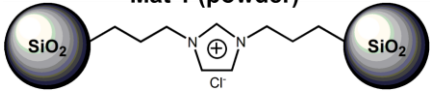
Table 10 Conversion and selectivity of the cycloaddition reactions of CO₂ to epichlorohydrin (R = CH₂Cl in Scheme 21) in presence of methylated mono- and bis-imidazolium based INN materials (**Mat 2** and **Mat 5**) as well as so-called mixed INN material (**Mat 36**) as the catalyst.

Catalyst	Time [h]	Conversion [%]	Selectivity [%]
<p>Mat 2</p> 	4	76.0	100
<p>Mat 5</p> 	4	80.7	94.6
<p>Mat 36</p> 	4	88.5	76.6

Finally, the recyclability of the reference material (**Mat 1**) was investigated. Between each run the catalyst was filtered off, washed with toluene and was dried at 150 °C under vacuum conditions.

Recycling tests with epichlorohydrin showed that the catalyst could be reused for at least four consecutive runs without a loss of conversions. However, the formation of side-products was promoted, as was observed by a significant drop in selectivity.

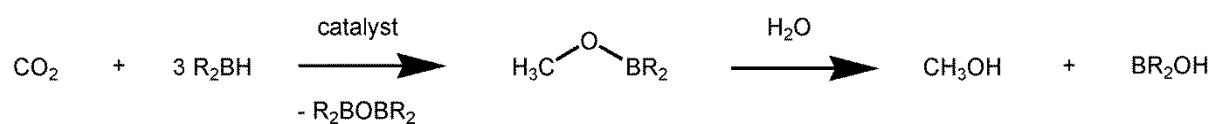
Table 11 Conversion and selectivity for run 1 and run 4 of the cycloaddition reactions of CO₂ to epichlorohydrin (R = CH₂Cl in Scheme 21) in presence of **Mat 1** for the investigation of the recyclability of the catalyst.

Catalyst	Run	Time [h]	Conversion [%]	Selectivity [%]
	1	4	100	88.7
	4	4	98	71

At this stage it is possible to conclude that the INN material catalyst remains active for four runs, which is in agreement to some results reported in literature for harsher conditions. (higher temperature, higher pressure and longer reaction times).^[280]

In conclusion, it could be shown that the INN materials are efficient heterogeneous catalysts for the conversion of CO₂ and different epoxides into organic cyclic carbonates. Reactions with epichlorohydrin showed that a quantitative conversion could be reached for all the tested catalysts under relatively mild conditions. The catalysts could be easily recycled for at least four runs without a loss in conversion, but a decrease in selectivity was observed. Furthermore, it was proven by testing the so-called mixed INN materials that the catalytic activity of the INN materials does not depend on the used nanoparticle species. According to literature and from our point of view an intermediate coordination of the CO₂ on the C2 position of the imidazolium ring, where the option of the presence and the interaction of an N-heterocyclic carbene could not be excluded, is quite probable.^[288–290]

Additionally, Thibault Cantat and Enguerrand Blondiaux at CEA Saclay (France) performed investigations on the metal-free reduction of CO₂ with hydroboranes to form methanol with the INN materials as catalysts (Scheme 22). For this reaction the catalysts have to exhibit a frustrated Lewis pair, which also can be a carbene.^[292]



Scheme 22 Formation of methanol from CO₂ and hydroboranes.

In comparison to the usually used catalyst the INN materials showed a reactivity of only 5 % for the tested reaction. However, this clearly suggests that some carbene moieties are present in the INN materials and indicate an N-heterolytic carbene mechanism for the INN material catalyzed cycloaddition of CO₂ and epoxides (Scheme 21).

3.6 Attempts on silica nanoparticle based self-healing materials

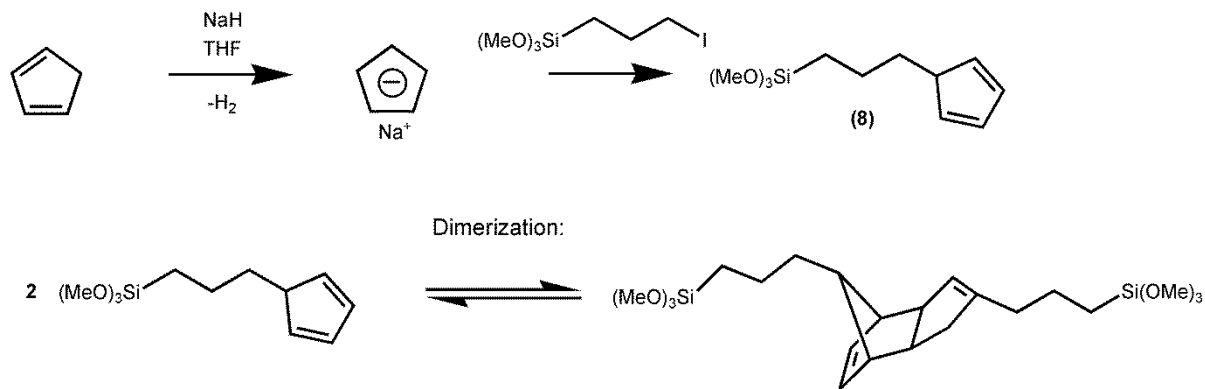
In most cases self-healing materials are polymers synthesized from bifunctional monomers. If the macroscopic structure of these polymers is destructed mechanically, these monomers are able to “repair” the material. This is in the most cases done by thermal activation.^[293–295] Major classes of thermally reversible polymers are made by using Diels-Alder reactions.^[296] Examples of this category of self-healing materials include cross-linking of furan group containing monomers and maleimide based monomers at low temperature. The retro-Diels-Alder reaction occurs at higher temperatures to break the chemical bonds of formed networks and to reverse the cross-linking process.^[297] Another example for self-healing materials are vitrimers, which are permanently cross-linked polymer networks, which are able to flow nonetheless.^[298] Leibler *et al.* reported the catalytic control of vitrimer glass transition, which corresponds to the self-healing abilities of this class of polymers.^[299,300] The essential compounds required for this reaction are bifunctional monomers offering epoxy groups, carboxylic acid groups as well as zinc acetate as the catalyst.^[301]

The INN hybrid materials showed a high functionality content, as mentioned in the previous chapters. Additionally, it is quite easy to modify their structure, which makes them good candidates to extend the family of self-healing materials. Therefore, it was tried to transfer the principles of Diels-Alder reaction based self-healing materials and vitrimer based self-healing materials to silica nanoparticle networks.

3.6.1 Dicyclopentadiene based silica nanoparticle networks

Adapting the principle of the Diels-Alder reactions based self-healing materials to the silica nanoparticle networks, the diene and the dienophile were covalently bonded on a propyltrimethoxysilane moiety. Originally maleimide was chosen as the dienophile, but the synthesis of the N-(3-propyltrimethoxysilane)maleimide was unfeasible. Instead 3-cyclopentadienylpropyltrimethoxysilane was synthesized, which can act as both: as diene and dienophile. The synthesis of the 3-cyclopentadienylpropyltrimethoxysilane is a nucleophilic substitution, comparable with the synthesis of the N-(3-propyltrimethoxysilane)imidazole (Scheme 23).^[302] For the synthesis itself freshly monomerized cyclopentadiene was added to a suspension of sodium hydride in THF under cooling and stirring. After complete addition the cyclopentadiene to the clear colorless solution, the color changed to slightly pink, which indicates the presence of the cyclopentadienyl anion. Then, an equimolar amount of 3-iodopropyltrimethoxysilane was added and the mixture was maintained under reflux overnight. After purification by distillation in vacuum

the product was cooled to approximately 0 °C to decelerate the dimerization of the cyclopentadienyl moiety (Scheme 23).



Scheme 23 Synthesis and dimerization of 3-cyclopentadienylpropyltrimethoxysilane.

However, ^1H - and ^{13}C NMR spectra were measured immediately. The dimerization of the product was so fast, that it could be observed during the NMR measurement, as can be seen in the ^{13}C NMR spectrum in Figure 51. Especially the doubling of the signals of the alkyl chains in the range between a chemical shift of 10 ppm and 50 ppm can be observed. In the range between a chemical shift of 120 ppm and 140 ppm both, the signals of the monocyclopentadiene and dicyclopentadiene moieties, can be observed. Due to this fact the silica nanoparticles were modified with the 3-cyclopentadienylpropyltrimethoxysilane as fast as possible.

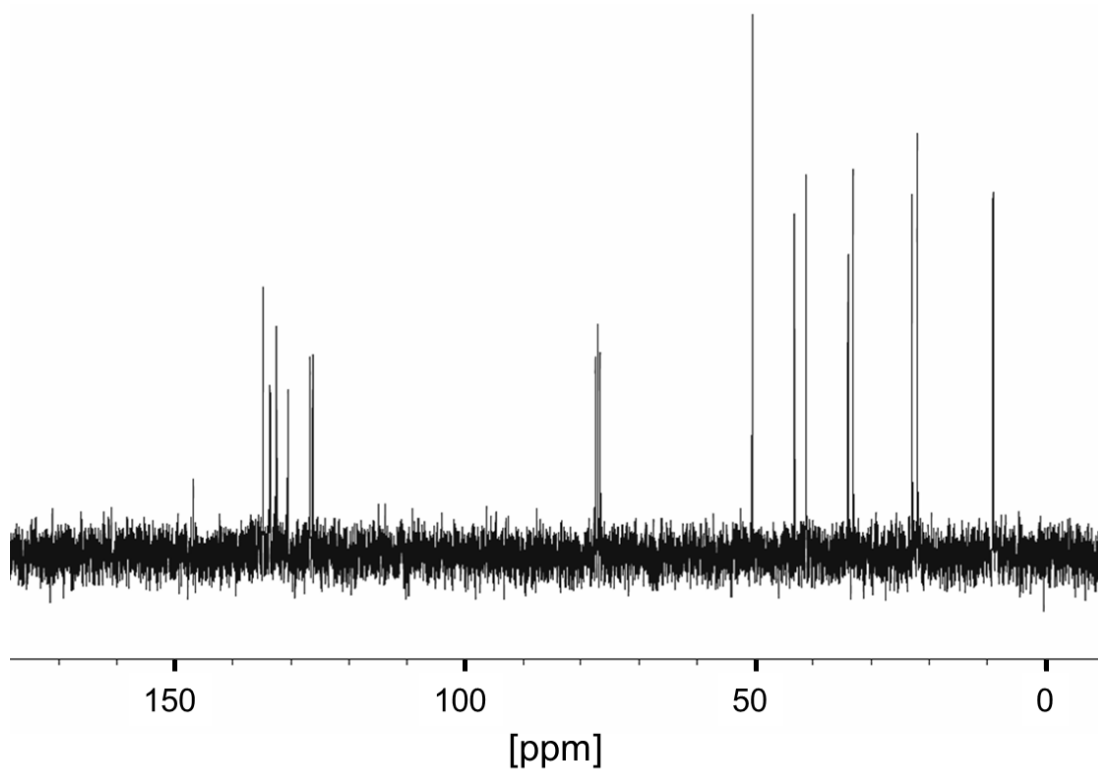
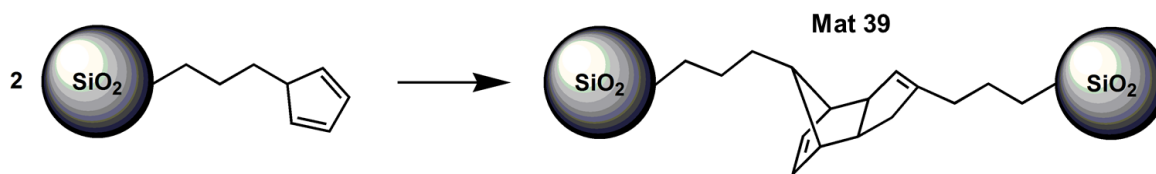


Figure 51 ^{13}C NMR spectrum of cyclopentadienylpropyltrimethoxysilane.

The modification of the silica nanoparticles (as a silica nanoparticle suspension in methanol) with the 3-cyclopentadienylpropyltrimethoxysilane was at the same time the synthesis of the hybrid material, because of the rapid dimerization of the cyclopentadienyl rings (Scheme 24). The reaction mixture was stirred for 24 hours at room temperature. After removing the solvent a colorless transparent gel was obtained.



Scheme 24 Material synthesis of the dicyclopentadiene based self-healing material (**Mat 39**).

SAXS measurements of the material (Figure 52) showed a complicated peak in the q -range between $q = 10 \text{ nm}^{-1}$ and $q = 20 \text{ nm}^{-1}$, which could be assembled by several effects in the material. At this stage no statement about the effects and their contributions can be made, because of the strong contribution of the amorphous character of the silica nanoparticles. Nevertheless, it can be stated that in the SAXS spectrum no short range order was observed for **Mat 39**. Unfortunately, it was impossible to fit the SAXS curve of **Mat 39**. In consequence no information about radii and hard sphere volume fraction was obtained for this material. In the thermogravimetric analysis a mass loss of 22 w% in the temperature range between 170 °C and 200 °C was observed. This may contribute to the degradation, monomerization and vaporization of the dicyclopentadiene moieties in **Mat 39**, because the boiling point of pure dicyclopentadiene is located at 170°C.^[303]

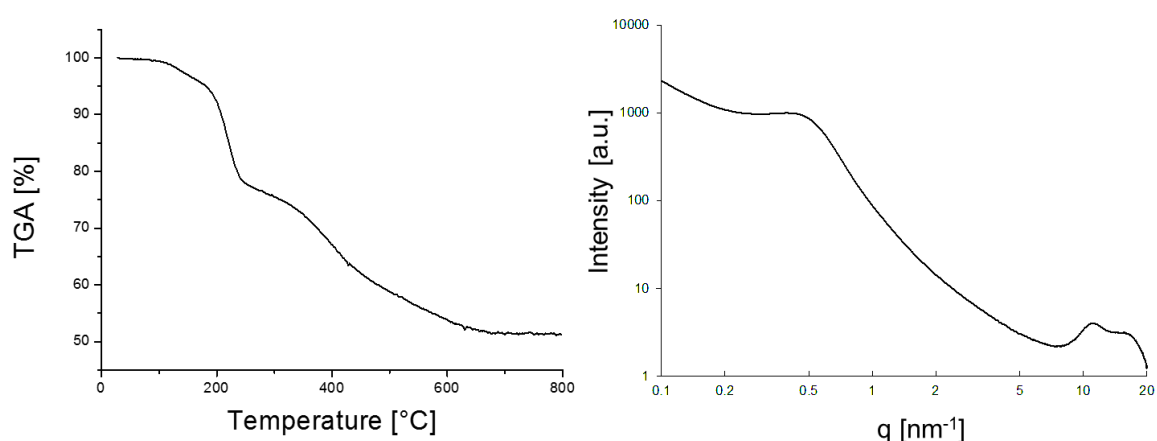
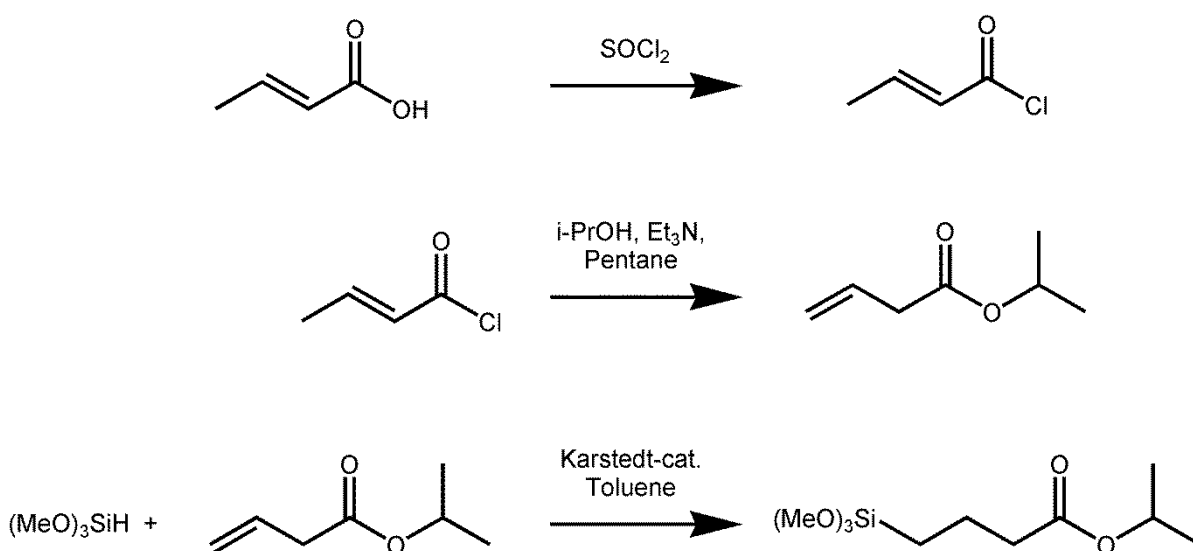


Figure 52 (left) TG analysis of **Mat 39**, (right) SAXS spectrum of **Mat 39**.

In conclusion the material offered no self-healing ability at this temperature, but rather it decomposes at higher temperatures. Furthermore, the self-healing ability of the material was tested. Therefore the material was powdered followed by heating up to 180 °C. Unfortunately, no self-healing activity of the material (**Mat 39**) was observed.

3.6.2 Vitrimer-type cross-linked silica nanoparticle networks

For the transfer of the principle of the vitrimer based self-healing materials on silica nanoparticle networks one functional group of the monomer was replaced by a trimethoxysilyl group. In consequence, for the epoxy part (3-glycidyloxypropyl)trimethoxysilane (GLYMO), which is commercially available, was used for the modification of the silica nanoparticles. For the adaption of the carboxylic acid part butanoic acid-4-(trimethoxysilyl)-isopropylester was synthesized in a three-step synthesis from crotonic acid, containing a hydrosilylation in the last step of the synthesis (Scheme 25).^[79,304] A yield of 18 % for the whole three-step synthesis was obtained.



Scheme 25 Three-step synthesis of butanoic acid-4-(trimethoxysilyl)-isopropylester.

The butanoic acid-4-(trimethoxysilyl)-isopropylester was chosen for the modification of the silica nanoparticles, because the 4-trimethoxysilyl butanoic acid is not stable as the acid group will take part in an intramolecular condensation reaction with the trimethoxysilyl group. For the synthesis of the hybrid material silica nanoparticles were modified on the one hand with butanoic acid-4-(trimethoxysilyl)-isopropylester and on the other hand with 3-glycidyloxypropyltrimethoxysilane. After the addition of 10 w% zinc acetate and a slightly molar excess of a 38 % hydrogen chloride solution in methanol, these two nanoparticle species were allowed to react with each other for 48 hours under stirring at room temperature. During this time the color of the clear colorless reaction mixture turned to yellow. After removing the solvent very carefully, a yellow transparent gel

monolith (**Mat 40**) was obtained (Figure 53). The strategy of the synthesis of this hybrid material was the following: during the reaction the epoxy ring opens by a nucleophilic attack of the carboxylate group of the zinc(II) acetate. In consequence, the alcoholate and the formed carboxylate ester coordinate to the zinc(II) ion. In addition, the carboxylate ester function on the surface of the nanoparticles react *in-situ* with the methanolic hydrogen chloride and form carboxylate groups, which are also able to coordinate to the zinc(II) ion (Figure 53). The advantage of this reaction is that the system is very flexible and there is a dynamic equilibrium of molecules, which are involved in the coordination to the zinc(II) ion.

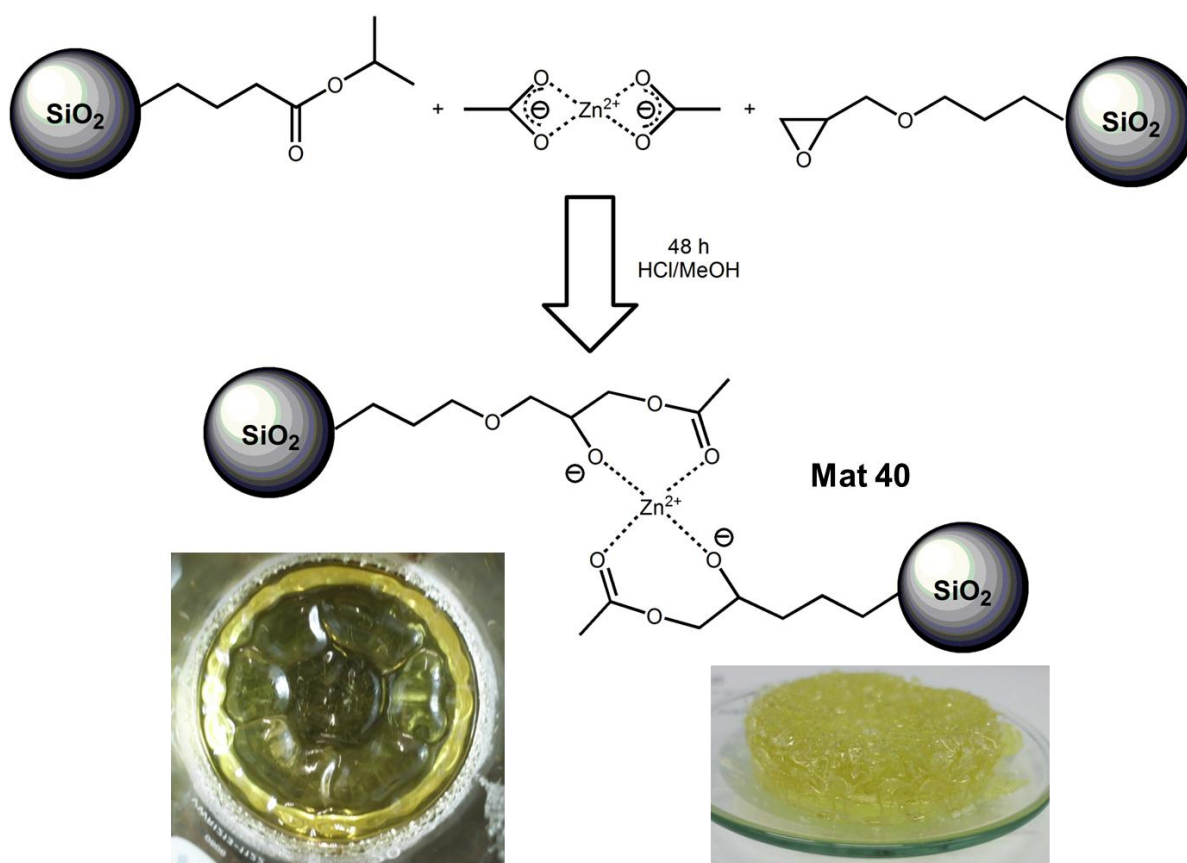


Figure 53 Synthesis of the vitrimer-type silica nanoparticle network and digital photos of the obtained material (**Mat 40**).

The SAXS spectrum showed two less distinct peaks at about $q = 5 \text{ nm}^{-1}$ and at about $q = 15 \text{ nm}^{-1}$ (Figure 54). The first peak suggests a short range order in the material, whereas the second peak is evidence for the amorphous character of **Mat 40**. Unfortunately, fitting of the SAXS curve was again not possible.

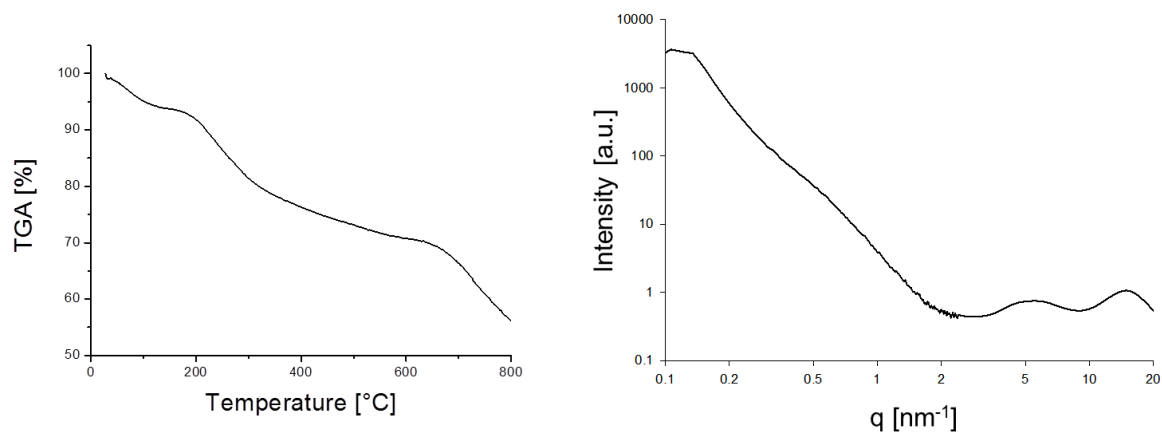


Figure 54 (left) TG analysis of **Mat 40**, (right) SAXS spectrum of **Mat 40**.

The self-healing ability of the material was investigated by heating the fresh-powdered material up to 200 °C. For **Mat 40** no self-healing ability was observed. Only the color of the material turned from yellow to dark brown during heating, which indicates a decomposition of the material. The thermogravimetric analysis supports these first observations, while showing a mass loss of about 20 w% in a temperature range between 200 °C and 300 °C (Figure 54). Then a plateau in the temperature range between 300 °C and 700 °C with a mass loss of about 8 % can be observed, which can maybe be assigned to a transformation and removing of the inorganic zinc(II) species. However, at this stage it was not possible to get proof for this assumption.

In conclusion, two novel hybrid materials were synthesized by the transfer of principles from self-healing polymers to silica nanoparticle networks. Unfortunately, at this stage the materials showed no self-healing ability. It has to be highlighted that these results are preliminary results. Nevertheless, interesting precursor molecules as well as hybrid materials were synthesized. Especially on **Mat 40** further investigations will be necessary in the future, because of the great potential of this material in self-healing applications and because of the convenient synthesis pathway for this material.

4 Summary and Outlook

In the course of this work metal organic synthesis and material synthesis were combined to obtain novel ionic nanoparticle networks and to investigate the versatile properties of these hybrid materials. Especially the influences of different organic linking units between the metal oxide nanoparticles on the properties of the hybrid materials were investigated. The metal oxide nanoparticles, used in this work, were prepared by sol-gel processing. Afterwards, the surface of these silica nanoparticles was modified on the one hand with ω -propyltrimethoxysilane, where ω was a cyclic nitrogen base such as imidazole, pyrazole or pyridine, and on the other hand with 3-chloropropyltrimethoxysilane. Zinc oxide nanoparticles could be only modified by 3-chloropropyltrimethoxysilane, as they agglomerated by the modification with the nitrogen base terminated trimethoxysilanes. The synthesis of these ω -propyltrimethoxysilanes was usually a nucleophilic substitution between the nitrogen base and 3-iodopropyltrimethoxysilane. Additionally, a new approach for this synthesis was found by the metal catalyst free hydrosilylation followed by a methanolysis reaction to obtain the pyridinepropyltrimethoxysilanes. The final synthesis of the hybrid materials was a nucleophilic substitution between cyclic nitrogen base modified nanoparticles and chloroalkyl modified nanoparticles or chloromethylene (-CH₂Cl) disubstituted aromatic linkers resulting in a three-dimensional cross-linked nanoparticle network. The obtained hybrid materials showed a very versatile processing as they could be processed into self-standing films, monolithic gels or thin films by dip-coating them on a substrate, but they could also be processed into colorless powders. For future works, it will be very interesting to synthesize modified INN materials with improved physicochemical properties. One possibility to achieve this could be the elongation of the alkyl chain between the particles, which may cause an improved self-assembly of the organic moieties between the nanoparticles. In general, it will be interesting to place other aromatic ring systems, which are able to build ions, between the nanoparticles, like pyrrole or different substituted pyridines *etc.* An useful approach for the precursors of such new INN materials would be the hydrosilylation of vinyl group containing nitrogen bases with trimethoxysilane ((MeO)₃SiH).

To proof that indeed these INN materials were synthesized, numerous analytical methods, such as powder XRD after anion exchange, SEM, TEM and elemental analysis *etc.*, were executed. Furthermore, the high thermal stability, which had been reported before in works by Marco Litschauer,^[168] was reinforced and further investigated^[168] by TGA/MS measurements. Short Angle X-ray Scattering (SAXS) measurements were executed on the INN materials revealing a short range order in the material, which most likely is caused by π - π stacking interactions between the aromatic

rings in the material. In summary, it was difficult to analyze the INN materials, because of the amorphous character of the metal oxide nanoparticles, which disturbed the majority of the standard analysis techniques. Therefore, it will be interesting to find some more convenient analysis techniques in the future to get an even better understanding of the composition of this kind of hybrid materials.

The kinetics of the building reaction of the INN materials was also investigated by Quartz Crystal Microbalance (QCM) measurements at Linköping University (Sweden) under the supervision of Prof. Nathaniel D. Robinson. These measurements clearly suggest that the formation of the INN materials, with a reaction time of only 30 to 90 minutes, took less time than assumed before. Due to some complications these measurements took very long and could not be finished. In consequence the results of these measurements should be regarded as preliminary results. For a more precisely determination of the kinetics of the INN materials formation there will be a lot more QCM measurements necessary in the future.

For a deeper understanding of the interactions in the material as well as of the composition of the INN materials, solid state NMR measurements and *ab-initio* calculations by Christel Gervais and DFT calculations by Frederik Tielens at Sorbonne Université Paris were conducted. It turned out that the calculated and measured chemical shift for the respective NMR experiments were in good agreement. These measurements also confirmed the hypothesis of π - π stacking interactions between the aromatic rings in the INN materials. Additionally, a band gap of 3.17 eV was determined by DFT calculations.

On account of the calculated band gap, the electrical properties of the INN materials were also investigated at Linköping University (Sweden) under the supervision of Prof. Nathaniel D. Robinson. In the course of these investigations Field Effect Transistors (FETs), consisting of the INN material, were built. Unfortunately, only one sample was working once and many technical problems with the preparation of the transistors and the setup occurred during these measurements, suggesting that silica based INN materials are minor applicable for building FETs. Nevertheless, zinc oxide in general shows semiconducting properties and therefore the so-called mixed INN materials will be highly attractive for investigations of their electrical properties in the future.

The core of this work was the investigation on photoluminescence properties of the INN materials. For a systematic investigation the substituents on the C2 position of the imidazolium moiety as well as the aromatic linkers were varied. The photoluminescence properties as well as the SAXS profiles of mono- and bis-imidazolium based INN materials, with or without substituents on the C2 position, as well as the pyrazolium and pyridinium based INN were examined and compared. In summary,

these investigations showed exciting tunable photoluminescence features for the INN materials. The photoluminescence activity was caused by the self-organization of the aromatic rings in the material by π - π stacking interactions, as suggested by the SAXS measurements. Furthermore, the SAXS experiments revealed the impact of different substituted imidazoles in combination with various aromatic chloromethylene (-CH₂Cl) disubstituted linker molecules on the structure and thus on the optical properties of the INN materials. It has to be highlighted that for these INN materials intensive photoluminescence features were observed without using a chromophore for the synthesis of the hybrid materials. Taking this fact under consideration, it will be very interesting for the future to use different linker molecules to expand the range of emission wavelengths of the materials. Furthermore, the use of an anion, which is able to take part in the π - π stacking interactions of the aromatic rings between the silica nanoparticles, such as the cyclopentadienyl anion, will have a positive influence on the photoluminescence performance of the INN materials.

In the course of this work, the formation of transition metal chloro complexes by the reaction of metal chlorides, such as CuCl₂·2H₂O, EuCl₃·6H₂O and PdCl₂, with the chloride ions of the INN materials was also investigated. In the case of CuCl₂·2H₂O a green INN material, containing the tetrachlorocuprate(II) [CuCl₄]²⁻ complex, was formed. The green material showed an irreversible thermochromic behavior, which was observed by a color change from green to yellow at 180 °C, which corresponds to a configurational change of the tetrachlorocuprate(II) complex from a square planar to a tetrahedral configuration. This configurational change was proven by using *in situ* SAXS and DSC measurements. The europium and palladium containing materials did not show thermochromic behavior at all. Photoluminescence measurements were also executed on these materials. Thereby, it turned out that the presence of bivalent metal complex anions disturbs the photoluminescence activity of the INN materials. In the case of the europium containing material adjustable photoluminescence properties were observed. The complexation of metal chlorides within the three-dimensional network of the INN material in general opens the door for various applications of the resulting INN materials as catalysts, sensors or surface active materials. In consequence, other metal chlorides, which are able to form chloro complexes, should be tested for this reaction to investigate the properties of the resulting INN materials in the future. Due to the known thermochromic and catalytic properties of their chloro complexes, NiCl₂ and CoCl₂ will be extremely high promising for such investigations.

Depending on the fact that ionic liquids offer a high affinity to carbon dioxide and that they are known to catalyze the cycloaddition of CO₂ and epoxides to form cyclic carbonates efficiently, the INN materials were also tested as catalysts for this reaction by Jérôme Roeser and Prof. Arne Thomas at Technische Universität Berlin. It turned out that the INN materials are efficient heterogeneous catalysts for the conversion of CO₂ and different epoxides into organic cyclic carbonates. Reactions with epichlorohydrin showed that a quantitative conversion could be reached for all of the tested catalysts under relatively mild conditions. The catalysts could be easily recycled for at least four runs without a loss in conversion, but a decrease in selectivity was observed. Furthermore, it was observed that the catalytic activity of the INN materials does not depend on the used nanoparticle species. Additionally, Thibault Cantat and Enguerrand Blondiaux at CEA Saclay (France) performed catalytically tests with the INN materials on the metal-free reduction of CO₂ with hydroboranes to form methanol. Here, a significant catalytic activity of the INN materials was also observed. Depending on their high reaction surface, their relatively high load of catalytically active moieties, their easy recyclability and the possibility to complex metal chlorides within the three-dimensional network, the INN materials are extremely high promising for various catalytic applications as shown impressively by the reactions mentioned above. In consequence, the catalytic investigations on the INN materials, with or without complexed metals, should be continued.

Finally, first attempts on silica nanoparticle based self-healing materials were made. Therefore, two principles from self-healing polymers were transferred to silica nanoparticle networks. On the one hand, a dicyclopentadiene connected silica nanoparticle network and, on the other hand, a vitrimer type hybrid material was synthesized. Unfortunately, at this stage the materials did not show any self-healing ability. Nevertheless, very interesting precursor molecules as well as novel hybrid materials were synthesized. In the future, further investigations should be conducted especially on the vitrimer type material, because of the great potential of this material in self-healing applications and because of the convenient synthesis pathway of this material.

5 Experimental

5.1 Materials

All chemicals used for syntheses were obtained by commercial suppliers and were used as received. Solvents were purified by conventional methods and stored under argon over molecular sieve (3 or 4 Å). Methanol, THF and Toluene were dried by a commercial apparatus (PureSolv) comprising dynamic drying using molecular sieve. Reactions under an inert atmosphere were carried out by standard Schlenk technique or were executed in the glove box.

ABCR	3-Chloropropyltrimethoxysilane; 2-Chloroethyltrichlorosilane; Triethoxysilane, ((Chloromethyl)phenylethyl)trimethoxysilane; Karstedt-cat.; $\text{EuCl}_3 \cdot 6\text{H}_2\text{O}$; 9,10-Bis(chloromethyl)anthracene; 3,6-bis(chloromethyl)durene; 3-Glycidyloxypropyltrimethoxysilane
Acros	NaI ; Dicyclopentadiene; SOCl_2
Alfa Aesar	Imidazole
Fluka	Trimethoxysilane; Maleinimide; $\text{Ag}(\text{CH}_3\text{COO})$
J.T. Baker	$\text{Zn}(\text{CH}_3\text{COO})_2 \cdot 2\text{H}_2\text{O}$
Merck	Decaline
Precious Metals online	PdCl_2
Riedel de Haën	$\text{CuCl}_2 \cdot 2\text{H}_2\text{O}$; Sodium
Sigma Aldrich	α, α' -Dibromo- <i>p</i> -xylene; α, α' -Dichloro- <i>p</i> -xylene; HSiCl_3 ; 4-Vinylpyridine; 2-Vinylpyridine; 1-Methylimidazole; 2-Methylimidazole; 2-Isopropylimidazole; 1-Vinylimidazole; Benzimidazole; Pyrazole; 3,5-Dimethylpyrazole; NaBF_4 ; KPF_6 ; Acetonitrile; Allylbromide; 1,2,4-Triazole; 4,4'-Bis(chloromethyl)-1,1'-biphenyl; 4,4'-Bipyridine; 1-Bromo-4-chlorobutane; Lithium; AgNO_3 ; 1,6-Dibromohexane
Sikemia	6-Chlorohexyltrimethoxysilane

5.2 Analysis Techniques

Nuclear magnetic resonance (NMR) spectroscopy

^1H and ^{13}C solution NMR spectra were recorded on a Bruker AVANCE 250 (250.13 MHz [^1H], 62.86 MHz [^{13}C]) equipped with a 5-mm inverse-broadband probe head and a z-gradient unit. The NMR spectra for 2- and 4-(2-trimethoxysilylethyl)pyridine were recorded on a Bruker Avance III Ultrashield Plus at TU Bergakademie Freiberg (500.13 MHz [^1H], 125.76 MHz [^{13}C] and 99.36 MHz [^{29}Si]).

Solid state NMR

The spectra were recorded on a Bruker AVANCE 300 (^{13}C at 75.40 MHz, ^{15}N at 30.38 MHz) equipped with a 4 mm broadband MAS probe head. The spectra were recorded with ramped CP MAS experiments. (Cross Polarization and Magic Angle Spinning). The sample holders were spun at 6 KHz for the ^{15}N and ^{13}C experiments. For **Mat 30** and **Mat 31** solid state NMR measurements were executed at Sorbonne Universite Paris: ^{13}C and ^{15}N CP MAS NMR spectra of BF_4^- imidazolium salt were recorded at 75.51 MHz and 30.44 MHz, respectively, on a Bruker AVANCE 300 spectrometer (7.0 T) using 7 mm Bruker probes and spinning frequencies of 5 kHz. Single-pulse ^{19}F MAS NMR experiments were performed on a 850 (20.0 T) Bruker spectrometer. 2D ^1H -X (X = ^{11}B , ^{31}P) HETCOR CP MAS NMR were performed on a Bruker AVANCE III 700 spectrometer at $B_0 = 16.4$ T, with $\nu_0(^{11}\text{B}) = 224.66$ MHz and $\nu_0(^{31}\text{P}) = 283.46$ MHz with respectively a 1.3mm double resonance and a 3.2 mm triple resonance Bruker MAS probe.

Raman spectroscopy

The samples were placed on a glass slide on the microscope (Olympus BX 51) to adjust the laser on the sample surface. The used instrument was a Horiba LabRam HR with a He-Ne laser (632.8 nm) with a source power of 25 mW. The spectral resolution was about 2-4 cm^{-1} using a 300 gr/mm grating.

Small and Wide Angle X-ray Scattering (SAXS/WAXS)

Small and wide angle X-ray scattering experiments were performed at a laboratory X-ray source (Nanostar, Bruker AXS) using a rotating anode generator. Cu K_α radiation was monochromatized and collimated by crossed Göbel mirrors and a pinhole system. The X-ray patterns were recorded with a position sensitive area detector (VÅNTEC 2000) and radially averaged to obtain the scattering

intensity in dependence on the scattering vector $q = (4\pi/\lambda) \sin\theta$, with 2θ being the scattering angle and $\lambda=0.1542$ nm the X-ray wavelength. SAXS and WAXS measurements were carried out at a sample to detector distance of 108 cm and 13 cm respectively. The integrated scattering data were merged together leading to a scattering curve ranging from 0.1 to 20 nm⁻¹. For the temperature dependent investigations the samples were measured from room temperature up to 200°C in 5°C steps. Each measurement lasted 900 seconds and the heating rate was < 2°C/min.

X-ray powder diffraction

The samples were measured on a Panalytical X'Pert Pro diffractometer with Bragg-Brentano geometry and Cu K_α 1,2 radiation (1.54060 Å, 1.54439 Å). Reflections were detected either with an X'Celerator multi-channel detector with 2.546° scan length or a MINI-PROP counting tube. Data was usually collected in the 2θ range 5 – 67° in 15 minutes with rotation of 4s/U. The data was evaluated using X'Pert software package (PANalytical 2009).

Thermogravimetric analysis (TGA)

The analyses were carried out with a NETZSCH TG 209 at heating rates of 10 K min⁻¹ under synthetic air.

Simultaneous Thermoanalysis and mass spectrometry (TGA/DTA/MS)

Thermoanalytical measurements were performed with a Netzsch Jupiter 449C (DTA/TG sensor: Pt/PtRh-thermocouple) coupled with a Quadrupole Mass Spectrometer Aeolos (Netzsch). The measurements were carried out in an aluminium oxide crucible under argon with a heating rate of 10 K min⁻¹.

Differential Scanning Calorimetry (DSC)

For the analysis, on a Mettler Toledo DSC 823e, few milligrams of sample were sealed in an aluminium crucible under nitrogen atmosphere. For the thermochromic samples the temperature program was recorded at a speed of 5K min⁻¹ and consisted in a first heating phase from room temperature to 250°C, followed by a cooling phase from 250 °C to room temperature.

Dynamic Light Scattering (DLS)

For the measurement, the nanoparticles were suspended in ethanol. The DLS experiments were carried out without previous sonication of the samples. The run time of each single measurement was 10 seconds. Every size distribution curve is obtained by averaging 5 measurements. The apparatus was an ALV/CGS-3 compact goniometer system, equipped with an ALV/LSE-5003 light scattering electronics and multiple τ digital correlator, and a 632,8nm JDSU laser 1145P.

Fluorescence and Quantum Yield

These measurements were carried out on an Edinburgh Instruments spectrometer (FSP 920) with a xenon arc lamp and double grating monochromators. The INN materials were measured in solid state. The excitation as well as the emission spectra were recorded with a slit width of 1.0 nm. The dwell time was adjusted to 0.5 s and the recording steps were 0.5 nm. For each spectrum three scans were executed. The quantum yield measurements were executed by using a photomultiplier tube equipped with a barium sulfate coated integration sphere (150 mm internal diameter). All Spectra were recorded at room temperature with excitation and emission slit widths of 3.0 nm. The dwell time was of 0.5 s and the recording steps were 0.2 nm. For each spectrum three scans were executed. The quantum yield was calculated by dividing the number of emitted photons by the number of absorbed photons. The number of absorbed photons was determined from the decrease of the scattered excitation light intensity compared to the measured intensity with an empty SUPRASIL glass cuvette. The spectra were corrected for system specific effects such as the detector sensitivity, monochromator efficiency and the BaSO₄ coating. The spectral distribution of the lamp intensity was corrected by using a Si photodiode reference detector.

Elemental Analysis

Elemental analysis was carried out on a 2400 CHN Elemental Analyzer by Perkin Elmer at the Microanalytical Laboratory at the University of Vienna.

Scanning Electron Microscopy (SEM)

SEM images were recorded on a JEOL-6400 Scanning Electron Microscope with a tungsten filament.

Transmission Electron Microscopy (TEM)

TEM images were recorded on a FEI TECNAI F20 high resolution transmission electron microscope (USTEM, Vienna University of Technology). The samples were prepared by suspending the hybrid material in ethanol and place one drop on a commercial available carbon coated copper TEM grid.

Quartz Crystal Microbalance (QCM)

The QCM used, was an E4-system (Q-Sense AB, Sweden) with a flow module with an internal volume of 140 μ l (flow channel = 100 μ l, above sensor crystal = 40 μ l). The sensors were quartz crystals (QSX 303, 5 MHz). After the washing procedure the quartz crystals were dried with N₂, placed in the flow cell and the resonant frequencies for the odd overtones between the 1st and 11th harmonic of the crystal were obtained (the sensor was removed and replaced a couple of times to get the error variation). Then the crystals were measured while pumping dry methanol through the flow cell. This was followed by an *ex situ* silanization of the crystals with the respective N-(3-propyltrimethoxysilane)imidazole. Afterwards the crystals were measured dry again to get the mass of bonded silane. Then two different types of reactions were carried out: on the one hand a methanolic chloropropyl modified silica nanoparticle solution was added (pumping in circle with a peristaltic pump) on the other hand a methanolic solution of a linker molecule was added. After completing the reaction, methanol was applied on the crystals again to remove some non-bonded reactants. Then the crystals were dried and measured again to get the mass of deposited material.

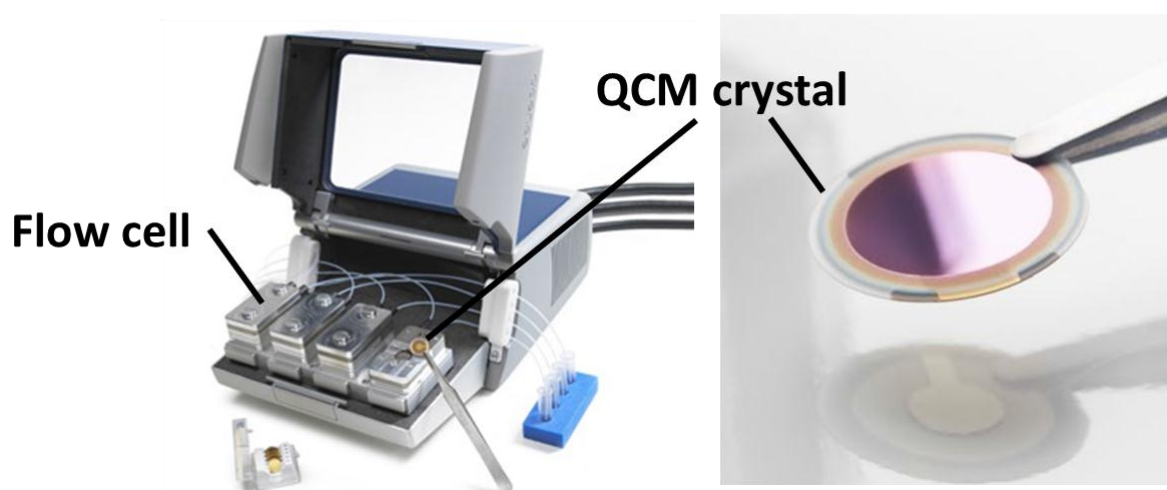


Figure 55 (left) principle composition of the QCM measurement, (right) enlarged QCM crystal (pictures from www.q-sense.com)

Preparation of the patterned ITO substrates for transistor measurements (dip coating)

The patterned ITO substrates are commercially available from Ossilia. Before dip coating the substrates were cleaned with acetone and fiber-free tissues. The coatings were applied via dip coating of a methanolic solution of the respective material on the substrate at a constant withdrawal speed of 24 cm/min and dried at the air at room temperature. The dielectric layer was placed on the previously prepared patterned ITO substrates by spray coating. For this procedure polyvinylphenol (PVPh) was solved in ethylacetate or methanol (alternatively: polymethylmethacrylate (PMMA) in ethylacetate) was spray coated by an airbrush gun on the INN materials surface by using a T-shaped mask on the material (in each case a 10 w% solution of the polymer was used). Then this polymer layer was dried at 70°C for 2 hours. After drying the dielectric layer, the gate electrode material (PEDOT = Poly-3,4-ethylendioxythiophen) was painted on the dielectric layer by using the T shaped mask again.

Transistor measurements

The measurements were carried out with an “old” and a “new” setup (see figure). The drain and gate current/voltage were measured with a Keithley digital multimeter.

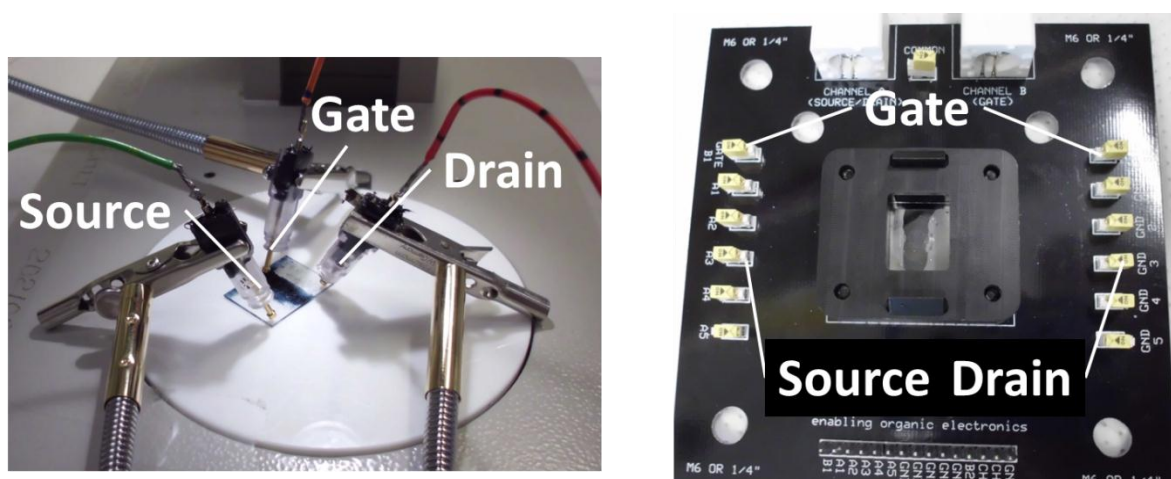


Figure 56 (left) “old” transistor setup, (right) “new” transistor setup

DFT Calculations

Computational details:

The DFT and *ab-initio* calculations were executed by Christel Gervais and Frederick Tielens at Sorbonne Université Paris. All geometry optimizations are performed using *ab initio* plane-wave pseudopotential approach as implemented in VASP.^[305,306] The Perdew-Burke-Ernzerhof (PBE)

functional^[307,308] has been chosen to perform the periodic DFT calculations with an accuracy on the overall convergence tested elsewhere.^[309,310] The valence electrons are treated explicitly and their interactions with the ionic cores are described by the Projector Augmented-Wave method (PAW),^[311,312] which allows to use a low energy cut off equal to 500 eV for the plane-wave basis. The Gamma point is used in the Brillouin-zone integration. The positions of all the atoms in the super cell are relaxed until the total energy differences decrease below 10^{-4} eV. The atom positions as well as the unit cell have been relaxed.

To explore and find the minima on the potential energy surface of the system we performed, initially, *ab initio* MD study within the micro-canonical ensemble in the microcanonical (NVE) approach, at T = 400 K, to scan the possible conformations of the system. We considered several starting conformations (but no statistics was performed on them) and the run was stopped after $t \geq 2$ ps. The local minima found from MD results were systematically re-optimized at 0 K, in order to achieve the absolute electronic minimum energy for each configuration.

The first principles NMR calculations were performed within Kohn-Sham DFT using the QUANTUM-ESPRESSO software.^[313] The PBE generalized gradient approximation was used and the valence electrons were described by norm conserving pseudopotentials^[314] in the Kleinman-Bylander form.^[315] The core definition for B, C, N, O and F is $1s^2$ and $1s^2 2s^2 2p^6$ for Si and P. The wave functions are expanded on a plane wave basis set with a kinetic energy cut-off of 1088 eV. The integral over the first Brillouin zone are performed using a Monkhorst-Pack $1 \times 1 \times 1$ k-point grid ($2 \times 2 \times 2$ in the case of BF_4^- and PF_6^- crystalline imidazolium salts) for the charge density and chemical shift tensor calculation. The shielding tensor is computed using the GIPAW^[316] approach, which permits the reproduction of the results of a fully converged all-electron calculation. The isotropic chemical shift δ_{iso} is defined as $\delta_{\text{iso}} = -[\sigma - \sigma^{\text{ref}}]$, where σ is the isotropic shielding and σ^{ref} is the isotropic shielding of the same nucleus in a reference system as previously described for ^1H , ^{11}B , ^{13}C , ^{15}N .²⁹⁻³² For ^{31}P and ^{19}F , BF_4^- and PF_6^- crystalline imidazolium salts were used as references.

Model description

Imidazolium salts containing BF_4^- and PF_6^- as the counter ion were investigated in crystalline bulk state. The crystal structure information, obtained after geometry optimization, was used as reference data in geometrical analysis and NMR shift calculations. The unit cell parameters optimized at the same level of calculation as for the silica model (using PBE) are: $a = 5.091 \text{ \AA}$, $b = 12.998 \text{ \AA}$, $c = 15.469 \text{ \AA}$, $\alpha = \gamma = 90^\circ$, $\beta = 92.818^\circ$, and $a = 6.166 \text{ \AA}$, $b = 13.437 \text{ \AA}$, $c = 15.361 \text{ \AA}$, $\alpha = \gamma = 90^\circ$, $\beta = 91,344^\circ$, for BF_4^- and PF_6^- , respectively.

For the silica model a hydroxylated structure was described and characterized in a previous work,^[317] and has already been used in the study of vanadium oxide,^[318] chromium oxide,^[319] and gold^[310] grafted on silica, but also in the study of the adsorption of bio-organic molecules on silica.^[320,321] The model consists of a silica slab (dimensions $12.77 \times 17.64 \times 25.17 \text{ \AA}^3$) made of 120 atoms ($\text{Si}_{27}\text{O}_{54}\cdot 13\text{H}_2\text{O}$) which enables to model a correct representation of a hydrated silica surface. This model accounts for the experimentally encountered ring size distribution, Si-O-Si and O-Si-O angles, silanols density and repartition (isolated, associated, geminals).^[322,323]

The vacuum between the silica slab structures was filled with 1,3-dipropylimidazolium bridging ligands with a density between 0.7 – 1.3 per nm^2 . It was assumed that all ligands have reacted. The z-coordinate was adjusted in order to fit the chains precisely *i.e.* $\pm 12.5 \text{ \AA}$. These ligands were grafted on Si-OH positions on both sides of the slab, forming slab-Si-(Im)-Si-slab linkages. The silane moieties are tri-coordinately grafted in the model. Different types of counter ions (Cl^- , BF_4^- , and PF_6^-) were introduced as well as different amounts of water molecules, the latter in order to investigate the effect of hydration of the system. In order to model the effect of 1,3-dipropylimidazolium chain density two types of models were built: one containing 3 chains and another containing 5 on the hydrated silica slab, which has a surface of 4.51 nm^2 . The chain densities correspond thus to 0.66 and 1.11 ligands per nm^2 , respectively. In the hydrated model, the same number of water molecules were introduced as silanol groups left on the surface (*i.e.* 14 - 10).

Catalytic tests

The catalytic tests were executed by Jérôme Roeser and Prof. Arne Thomas at the Technische Universität Berlin. The quantitative analysis was conducted by GC-MS, for which an Agilent Technologies 7890A GC system running with an HP-5MS capillary column and an Agilent Technologies 5975C mass selective detector were employed with a known amount of toluene as an external standard. Solution NMR spectra were recorded on a Bruker Avance 300 (^1H at 300.13 MHz and ^{13}C at 75.40 MHz) equipped with a 5 mm inverse-broadband probe head with a z gradient unit. ^{13}C spectra were recorded with ramped CP/MAS spectra.

For the catalytic test itself the reactor setup consisted of a 100 mL stainless steel Berghof BR-100 high pressure reactor with simple heating and stirrer using a standard laboratory heating plate. The reactor was fitted with a Teflon insert, a pressure indicator, a temperature probe submersion tube to measure the internal reactor temperature, a pressure relief valve and a metal rupture disk to safely limit the maximum pressure. In a typical reaction, 100 mg of catalyst and 18 mmol of epichlorohydrin were charged in a 100 mL Teflon insert. The reactor was sealed and flushed 5 times at room temperature with CO_2 to remove the air from the vessel. The pressure was adjusted to 6.9

bar and the reactor was heated to 130 °C. After 4 hours reaction time, the reactor was cooled to room temperature and the pressure was released. The collected sample was centrifuged, filtered and analyzed by GC-MS. To ensure reliability of the GC-MS analysis, the activities were also evaluated by ^1H NMR spectroscopy, for which concordant results were systematically obtained.

Digital photos

Digital photos were made using a Medion Life P44016 MD 86535.

5.3 Syntheses

5.3.1 Nanoparticle Syntheses

SiO₂ Nanoparticles

In a 250 mL round bottom flask, 60 μl (0.01 mol) ammonia solution (32 %) and 1.98 g (0.11 mol) water were added to 100 mL of absolute methanol. 10.41 g (0,05mol) Tetraethoxysilane were added dropwise under stirring. The solution was stirred for three days at room temperature. The resulting silica nanoparticles had an average hydrodynamic diameter of 16 nm (DLS).

ZnO Nanoparticles ^[159]

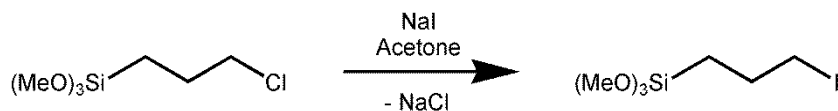
In a 250 mL round bottom flask 2.2 g (0.01 mol) $\text{Zn}(\text{CH}_3\text{COO})_2 \cdot 2\text{H}_2\text{O}$ were dissolved in 150 mL ethanol by stirring at 80°C for 30 minutes. Afterwards the solution was cooled for 5 minutes in an ice bath. Then 0.68 g (0.017 mol) sodium hydroxide were dissolved in 40 mL ethanol. This solution was added dropwise by cooling with an icebath to the zinc acetate solution. The final solution was stirred for 48 hours at room temperature. The resulting zinc oxide nanoparticles had an average diameter of 6 nm (DLS).

5.3.2 Syntheses of different functionalized trimethoxysilanes

Synthesis of 3-iodopropyltrimethoxysilane

The synthesis was carried out under argon atmosphere. Sodium iodide (36.9 g, 0.246 mol) was dissolved in 150 mL absolute acetone. 3-chloropropyltrimethoxysilane (48.9 g, 0.246 mol) was added dropwise under stirring. The mixture was refluxed under stirring overnight. The precipitated sodium chloride was filtered off under argon atmosphere. The solvent was removed in vacuum.

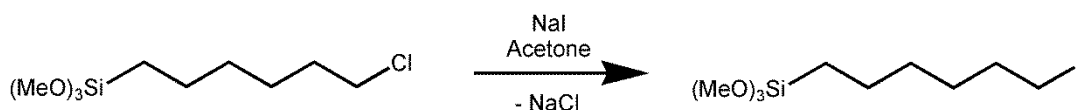
Then the product was distilled at 52 °C under vacuum conditions (1 mbar) with a yield of 96 %. The resulting 3-iodopropyltrimethoxysilane was a yellowish liquid.



^1H NMR (250 MHz, CDCl_3): δ [ppm] 3.58 (s, 9H, $\text{Si}(\text{OCH}_3)_3$); 3.22 (t, 2H, I- CH_2 -); 1.93 (q, 2H, I- CH_2 - CH_2 - CH_2 -); 0.75 (t, 2H, - CH_2 -Si).

Synthesis of 6-iodohexyltrimethoxysilane

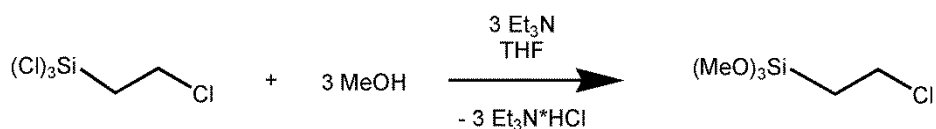
The synthesis was carried out under argon atmosphere. Sodium iodide (36.9 g, 0.246 mol) was dissolved in 150 mL absolute acetone. 3-chloropropyltrimethoxysilane (48.9 g, 0.246 mol) was added dropwise under stirring. The mixture was refluxed under stirring overnight. The precipitated sodium chloride was filtered off under argon atmosphere. The solvent was removed in vacuum. The crude product was washed with 100 mL THF and a colorless solid precipitated again. The precipitate was filtered off and the THF was removed under vacuum conditions. Due to the fact that the product is hard to purify by distillation and that there is no possibility for column chromatography, no further purification steps were carried out. The synthesis resulted in a brownish liquid with a yield of 62%.



^1H NMR (250 MHz, CDCl_3): δ [ppm] 3.62 (s, 9H, $\text{Si}(\text{OCH}_3)_3$); 3.28 (t, 2H, I- CH_2 -); 1.88 (q, 2H, I- CH_2 - CH_2 - CH_2 -); 1.48 (very broad signal, 6H, - CH_2 - CH_2 - CH_2 - CH_2 -Si); 0.75 (t, 2H, - CH_2 -Si).

Synthesis of 2-chloroethyltrimethoxysilane

The synthesis was carried out under argon atmosphere. 9.9 g (50 mmol) 2-chloroethyltrichlorosilane were dissolved in dry tetrahydrofuran (150 mL). Then the reaction mixture was cooled to approximately 0 °C with an ice bath and 15.2 g (150 mmol) triethylamine and 30 ml of dry methanol were added dropwise. The obtained colorless precipitate was filtered off under argon and the solvent was removed under vacuum conditions. For purification the crude product was distilled at 42 °C in vacuum (1 mbar). 2-chloroethyltrimethoxysilane was obtained with a yield of 95 % as a colorless and transparent liquid.



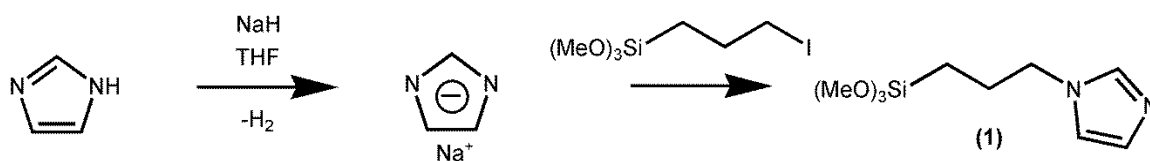
^1H NMR (250 MHz, CDCl_3): δ [ppm] 3.77 (t, 2H, $\text{Cl}-\text{CH}_2-$); 3.67 (s, 9H, $\text{Si}(\text{OCH}_3)_3$); 1.41 (t, 2H, $\text{Cl}-\text{CH}_2-\text{CH}_2-$).

^{13}C NMR (250 MHz, CDCl_3): δ [ppm] 50.4 ($-\text{Si}(\text{OCH}_3)_3$); 40.9 (CH_2-Cl), 16.1 ($\text{Si}-\text{CH}_2$).

Synthesis of N-(3-propyltrimethoxysilane)imidazole (1), N-(3-propyltrimethoxysilane)-2-methylimidazole (2) and N-(3-propyltrimethoxysilane)-2-isopropylimidazole (3)

The synthesis was carried out under argon atmosphere. Sodium hydride (2.9 g, 0.12 mol) was dissolved in 150 mL absolute THF, the mixture is cooled to approximately 0°C with an ice bath. 0.12 mol of the respective imidazole [(**1**) = 8.3 g, (**2**) = 9.8 g, (**3**) = 13.2 g] was added portionwise under stirring. After completely adding the respective imidazole, the ice bath was removed and the mixture was maintained under stirring until no more hydrogen gas is evacuated. Then 23.12 g (0.09 mol) of 3-iodopropyltrimethoxysilane were added and the mixture was maintained at reflux overnight. The orange suspension was filtered off and the solvent was removed under vacuum conditions. By addition of 150 mL absolute dichloromethane a colorless precipitate appeared and was filtered off under argon atmosphere. For purification the crude product was distilled under vacuum conditions.

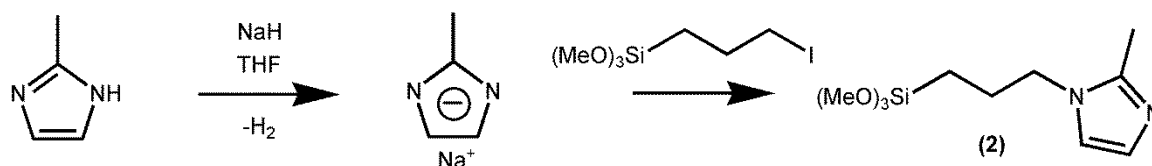
Compound (**1**) was distilled at 105°C in vacuum (1 mbar). N-(3-propyltrimethoxysilane)imidazole was obtained with a yield of 89 % as a colorless and transparent liquid.



^1H NMR (250 MHz, CDCl_3): δ [ppm] 7.54 (s, 1H, $-\text{N}-\text{CH}-\text{N}-$); 7.01 (s, 1H, $-\text{N}-\text{CH}-\text{CH}-\text{N}=\text{}$); 6.88 (s, 1H, $-\text{N}-\text{CH}-\text{CH}-\text{N}=\text{}$); 3.88 (t, 2H, $=\text{N}-\text{CH}_2-\text{CH}_2-$); 3.53 (s, 9H, $\text{Si}(\text{OCH}_3)_3$); 1.83 (q, 2H, $=\text{N}-\text{CH}_2-\text{CH}_2-\text{CH}_2-\text{Si}$), 0.54 (t, 2H, $-\text{CH}_2-\text{Si}$).

^{13}C NMR (250 MHz, CDCl_3): δ [ppm] 136.8 ($-\text{N}-\text{CH}-\text{N}-$); 128.1 ($-\text{N}-\text{CH}-\text{CH}-\text{N}=\text{}$), 120.7 ($-\text{N}-\text{CH}-\text{CH}-\text{N}=\text{}$), 56.2 ($-\text{Si}(\text{OCH}_3)_3$), 55.7 ($=\text{N}-\text{CH}_2-\text{CH}_2-$), 25.1 ($=\text{N}-\text{CH}_2-\text{CH}_2-\text{CH}_2-\text{Si}$), 7.4 ($-\text{CH}_2-\text{Si}$).

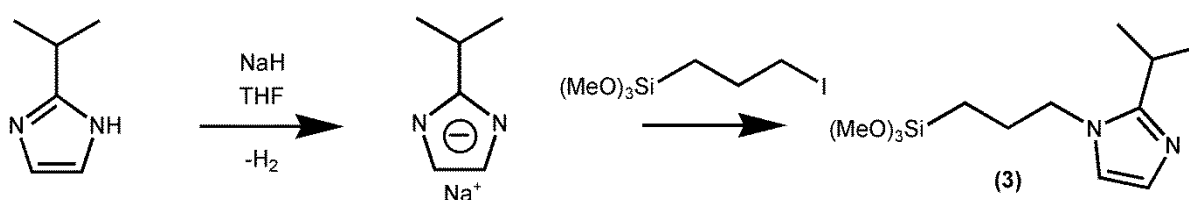
Compound (**2**) was distilled at 107°C in vacuum (1 mbar). N-(3-propyltrimethoxysilane)-2-methylimidazole was obtained with a yield of 78 % as a colorless and transparent liquid.



¹H NMR (250 MHz, CDCl₃): δ [ppm] 6.78 (s, 1H, -N-CH-CH-N=); 6.71 (s, 1H, -N-CH-CH-N=); 3.71 (t, 2H, =N-CH₂-CH₂-); 3.46 (s, 9H, Si(OCH₃)₃); 2.26 (s, 3H, -N-C-CH₃); 1.72 (q, 2H, =N-CH₂-CH₂-CH₂-Si), 0.49 (t, 2H, -CH₂-Si).

¹³C NMR (250 MHz, CDCl₃): δ [ppm] 144.2 (-N-C(CH₃)-N-); 126.8 (-N-CH-CH-N=), 119.0 (-N-CH-CH-N=), 50.5 (-Si(OCH₃)₃), 48.0 (=N-CH₂-CH₂-), 24.1 (=N-CH₂-CH₂-CH₂-Si), 12.8 (-CH₂-Si), 6.0 (-N-C-CH₃).

Compound **(3)** was distilled at 138 °C in vacuum (1 mbar). N-(3-propyltrimethoxysilane)-2-isopropylimidazole was obtained with a yield of 76 % as a colorless and transparent liquid.



¹H NMR (250 MHz, CDCl₃): δ [ppm] 7.04 (d, 1H, -N-CH-CH-N=); 6.88 (d, 1H, -N-CH-CH-N=); 3.95 (t, 2H, =N-CH₂-CH₂-); 3.67 (s, 9H, Si(OCH₃)₃); 3.09 (m, 1H, -N-C-CH); 1.95 (q, 2H, =N-CH₂-CH₂-CH₂-Si); 1.44 (d, 6H, CH₃-CH-CH₃); 0.72 (t, 2H, -CH₂-Si).

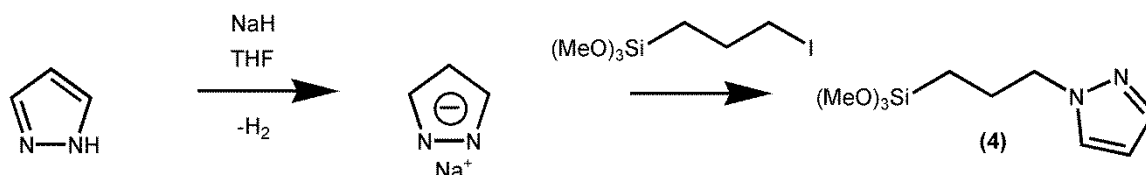
¹³C NMR (250 MHz, CDCl₃): δ [ppm] 152.7 (-N-C(CH)-N-); 126.9 (-N-CH-CH-N=), 118.4 (-N-CH-CH-N=), 50.5 (-Si(OCH₃)₃), 47.4 (=N-CH₂-CH₂-), 25.7 (CH-(CH₃)₂), 24.6 (=N-CH₂-CH₂-CH₂-Si), 21.8 (CH-(CH₃)₂), 6.1 (-CH₂-Si).

Synthesis of N-(3-propyltrimethoxysilane)pyrazole **(4)** and N-(3-propyltrimethoxysilane)-3,5-dimethylpyrazole **(5)**

The synthesis was carried out under argon atmosphere. Sodium hydride (2.9 g, 0.12 mol) was dissolved in 150 mL absolute THF, the mixture was cooled to approximately 0 °C with an ice bath. 0.12 mol of the respective pyrazole [**(4)** = 8.3 g, **(5)** = 11.5g] was added portionwise under stirring. After completely adding the respective pyrazole, the ice bath was removed and the mixture was maintained under stirring until no more hydrogen gas was evacuated. Then 23.12 g (0.09 mol) of 3-iodopropyltrimethoxysilane were added and the mixture was maintained at reflux overnight. The slightly yellow suspension was filtered off and the solvent was removed under vacuum conditions. By addition of 150 mL absolute dichloromethane a colorless precipitate appeared and was filtered

off under argon atmosphere. For purification the crude product was distilled under vacuum conditions.

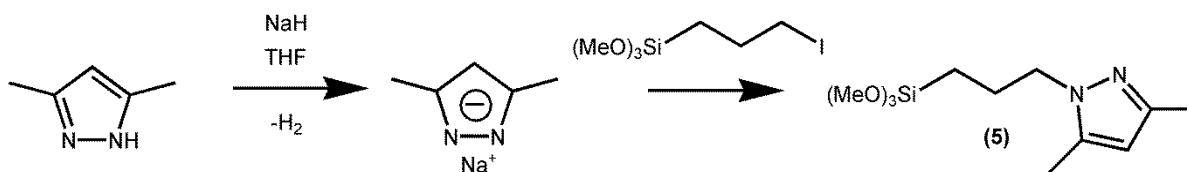
Compound **(4)** was distilled at 91 °C in vacuum (1 mbar). N-(3-propyltrimethoxysilane)pyrazole was obtained with a yield of 82 % as a colorless and transparent liquid.



¹H NMR (250 MHz, CDCl₃): δ [ppm] 7.60 (d, 1H, CH₂-N-CH-CH-CH-); 7.48 (d, 1H, CH₂-N-CH-CH-CH-); 6.33 (t, 1H, CH₂-N-CH-CH-CH-); 4.22 (t, 2H, =N-CH₂-CH₂-); 3.65 (s, 9H, Si(OCH₃)₃); 2.08 (q, 2H, =N-CH₂-CH₂-CH₂-Si), 0.72 (t, 2H, -CH₂-Si).

¹³C NMR (250 MHz, CDCl₃): δ [ppm] 140.0 (CH₂-N-CH-CH-CH-); 129.0 (CH₂-N-CH-CH-CH-), 105.0 (CH₂-N-CH-CH-CH-), 54.1 (=N-CH₂-CH₂-), 50.4 (-Si(OCH₃)₃), 23.8 (=N-CH₂-CH₂-), 6.0 (-CH₂-Si).

Compound **(5)** was distilled at 119 °C in vacuum (1 mbar). N-(3-propyltrimethoxysilane)-3,5-dimethylpyrazole was obtained with a yield of 63 % as a colorless and transparent liquid.



¹H NMR (250 MHz, CDCl₃): δ [ppm] 5.85 (s, 1H, CH₂-N-C-CH-); 4.02 (t, 2H, =N-CH₂-CH₂-); 3.64 (s, 9H, Si(OCH₃)₃); 2.30 (d, 6H, -N-C-CH₃), 1.99 (q, 2H, =N-CH₂-CH₂-CH₂-Si), 0.70 (t, 2H, -CH₂-Si).

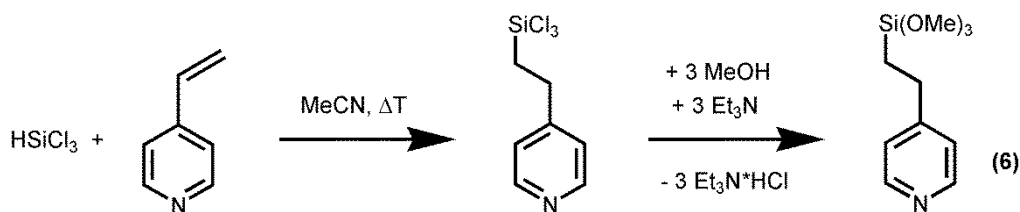
¹³C NMR (250 MHz, CDCl₃): δ [ppm] 146.9 (CH₂-N-C-CH-C-); 138.4 (CH₂-N-C-CH-C-), 104.6 (CH₂-N-C-CH-C-), 50.7 (=N-CH₂-CH₂-), 50.4 (-Si(OCH₃)₃), 23.7 (=N-CH₂-CH₂-), 13.3 (CH₂-N-C-CH₃), 10.8 (CH₂-N-N-C-CH₃), 6.0 (-CH₂-Si).

Synthesis of 4-(2-trimethoxysilylethyl)pyridine (**6**) and 2-(2-trimethoxysilylethyl)pyridine (**7**)

The synthesis was carried out under argon atmosphere. 10.84 g (80 mmol) trichlorosilane were dissolved in dry acetonitrile (250 mL) and 8.41 g (80 mmol) 4-vinylpyridine or 2-vinylpyridine were added dropwise under stirring at room temperature. After completely adding the vinylpyridine the reaction mixture was refluxed for two hours. After cooling to ambient temperature a yellowish solution was obtained. Then the mixture was cooled to approximately 0 °C and 24.3 g (0.24 mol) dry triethylamine and 25 mL dry methanol were added. The obtained colorless precipitate was filtered off under argon and the solvent was removed under vacuum conditions. The crude product was

washed with 150 mL THF and a colorless solid precipitated again. The precipitate was filtered off and the solvent was removed under vacuum conditions. For purification the crude product was distilled under vacuum conditions.

Compound **(6)** was distilled at 111 °C in vacuum (1 mbar). 4-(2-trimethoxysilylethyl)pyridine was obtained with a yield of 75 % as a colorless and transparent liquid.



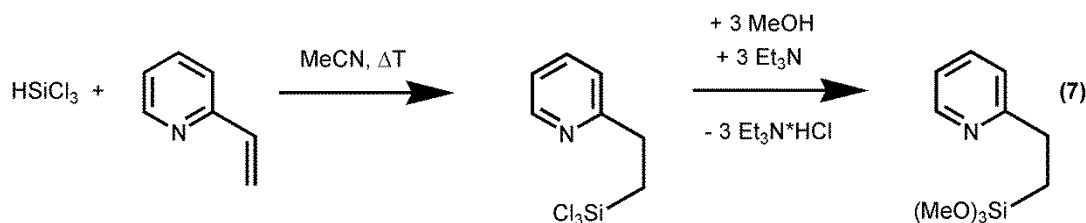
^1H NMR (500 MHz, CDCl_3): δ [ppm] 7.97 (d, 2H, N-CH-CH-), 6.62 (d, 2H, N-CH-CH-), 3.04 (s, 9H, Si-(OCH₃)₃), 2.20 (d-t, 2H, Si-CH₂-CH₂-), 0.45 (d-t, 2H, Si-CH₂-CH₂-).

^{13}C NMR (500 MHz, CDCl_3): δ [ppm] 152.2 (N-CH-CH-C-), 148.6 (N-CH-CH-), 122.3 (N-CH-CH-), 49.3 (Si-(OCH₃)₃), 27.2 (Si-CH₂-CH₂-), 9.2 (Si-CH₂-CH₂-).

^{29}Si NMR (IGATED, 500 MHz, CDCl_3): δ [ppm] -44.4 (Si-(OCH₃)₃).

This hydrosilylation reaction was also tried with the Karstedt catalyst, but this resulted in a yield of only 5 %.

Compound **(7)** was distilled at 106 °C in vacuum (1 mbar). 2-(2-trimethoxysilylethyl)pyridine was obtained with a yield of 33 % as a colorless and transparent liquid.



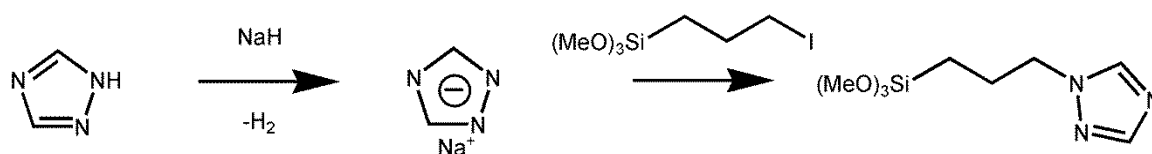
^1H NMR (500 MHz, CDCl_3): δ [ppm] 8.06 (d, 1H, N-CH-CH-), 7.11 (t, 1H, N-CH-CH-CH-), 6.70 (d, 1H, N-C-CH-), 6.62 (t, 1H, N-CH-CH-), 3.10 (s, 9H, Si-(OCH₃)₃), 2.44 (d-t, 2H, Si-CH₂-CH₂-), 0.68 (d-t, 2H, Si-CH₂-CH₂-).

^{13}C NMR (500 MHz, CDCl_3): δ [ppm] 162.5 (N-C-CH-), 148.2 (N-CH-CH-CH), 135.3 (N-CH-CH-CH-), 121.2 (N-C-CH-), 119.8 (N-CH-CH-), 49.3 (Si-(OCH₃)₃), 30.2 (Si-CH₂-CH₂-), 8.41 (Si-CH₂-CH₂-).

^{29}Si NMR (IGATED, 500 MHz, CDCl_3): δ [ppm] -43.2 (Si-(OCH₃)₃).

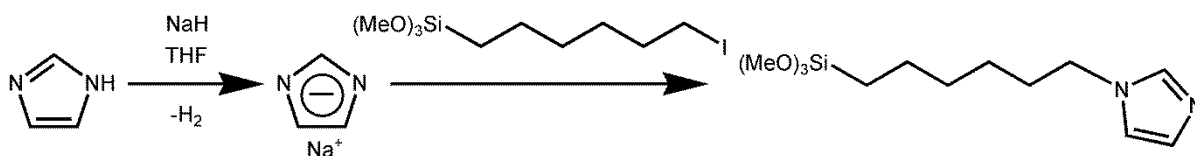
Synthesis of *N*-(3-propyltrimethoxysilane)-1,2,4-triazole

The synthesis was carried out under argon atmosphere. Sodium hydride (2.9 g, 0.12 mol) was dissolved in 150 mL absolute THF, the mixture was cooled to approximately 0 °C with an ice bath. 0.12 mol of 1,2,4-triazole (8.29 g) were added portionwise under stirring. After completely adding the 1,2,4-triazole the ice bath is removed and the mixture was maintained under stirring until no more hydrogen gas was evacuated. Then 23.12 g (0.09 mol) of 3-iodopropyltrimethoxysilane were added and the mixture was maintained at reflux overnight. The colorless suspension was filtered off and the solvent was removed under vacuum conditions. By addition of 150 mL absolute dichloromethane a colorless precipitate appeared and was filtered off under argon atmosphere. For further purification the crude product was distilled under vacuum conditions. After purification the product was investigated by ^1H NMR, but only the reactant (3-chloro- or 3-iodopropyltrimethoxysilane) was observed. The presence of the white precipitate suggests that the reaction itself (shown in the equation shown below) was working. Most likely the product was thermally destroyed by the distillation step. Depending on this fact no further experiments with 1,2,4-triazole were carried out, because there is no alternative for purification than distillation for these trimethoxysilanes.



Synthesis of *N*-(6-hexyltrimethoxysilane)imidazole

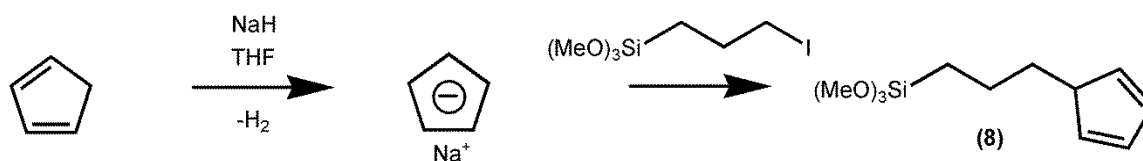
The synthesis was carried out under argon atmosphere. Sodium hydride (0.39 g, 0.016 mol) was dissolved in 40 mL absolute THF, the mixture is cooled to approximately 0 °C with an ice bath. 0.016 mol imidazole (1.09 g) were added portionwise under stirring. After completely adding the imidazole, the ice bath was removed and the mixture was maintained under stirring until no more hydrogen gas is evacuated. Then 4.13 g (0.012 mol) of 6-iodohexyltrimethoxysilane were added and the mixture was maintained at reflux overnight. The brown suspension was filtered off and the solvent was removed under vacuum conditions. By addition of 150 mL absolute dichloromethane a colorless precipitate appeared and was filtered off under argon atmosphere. The crude product was a high viscous liquid and could not be purified by common purification techniques. The NMR showed signals of the expected product as well from the reactants and other pollutions. In consequence this compound was not used for materials synthesis.



5.3.3 Syntheses of precursor molecules for silica nanoparticle based self-healing materials

Synthesis of 3-Cyclopentadienylpropyltrimethoxysilane (**8**)

The synthesis was carried out under argon atmosphere. Dicyclopentadiene was cracked in decaline at 190 °C. Sodium hydride (2.9 g, 0.12 mol) was dissolved in 150 mL absolute THF, the mixture was cooled to approximately 0°C with an ice bath. 0.12 mol of the monomerized cyclopentadiene (7.93 g) was added under stirring. After completely adding the cyclopentadiene the color of the solution changed to slightly pink. Now the ice bath was removed and the mixture was maintained under stirring until no more hydrogen gas evacuated. Then 23.12 g (0.09 mol) of 3-iodopropyltrimethoxysilane were added and the mixture was maintained under reflux overnight. The deep red suspension was filtered off and the solvent was removed under vacuum conditions. By addition of 150 mL absolute dichloromethane a colorless precipitate appeared and was filtered off under argon atmosphere. For purification the crude product was distilled at 83°C under vacuum conditions (1 mbar) with a yield of 19 % as a yellowish and transparent liquid. Furthermore there was a significant amount of black residue after distillation, which probably refers to polymerized cyclopentadiene.



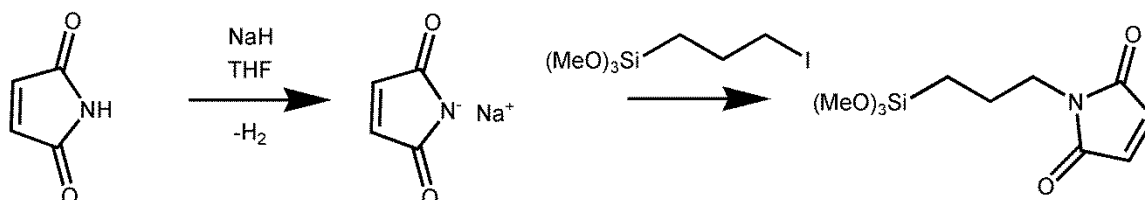
^1H NMR (300 MHz, CDCl_3): δ [ppm] 6.44 (t, 1H, $-\text{CH}-\text{CH}-\text{CH}-\text{CH}_2-$); 6.26 (t, 1H, $-\text{CH}-\text{CH}-\text{CH}-\text{CH}_2-$); 6.17 (t, 1H, $-\text{CH}-\text{CH}-\text{CH}-\text{CH}_2-$); 6.03 (t, 1H, $-\text{CH}-\text{CH}-\text{CH}-\text{CH}_2-$); 3.58 (s, 9H, $\text{Si}(\text{OCH}_3)_3$); 2.95 (s, 1H, $\text{CH}-\text{CH}_2-\text{CH}_2-\text{CH}_2-\text{Si}$); 2.88 (s, 1H, $\text{CH}-\text{CH}_2-\text{CH}_2-\text{CH}_2-\text{Si}$); 2.43 (q, 2H, $\text{cp}-\text{CH}_2-\text{CH}_2-$); 1.69 (q, 2H, $\text{cp}-\text{CH}_2-\text{CH}_2-\text{CH}_2-\text{Si}$); 0.70 (t, 2H, $-\text{CH}_2-\text{Si}$). All signals in the ^1H NMR spectrum of the cyclopentadiene ring are doubled, which suggests a fast dimerization of compound (**8**).

^{13}C NMR (300 MHz, CDCl_3): δ [ppm] 134.7, 133.5, 132.4, 130.4, 126.6, 126.2 (cp ring), 50.4 ($-\text{Si}(\text{OCH}_3)_3$), 43.1 and 41.2 ($\text{CH}-\text{CH}_2-\text{CH}_2-\text{CH}_2-\text{Si}$), 33.9 and 33.0 ($\text{cp}-\text{CH}_2-\text{CH}_2-$), 22.8 and 22.0 ($\text{cp}-\text{CH}_2-\text{CH}_2-$), 9.0 and 8.9 ($-\text{CH}_2-\text{Si}$). The signals of the cyclopentadiene ring are contributed to the monomer

and dimer form of cyclopentadiene, all other signals (except the methoxy carbon atom) are doubled, which also suggests a fast dimerization (**8**).

Synthesis of N-(3-propyltrimethoxysilane)maleimide

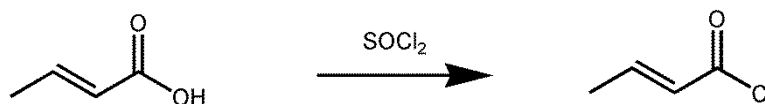
The synthesis was carried out under argon atmosphere. Sodium hydride (2.9 g, 0.12 mol) was dissolved in 150 mL absolute THF, the mixture was cooled to approximately 0 °C with an ice bath. 0.12 mol of maleinimide (11.65 g) were added portionwise under stirring. After completely adding the ice bath is removed and the mixture was maintained under stirring until no more hydrogen gas was evacuated. Then 23.12 g (0.09 mol) of 3-iodopropyltrimethoxysilane were added and the mixture was maintained at reflux overnight. The strawberry red suspension was filtered off and the solvent was removed under vacuum conditions. By addition of 150 mL absolute dichloromethane a colorless precipitate appeared (but not that much compared to the imidazole coupling reactions) and was filtered off under argon atmosphere. For further purification the crude product was distilled under vacuum conditions. After purification the product was investigated by ¹H NMR, but only the reactant (3-chloro- or 3-iodopropyltrimethoxysilane) could be observed. The presence of less white precipitate suggests that the reaction itself was not working very well. Most likely the reactant (maleimide) was destroyed by refluxing overnight.



Synthesis of Butanoic acid-4-(trimethoxysilyl)-isopropylester (3 step synthesis)

Synthesis of crotonic chloride

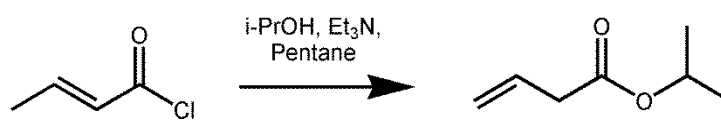
The synthesis was carried out under argon atmosphere. A 500 mL three necked flask equipped with dimroth chiller and a 100 mL dripping funnel was charged with 1.16 mol crotonic acid (100 g) and 150 ml hexane. Then 1.16 mol thionyl chloride (84.3 mL) were added dropwise through the dripping funnel. After the addition was complete the reaction mixture was heated to 50°C until no further gas evolution took place (5 hours). After this procedure the color of the reaction mixture turned to orange-brown. The solvent was removed under vacuum conditions. The crude product was purified by distillation a 115-120 °C at 1bar. Crotonic chloride was obtained with a yield of 76 % as a colorless and transparent liquid.



^1H NMR (250 MHz, CDCl_3): δ [ppm] 7.16 (q, 1H, $\text{CH}_3\text{-CH-CH-}$); 6.07 (q, 1H, $\text{CH}_3\text{-CH-CH-}$); 1.91 (q, 3H, $\text{CH}_3\text{-CH-CH-}$).

Synthesis of Isopropyl but-3-enoate

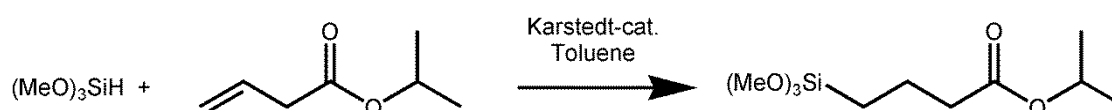
A 500 mL three necked flask equipped with dimroth chiller and a 50 mL dripping funnel was charged with 0.1 mol crotonic chloride (10.45 g) and 200 ml pentane. Then 0.1 mol triethylamine (10.11 g) were added by a syringe. This mixture was cooled to approximately 0 °C with an ice bath, followed by a dropwise addition of 0.15 mol isopropanol (9.1 g) through the dripping funnel. A colorless precipitate was formed immediately. The slightly yellow suspension was filtered off and the solvent was removed under vacuum conditions. The crude product was washed with 100 mL THF and a colorless solid precipitated again. The precipitate was filtered off and the solvent was removed under vacuum conditions. For purification the crude product was distilled at 68 °C under vacuum conditions (100 mbar) with a yield of 52 % as a colorless and transparent liquid.



^1H NMR (250 MHz, CDCl_3): δ [ppm] 5.85 (q, 1H, $\text{CH}_2\text{-CH-CH}_2\text{-}$); 5.11 (m, 1H, $\text{CH}_2\text{-CH-CH}_2\text{-}$); 5.05 (m, 1H, $\text{CH}_2\text{-CH-CH}_2\text{-}$); 4.95 (m, 1H, $\text{CH-}(\text{CH}_3)_2$); 2.98 (d, 2H, $\text{CH}_2\text{-CH-CH}_2\text{-}$); 1.15 (d, 6H, $\text{CH-}(\text{CH}_3)_2$).

Synthesis of Butanoic acid-4-(trimethoxysilyl)-isopropylester (hydrosilylation)

The synthesis was carried out under argon atmosphere. A 250 mL three necked flask equipped with dimroth chiller was charged with 0.047 mol trimethoxysilane (5.75 g), 0.047 mol isopropyl but-3-enoate (6 g), 70 ml toluene and 5 drops of Karstedt catalyst solution. This mixture was heated to 50 °C for 48 hours. Afterwards the toluene was removed under vacuum conditions. For purification the crude product was distilled at 86 °C under vacuum conditions (1 mbar) with a yield of 45 % as a colorless and transparent liquid.



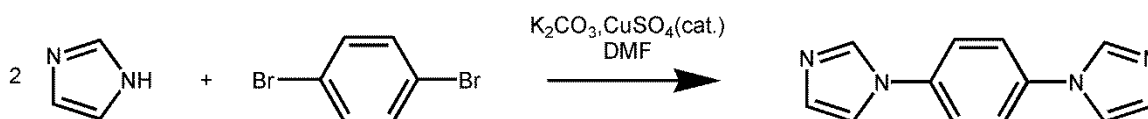
^1H NMR (250 MHz, CDCl_3): δ [ppm] 5.01 (m, 1H, $\text{CH-}(\text{CH}_3)_2$); 3.56 (s, 9H, $\text{Si}(\text{OCH}_3)_3$); 2.30 (t, 2H, $\text{Si-CH}_2\text{-CH}_2\text{-CH}_2\text{-}$); 1.74 (q, 2H, $\text{Si-CH}_2\text{-CH}_2\text{-CH}_2\text{-}$); 1.21 (d, 6H, $\text{CH-}(\text{CH}_3)_2$), 0.67 (t, 2H, $\text{Si-CH}_2\text{-CH}_2\text{-CH}_2\text{-}$).

^{13}C NMR (250 MHz, CDCl_3): δ [ppm] 172.8 (C=O); 67.3 ($\text{CH}-(\text{CH}_3)_2$); 50.4 ($\text{Si}(\text{OCH}_3)_3$); 37.4 ($\text{O}=\text{C}-\text{CH}_2$); 21.7 ($\text{CH}-(\text{CH}_3)_2$); 18.4 ($\text{Si}-\text{CH}_2-\text{CH}_2$); 8.7 ($\text{Si}-\text{CH}_2-\text{CH}_2$).

5.3.4 Linker syntheses

Synthesis of 1,4-bis(1H-imidazol-1-yl)benzene ^[324]

The synthesis was carried out under argon atmosphere. A 500 mL three necked flask equipped with dimroth chiller was charged with 31.8 mmol 1,4-dibromobenzene (7.5 g), 133.6 mmol imidazole (9.1 g), 101.8 mmol K_2CO_3 (14.1 g), a catalytic amount of CuSO_4 (0.1 g) and 120 ml dimethylformamide (DMF). This mixture was maintained at reflux for 24 hours. After this procedure the color of the reaction mixture turned to red –brown. The solvent was removed under vacuum conditions. Afterwards the solid residue was washed 3 times with water. The obtained brown solid was recrystallized 3 times from toluene. The product was obtained as a colorless solid with a yield of 65 %.



^1H NMR (250 MHz, CDCl_3): δ [ppm] 7.82 (s, H, N-CH-N); 7.46 (d, 4H, C-CH-CH-); 7.24 (d, 2H, C-N-CH-CH-N); 7.19 (d, 2H, C-N-CH-CH-N).

^{13}C NMR (250 MHz, CDCl_3): δ [ppm] 135.5 (N-CH-N); 130.9 (N-C-CH-); 122.9 (N-C-CH-); 118.3 (C-N-CH-CH-N), 118.2 (C-N-CH-CH-N).

5.3.5 Nanoparticle modification reactions

Synthesis of chloropropyl modified silica nanoparticles (SiO_2 Cl)

32 mL of the previously prepared silica nanoparticle solution were degassed in vacuum for several minutes to remove excessive ammonia. Then 14.29 mmol of 2-chloropropyltrimethoxysilane (2.84 g) were added dropwise. The solution was stirred at room temperature for 24 hours.

Synthesis of chloroethyl modified silica nanoparticles (SiO_2 EtCl)

32 mL of the previously prepared silica nanoparticle solution were degassed in vacuum for several minutes to remove excessive ammonia. Then 14.29 mmol of 2-chloroalkyltrimethoxysilane (2.64 g) were added dropwise. The solution was stirred at room temperature for 24 hours.

Synthesis of (Chloromethyl)phenylethyl modified silica nanoparticles (SiO₂ PhCl)

32 mL of the previously prepared silica nanoparticle solution were degassed in vacuum for several minutes to remove excessive ammonia. Then 14.29 mmol of ((Chloromethyl)phenylethyl)trimethoxysilane (3.93 g) were added dropwise. The solution was stirred at room temperature for 24 hours.

Synthesis of chloropropyl modified ZnO nanoparticles (ZnO Cl)

100 mL of the previously prepared zinc oxide nanoparticle solution were transferred to a round bottom flask. Then 1,0 g (5 mmol) 3-chloropropyltrimethoxysilane were added dropwise. The solution was stirred at room temperature for 24 hours.

Synthesis of N-propylimidazole modified silica nanoparticles (SiO₂ ImR with R = H, Me, i-Pr)

32 mL of the previously prepared silica nanoparticle solution were degassed in vacuum for several minutes to remove excessive ammonia. Then 14.29 mmol of the respective N-(3-propyltrimethoxysilane)imidazole (**1**, **2** and **3**) were added dropwise. The solution was stirred at room temperature for 24 hours.

Synthesis of N-propylpyrazole modified silica nanoparticles (SiO₂ PyrazoleR₂ with R = H, Me)

32 mL of the previously prepared silica nanoparticle solution were degassed in vacuum for several minutes to remove excessive ammonia. Then 3.3 g (14.29 mmol) N-(3-propyltrimethoxysilane)pyrazole (**4**) or 3.7 g (14.29 mmol) N-(3-propyltrimethoxysilane)-3,5-dimethylpyrazole (**5**) were added dropwise. The solution was stirred at room temperature for 24 hours.

Synthesis of 4-ethylpyridine and 2-ethylpyridine modified silica nanoparticles (SiO₂ 4-Py and SiO₂ 2-Py)

32 mL of the previously prepared silica nanoparticle solution were degassed in vacuum for several minutes to remove excessive ammonia. Then 3.2 g (14.29 mmol) 4-(2-trimethoxysilylethyl)pyridine or 3.2 g (14.29 mmol) 2-(2-trimethoxysilylethyl)pyridine were added dropwise. The solution was stirred at room temperature for 24 hours.

5.3.6 INN Materials syntheses

Synthesis of the mono-imidazolium chloride based INN (Mat 1 – Mat 3)

16 mL solution of silica nanoparticles modified with the respective N-(3-propyltrimethoxysilane)imidazole, SiO_2 ImR with R = H, Me, i-Pr, and 16 mL solution of silica nanoparticles modified with 3-chloropropyltrimethoxysilane were transferred to a 100 mL round bottom flask. Then 10 mL of dry methanol were added. The solution was stirred for 2 days at room temperature. Afterwards, the bigger part of the solvent was removed under vacuum conditions and the material was transferred to a petri dish and was finally dried in the oven at 45 °C. A transparent gel was obtained.

Synthesis of the bis-imidazolium xylene based INN (Mat 4 – Mat 6)

32 mL solution of silica nanoparticles modified with the respective N-(3-propyltrimethoxysilane)imidazole, SiO_2 ImR with R = H, Me, i-Pr, and 20 mL of dry methanol were transferred to a 100 mL round bottom flask. Then 1.25 g (7.14 mmol) of α,α' -dichloro-*p*-xylene were added. The solution was stirred for 2 days at room temperature. Afterwards, the bigger part of the solvent was removed under vacuum conditions and the material was transferred to a petri dish and was finally dried in the oven at 45 °C. A transparent gel was obtained.

Synthesis of the bis-imidazolium biphenyl based INN (Mat 7 – Mat 9)

32 mL solution of silica nanoparticles modified with the respective N-(3-propyltrimethoxysilane)imidazole, SiO_2 ImR with R = H, Me, i-Pr, and 20 mL of dry methanol were transferred to a 100 mL round bottom flask. Then 1.8 g (7.14 mmol) of 4,4'-bis(chloromethyl)-1,1'-biphenyl were added. The solution was stirred for 2 days at room temperature. Afterwards, the bigger part of the solvent was removed under vacuum conditions and the material was transferred to a petri dish and was finally dried in the oven at 45 °C. A slightly yellow transparent gel was obtained.

Synthesis of the bis-imidazolium anthracene based INN (Mat 10 – Mat 12)

32 mL solution of silica nanoparticles modified with the respective N-(3-propyltrimethoxysilane)imidazole, SiO_2 ImR with R = H, Me, i-Pr, and 20 mL of dry methanol were transferred to a 100 mL round bottom flask. Then 0.98 g (3.57 mmol) of 9,10-bis(chloromethyl)anthracene are added. The solution is stirred for 2 days at room temperature

Some excessive linker was removed by centrifugation. Afterwards, the bigger part of the solvent was removed under vacuum conditions and the material was transferred to a petri dish and was finally dried in the oven at 45 °C. An orange transparent gel is obtained.

Synthesis of the bis-imidazolium durene based INN (Mat 13 – Mat 14)

40 mL solution of silica nanoparticles modified with the respective N-(3-propyltrimethoxysilane)imidazole, **SiO₂ ImR** with **R = H, Me, i-Pr**, and 20 mL of dry methanol were transferred to a 100 mL round bottom flask. Then 2.28 g (7.14 mmol) of 3,6-bis(chloromethyl)durene were added. The solution was stirred for 2 days at room temperature. Afterwards, the bigger part of the solvent was removed under vacuum conditions and the material was transferred to a petri dish and was finally dried in the oven at 45 °C. Some excessive linker was removed by centrifugation. A colorless transparent gel was obtained.

Synthesis of the mono-imidazolium xylene based INN (Mat 15 – Mat 16)

16 mL solution of silica nanoparticles modified with the respective N-(3-propyltrimethoxysilane)imidazole, **SiO₂ ImR** with **R = Me, i-Pr**, and 16 mL solution of silica nanoparticles modified with ((Chloromethyl)phenylethyl)trimethoxysilane were transferred to a 100 mL round bottom flask. Then 10 mL of dry methanol were added. The solution was stirred for 2 days at room temperature. Afterwards, the bigger part of the solvent was removed under vacuum conditions and the material was transferred to a petri dish and was finally dried in the oven at 45 °C. A colorless transparent gel was obtained.

Synthesis of the bis-imidazolium diacetylene based INN (Mat 17)

16 mL solution of silica nanoparticles modified with N-(3-propyltrimethoxysilane)imidazole, **SiO₂ ImH** and 10 mL of dry methanol were transferred to a 100 mL round bottom flask. Then 0.84 g (3.57 mmol) of 1,4-dibromo-1,3-butadiene were added. The solution was stirred for 2 days at room temperature. Afterwards, the bigger part of the solvent was removed under vacuum conditions and the material was transferred to a petri dish and was finally dried in the oven at 45 °C. A brown transparent gel was obtained.

Synthesis of the mono-pyrazolium based INN (Mat 18 and Mat 19)

16 mL solution of silica nanoparticles modified with the respective N-(3-propyltrimethoxysilane)pyrazole (SiO_2 Pyrazole R_2 with $\text{R} = \text{H}, \text{Me}$) and 16 mL solution of silica nanoparticles modified with 3-chloropropyltrimethoxysilane are transferred to a 100 mL round bottom flask. Then 10 mL of dry methanol are added. The solution is stirred for 2 days at room temperature. Afterwards, the bigger part of the solvent was removed under vacuum conditions and the material was transferred to a petri dish and was finally dried in the oven at 45 °C. A colorless transparent gel was obtained.

Synthesis of the bis-pyrazolium xylene based INN (Mat 20 and Mat 21)

32 mL solution of silica nanoparticles modified with the respective N-(3-propyltrimethoxysilane)pyrazole, SiO_2 Pyrazole R_2 with $\text{R} = \text{H}, \text{Me}$ and 20 mL of dry methanol were transferred to a 100 mL round bottom flask. Then 1.25 g (7.14 mmol) of α, α' -dichloro-*p*-xylene were added. The solution was stirred for 2 days at room temperature. Afterwards, the bigger part of the solvent was removed under vacuum conditions and the material was transferred to a petri dish and was finally dried in the oven at 45 °C. A transparent gel was obtained.

Synthesis of the bis-pyrazolium biphenyl based INN (Mat 22)

32 mL solution of silica nanoparticles modified with the respective N-(3-propyltrimethoxysilane)pyrazole, SiO_2 Py R_2 with $\text{R} = \text{H}$ and 20 mL of dry methanol were transferred to a 100 mL round bottom flask. Then 1.8 g (7.14 mmol) of 4,4'-bis(chloromethyl)-1,1'-biphenyl were added. The solution was stirred for 2 days at room temperature. Afterwards, the bigger part of the solvent was removed under vacuum conditions and the material was transferred to a petri dish and was finally dried in the oven at 45 °C. A colorless transparent gel was obtained.

Synthesis of the pyridinium based INN (Mat 23 and Mat 24)

16 mL solution of silica nanoparticles modified with the respective 2-trimethoxysilylethylpyridine, SiO_2 4-Py or SiO_2 2-Py, and 16 mL solution of silica nanoparticles modified with 2-chloroethyltrimethoxysilane are transferred to a 100 mL round bottom flask. Then 10 mL of dry methanol are added. The solution is stirred for 2 days at room temperature and is finally dried under vacuum conditions (3 mbar). A colorless transparent gel is obtained.

Synthesis of the bis-pyridinium xylene based INN (Mat 25 and Mat 26)

32 mL solution of silica nanoparticles modified with the respective 2-trimethoxysilylethylpyridine, **SiO₂ 4-Py** or **SiO₂ 2-Py**, and 20 mL of dry methanol were transferred to a 100 mL round bottom flask. Then 1.25 g (7.14 mmol) of α,α' -dichloro-*p*-xylene were added. The solution was stirred for 2 days at room temperature. Afterwards, the bigger part of the solvent was removed under vacuum conditions and the material was transferred to a petri dish and was finally dried in the oven at 45 °C. A transparent gel was obtained.

Synthesis of the bis-pyridinium biphenyl based INN (Mat 27 and Mat 28)

32 mL solution of silica nanoparticles modified with the respective 2-trimethoxysilylethylpyridine, **SiO₂ 4-Py** or **SiO₂ 2-Py**, and 20 mL of dry methanol were transferred to a 100 mL round bottom flask. Then 1.8 g (7.14 mmol) of 4,4'-bis(chloromethyl)-1,1'-biphenyl were added. The solution was stirred for 2 days at room temperature. Afterwards the bigger part of the solvent was removed under vacuum conditions and the material was transferred to a petri dish and was finally dried in the oven at 45 °C. A colorless transparent gel was obtained.

Synthesis of the bis-imidazolium anthracene based INN (Mat 29)

32 mL solution of silica nanoparticles modified with 4-(2-trimethoxysilylethyl)pyridine, **SiO₂ 4-Py** and 20 mL of dry methanol were transferred to a 100 mL round bottom flask. Then 0.98 g (3.57 mmol) of 9,10-bis(chloromethyl)anthracene are added. The solution was stirred for 2 days at room temperature. Some excessive linker was removed by centrifugation. Afterwards, the bigger part of the solvent was removed under vacuum conditions and the material was transferred to a petri dish and was finally dried in the oven at 45 °C. An orange transparent gel was obtained.

Synthesis of the mono-imidazolium chloride based mixed INN (Mat 36 and Mat 37)

12 mL solution of silica nanoparticles modified with the respective N-(3-propyltrimethoxysilane)imidazole, **SiO₂ ImR** with **R = H, Me** and 100 mL solution of zinc oxide nanoparticles modified with 3-chloropropyltrimethoxysilane were transferred to a 250 mL round bottom flask. The solution was stirred for 2 days at room temperature and was finally dried under vacuum conditions (3 mbar). A white powder was obtained.

Synthesis of the bis-imidazolium benzene based INN (Mat 38)

32 mL solution of silica nanoparticles modified with 3-chloropropyltrimethoxysilane and 20 mL dry methanol were transferred to a 100 mL round bottom flask. Afterwards, 7.14 mmol of 1,4-bis(1H-imidazol-1-yl)benzene (1.5 g) were added. The reaction mixture was stirred for 2 days at room temperature. The biggest part of the solvent was removed under vacuum conditions. The product was finally dried carefully at 50 °C in the oven. A yellowish gel covered with a colorless powder (pure linker molecule) was obtained.

5.3.7 Anion Metathesis and Metal Complexation reactions

Anion metathesis reactions with NaBF₄ and KPF₆ (Mat 30 and Mat 31)

In a 100 mL round bottomed flask 0.3 g of the previously obtained INN hybrid material (**Mat 1**) were dispersed in 20 mL of acetone. Then 0.3 g of NaBF₄ or KPF₆ were added. The dispersions were stirred for 24 hours at room temperature. Then the products were washed and centrifuged with water, ethanol and acetone, 20 mL respectively. The reaction solvent and the washing phases were combined and dried under vacuum conditions. The obtained salts, NaCl and KCl, were isolated to proof the exchange reaction by powder XRD investigations.

*Complexation of CuCl₂*2H₂O in INN hybrid materials (Mat 32)*

0.15 g (0.85 mmol) of CuCl₂*2H₂O were added to 17 mL of the methanolic solution of **Mat 1** in a 100 mL round bottom flask. The solution was stirred overnight at room temperature and was finally dried in vacuum. A green transparent gel was obtained.

*Complexation of CuCl₂*2H₂O in 1-butyl-3-methylimidazoliumchloride ((BuMelm)₂[CuCl₄])*

3.11 g (18.25 mmol) of CuCl₂*2H₂O were added to 6.37 g (36.5 mmol) 1-butyl-3-methylimidazoliumchloride in 5 mL ethylacetate. By adding the copper salt the temperature rose highly and the color of the reaction mixture changed to dark blue. After a few minutes the solution cooled down and the color began to turn green. The reaction mixture was stirred at room temperature overnight and the resulting water was visible as a second, transparent phase. The product was washed with water and was dried under vacuum conditions (3 mbar).

Complexation of PdCl₂ in INN hybrid materials (Mat 33)

0.63 g (3.57 mmol) of PdCl₂ and 20 ml of methanol were added to 32 mL of the methanolic INN material solution (**Mat 1**) in a 100 mL round bottom flask. By adding the PdCl₂ the color of the reaction mixture turned to deep red. The solution was stirred for 24 h at room temperature and the color of the solution turned to olive green within this time. The solvent was removed under vacuum conditions. After drying an olive green gel was obtained.

*Complexation of EuCl₃*6H₂O in INN hybrid materials (Mat 34)*

0.29 g (0.80 mmol) of EuCl₃*6H₂O and 20 ml of methanol were added to 32 mL of the methanolic INN material solution (**Mat 1**) in a 100 mL round bottom flask. The solution was stirred overnight at room temperature and was finally dried in vacuum. A colorless transparent gel was obtained.

5.3.8 Silica nanoparticle based self-healing materials

Synthesis of the dicyclopentadiene based self-healing material (Mat 39)

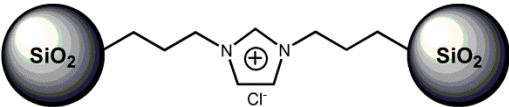
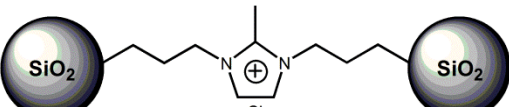
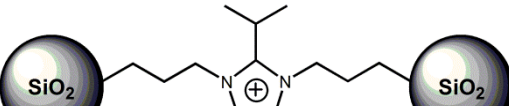
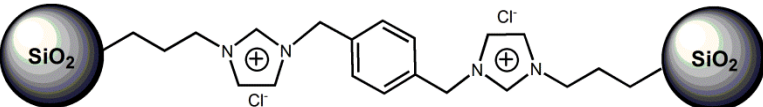
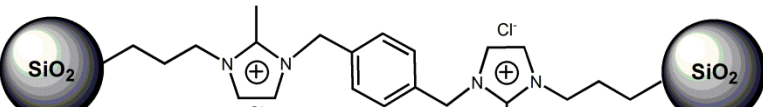
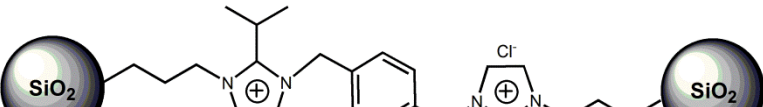
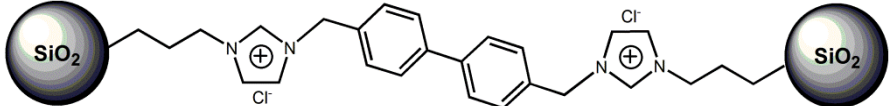
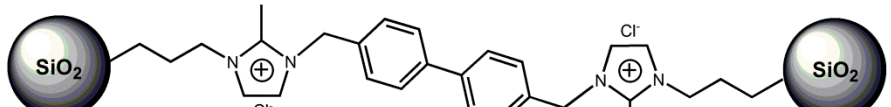
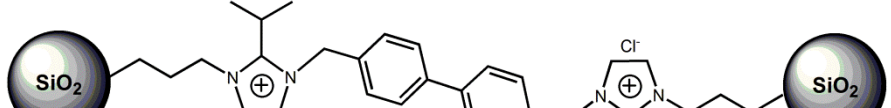
48 mL of the previously prepared silica nanoparticle solution were degassed in vacuum for several minutes to remove excessive ammonia. Then 15.5 mmol of the 3-cyclopentadienylpropyltrimethoxysilane (3.5 g of **8**) were added dropwise. The solution was stirred at room temperature for 24 hours. Afterwards the bigger part of the solvent was removed under vacuum conditions. Then the material was transferred to a petri dish and was dried in the oven at 55 °C. After drying a colorless transparent gel was obtained.

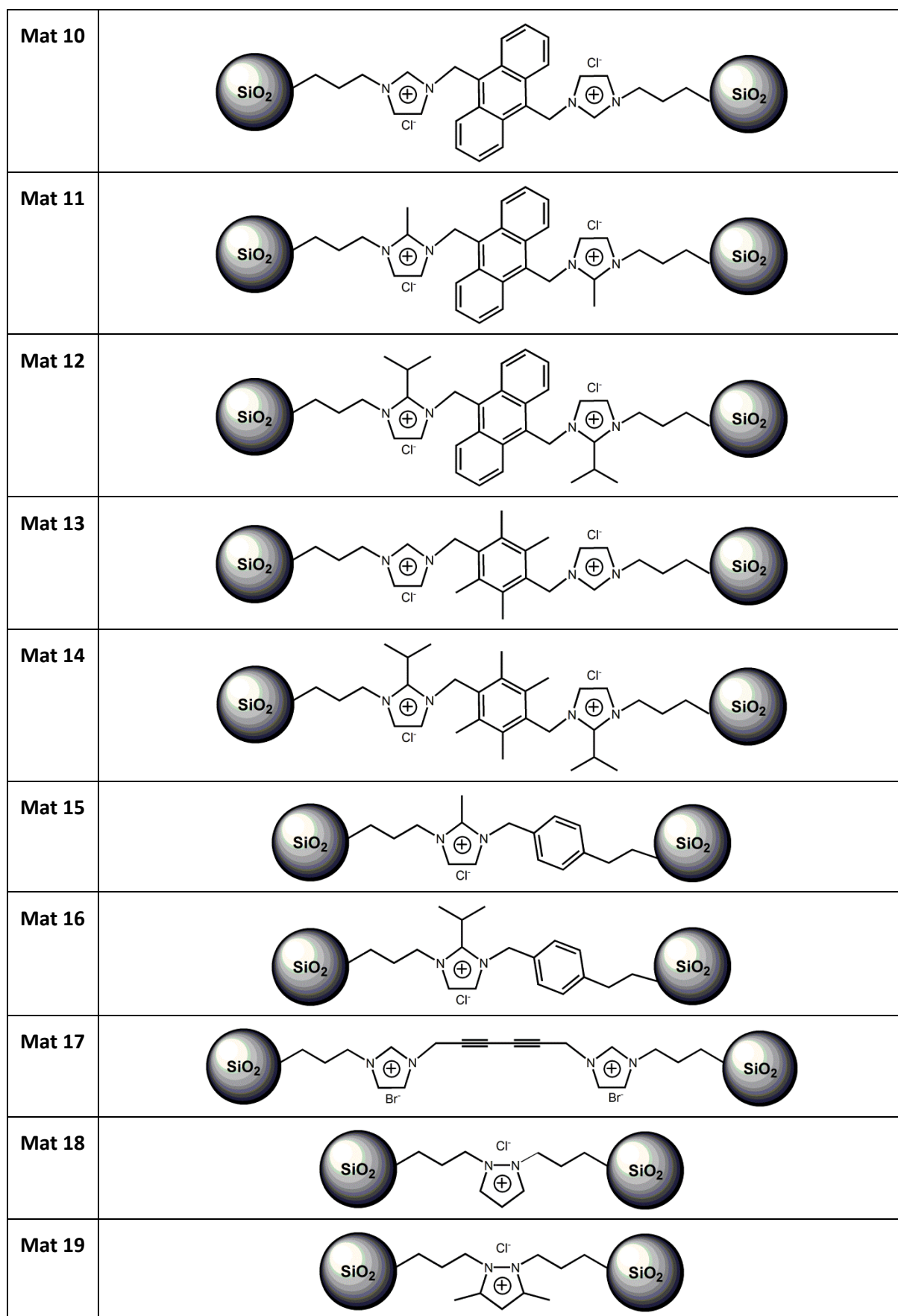
Synthesis of the silylester based self-healing material (Mat 40)

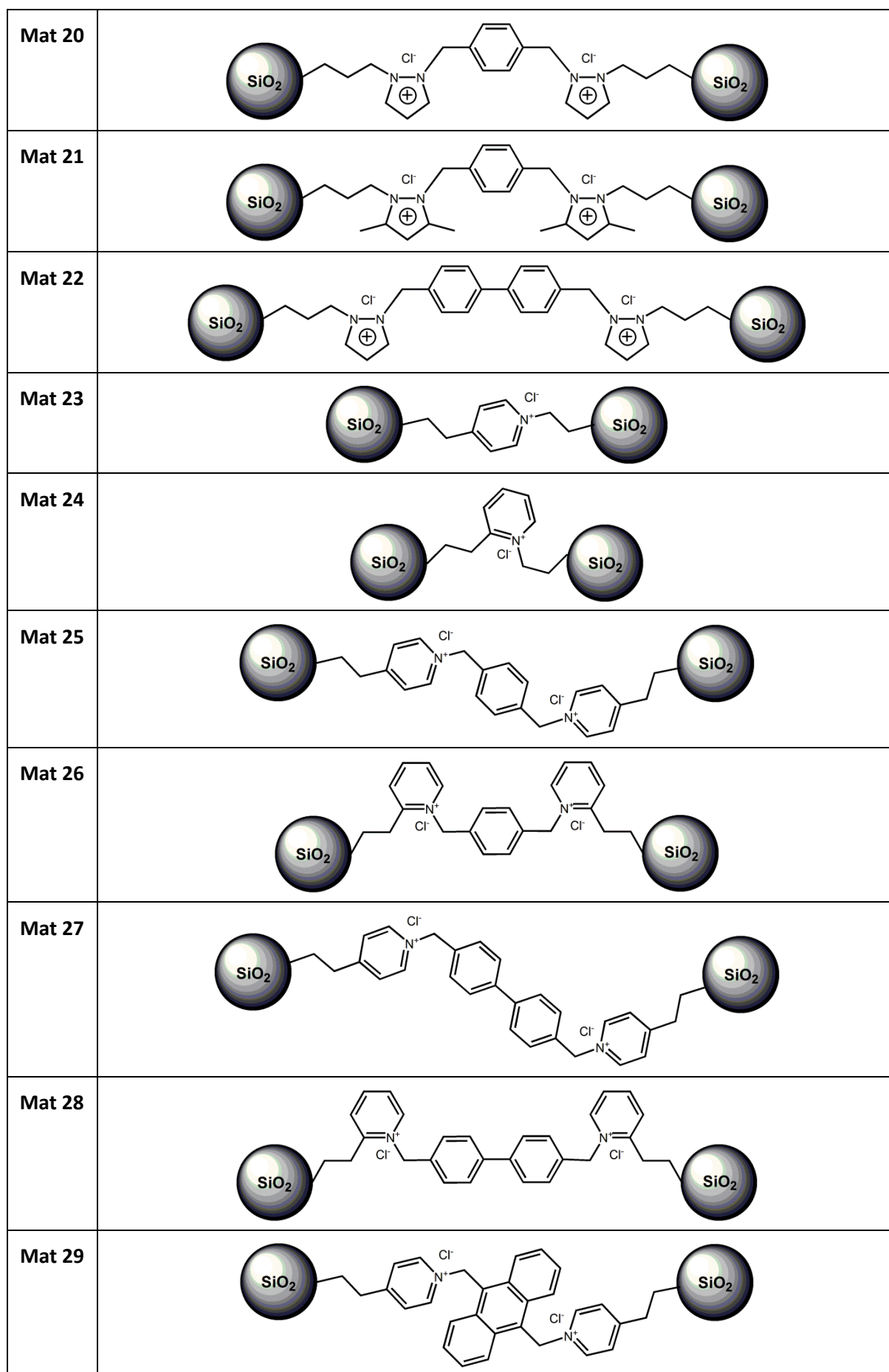
64 mL of the previously prepared silica nanoparticle solution were degassed in vacuum for several minutes to remove excessive ammonia. Then 32 mL of the nanoparticle suspension were modified with 14.28 mmol (3.37 g) 3-Glycidyloxypropyltrimethoxysilane (GLYMO) and 32 ml of the nanoparticle suspension were modified with 14.28 mmol (3.96 g) Butanoic acid-4-(trimethoxysilyl)-isopropylester by stirring the reactants for 24 hours at room temperature. After this procedure the two different nanoparticle solutions were mixed in a 250 mL round bottomed flask followed by adding 15 mL of dry methanol, 20 ml of a 38 w% solution of HCl in MeOH and 1.4 mmol (0.3 g) of Zn(CH₃COO)*2H₂O. By adding these components the reaction mixture stayed clear and colorless. Afterwards, the reaction mixture was stirred for 2 days at room temperature. After this time the

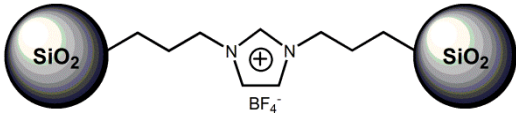
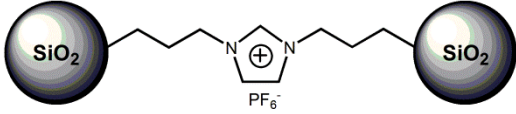
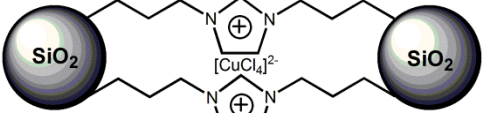
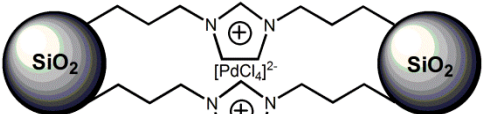
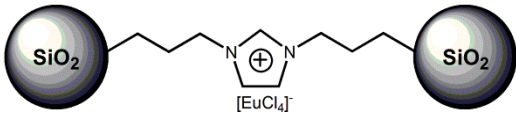
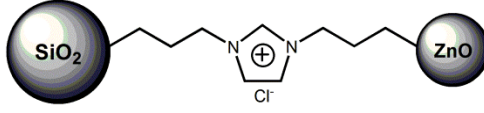
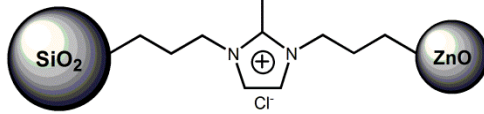
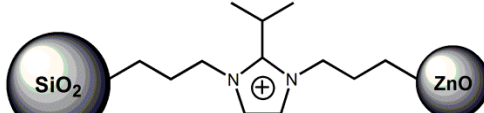
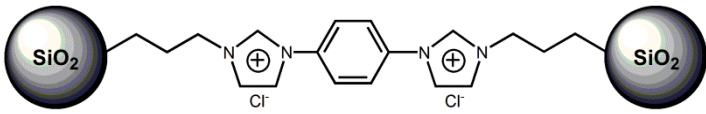
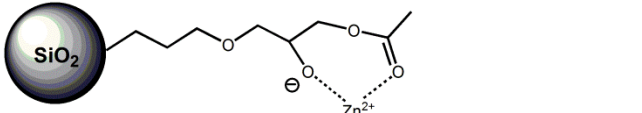
color of the solution turned to yellow. The bigger part of the solvent was removed under vacuum conditions and the product was dried carefully at 45 °C for 24 hours. A yellow transparent gel monolith was obtained.

5.3.9 Materials overview

Nr.	Material
Mat 1	
Mat 2	
Mat 3	
Mat 4	
Mat 5	
Mat 6	
Mat 7	
Mat 8	
Mat 9	





Mat 30	
Mat 31	
Mat 32	
Mat 33	
Mat 34	
Mat 35	
Mat 36	
Mat 37	
Mat 38	
Mat 39	
Mat 40	

6 Appendix

6.1 Abbreviations

a.u.	Arbitrary units
CP	Cross polarization
DFT	Density functional theory
DLS	Dynamic light scattering
EDX	Energy dispersive X-ray spectroscopy
FET	Field effect transistor
GIPAW	Gauge including projector augmented waves
HETCOR	Heteronuclear correlation spectroscopy
HR	High resolution
INN	Ionic Nanoparticle Network
ITO	Indium tin oxide
MAS	Magic angle spinning
MS	Mass spectroscopy
NMR	Nuclear magnetic resonance
PEDOT	Poly-3,4-ethylenedioxythiophene
PMMA	Poly(methyl methacrylate)
ppm	Parts per million
PVPh	Poly-4-vinylphenol
q	Scattering vector
QCM	Quartz crystal microbalance
SAXS	Small angle X-ray scattering
SEM	Scanning electron microscopy
TEM	Transmission electron microscopy
TGA	Thermogravimetric analysis
w%	Weight percent
XRD	X-ray diffraction

6.2 Bibliography

- [1] G. Kickelbick, *Hybrid Materials: Synthesis, Characterization and Applications*, Wiley-VCH, Weinheim, **2007**.
- [2] C. Sanchez, P. Belleville, M. Popall, L. Nicole, *Chem. Soc. Rev.* **2011**, *40*, 696–753.
- [3] C. Sanchez, B. Julián, P. Belleville, M. Popall, *J. Mater. Chem.* **2005**, *15*, 3559–3592.
- [4] B. O'Regan, M. Grätzel, *Nature* **1991**, *353*, 737–740.
- [5] S. Mann, *J. Chem. Soc. Dalton Trans.* **1993**, 1–9.
- [6] S. Bondy, M. Harrington, *Science* **1979**, *203*, 1243–1244.
- [7] C. Huber, *Science* **1998**, *281*, 670–672.
- [8] P. Gomez-Romero, C. Sanchez, *New J. Chem.* **2005**, *29*, 57–58.
- [9] A. Doménech, M. T. Doménech-Carbó, M. Sánchez del Río, M. L. Vázquez de Agredos Pascual, E. Lima, *New J. Chem.* **2009**, *33*, 2371–2379.
- [10] B. Boury, R. J. P. Corriu, *Chem. Commun.* **2002**, 795–802.
- [11] D. Feng, H.-L. Jiang, Y.-P. Chen, Z.-Y. Gu, Z. Wei, H.-C. Zhou, *Inorg. Chem.* **2013**, *52*, 12661–12667.
- [12] O. M. Yaghi, M. O'Keeffe, N. W. Ockwig, H. K. Chae, M. Eddaoudi, J. Kim, *Nature* **2003**, *423*, 705–714.
- [13] H.-C. Zhou, J. R. Long, O. M. Yaghi, *Chem. Rev.* **2012**, *112*, 673–674.
- [14] G. Férey, *Chem. Mater.* **2001**, *13*, 3084–3098.
- [15] X. Lin, J. Jia, P. Hubberstey, M. Schröder, N. R. Champness, *CrystEngComm* **2007**, *9*, 438–448.
- [16] E. Bourgeat-Lami, *J. Nanosci. Nanotechnol.* **2002**, *2*, 1–24.
- [17] S. Reculosa, C. Poncet-Legrand, S. Ravaine, C. Mingotaud, E. Duguet, E. Bourgeat-Lami, *Chem. Mater.* **2002**, *14*, 2354–2359.
- [18] E. Ruiz-Hitzky, R. Jimenez, B. Casal, V. Manriquez, A. S. Ana, G. Gonzalez, *Adv. Mater.* **1993**, *5*, 738–741.
- [19] E. P. Giannelis, *Appl. Organomet. Chem.* **1998**, *12*, 675–680.
- [20] F. Leroux, J.-P. Besse, *Chem. Mater.* **2001**, *13*, 3507–3515.
- [21] C. Sanchez, G. J. de A. A. Soler-Illia, F. Ribot, T. Lalot, C. R. Mayer, V. Cabuil, *Chem. Mater.* **2001**, *13*, 3061–3083.

- [22] M. Litschauer, M.-A. Neouze, *J. Mater. Chem.* **2008**, *18*, 640–646.
- [23] C. G. Goltner, M. Antonietti, *Adv. Mater.* **1997**, *9*, 431–436.
- [24] C. T. Kresge, M. E. Leonowicz, W. J. Roth, J. C. Vartuli, J. S. Beck, *Nature* **1992**, *359*, 710–712.
- [25] R. J. P. Corriu, A. Mehdi, C. Reye, C. Thieuleux, *New J. Chem.* **2003**, *27*, 905–908.
- [26] U. Schubert, N. Hüsing, *Synthesis of Inorganic Materials*, Wiley-VCH, Weinheim, **2012**.
- [27] A. N. Shipway, E. Katz, I. Willner, *Chemphyschem* **2000**, *1*, 18–52.
- [28] A. Kumar, P. K. Vemula, P. M. Ajayan, G. John, *Nat. Mater.* **2008**, *7*, 236–241.
- [29] J.-P. Kaiser, L. Diener, P. Wick, *J. Phys. Conf. Ser.* **2013**, *429*, 012036/1–012036/10.
- [30] C. R. Crick, I. P. Parkin, *Chemistry* **2010**, *16*, 3568–3588.
- [31] D. Lee, M. F. Rubner, R. E. Cohen, *Nano Lett.* **2006**, *6*, 2305–2312.
- [32] I. I. Slowing, B. G. Trewyn, S. Giri, V. S.-Y. Lin, *Adv. Funct. Mater.* **2007**, *17*, 1225–1236.
- [33] O. C. Farokhzad, R. Langer, *ACS Nano* **2009**, *3*, 16–20.
- [34] R. Elghanian, J. J. Storhoff, R. C. Mucic, R. L. Letsinger, M. L. Mirkin, *Science (80-.)*. **1997**, *277*, 1078–1081.
- [35] Y.-S. Lin, C.-P. Tsai, H.-Y. Huang, C.-T. Kuo, Y. Hung, D.-M. Huang, Y.-C. Chen, C.-Y. Mou, *Chem. Mater.* **2005**, *17*, 4570–4573.
- [36] Y. Wang, Y. Xia, *Nano Lett.* **2004**, *4*, 2047–2050.
- [37] Y. Wang, Y. Li, C. Rong, J. P. Liu, *Nanotechnology* **2007**, *18*, 465701.
- [38] M. Yue, Y. P. Wang, N. Poudyal, C. B. Rong, J. P. Liu, *J. Appl. Phys.* **2009**, *105*, 07A708/1–07A708/3.
- [39] P. M. Mendes, S. Jacke, K. Critchley, J. Plaza, Y. Chen, K. Nikitin, R. E. Palmer, J. A. Preece, S. D. Evans, D. Fitzmaurice, *Langmuir* **2004**, *20*, 3766–3768.
- [40] S. Donthu, T. Sun, V. Dravid, *Adv. Mater.* **2007**, *19*, 125–128.
- [41] T. J. Merkel, K. P. Herlihy, J. Nunes, R. M. Orgel, J. P. Rolland, J. M. DeSimone, *Langmuir* **2010**, *26*, 13086–13096.
- [42] T. Xing, J. Sunarso, W. Yang, Y. Yin, A. M. Glushenkov, L. H. Li, P. C. Howlett, Y. Chen, *Nanoscale* **2013**, *5*, 7970–7976.
- [43] C. L. Haynes, R. P. Van Duyne, *J. Phys. Chem. B* **2001**, *105*, 5599–5611.

- [44] J. C. Brinker, G. W. Scherer, *Sol-Gel Science - The Physics and Chemistry of Sol-Gel Processing*, Academic Press, **1990**.
- [45] Y. Ikeda, Y. Kameda, *J. Sol-Gel Sci. Technol.* **2004**, *31*, 137–142.
- [46] J. Livage, C. Sanchez, *J. Non. Cryst. Solids* **1992**, *145*, 11–19.
- [47] W. Stöber, A. Fink, E. Bohn, *J. Colloid Interface Sci.* **1968**, *26*, 62–69.
- [48] H. Okudera, A. Hozumi, *Thin Solid Films* **2003**, *434*, 62–68.
- [49] M. J. van Bommel, A. B. de Haan, *J. Non. Cryst. Solids* **1995**, *186*, 78–82.
- [50] M.-A. Neouze, U. Schubert, *Monatshefte für Chemie - Chem. Mon.* **2008**, *139*, 183–195.
- [51] R. P. Bagwe, L. R. Hilliard, W. Tan, *Langmuir* **2006**, *22*, 4357–4362.
- [52] S. G. Grancharov, H. Zeng, S. Sun, S. X. Wang, S. O'Brien, C. B. Murray, J. R. Kirtley, G. A. Held, *J. Phys. Chem. B* **2005**, *109*, 13030–13035.
- [53] S. A. Simakov, Y. Tsur, *J. Nanoparticle Res.* **2006**, *9*, 403–417.
- [54] R. C. Doty, T. R. Tshikhudo, M. Brust, D. G. Fernig, *Chem. Mater.* **2005**, *17*, 4630–4635.
- [55] J. H. Moon, Y. G. Shul, S. Y. Hong, Y. S. Choi, H. T. Kim, *Int. J. Adhes. Adhes.* **2005**, *25*, 534–542.
- [56] A. Zabet-Khosousi, A.-A. Dhirani, *Chem. Rev.* **2008**, *108*, 4072–4124.
- [57] M. Joselevich, F. J. Williams, *Langmuir* **2008**, *24*, 11711–11717.
- [58] T. Lummerstorfer, H. Hoffmann, *J. Phys. Chem. B* **2004**, *108*, 3963–3966.
- [59] F. Grasset, N. Saito, D. Li, D. Park, I. Sakaguchi, N. Ohashi, H. Haneda, T. Roisnel, S. Mornet, E. Duguet, *J. Alloys Compd.* **2003**, *360*, 298–311.
- [60] W. Gu, C. P. Tripp, *Langmuir* **2006**, *22*, 5748–5752.
- [61] C. Viorner, Y. Chevolot, D. Léonard, B.-O. Aronsson, P. Péchy, H. J. Mathieu, P. Descouts, M. Grätzel, *Langmuir* **2002**, *18*, 2582–2589.
- [62] G. Guerrero, P. H. Mutin, A. Vioux, *Chem. Mater.* **2001**, *13*, 4367–4373.
- [63] G. P. Holland, R. Sharma, J. O. Agola, S. Amin, V. C. Solomon, P. Singh, D. A. Buttry, J. L. Yarger, *Chem. Mater.* **2007**, *19*, 2519–2526.
- [64] Y. Sahoo, H. Pizem, T. Fried, D. Golodnitsky, L. Burstein, C. N. Sukenik, G. Markovich, *Langmuir* **2001**, *17*, 7907–7911.
- [65] B. Basly, D. Felder-Flesch, P. Perriat, C. Billotey, J. Taleb, G. Pourroy, S. Begin-Colin, *Chem. Commun. (Camb)*. **2010**, *46*, 985–987.

- [66] C. A. Traina, J. Schwartz, *Langmuir* **2007**, *23*, 9158–9161.
- [67] M. A. White, J. A. Johnson, J. T. Koberstein, N. J. Turro, *J. Am. Chem. Soc.* **2006**, *128*, 11356–11357.
- [68] M. Schulz-Dobrick, K. V. Sarathy, M. Jansen, *J. Am. Chem. Soc.* **2005**, *127*, 12816–12817.
- [69] S. Roux, B. Garcia, J.-L. Bridot, M. Salomé, C. Marquette, L. Lemelle, P. Gillet, L. Blum, P. Perriat, O. Tillement, *Langmuir* **2005**, *21*, 2526–2536.
- [70] A. Stewart, S. E. J. Bell, *Chem. Commun. (Camb)*. **2011**, *47*, 4523–4525.
- [71] I. Quiros, M. Yamada, K. Kubo, J. Mizutani, M. Kurihara, H. Nishihara, *Langmuir* **2002**, *18*, 1413–1418.
- [72] E. Ramirez, S. Jansat, K. Philippot, P. Lecante, M. Gomez, A. M. Masdeu-Bultó, B. Chaudret, *J. Organomet. Chem.* **2004**, *689*, 4601–4610.
- [73] H. Jiang, K. Moon, Y. Li, C. P. Wong, *Chem. Mater.* **2006**, *18*, 2969–2973.
- [74] J. Kimling, M. Maier, B. Okenve, V. Kotaidis, H. Ballot, A. Plech, *J. Phys. Chem. B* **2006**, *110*, 15700–15707.
- [75] G. H. Woehrle, M. G. Warner, J. E. Hutchison, *J. Phys. Chem. B* **2002**, *106*, 9979–9981.
- [76] S.-K. Oh, Y.-G. Kim, H. Ye, R. M. Crooks, *Langmuir* **2003**, *19*, 10420–10425.
- [77] A. F. Hollemann, E. Wiberg, *Lehrbuch Der Anorganischen Chemie*, De Gruyter, **1995**.
- [78] M. Litschauer, M.-A. Neouze, *J. Mater. Chem.* **2008**, *18*, 640–646.
- [79] K. Rahimian, D. A. Loy, D. R. Wheeler, *Macromolecules* **2002**, *35*, 2452–2454.
- [80] R. C. Mehrotra, S. Sogani, *Chem. Rev.* **1994**, *94*, 1643–1660.
- [81] E. Riedel, *Moderne Anorganische Chemie*, De Gruyter, **2007**.
- [82] S. Gabriel, J. Weiner, *Berichte der Dtsch. Chem. Gesellschaft* **1888**, *21*, 2669–2679.
- [83] T. Welton, *Chem. Rev.* **1999**, *99*, 2071–2084.
- [84] J.-P. Belieres, C. A. Angell, *J. Phys. Chem. B* **2007**, *111*, 4926–4937.
- [85] P. Walden, *Bull. Acad. Sci. St. Petersburg*. **1914**, 405–422.
- [86] P. Walden, *Berichte der Dtsch. Chem. Gesellschaft* **1896**, *29*, 133–138.
- [87] P. Wasserscheid, *Ionic Liquids in Synthesis*, Wiley-VCH, Weinheim, **2008**.
- [88] M. J. Earle, K. R. Seddon, *Pure Appl. Chem.* **2000**, *72*, 1391–1398.

- [89] J. S. Wilkes, J. A. Levisky, R. A. Wilson, C. L. Hussey, *Inorg. Chem.* **1982**, *21*, 1263–1264.
- [90] J. L. Atwood, J. D. Atwood, *Adv. Chem.* **1976**, *150*, 112–127.
- [91] P. Wasserscheid, W. Keim, *Angew. Chem. Int. Ed. Engl.* **2000**, *39*, 3772–3789.
- [92] R. Sheldon, *Chem. Commun. (Camb)*. **2001**, 2399–2407.
- [93] F. H. Hurley, T. P. Wler, *J. Electrochem. Soc.* **1951**, *98*, 203–206.
- [94] B. Chan, N. Chang, M. Grimmett, *Aust. J. Chem.* **1977**, *30*, 2005–2013.
- [95] P. J. Dyson, M. C. Grossel, N. Srinivasan, T. Vine, T. Welton, D. J. Williams, J. P. White, T. Zigras, *J. Chem. Soc.* **1997**, 3465–3469.
- [96] J. S. Wilkes, M. J. Zaworotko, *J. Chem. Soc. Chem. Commun.* **1992**, 965–967.
- [97] J. Fuller, *J. Electrochem. Soc.* **1997**, *144*, 3881–3886.
- [98] M. Litschauer, M. Puchberger, H. Peterlik, M.-A. Neouze, *J. Mater. Chem.* **2010**, *20*, 1269–1276.
- [99] C. F. Poole, B. R. Kersten, S. S. J. Ho, M. E. Coddens, K. G. Furton, *J. Chromatogr. A* **1986**, *352*, 407–425.
- [100] S. K. Poole, P. H. Shetty, C. F. Poole, *Anal. Chim. Acta* **1989**, *218*, 241–264.
- [101] S. A. Bolkan, J. T. Yoke, *Inorg. Chem.* **1986**, *25*, 3587–3590.
- [102] S. A. Bolkan, J. T. Yoke, *J. Chem. Eng. Data* **1986**, *31*, 194–197.
- [103] M. Freemantle, *Chem. Eng. News* **1998**, 32–37.
- [104] J. D. Holbrey, K. R. Seddon, *J. Chem. Soc. Dalton Trans.* **1999**, 2133–2139.
- [105] C. M. Gordon, J. D. Holbrey, R. Kennedy, K. R. Seddon, *J. Mater. Chem.* **1998**, 2627–2636.
- [106] D. A. Jaeger, C. E. Tucker, *Tetrahedron Lett.* **1989**, *30*, 1785–1788.
- [107] T. Fischer, A. Sethi, T. Welton, J. Woolf, *Tetrahedron Lett.* **1999**, *40*, 793–796.
- [108] D. C. Rideout, R. Breslow, *J. Am. Chem. Soc.* **1980**, *102*, 7816–7817.
- [109] M. J. Earle, P. B. McCormac, K. R. Seddon, *Green Chem.* **1999**, *1*, 23–25.
- [110] M. Badri, J.-J. Brunet, R. Perron, *Tetrahedron Lett.* **1992**, *33*, 4435–4438.
- [111] M. J. Earle, P. B. McCormac, K. R. Seddon, *Chem. Commun.* **1998**, 2245–2246.
- [112] C. E. Song, E. J. Roh, *Chem. Commun.* **2000**, 837–838.

- [113] Y. Chauvin, L. Mussmann, H. Olivier, *Angew. Chemie Int. Ed. English* **1996**, *34*, 2698–2700.
- [114] P. Wasserscheid, H. Waffenschmidt, *J. Mol. Catal. A Chem.* **2000**, *164*, 61–67.
- [115] J. F. Knifton, *J. Mol. Catal.* **1987**, *43*, 65–77.
- [116] D. E. Kaufmann, M. Nouroozian, H. Henze, *Synlett* **1996**, *1996*, 1091–1092.
- [117] V. Bohm, W. Herrmann, *Chemistry* **2000**, *6*, 1017–25.
- [118] W. A. Herrmann, V. P. W. Böhm, *J. Organomet. Chem.* **1999**, *572*, 141–145.
- [119] A. J. Carmichael, M. J. Earle, J. D. Holbrey, P. B. McCormac, K. R. Seddon, *Org. Lett.* **1999**, *1*, 997–1000.
- [120] R. Bernini, A. Coratti, G. Fabrizi, A. Goggiamani, *Tetrahedron Lett.* **2003**, *44*, 8991–8994.
- [121] J. Gui, Y. Deng, Z. Hu, Z. Sun, *Tetrahedron Lett.* **2004**, *45*, 2681–2683.
- [122] J. A. Boon, J. A. Levisky, J. L. Pflug, J. S. Wilkes, *J. Org. Chem.* **1986**, *51*, 480–483.
- [123] M. J. Earle, K. R. Seddon, C. J. Adams, G. Roberts, *Chem. Commun.* **1998**, 2097–2098.
- [124] B. Ellis, W. Keim, P. Wasserscheid, *Chem. Commun.* **1999**, 337–338.
- [125] Y. Chauvin, H. Olivier, C. N. Wyrvalski, L. C. Simon, R. F. de Souza, *J. Catal.* **1997**, *165*, 275–278.
- [126] E. Janus, I. Goc-Maciejewska, M. Łożyński, J. Pernak, *Tetrahedron Lett.* **2006**, *47*, 4079–4083.
- [127] K. Sahandzhieva, D. Naydenov, A. Pérez-Salado Kamps, H.-J. Bart, G. Maurer, *J. Chem. Eng. Data* **2010**, *55*, 4903–4906.
- [128] K. Sahandzhieva, G. Maurer, *J. Chem. Thermodyn.* **2012**, *46*, 29–41.
- [129] J. G. Huddleston, R. D. Rogers, *Chem. Commun.* **1998**, 1765–1766.
- [130] S. H. Ha, N. L. Mai, Y.-M. Koo, *Process Biochem.* **2010**, *45*, 1899–1903.
- [131] M. Antonietti, D. Kuang, B. Smarsly, Y. Zhou, *Angew. Chem. Int. Ed. Engl.* **2004**, *43*, 4988–4992.
- [132] S. Dai, Y. H. Ju, H. J. Gao, J. S. Lin, S. J. Pennycook, C. E. Barnes, *Chem. Commun.* **2000**, 243–244.
- [133] Y. Zhou, M. Antonietti, *J. Am. Chem. Soc.* **2003**, *125*, 14960–14961.
- [134] A. Taubert, Z. Li, *Dalton Trans.* **2007**, 723–727.
- [135] T. Nakashima, N. Kimizuka, *J. Am. Chem. Soc.* **2003**, *125*, 6386–6387.

- [136] E. R. Cooper, C. D. Andrews, P. S. Wheatley, P. B. Webb, P. Wormald, R. E. Morris, *Nature* **2004**, *430*, 1012–1016.
- [137] Z. Li, J. Zhang, J. Du, H. Gao, Y. Gao, T. Mu, B. Han, *Mater. Lett.* **2005**, *59*, 963–965.
- [138] E. R. Parnham, R. E. Morris, *J. Mater. Chem.* **2006**, *16*, 3682–3684.
- [139] E. R. Parnham, R. E. Morris, *Chem. Mater.* **2006**, *18*, 4882–4887.
- [140] C.-P. Tsao, C.-Y. Sheu, N. Nguyen, K.-H. Lii, *Inorg. Chem.* **2006**, *45*, 6361–6364.
- [141] A. Taubert, P. Steiner, A. Manton, *J. Phys. Chem. B* **2005**, *109*, 15542–15547.
- [142] J. Yuan, D. Mecerreyes, M. Antonietti, *Prog. Polym. Sci.* **2013**, *38*, 1009–1036.
- [143] J. C. Salamone, S. C. Israel, P. Taylor, B. Snider, *Polymer (Guildf)*. **1973**, *14*, 639–644.
- [144] O. Green, S. Grubjesic, S. Lee, M. A. Firestone, *Polym. Rev.* **2009**, *49*, 339–360.
- [145] D. Mecerreyes, *Prog. Polym. Sci.* **2011**, *36*, 1629–1648.
- [146] M. H. Valkenberg, C. DeCastro, W. F. Hölderich, *Green Chem.* **2002**, *4*, 88–93.
- [147] A. B. Bourlinos, R. Herrera, N. Chalkias, D. D. Jiang, Q. Zhang, L. A. Archer, E. P. Giannelis, *Adv. Mater.* **2005**, *17*, 234–237.
- [148] B. Xin, J. Hao, *Chem. Soc. Rev.* **2014**, *4*, 88–93.
- [149] C. P. Mehnert, R. A. Cook, N. C. Dispenziere, M. Afeworki, *J. Am. Chem. Soc.* **2002**, *124*, 12932–12933.
- [150] T. D. Ho, H. Yu, W. T. S. Cole, J. L. Anderson, *Anal. Chem.* **2012**, *84*, 9520–9528.
- [151] A. Berthod, M. J. Ruiz-Angel, S. Carda-Broch, *J. Chromatogr. A* **2008**, *1184*, 6–18.
- [152] H. Qiu, M. Takafuji, X. Liu, S. Jiang, H. Ihara, *J. Chromatogr. A* **2010**, *1217*, 5190–5196.
- [153] J. Le Bideau, L. Viau, A. Vioux, *Chem. Soc. Rev.* **2011**, *40*, 907–925.
- [154] M. Armand, F. Endres, D. R. MacFarlane, H. Ohno, B. Scrosati, *Nat. Mater.* **2009**, *8*, 621–629.
- [155] E. Delahaye, Z. Xie, A. Schaefer, L. Douce, G. Rogez, P. Rabu, C. Günter, J. S. Gutmann, A. Taubert, *Dalton Trans.* **2011**, *40*, 9977–9988.
- [156] A. Noda, M. A. B. H. Susan, K. Kudo, S. Mitsushima, K. Hayamizu, M. Watanabe, *J. Phys. Chem. B* **2003**, *107*, 4024–4033.
- [157] P. Wang, S. M. Zakeeruddin, P. Comte, I. Exnar, M. Grätzel, *J. Am. Chem. Soc.* **2003**, *125*, 1166–1167.
- [158] B. A. Voss, J. E. Bara, D. L. Gin, R. D. Noble, *Chem. Mater.* **2009**, *21*, 3027–3029.

- [159] F. B. Dejene, A. G. Ali, H. C. Swart, R. J. Botha, K. Roro, L. Coetsee, M. M. Biggs, *Cent. Eur. J. Phys.* **2011**, *9*, 1321–1326.
- [160] C. S. Cazin, M. Veith, P. Braunstein, R. B. Bedford, *Synthesis (Stuttg)*. **2005**, 622–626.
- [161] H.-R. Grüniger, G. Calzaferri, *Helv. Chim. Acta* **1979**, *62*, 2547–2550.
- [162] G. W. Fester, Höherkoordinierte Pyridin-Addukte von Hydridochlorsilanen - Synthesen Und Anwendungen, TU Bergakademie Freiberg, **2009**.
- [163] E. Fanghänel, K. Gewalt, H. Schmidt, P. Metz, *Organikum Organisch-Chemisches Grundpraktikum*, Wiley-VCH, Weinheim, **2001**.
- [164] K. Keis, C. Bauer, G. Boschloo, a. Hagfeldt, K. Westermark, H. Rensmo, H. Siegbahn, *J. Photochem. Photobiol. A Chem.* **2002**, *148*, 57–64.
- [165] J. S. Noh, J. A. Schwarz, *J. Colloid Interface Sci.* **1989**, *130*, 157–164.
- [166] M. Litschauer, M. Puchberger, H. Peterlik, M.-A. Neouze, *J. Mater. Chem.* **2010**, *20*, 1269–1276.
- [167] J.-Z. Yang, Z.-H. Zhang, D.-W. Fang, J.-G. Li, W. Guan, J. Tong, *Fluid Phase Equilib.* **2006**, *247*, 80–83.
- [168] M. Litschauer, Materials from Functionalised Metal Oxide Surfaces: Ionic Nanoparticle Networks and Cellulose Aerogels, TU Wien, **2011**.
- [169] P. Migowski, J. Dupont, *Chemistry* **2007**, *13*, 32–39.
- [170] A. T. Balaban, D. J. Klein, N. H. March, C. C. Matthai, *Phys. Chem. Liq.* **2005**, *43*, 403–407.
- [171] H. Peterlik, P. Fratzl, *Monatshefte für Chemie - Chem. Mon.* **2006**, *137*, 529–543.
- [172] G. Beaucage, *J. Appl. Crystallogr.* **1995**, *28*, 717–728.
- [173] G. Beaucage, *J. Appl. Crystallogr.* **1996**, *29*, 134–146.
- [174] J. S. Pedersen, *Adv. Colloid Interface Sci.* **1997**, *70*, 171–210.
- [175] D. J. Kinning, E. L. Thomas, *Macromolecules* **1984**, *17*, 1712–1718.
- [176] J. Akbarzadeh, Structure and Kinetics of Nanoscaled Soft Matter, University of Vienna, **2014**.
- [177] J. Yang, J. Akbarzadeh, C. Maurer, H. Peterlik, U. Schubert, *J. Mater. Chem.* **2012**, *22*, 24034–24041.
- [178] S. Pabisch, B. Feichtenschlager, G. Kickelbick, H. Peterlik, *Chem. Phys. Lett.* **2012**, *521*, 91–97.
- [179] Y. Zhou, J. H. Schattka, M. Antonietti, *Nano Lett.* **2004**, *4*, 477–481.
- [180] R. P. Matthews, T. Welton, P. A. Hunt, *Phys. Chem. Chem. Phys.* **2014**, *16*, 3238–3253.

- [181] M. Litschauer, H. Peterlik, M.-A. Neouze, *J. Phys. Chem. C* **2009**, *113*, 6547–6552.
- [182] G. Sauerbrey, *Zeitschrift für Phys.* **1959**, *155*, 206–222.
- [183] S. Nilsson, F. Björefors, N. D. Robinson, *Appl. Surf. Sci.* **2013**, *280*, 783–790.
- [184] M. Rodahl, F. Höök, A. Krozer, P. Brzezinski, B. Kasemo, *Rev. Sci. Instrum.* **1995**, *66*, 3924–3930.
- [185] M. V. Voinova, M. Rodahl, M. Jonson, B. Kasemo, *Phys. Scr.* **1999**, *59*, 391–396.
- [186] H. Ibrahim, N. A. Koorbanally, D. Ramjugernath, M. D. Bala, V. O. Nyamori, *Zeitschrift für Anorg. und Allg. Chemie* **2012**, *638*, 2304–2309.
- [187] J. M. Griffin, A. J. Miller, A. J. Berry, S. Wimperis, S. E. Ashbrook, *Phys. Chem. Chem. Phys.* **2010**, *12*, 2989–2998.
- [188] A. Sadoc, M. Body, C. Legein, M. Biswal, F. Fayon, X. Rocquefelte, F. Boucher, *Phys. Chem. Chem. Phys.* **2011**, *13*, 18539–18550.
- [189] C. P. Fredlake, J. M. Crosthwaite, D. G. Hert, S. N. V. K. Aki, J. F. Brennecke, *J. Chem. Eng. Data* **2004**, *49*, 954–964.
- [190] J. A. Gerbec, D. Magana, A. Washington, G. F. Strouse, *J. Am. Chem. Soc.* **2005**, *127*, 15791–15800.
- [191] D. D. Lovingood, G. F. Strouse, *Nano Lett.* **2008**, *8*, 3394–3397.
- [192] M.-A. Neouze, *J. Mater. Chem.* **2010**, *20*, 9593–9607.
- [193] C. A. Hunter, J. K. M. Sanders, *J. Am. Chem. Soc.* **1990**, *112*, 5525–5534.
- [194] D. Esposito, S. Kirchhecker, M. Antonietti, *Chem. a Eur. J.* **2013**, *19*, 15097–15100.
- [195] S. Machida, S. Miyata, A. Techagumpuch, *Synth. Met.* **1989**, *31*, 311–318.
- [196] A. Paul, A. Samanta, *J. Phys. Chem. B* **2007**, *111*, 1957–62.
- [197] U. Özgür, Y. I. Alivov, C. Liu, A. Teke, M. A. Reshchikov, S. Doğan, V. Avrutin, S.-J. Cho, H. Morkoç, *J. Appl. Phys.* **2005**, *98*, 041301.
- [198] J. Graffion, A. M. Cojocariu, X. Cattoën, R. A. S. Ferreira, V. R. Fernandes, P. S. André, L. D. Carlos, M. Wong Chi Man, J. R. Bartlett, *J. Mater. Chem.* **2012**, *22*, 13279–13285.
- [199] D. Giaume, M. Poggi, D. Casanova, G. Mialon, K. Lahlil, A. Alexandrou, T. Gacoin, J.-P. Boilot, *Langmuir* **2008**, *24*, 11018–11026.
- [200] L. D. Carlos, R. A. S. Ferreira, V. de Zea Bermudez, B. Julián-López, P. Escibano, *Chem. Soc. Rev.* **2011**, *40*, 536–549.

- [201] L. D. Carlos, R. A. S. Ferreira, V. de Z. Bermudez, S. J. L. Ribeiro, *Adv. Mater.* **2009**, *21*, 509–534.
- [202] C. A. Strassert, C.-H. Chien, M. D. Galvez Lopez, D. Kourkoulos, D. Hertel, K. Meerholz, L. De Cola, *Angew. Chem. Int. Ed. Engl.* **2011**, *50*, 946–950.
- [203] J. M. Fernández-Hernández, J. I. Beltrán, V. Lemauro, M.-D. Gálvez-López, C.-H. Chien, F. Polo, E. Orselli, R. Fröhlich, J. Cornil, L. De Cola, *Inorg. Chem.* **2013**, *52*, 1812–1824.
- [204] C.-H. Yang, M. Mauro, F. Polo, S. Watanabe, I. Muenster, R. Fröhlich, L. De Cola, *Chem. Mater.* **2012**, *24*, 3684–3695.
- [205] P. C. Marr, K. McBride, R. C. Evans, *Chem. Commun. (Camb)*. **2013**, *49*, 6155–6157.
- [206] J. Graffion, X. Cattoën, V. T. Freitas, R. A. S. Ferreira, M. W. Chi Man, L. D. Carlos, *J. Mater. Chem.* **2012**, *22*, 6711–6715.
- [207] A. Samanta, *J. Phys. Chem. B* **2006**, *110*, 13704–13716.
- [208] A. J. Boydston, P. D. Vu, O. L. Dykhno, V. Chang, A. R. Wyatt, A. S. Stockett, E. T. Ritschdorff, J. B. Shear, C. W. Bielawski, *J. Am. Chem. Soc.* **2008**, *130*, 3143–3156.
- [209] A. Paul, P. K. Mandal, A. Samanta, *J. Phys. Chem. B* **2005**, *109*, 9148–9153.
- [210] A. J. Boydston, C. S. Pecinovsky, S. T. Chao, C. W. Bielawski, *J. Am. Chem. Soc.* **2007**, *129*, 14550–14551.
- [211] A. J. Boydston, P. D. Vu, O. L. Dykhno, V. Chang, A. R. Wyatt, A. S. Stockett, E. T. Ritschdorff, J. B. Shear, C. W. Bielawski, *J. Am. Chem. Soc.* **2008**, *130*, 3143–3156.
- [212] T. Tang, D. J. Coady, A. J. Boydston, O. L. Dykhno, C. W. Bielawski, *Adv. Mater.* **2008**, *20*, 3096–3099.
- [213] K. M. Wiggins, R. L. Kerr, Z. Chen, C. W. Bielawski, *J. Mater. Chem.* **2010**, *20*, 5709–5714.
- [214] R. Martín, L. Teruel, C. Aprile, J. F. Cabeza, M. Álvaro, H. García, *Tetrahedron* **2008**, *64*, 6270–6274.
- [215] R. C. Evans, P. C. Marr, *Chem. Commun. (Camb)*. **2012**, *48*, 3742–3744.
- [216] M. Czakler, M. Litschauer, K. Föttinger, H. Peterlik, M.-A. Neouze, *J. Phys. Chem. C. Nanomater. Interfaces* **2010**, *114*, 21342–21347.
- [217] A. Paul, P. K. Mandal, A. Samanta, *Chem. Phys. Lett.* **2005**, *402*, 375–379.
- [218] P. K. Mandal, A. Paul, A. Samanta, *J. Photochem. Photobiol. A Chem.* **2006**, *182*, 113–120.
- [219] D. Zhang, R. Pelton, *Langmuir* **2012**, *28*, 3112–3119.
- [220] N. K. Al-Rasbi, C. Sabatini, F. Barigelletti, M. D. Ward, *Dalton Trans.* **2006**, 4769–4772.

- [221] W.-Q. Kan, J. Yang, Y.-Y. Liu, J.-F. Ma, *Polyhedron* **2011**, *30*, 2106–2113.
- [222] P. Suresh, S. Radhakrishnan, C. Naga Babu, A. Sathyanarayana, N. Sampath, G. Prabusankar, *Dalton Trans.* **2013**, *42*, 10838–10846.
- [223] H. Xiong, R. Ma, S. Wang, Y. Xia, *J. Mater. Chem.* **2011**, *21*, 3178.
- [224] Y. Lin, D. Wang, Q. Zhao, Z. Li, Y. Ma, M. Yang, *Nanotechnology* **2006**, *17*, 2110–2115.
- [225] A. Tolkki, E. Vuorimaa, V. Chukharev, H. Lemmetyinen, P. Ihalainen, J. Peltonen, V. Dehm, F. Würthner, *Langmuir* **2010**, *26*, 6630–6637.
- [226] G.-P. Yong, C.-F. Li, Y.-Z. Li, S.-W. Luo, *Chem. Commun. (Camb)*. **2010**, *46*, 3194–3196.
- [227] T. Singh, A. Kumar, *J. Phys. Chem. B* **2008**, *112*, 4079–4086.
- [228] D. R. Bloomquist, M. R. Pressprich, R. D. Willett, *J. Am. Chem. Soc.* **1988**, *110*, 7391–7398.
- [229] S. Gadžurić, M. Vraneš, S. Dožić, *Sol. Energy Mater. Sol. Cells* **2012**, *105*, 309–316.
- [230] X. Wei, L. Yu, D. Wang, X. Jin, G. Z. Chen, *Green Chem.* **2008**, *10*, 296–305.
- [231] J. H. Day, *Chem. Rev.* **1968**, *68*, 649–657.
- [232] E. Negishi, *Handbook of Organopalladium Chemistry for Organic Synthesis*, John Wiley & Sons, **2002**.
- [233] H. G. Brittain, G. Meyer, *J. Solid State Chem.* **1985**, *59*, 183–189.
- [234] I. Díaz, V. Fernández, J. L. Martínez, L. Beyer, A. Pilz, U. Müller, *Zeitschrift für Naturforsch.* **1998**, *53*, 933–938.
- [235] C. M. Tollan, R. Marcilla, J. A. Pomposo, J. Rodriguez, J. Aizpurua, J. Molina, D. Mecerreyes, *ACS Appl. Mater. Interfaces* **2009**, *1*, 348–352.
- [236] R. Bhattacharya, M. Sinha Ray, R. Dey, L. Righi, G. Bocelli, A. Ghosh, *Polyhedron* **2002**, *21*, 2561–2565.
- [237] M. Kronstein, K. Kriechbaum, J. Akbarzadeh, H. Peterlik, M.-A. Neouze, *Phys. Chem. Chem. Phys.* **2013**, *15*, 12717–12723.
- [238] R. D. Willett, J. A. Haugen, J. Lebsack, J. Morrey, *Inorg. Chem.* **1974**, *13*, 2510–2513.
- [239] W. Zawartka, A. Gniewek, A. M. Trzeciak, J. J. Ziółkowski, J. Pernak, *J. Mol. Catal. A Chem.* **2009**, *304*, 8–15.
- [240] G. Blasse, *J. Chem. Phys.* **1966**, *45*, 2356–2360.
- [241] V. Ravi Kumar, N. Veeraiah, B. Appa Rao, S. Bhuddudu, *J. Mater. Sci.* **1998**, *33*, 2659–2662.
- [242] C.-C. Lin, K.-M. Lin, Y.-Y. Li, *J. Lumin.* **2007**, *126*, 795–799.

- [243] Z. Tao, T. Tsuboi, Y. Huang, W. Huang, P. Cai, H. J. Seo, *Inorg. Chem.* **2014**, *53*, 4161–4168.
- [244] I. L. V Rosa, L. H. Oliveira, E. Longo, J. A. Varela, *J. Fluoresc.* **2011**, *21*, 975–981.
- [245] K. Lunstroot, K. Driesen, P. Nockemann, C. Görrler-Walrand, K. Binnemans, S. Bellayer, J. Le Bideau, A. Vioux, *Chem. Mater.* **2006**, *18*, 5711–5715.
- [246] A. Schoenberg, R. F. Heck, *J. Am. Chem. Soc.* **1974**, *96*, 7761–7764.
- [247] A. De Meijere, F. E. Meyer, *Angew. Chemie* **1994**, *106*, 2473–2506.
- [248] A. R. Lim, *Chem. Phys.* **2014**, *436-437*, 46–50.
- [249] C. Changyun, Z. Zhihua, Z. Yiming, D. Jiangyan, *J. Chem. Educ.* **2000**, *77*, 1206–1207.
- [250] A. J. Swarts, S. F. Mapolie, *Dalton Trans.* **2014**, *43*, 9892–9900.
- [251] A. Chinnappan, A. H. Jadhav, H. Kim, W.-J. Chung, *Chem. Eng. J.* **2014**, *237*, 95–100.
- [252] C. Wang, H. Luo, X. Luo, H. Li, S. Dai, *Green Chem.* **2010**, *12*, 2019–2023.
- [253] A.-L. Revelli, F. Mutelet, J.-N. Jaubert, *J. Phys. Chem. B* **2010**, *114*, 12908–12913.
- [254] W. Shi, D. C. Sorescu, *J. Phys. Chem. B* **2010**, *114*, 15029–15041.
- [255] Y. Chen, Z. Hu, K. M. Gupta, J. Jiang, *J. Phys. Chem. C* **2011**, *115*, 21736–21742.
- [256] K. M. Gupta, Y. Chen, Z. Hu, J. Jiang, *Phys. Chem. Chem. Phys.* **2012**, *14*, 5785–5794.
- [257] K. M. Gupta, Y. Chen, J. Jiang, *J. Phys. Chem. C* **2013**, *117*, 5792–5799.
- [258] L. E. Kreno, K. Leong, O. K. Farha, M. Allendorf, R. P. Van Duyne, J. T. Hupp, *Chem. Rev.* **2012**, *112*, 1105–1125.
- [259] O. Tziolla, C. Veziri, X. Papatryfon, K. G. Beltsios, A. Labropoulos, B. Iliev, G. Adamova, T. J. S. Schubert, M. C. Kroon, M. Francisco, et al., *J. Phys. Chem. C* **2013**, *117*, 18434–18440.
- [260] T. Sakakura, K. Kohno, *Chem. Commun. (Camb)*. **2009**, 1312–1330.
- [261] B. Schöffner, F. Schöffner, S. P. Verevkin, A. Börner, *Chem. Rev.* **2010**, *110*, 4554–4581.
- [262] C. M. White, B. R. Strazisar, E. J. Granite, J. S. Hoffman, H. W. Pennline, *J. Air Waste Manage. Assoc.* **2003**, *53*, 645–715.
- [263] A. Ansmann, B. Boutty, M. Dierker, *Dialkylcarbonates of Branched Alcohols and Their Use in Cosmetic Emulsions*, **2008**, EP 1930331.
- [264] K. Xu, *Chem. Rev.* **2004**, *104*, 4303–4418.
- [265] J. Peng, Y. Deng, *New J. Chem.* **2001**, *25*, 639–641.

- [266] M. H. Anthofer, M. E. Wilhelm, M. Cokoja, I. I. E. Markovits, A. Pöthig, J. Mink, W. A. Herrmann, F. E. Kühn, *Catal. Sci. Technol.* **2014**, *4*, 1749–1758.
- [267] S. Ghazali-Esfahani, H. Song, E. Păunescu, F. D. Bobbink, H. Liu, Z. Fei, G. Laurenczy, M. Bagherzadeh, N. Yan, P. J. Dyson, *Green Chem.* **2013**, *15*, 1584–1589.
- [268] A.-L. Girard, N. Simon, M. Zanatta, S. Marmitt, P. Gonçalves, J. Dupont, *Green Chem.* **2014**, *16*, 2815–2825.
- [269] S. Udayakumar, S.-W. Park, D.-W. Park, B.-S. Choi, *Catal. Commun.* **2008**, *9*, 1563–1570.
- [270] T. Sakai, Y. Tsutsumi, T. Ema, *Green Chem.* **2008**, *10*, 337–341.
- [271] W.-L. Dai, S.-F. Yin, R. Guo, S.-L. Luo, X. Du, C.-T. Au, *Catal. Letters* **2009**, *136*, 35–44.
- [272] Y.-Y. Zhang, L. Chen, S.-F. Yin, S.-L. Luo, C.-T. Au, *Catal. Letters* **2012**, *142*, 1376–1381.
- [273] J. Song, Z. Zhang, S. Hu, T. Wu, T. Jiang, B. Han, *Green Chem.* **2009**, *11*, 1031–1036.
- [274] O. V. Zalomaeva, A. M. Chibiryayev, K. A. Kovalenko, O. A. Kholdeeva, B. S. Balzhinimaev, V. P. Fedin, *J. Catal.* **2013**, *298*, 179–185.
- [275] T. Sakakura, J.-C. Choi, H. Yasuda, *Chem. Rev.* **2007**, *107*, 2365–2387.
- [276] M. North, R. Pasquale, C. Young, *Green Chem.* **2010**, *12*, 1514–1539.
- [277] J.-Q. Wang, K. Dong, W.-G. Cheng, J. Sun, S.-J. Zhang, *Catal. Sci. Technol.* **2012**, *2*, 1480–1484.
- [278] Y. Xie, Z. Zhang, T. Jiang, J. He, B. Han, T. Wu, K. Ding, *Angew. Chem. Int. Ed. Engl.* **2007**, *46*, 7255–7258.
- [279] K. Qiao, F. Ono, Q. Bao, D. Tomida, C. Yokoyama, *J. Mol. Catal. A Chem.* **2009**, *303*, 30–34.
- [280] C. Aprile, F. Giacalone, P. Agrigento, L. F. Liotta, J. A. Martens, P. P. Pescarmona, M. Gruttadauria, *ChemSusChem* **2011**, *4*, 1830–1837.
- [281] J. Roeser, M. Kronstein, M. Litschauer, A. Thomas, M.-A. Neouze, *Eur. J. Inorg. Chem.* **2012**, 5305–5311.
- [282] C. M. Miralda, E. E. Macias, M. Zhu, P. Ratnasamy, M. A. Carreon, *ACS Catal.* **2012**, *2*, 180–183.
- [283] M.-A. Neouze, M. Litschauer, M. Puchberger, H. Peterlik, *Langmuir* **2011**, *27*, 4110–4116.
- [284] M.-A. Neouze Gauthey, M. Litschauer, M. Puchberger, M. Kronstein, H. Peterlik, *J. Nanoparticles* **2013**, *2013*, 1–9.
- [285] J. He, T. Wu, Z. Zhang, K. Ding, B. Han, Y. Xie, T. Jiang, Z. Liu, *Chemistry* **2007**, *13*, 6992–6997.
- [286] J. Sun, J. Ren, S. Zhang, W. Cheng, *Tetrahedron Lett.* **2009**, *50*, 423–426.

- [287] X. Zheng, S. Luo, L. Zhang, J.-P. Cheng, *Green Chem.* **2009**, *11*, 455–458.
- [288] D. Yu, Y. Zhang, *Proc. Natl. Acad. Sci. U. S. A.* **2010**, *107*, 20184–20189.
- [289] H. Zhou, W.-Z. Zhang, C.-H. Liu, J.-P. Qu, X.-B. Lu, *J. Org. Chem.* **2008**, *73*, 8039–8044.
- [290] M. Besnard, M. I. Cabaço, F. V. Chávez, N. Pinaud, P. J. Sebastião, J. A. P. Coutinho, Y. Danten, *Chem. Commun. (Camb)*. **2012**, *48*, 1245–1247.
- [291] L. Yang, H. Wang, *ChemSusChem* **2014**, *7*, 962–998.
- [292] C. Das Neves Gomes, E. Blondiaux, P. Thuery, T. Cantat, *Chem. (Weinheim an der Bergstrasse, Ger. J.)* **2014**, *20*, 7098–7106.
- [293] S. D. Bergman, F. Wudl, *J. Mater. Chem.* **2008**, *18*, 41–62.
- [294] R. J. Wojtecki, M. a Meador, S. J. Rowan, *Nat. Mater.* **2011**, *10*, 14–27.
- [295] C. N. Bowman, C. J. Kloxin, *Angew. Chem. Int. Ed. Engl.* **2012**, *51*, 4272–4274.
- [296] S. K. Gosh, *Self-Healing Materials - Fundamentals, Design Strategies and Applications*, Wiley-VCH, Weinheim, **2009**.
- [297] X. Chen, M. A. Dam, K. Ono, A. Mal, H. Shen, S. R. Nutt, K. Sheran, F. Wudl, *Science* **2002**, *295*, 1698–1702.
- [298] D. Montarnal, M. Capelot, F. Tournilhac, L. Leibler, *Science* **2011**, *334*, 965–968.
- [299] M. Capelot, D. Montarnal, F. Tournilhac, L. Leibler, *J. Am. Chem. Soc.* **2012**, *134*, 7664–7667.
- [300] M. Capelot, M. M. Unterlass, F. Tournilhac, L. Leibler, *ACS Macro Lett.* **2012**, *1*, 789–792.
- [301] M. M. Unterlass, *Priv. Commun.* **2014**.
- [302] M. Morán, I. Cuadrado, J. R. Masaguer, J. Losada, *J. Organomet. Chem.* **1987**, *335*, 255–268.
- [303] B. J. Blaiszik, N. R. Sottos, S. R. White, *Compos. Sci. Technol.* **2008**, *68*, 978–986.
- [304] P. V. Ramachandran, D. Nicponski, B. Kim, *Org. Lett.* **2013**, *15*, 1398–1401.
- [305] G. Kresse, J. Hafner, *Phys. Rev. B* **1993**, *47*, 558–561.
- [306] G. Kresse, J. Hafner, *Phys. Rev. B* **1994**, *49*, 14251–14269.
- [307] J. P. Perdew, K. Burke, M. Ernzerhof, *Phys. Rev. Lett.* **1996**, *77*, 3865–3868.
- [308] J. P. Perdew, K. Burke, M. Ernzerhof, *Phys. Rev. Lett.* **1997**, *78*, 1396–1396.
- [309] A. Wojtaszek, I. Sobczak, M. Ziolek, F. Tielens, *J. Phys. Chem. C* **2009**, *113*, 13855–13859.
- [310] A. Wojtaszek, I. Sobczak, M. Ziolek, F. Tielens, *J. Phys. Chem. C* **2010**, *114*, 9002–9007.

-
- [311] P. E. Blöchl, O. Jepsen, O. K. Andersen, *Phys. Rev. B* **1994**, *49*, 17953–17979.
- [312] G. Kresse, D. Joubert, *Phys. Rev. B* **1999**, *59*, 1758–1775.
- [313] P. Giannozzi, S. Baroni, N. Bonini, M. Calandra, R. Car, C. Cavazzoni, D. Ceresoli, G. L. Chiarotti, M. Cococcioni, I. Dabo, et al., *J. Phys. Condens. Matter* **2009**, *21*, 395502.
- [314] N. Troullier, J. L. Martins, *Phys. Rev. B* **1993**, *43*, 1993–2006.
- [315] L. Kleinman, D. Bylander, *Phys. Rev. Lett.* **1982**, *48*, 1425–1428.
- [316] C. Pickard, F. Mauri, *Phys. Rev. B* **2001**, *63*, 245101/1–245101/13.
- [317] F. Tielens, C. Gervais, J. F. Lambert, F. Mauri, D. Costa, *Chem. Mater.* **2008**, *20*, 3336–3344.
- [318] M. M. Islam, D. Costa, M. Calatayud, F. Tielens, *J. Phys. Chem. C* **2009**, *113*, 10740–10746.
- [319] H. Guesmi, F. Tielens, *J. Phys. Chem. C* **2012**, *116*, 994–1001.
- [320] N. Folliet, C. Roiland, S. Bégu, A. Aubert, T. Mineva, A. Goursot, K. Selvaraj, L. Duma, F. Tielens, F. Mauri, et al., *J. Am. Chem. Soc.* **2011**, *133*, 16815–16827.
- [321] N. Folliet, C. Gervais, D. Costa, G. Laurent, F. Babonneau, L. Stievano, J.-F. Lambert, F. Tielens, *J. Phys. Chem. C* **2013**, *117*, 4104–4114.
- [322] B. P. Feuston, S. H. Garofalini, *J. Appl. Phys.* **1990**, *68*, 4830–4836.
- [323] L. V. Woodcock, *J. Chem. Phys.* **1976**, *65*, 1565–1577.
- [324] J. Z. Vlahakis, S. Mitu, G. Roman, E. Patricia Rodriguez, I. E. Crandall, W. A. Szarek, *Bioorg. Med. Chem.* **2011**, *19*, 6525–6542.